Insights into the plasma and beam physics close to the extraction surface in H^-/D^- sources for fusion based on 3D-PIC MCC modeling

Dissertation

zur Erlangung des akademischen Grades

Dr. rer. nat.

eingereicht an der

Mathematisch-Naturwissenschaftlich-Technischen Fakultät

der Universität Augsburg

von

Max Lindqvist

Augsburg, November 7, 2024

Tag der mündlichen Prüfung: 2024-11-07

Erste Gutachterin: apl. Prof. Dr.-Ing. Ursel Fantz

Zweiter Gutachter: Prof. Tiberiu Minea

THESE DE DOCTORAT

NNT : 2024UPASP133

Insights into the plasma and beam physics close to the extraction surface in H^-/D^- sources for fusion based on 3D-PIC MCC modeling

Aperçu de la physique des plasmas et des faisceaux à proximité de la surface d'extraction dans les sources H^-/D^- pour la fusion basée sur la modélisation 3D-PIC MCC

Thèse de doctorat de l'université Paris-Saclay et de l'université d'Augsbourg

École doctorale n° 572, Ondes et Matière (EDOM)
Spécialité de doctorat : Physique
Graduate School : Physique
Référent : Faculté des sciences d'Orsay

Thèse préparée dans les unités de recherche **Laboratoire de Physique des Gaz et des Plasmas (Université Paris-Saclay, CNRS)** et **Max Planck Institute for Plasma Physics (University of Augsburg)**, sous la direction de **Tiberiu MINEA**, Professeur des Universités, et la co-direction de **Ursel FANTZ**, Professeur

Thèse soutenue à Augsburg, le 07 Novembre 2024, par

Max LINDQVIST

Composition du jury

Membres du jury avec voix délibérative

Wolfgang BRÜTTING Professeur, Université d'Augsbourg	Président
Francesco TACCOGNA Chercheur (équiv. HDR), Istituto per la Scienza e Tecnologia dei Plasmi	Rapporteur & Examinateur
Thomas MUSSENBROCK Professeur, Université de la Ruhr à Bochum	Rapporteur & Examinateur
Gert-Ludwig INGOLD Professeur, Université d'Augsbourg	Examinateur
Adrien REVEL Ingénieur de Recherche, Université Paris-Saclay, CNRS	Examinateur

université PARIS-SACLAY | ÉCOLE DOCTORALE Ondes et matière (EDOM)

Titre : Aperçu de la physique des plasmas et des faisceaux à proximité de la surface d'extraction dans les sources H^-/D^- pour la fusion basée sur la modélisation 3D-PIC MCC
Mots clés : source d'ions, physique du plasma, particle-in-cell, modélisation

Résumé : Les ions négatifs d'hydrogène et de deutérium pour le système d'injecteur de neutres d'ITER sont produits dans des sources ioniques radio-fréquences, principalement par production de surface, et accélérés à travers un système de diaphragmes multiples. Un des principaux facteurs limitants durant l'opération de telles sources ioniques est la quantité d'électrons co-extraits, en particulier en opérant avec du deutérium. Pour une description précise de la dynamique des particules près de la grille plasma (PG), où se trouve une configuration magnétique tridimensionnelle, une modélisation 3D-PIC MCC est requise.

Le code 3D-PIC MCC a été utilisé pour simuler un des diaphragmes de la PG de la source d'ions ELISE à l'IPP Garching, un analogue à l'échelle un-demi de la source d'ions d'ITER. Le code original a d'abord été amélioré en ajoutant un module de génération de plasma permettant de modéliser la polarisation de la PG par rapport aux parois de la source. ONIX a été couplé avec le code de modélisation de faisceau IBSimu pour permettre la corrélation des propriétés des particules du plasma au faisceau. Ceci permet d'étudier la probabilité d'extraction, la divergence du faisceau d'ions négatifs dans différentes configurations et géométries de la PG, et fournit des renseignements sur l'optimisation de la grille.

L'impact des paramètres plasma, de la polarisation de la grille plasma, et de la géométrie sur la co-extraction d'éléctrons est présenté. En augmentant la polarisation de la PG au dessus du potentiel flottant, la quantité et l'instabilité temporelle des électrons co-extraits est fortement réduite, en accord avec l'expérience. De plus, une température électronique moindre, autour d'1 eV, peut réduire la quantité d'électrons co-extraits par un facteur 4 par rapport à 2 eV. Bien que les géométries de la PG n'aient pas eu d'impact significatifs sur la co-extraction d'électrons, l'angle de la face de la PG exposée au plasma affecte la probabilité d'extraction et l'accumulation d'ions négatifs produits en surface (H^-_{SP}) à cause de l'accélération par la gaine de Debye. Avec un angle réduit, plus d'ions sont transportés vers la région centrale près du ménisque, résultant en une plus faible divergence au cœur.

Pour de futurs travaux, il est important de développer un procédé physique autocohérent de modélisation de l'accumulation d'ions H^-_{SP} dans le volume du plasma. Les contraintes inhérentes aux modélisations 3D-PIC MCC imposées par les échelles temporelles et spatiales du domaine représentent un défi pour cela. Actuellement, il n'a pas été possible de reproduire dans une simulation 3D-PIC MCC la densité mesurée expérimentalement d'ions H^-_{SP}.

université PARIS-SACLAY

ÉCOLE DOCTORALE
Ondes et matière
(EDOM)

Title : Insights into the plasma and beam physics close to the extraction surface in H^-/D^- sources for fusion based on 3D-PIC MCC modeling

Keywords : ion sources, plasma physics, particle-in-cell, modeling

Abstract : Negative hydrogen or deuterium ions for the ITER Neutral Beam Injection system are produced in radio-frequency ion sources, mainly by surface production, and accelerated through a multi-aperture grid system. One of the main limiting factors during the operation of such ion sources is the amount of co-extracted electrons, particularly during operation with D. For a correct description of the particle dynamics close to the Plasma Grid (PG), where a 3D magnetic field is present, self-consistent 3D-PIC MCC modeling is needed.

The 3D-PIC MCC code ONIX has been used to simulate one PG aperture in the ELISE ion source, a half-size ITER-like prototype ion source at IPP Garching. The original code was improved by adding a plasma generation module that allows modeling the biasing of the PG with respect to the source walls. ONIX was coupled with the beam code IBSimu to allow the correlation of particle properties from the plasma to the beam and to study the extraction probability and beam divergence of negative ions during different configurations of PG biases and PG geometries, providing insights into grid optimization.

The impact of plasma parameters, PG bias, and geometry of the grid on the co-extraction of electrons is presented. By increasing the PG bias above the floating potential, the amount and temporal instability of co-extracted electrons are strongly decreased, in agreement with experiments. Additionally, a lower electron temperature of around 1 eV can reduce the amount of co-extracted electrons by a factor of 4 compared to 2 eV. While the PG geometries studied did not have a significant impact on the co-extraction of electrons, the plasma-facing angle of the PG affects the extraction probability and accumulation of surface-produced negative ions (H^-_{SP}) due to the acceleration by the Debye sheath. With a shallow angle, more ions are transported to the central region near the meniscus, resulting in a lower core divergence.

As for future work, developing a self-consistent physical process for simulating the accumulation of H^-_{SP} ions in the plasma volume is important. This is challenging due to the time scale and domain size constraints inherent in 3D-PIC MCC modeling. As of now, achieving the experimentally measured density of H^-_{SP} ions has not been realized in 3D-PIC MCC simulations.

Résumé étendu de la thèse

La fusion nucléaire représente une solution prometteuse aux défis énergétiques mondiaux en offrant une source d'énergie durable, abondante, peu polluante, et sûre. À partir de 2024, le projet ITER est la plus grande entreprise dans le domaine de l'énergie de fusion, avec le plus grand tokamak au monde, un dispositif toroïdal conçu pour confiner un plasma chaud à l'aide de champs magnétiques puissants. ITER vise à réaliser une fusion nucléaire auto-entretenue dans un plasma de deutérium-tritium et à démontrer l'obtention d'un rendement énergétique positif $Q > 1$, c'est-à-dire que la puissance produite est supérieure à la puissance de chauffage. Pour atteindre les températures très élevées nécessaires pour que la fusion se produise ($150,000,000°$C), le plasma du tokamak et particulièrement les ions (bien plus lourds que les électrons) sont chauffés de l'extérieur par injection de faisceaux de neutres (NBI) énergétiques fournissant 33 MW. Cette technique s'additionne à celles par micro-ondes pour le chauffage des électrons par Résonance Cyclotronique Électronique (ECRH, 20 MW), et pour le chauffage des ions par Résonance Cyclotronique Ionique (ICRH, aussi 20 MW).

Le système NBI d'ITER repose sur la génération, l'extraction, l'accélération et la neutralisation d'ions négatifs (NI) pour produire des neutres de très haute énergie (1 MeV). Les neutres énergétiques ainsi créés sont injectés dans le tokamak, où ils déposent leur énergie par collisions dans le plasma. A l'origine, les ions négatifs (H^- et D^-) sont générés dans des sources d'ions à basse température et à basse pression, pilotées par radiofréquence (RF). Le mécanisme principal est l'ionisation de surface qui permet la transformation de l'hydrogène (ou ses isotopes) neutre en ion négatif lors de l'interaction avec les surfaces internes (SP pour "surface production" H^-, notés H^-_{SP}) des sources d'ions. Toutefois, une minorité (typiquement 10%) de H^- est produite dans le volume du plasma (VP pour "volume production" H^-, notés H^-_{VP}). Un champ magnétique externe parallèle à la grille côté plasma ($\mathbf{B}_{FF}$) est utilisé pour réduire la température et la densité des électrons, minimisant ainsi la destruction des ions négatifs par collisions avec les électrons énergétiques du plasma.

Les ions sont extraits à travers 1280 orifices (apertures) dans la grille plasma (PG) de 2×1 m et accélérés par des champs électrostatiques jusqu'à une énergie cinétique de 1 MeV par l'intermédiaire d'un système multi-grilles à ouvertures multiples. Juste devant le plasma, le potentiel d'extraction est 10 kV entre la grille plasma et la grille d'extraction (EG), permettant l'accélération initiale des ions.

Quand les H^-_{SP} sont produits à la surface, un puits de potentiel se forme juste devant cette surface avec un minimum local dû à l'accumulation de la charge d'espace négative des ions H^-_{SP},

structure appelée Cathode Virtuelle (VC). La présence de la VC limite le taux effectif d'émission des ions H^-_{SP}, c'est-à-dire le nombre de NIs qui peuvent rejoindre le volume du plasma, par un phénomène de "réflexion" lors de la rencontre du puits de potentiel négatif.

A l'état stationnaire, la surface équipotentielle nulle désigne le ménisque. Cette surface se forme entre le plasma quasi-neutre d'une part de la PG et le faisceau de NI, d'autre part. Le ménisque agit comme une surface d'émission de particules chargées, marquant le début de la région d'accélération des charges négatives contenues dans le plasma alors qu'il réfléchit les ions positifs vers le plasma. Ainsi, outre les ions négatifs, des électrons quittent également le plasma à travers le ménisque. Un champ magnétique de déflexion ($\mathbf{B}_{\mathrm{DF}}$), perpendiculairement au $\mathbf{B}_{\mathrm{FF}}$, permet de les dévier vers la EG. $\mathbf{B}_{\mathrm{DF}}$ est généré par des barres d'aimants permanents insérées dans la EG avec des polarités alternées. L'impact des électrons sur la EG génère de la chaleur. Afin de limiter l'apport en calories, la densité d'électrons co-extraits doit être maintenue inférieure à celle des ions négatifs, et ceci pendant toute la durée de fonctionnement de la source. Un premier défi est donc de limiter l'extraction d'électrons et assurer la stabilité temporelle du système (pour une durée $\sim$ 1 h), en particulier pendant le fonctionnement avec du deutérium. Le NBI d'ITER doit travailler en H et en D, exigeant l'étude des deux isotopes. Les expériences menées ont montré que le remplacement de l'hydrogène avec du deutérium augmente la quantité d'électrons co-extraits particulièrement pour un fonctionnement à haute densité. Ceci engendre l'utilisation d'un filtre magnétique $\mathbf{B}_{\mathrm{FF}}$ plus intense, afin de limiter le phénomène.

Dans les deux prototypes expérimentaux développés au IPP - Large Ion Source Experiment (ELISE) et BATMAN Upgrade (BUG) pour produire et extraire des ions négatifs d'un plasma, une électrode additionnelle - Bias Plate (BP) est placée à côté de la PG et elle est connectée à la source de tension continue, mais isolée électriquement de la PG. La BP sert à contrôler le potentiel plasma à proximité de la PG et limiter ainsi le transport des électrons vers l'aperture d'extraction. En polarisant positivement la PG par rapport à la BP et les parois de la source, il a été montré expérimentalement la réduction du courant des électrons co-extraits.

Pour décrire précisément la physique sous-jacente dans la zone d'extraction il est nécessaire d'avoir une bonne représentation de la topologie spécifique 3D des champs magnétiques, des interactions entre les particules composant le plasma en volume, des espèces du plasma avec les surfaces, et du système de grilles. Ces processus impliquent la présence des phénomènes 3D complexes, dépendant de la topologie 3D du champ magnétique, des caractéristiques du plasma dans la source, du champ électrique d'extraction, et de l'optique électro-magnétique du faisceau. Les approches expérimentales et analytiques sont souvent limitées pour décrire finement cette

zone. Il est donc nécessaire de prédire numériquement par le biais de la modélisation et la simulation l'extraction d'ions négatifs et les phénomènes associés.

La modélisation des processus engendrés dans le plasma dans la région avoisinant la grille peut être traitée par différents modèles. Les simulations fluides traitent l'ensemble de la source RF, mais elles considèrent les électrons en équilibre de Maxwell. De plus, elles traitent difficilement les gaines et n'ont pas de résolution microscopique pour les quantités représentative du plasma. Les modèles particulaires (Particle-in-cell - PIC), s'appuyant sur la description de la fonction de distribution en énergie des espèces, semblent bien plus adaptés pour simuler l'extraction des particules chargées du plasma et la formation du faisceau dans un système à grille. Ainsi, pour la simulation de la région d'accélération des NIs, un modèle PIC 3D avec un traitement Monte Carlo des collisions (Monte Carlo Collisions - MCC) a été employé. Ces modèles incluent les processus collisionnels, la formation du ménisque, les effets des champs $\mathbf{B}_{\mathrm{FF}}$ et $\mathbf{B}_{\mathrm{DF}}$ sur le transport des espèces. Toutefois, ils demandent des ressources numériques significatives imposées par la haute densité du plasma et le besoin de respecter des critères de stabilité numérique (taille de grille, pas de temps, nombre moyen de particules par cellule, etc.).

La réduction dimensionnelle et la simulation des plasmas de moindre densité ont permis de pallier aux problèmes complexes évoqués et de rendre abordable numériquement ce problème. Avec des modèles 1D et 2D, pour des géométries simplifiées, il est possible de capturer certains effets des champs magnétiques. Les modèles 2,5D ajoutent de la complexité par la prise en compte des vitesses en 3D, mais réduisant le domaine simulé à un plan (2D). Les modèles complets 3D simulent naturellement l'ensemble des phénomènes, mais ils nécessitent des ressources numériques considérables, par exemple des calculs parallèles sur des super-calculateurs ou des clusters. Les approches avec changement d'échelle aident à réaliser des simulations sur de larges domaines, mais la clé de leur succès repose sur la connaissance fine des paramètres plasma, données fournies par l'expérience.

Cette thèse exploite des simulations 3D PIC-MCC avec le code Orsay Negative Ion eXtraction (ONIX) pour étudier le processus d'extraction d'ions négatifs et d'électrons co-extraits dans des conditions réalistes, sans changement d'échelle des paramètres plasma. Les simulations sont basées sur les paramètres plasma mesurés à l'Institut Max Planck de Physique des Plasmas (IPP), en particulier les expériences ELISE et BUG, qui servent de prototypes pour le système NBI d'ITER. De plus, des simulations avec des plasmas de moindre densité et des domaines 1D ont permis de réaliser des études paramétriques dans un temps réduit. Ces recherches incluent des interactions à longue portée, l'influence de la polarisation de la BP et l'étude des pertes électroniques le long des lignes de champ magnétique. Les résultats obtenus donnent des

informations sur la façon dont le plasma et les conditions de création des ions négatifs affectent la mise en forme du faisceau.

Plusieurs améliorations du code ONIX ont été mises en œuvre au cours de cette thèse. Parmi les contributions majeures, on note, d'une part, le développement d'un nouveau schéma d'injection de particules pour permettre la polarisation de la PG par rapport au plasma. D'autre part, le code a été révisé pour inclure des géométries plus complexes, par exemple la possibilité de simuler de multiples apertures d'extraction dans la PG. Enfin, ONIX a également été couplé au code d'optique ionique IBSimu (Ion Beam Simulator) afin d'étendre le domaine de calcul du plasma jusqu'à la dernière grille du système d'accélération en laboratoire afin de décrire les propriétés d'un faisceau singulier (beamlet, généré par une seule aperture).

L'injection de particules chargées dans la région du plasma quasi-neutre peut être faite par différentes méthodes dans un modèle PIC, par exemple l'injection de paires (électron-ion) ou l'injection des flux de particules chargées. L'injection de paires est la plus courante dans les modèles particulaires incluant des NI. La simulation démarre avec une distribution uniforme d'électrons et d'ions dans un volume délimité du plasma, zone nommée 'région d'injection'. Les ions H^-_{VP} sont re-injectés quand ils quittent le volume de simulation tout comme les ions positifs mais avec un électron (paire ion-électron). La quantité totale d'électrons dans le domaine de simulation évolue ainsi au cours de la simulation. Quant aux ions H^-_{SP}, ils sont perdus quand ils quittent le domaine de simulation. De plus, les électrons sont thermalisés dans la région d'injection pour éviter leur refroidissement artificiel. La technique d'injection de paires dans le plasma est comparée à celle d'injection des flux contrôlés de particules chargés à travers un plan (virtuel dans le plasma) afin d'obtenir les densités de particules souhaitées.

La technique d'injection de paires permet à l'utilisateur de fixer la densité du plasma dans la région d'injection au début de la simulation. Au fur et à mesure que le plasma évolue, l'ensemble des densités diminue car le plasma diffuse dans le volume de simulation. Cependant, cette approche évite d'imposer des flux aux frontières. En revanche, avec l'approche d'injection des flux, il est possible de contrôler l'apport de particules à travers les surfaces, notamment à travers un plan choisi. De plus, il est possible d'imposer un profil de potentiel plasma plat à travers cette frontière. Cette situation est semblable à celle d'un plasma, sans gaine de Debye dans son volume (ou au voisinage du plan virtuel). Enfin, la méthode des flux laisse au plasma une zone plus large d'évolution auto-cohérente, pour un même domaine de simulation, puisqu'il n'y a pas de région de thermalisation. Les flux de particules chargées injectées à travers ce plan sont régulés de telle façon que les paramètres plasma voulus sont obtenus.

Comme le domaine d'évolution du plasma se trouve élargi avec la méthode des flux, les électrons

du plasma peuvent circuler le long des lignes de champ magnétique sans traverser une zone de thermalisation (artificielle). Ainsi, l'effet de la thermalisation sur les trajectoires électroniques a été étudié en comparant les trajectoires des électrons avec et sans thermalisation. Il a été démontré que la thermalisation réduit le transport des électrons le long de $\mathbf{B}_{\mathrm{FF}}$. Sans thermalisation, 29,2% des électrons sont extraits par la même aperture correspondant au domaine d'injection, alors qu'en présence de la thermalisation 46% d'entre eux quittent le domaine par cette même aperture. La méthode d'injection des flux permet d'enlever ce biais du code puisque les électrons ne sont pas thermalisés.

Des simulations ont été réalisées afin d'étudier l'impact des paramètres plasma sur les NIs extraits et les électrons co-extraits. Deux cas ont été comparés de manière poussée et pour une seule aperture, afin de comprendre le rôle joué par la densité du plasma, la température électronique, le taux de production de H^- à la surface (H^-_{SP}), la formation du ménisque et du potentiel plasma. Dans un premier temps, les paramètres de la source d'ions BATMAN ont été utilisés, avec $\mathbf{B}_{\mathrm{FF}}$ généré par des aimants permanents - cas nommé haute-densité/basse-température (HD/LT) et dans un second temps, les conditions de la source ELISE et BUG ont servis de données d'entrée, avec le champ magnétique filtre généré par un courant continu traversant la PG, - cas nommé basse-densité/haute température (LD/HT). Les différences majeures sont la valeur de la température électronique, deux fois supérieure pour LD/HT, alors que la densité plasma est deux fois plus grande dans le cas HD/LT ainsi que la production de NI à la surface.

Pour une densité plasma réduite, le ménisque pénètre davantage dans le plasma pour le cas LD/HT. La température électronique supérieure (2 eV par rapport à 1 eV) et un ménisque plus profond se traduit par une augmentation du courant d'électrons co-extrait dans le cas LD/HT. Malgré la réduction de 64% de la production d'NIs à la surface, valeur considérée dans cette simulation, la densité de H^- extraite diminue de seulement 11%, car de nombreux ions H^-_{SP} sont directement extraits. La cathode virtuelle (VC) et la gaine devant la PG sont distribuées de manière non-uniforme avec un puits de potentiel de 1,1 V de la VC dans le cas LD/HT alors que la valeur extrême du puits atteint 1,5 V dans le cas HD/LT, localisée à environ 0,5 mm de la région d'ancrage du ménisque dans les deux cas.

La comparaison des courants extraits dans le deux cas, HD/LT and LD/HT, montre que pour une même production de H^- à la surface de la PG, les conditions LD/HT favorisent l'extraction d'ions négatifs de 25% de la paroi, mais également 3 fois plus (300%) d'électrons sont co-extraits, et 50% de H^- du volume en moins. Ce sont des effets induits par la pénétration plus profonde du ménisque, mais également de l'augmentation de l'énergie moyenne des électrons. Les conditions

pour le fonctionnement en deutérium ont aussi été simulées par PIC 3D visant à expliquer les résultats expérimentaux qui ont constaté une augmentation du courant d'électrons co-extrait et une réduction de la quantité d'ions négatifs (D^-) dans le faisceau. Le potentiel plasma étant supérieur à celui du plasma d'hydrogène, il réduit le flux d'électrons vers la PG et favorise l'accumulation d'électrons devant le ménisque. La conséquence directe est l'augmentation du nombre d'électrons accompagnant le faisceau de D^- extrait. Par ailleurs, la masse plus grande du D est responsable de l'augmentation du potentiel plasma. L'effet de la polarisation de la grille plasma (PG) a été étudié, particulièrement sur la quantité d'électrons extraits du plasma et les propriétés du plasma à proximité de la PG. À la fois les résultats des simulations et expérimentaux démontrent qu'en polarisant la PG au-dessus du potentiel flottant, les électrons y sont attirés, induisant immédiatement une réduction du nombre d'électrons devant le ménisque et donc une réduction de leur extraction. De plus, l'introduction de surfaces polarisées, telles que l'Electron Fence (EF), réduit considérablement le courant d'électrons co-extraits. De plus, l'usage d'une EF de rayon 2,5 mm à proximité de la PG a montré des résultats encourageants expérimentalement avec une réduction du courant d'électrons co-extraits. Dans la simulation, une EF est considérée comme une barre cylindrique parallèle à chaque rangée d'apertures, proche de la PG. Les calculs montrent une réduction significative du courant d'électrons co-extrait notamment en polarisant l'EF proche du potentiel plasma. Sans EF, les électrons dérivent en grande proportion d'une aperture vers une autre, en direction horizontale (le long de $\mathbf{B}_{\mathrm{FF}}$), avant l'extraction. Quand cette électrode electron fence' est présente et polarisée convenablement, elle collecte de nombreux électrons du plasma, proche de la zone d'extraction. Comme la BP n'a pas été incluse dans le domaine de simulation ONIX, des comparaisons peuvent être réalisées entre les simulations avec EF et avec BP.

Le couplage entre ONIX et un code de simulation de l'optique ionique IBSimu a été réalisé afin d'étendre le domaine de simulation à la région des grilles d'accélération et d'obtenir des informations sur les caractéristiques du faisceau (beamlet). Ceci met en évidence l'impact de la connaissance fine des paramètres plasma proche de la région d'extraction qui sont souvent négligés dans les modèles de faisceau. Il a été montré que l'extraction directe des NIs, notamment proche de l'angle de biseau de l'aperture de la PG côté plasma, est responsable de la grande divergence du faisceau. Comme attendu, si la composante transverse de l'énergie cinétique augmente, ceci accroît la divergence finale même pour les NIs quittant le ménisque dans la zone centrale (provenant du plasma et non de la surface). En revanche, la présence de la gaine de Debye entre le plasma et la PG réduit la divergence de H^-_{VP}, car la gaine réfléchit les NIs et les concentre vers le centre de l'aperture. La distribution angulaire des ions H^-_{SP} n'est pas Gaussienne mais avec une population massive centrale et deux pics divergents. La

polarisation de la PG affecte l'énergie de H^-_{SP} en changeant la gaine de Debye entre le plasma et la PG. Pour une gaine au potentiel flottant, les H^-_{SP} sont accélérés à environ 5 eV suivant la direction normale au biseau de la PG. Ceci augmente la composante transverse de l'énergie des ions H^-_{SP} à ≈ 3.5 eV. Ces ions négatifs auront une plus grande divergence une fois les grilles d'accélérations traversées. Comme le faisceau est alimenté en majeure partie par des ions négatifs extraits directement, la polarisation de la PG joue peu sur la divergence finale du faisceau (quelques mrad).

Diverses géométries de l'aperture (l'angle de biseau) de la PG côté plasma ont été étudiées pour comprendre l'impact sur la formation du faisceau et l'optique ionique et les électrons co-extraits. La géométrie de la grille a un effet mineur sur la pénétration du ménisque qui est principalement influencé par le potentiel d'extraction, la densité plasma, et la distance entre PG et EG. Cependant, réduire l'angle du biseau de la PG réduit directement l'extraction des ions H^-_{SP}, et par conséquent réduit la divergence du faisceau. Le courant maximal d'ions négatifs extrait a été obtenu avec la géométrie de grille utilisée pour ELISE et BUG. Ce phénomène a été attribué à une grande fraction d'extraction directe des ions H^-_{SP}, formant aussi un grand halo divergent. En revanche, une moindre divergence a été obtenue pour une géométrie moins tranchante (moins pointue) de la PG.

L'étude numérique menée a aussi montré que l'angle de biseau côté plasma de la PG affecte significativement l'extraction de H^-_{SP} et leur accumulation induite par l'accélération dans la gaine de Debye. Une version allongée du biseau de la PG pourrait doubler la densité de H^-_{SP} dans la zone centrale du ménisque par rapport à la géométrie standard IPP de la PG, avec comme conséquence immédiate la réduction de la divergence.

Une limitation majeure des résultats obtenus par ONIX et d'autres codes 3D-PIC pour l'extraction de NIs est l'impossibilité de reproduire les densités de courants obtenues expérimentalement, car ces résultats correspondent au régime sous-pervéant. Ainsi, les divergences obtenues sont loin des spécifications de ITER de 7 mrad. En perspective, l'incorporation des processus d'accumulation de H^- dans le volume de simulation sera à poursuivre afin de s'approcher des valeurs de NI mesurées. Ceci est un grand défi par rapport au temps de simulation nécessaire et à la taille de la zone plasma simulée avec ONIX. Expérimentalement, la majorité des ions négatifs dans le volume provient bien de la surface, mais sans être directement extraits. Le mécanisme équivalent devra être introduit dans la simulation, ce qui n'a pas encore été possible.

Selected publications

Particle injection methods in 3D-PIC MCC simulations applied to plasma grid biasing

M. Lindqvist, D. Wünderlich, S. Mochalskyy, N. den Harder, A. Revel, T. Minea, U. Fantz, *Phys. of Plasmas* **31**, 033903 (2024), 10.1063/5.0187850

Computationally studying H^- extraction and beamlet formation: the impact of the plasma model

N. den Harder, **M. Lindqvist**, A. Mimo, T. Minea, S. Mochalskyy, R. Nocentini, A. Revel, D. Wünderlich, U. Fantz, *J. Instrum.* **18** C08005 (2023), 10.1088/1748-0221/18/08/C08005

From meniscus formation to accelerated H^- beam: coupling of 3D-PIC and ion-optics simulations

M. Lindqvist, N. den Harder, A. Revel, S. Mochalskyy, A. Mimo, R. Nocentini, T. Minea, U. Fantz, *Nucl. Fusion* **62** 126068 (2022), 10.1088/1741-4326/ac9c6f

Sensitivity of the negative ion beam extraction to initial plasma parameters by 3D particle modeling

M. Lindqvist, D. Wünderlich, A. Mimo, S. Mochalskyy, A. Revel, R. Nocentini, T. Minea, U. Fantz, *Plasma Sources Sci. Technol.* **31** 125001 (2022), 10.1088/1361-6595/ac9a6d

Effects of the magnetic field topology on the co-extracted electron current in a negative ion source for fusion

Dirk Wünderlich, I. M. Montellano, **M. Lindqvist**, A. Mimo, S. Mochalskyy, U. Fantz, *J. Appl. Phys.* **130**, 053303 (2021), 10.1063/5.0054949

Contents

Acronyms

3D-PIC 3D Particle-in-Cell

B_{DF} Magnetic Deflection Field

B_{FF} Magnetic Filter Field

AD Associative Detachment

AG Acceleration Grid

Bari-Ex Bari-Extraction

BATMAN BAvarian Test MAchine for Negative ions

BC Boundary Condition

BES Beam Emission Spectroscopy

BP Bias Plate

BUG BATMAN Upgrade

CFC Carbon Fiber Composite

CFETR China's Fusion Engineering Test Reactor

CFL Courant-Friedrichs-Lewy

CG Conjugate Gradient

CRDS Cavity Ring-Down Spectroscopy

Cs Caesium

CX Charge Exchange

DA Dissociative e^- Attachment

DEMO Demonstration Power Plant

DNB Diagnostic Neutral Beams

DSMC Direct Simulation Monte Carlo

ECRH Electron Cyclotron Resonance Heating

ED Electron Detachment

eEC Electron Elastic Collisions

EF Electron Fence

EG Extraction Grid

ELISE Extraction from a Large Ion Source Experiment

GG Grounded Grid

H^-_{SP} Surface Produced H^-

H^-_{VP} Volume Produced H^-

HNB Heating Neutral Beams

IBSimu Ion Beam Simulator

ICRH Ion Cyclotron Resonance Heating

IPP Max Planck-Institut für Plasmaphysik

IR Infrared

ITED ITER Technology & Diagnostics

JAEA Japan Atomic Energy Agency

JET Joint European Torus

Keio-BFX Keio-Beam Formation and eXtraction

LHD Large Helical Device

LOS Line of Sight

LPGP Laboratoire de Physique des Gaz et des Plasmas

MAMuG Multi-Aperture Multi-Grid

MCC Monte Carlo Collisions

MITICA Megavolt ITER Injector and Concept Advancement

MN Mutual Neutralization

MPI Message Passing Interface

NAD Non-Associative Detachment

NBI Neutral Beam Injection

NI Negative Ion

NIF National Ignition Facility

NIFS National Institute for Fusion Science

OES Optical Emission Spectroscopy

ONAC Orsay Negative ion ACceleration

ONIX Orsay Negative Ion eXtraction

PE Processing Element

PG Plasma Grid

PI Positive Ion

PIC Particle-In-Cell

PID Proportional-Integral-Derivative

PRIMA Padova Research on ITER Megavolt Accelerator

RF Radio Frequency

RID Residual Ion Dump

SINGAP SINGle APerture - SINgle GAP

SP Surface Production

SPIDER Source for Production of Ion of Deuterium Extracted from RF Plasma

TDLAS Tunable Diode Laser Absorption Spectroscopy

TFTR Tokamak Fusion Test Reactor

VC Virtual Cathode

VDF Velocity Distribution Function

VP Volume Production

ZETA Zero Energy Thermonuclear Assembly

CHAPTER 1

Introduction

Energy is essential for various aspects of human life, from necessities such as electronic appliances to heating our living spaces to the operation of machinery in heavy industry. A nation's energy consumption level correlates with its progress and prosperity [1]. However, the reliance on fossil fuels for energy has detrimental effects on the environment, contributing significantly to climate change. Research indicates that global temperatures follow suit as CO_2 levels in the atmosphere rise. The international community, recognizing these adverse effects, has set a goal to limit the rise in global temperatures to below 2°C compared to pre-industrial levels [2]. Achieving this target requires heavily reducing CO_2 emissions and a shift towards more sustainable energy sources [3].

A viable long-term energy solution must be environmentally friendly, widely accepted, abundant, scalable to meet global demands, and geopolitically sustainable. Fusion energy combines light atomic nuclei to release energy and is a promising candidate. The fuel sources are plentiful; deuterium (D) and tritium (T) can be used as fuel in fusion reactions. deuterium, naturally abundant, is found in significant quantities in seawater. While scarce due to its radioactive decay, tritium can be synthesized by bombarding lithium with neutrons. Notably, in fusion devices, tritium breeding will take place within the device itself. Additionally, fusion does not produce any greenhouse gases. The amount of long-lived radioactive waste is negligible; the half-life for tritium is 12.3 years and there is no risk of a runaway reaction (meltdown), unlike in fission power plants [4].

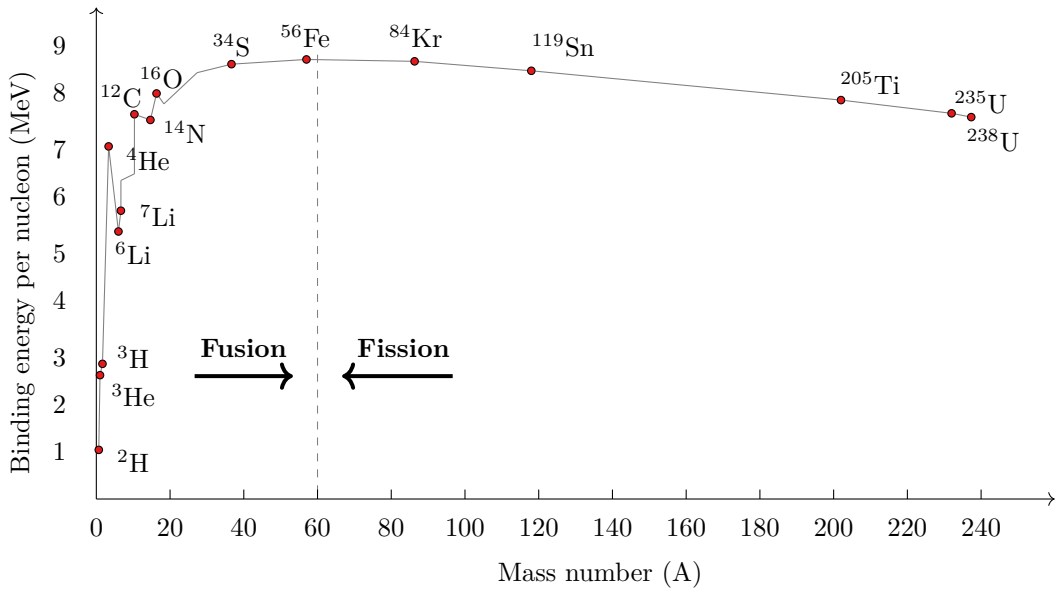

Figure 1.1: *Binding energy per nucleon as a function of mass number. Adapted from [5].*

1.1 Nuclear fusion in nature

Nuclear fusion is the process of fusing nuclei (neutrons and protons) to produce heavier elements. The binding energy per nucleon as a function of the mass number A of the atom is given in Figure 1.1. It can be seen that the curve is relatively constant except for the lightest atoms and that the maximum binding energy is found for atomic number $A = 60$, where the nucleons are the most strongly bound. Thus, energy can be released through fusion by combining lighter nuclei into heavier ones for mass numbers $A \leq 60$, and through fission by splitting heavier nuclei into lighter ones for mass numbers $A > 60$.

Nuclear fusion is prevalent across a variety of cosmic environments and serves as the primary mechanism for the formation of elements heavier than hydrogen through a process known as nucleosynthesis. The Sun, for instance, generates energy by fusing hydrogen nuclei into helium, with approximately 0.7% of the mass being converted into kinetic energy in the produced alpha particle. Within the Sun, the fusion processes take place in its core under extreme temperatures ($\sim 1.5 \cdot 10^7$ K) where the particles exist in a plasma state, where electrons are dissociated from their nuclei [6]. Additionally, nuclear fusion plays a crucial role during the core collapse of supernovae and mergers of neutron stars, leading to the rapid synthesis of heavier elements [5]. It was also integral to forming light elements during the primordial Big Bang Nucleosynthesis [5]. The primary forces governing fusion processes are the strong nuclear force, which is attractive and dominant at distances $\leq 10^{-15}$ m, and the Coulomb force, a repulsive force between like

charges, dominant at distances $\geq 10^{-15}$ m. For fusion to occur, nuclei, which are positively charged, must approach each other closely, overcoming the repulsive Coulomb force. The energy barrier that must be overcome for fusion to occur is called the Coulomb barrier. To overcome the Coulomb barrier, the kinetic energy of the nuclei must be exceedingly high [7]. When the kinetic energy is below the Coulomb barrier, quantum tunneling permits particles to pass through it.

A consistent characteristic of the natural fusion processes is the reliance on the gravitational force to confine the plasma and sustain the high pressure and close distances required for fusion to occur [7]. However, replicating such gravitational containment conditions on Earth to harness fusion energy is infeasible, necessitating exploring alternative containment methods and technologies.

1.2 Controlled fusion on Earth

Achieving *controlled fusion* is crucial for humans to take advantage of the energy released during fusion processes. Unlike the spontaneous fusion reactions observed in natural processes, the term "controlled" in controlled fusion signifies a sustained, regulated fusion process. The primary challenge in achieving controlled fusion stems from the difficulty of confining a plasma at sufficiently high temperature and density.

The two main techniques for plasma confinement are magnetic confinement and inertial confinement. Magnetic confinement devices contain the plasma by magnetic fields generated by external coils and by currents in the plasma. The size of magnetic fusion plasma tends to be $1-10$ m, the number density of the particles $\sim 10^{20}$ m^{-3}, and have a confinement time ~ 10 s [8, 9]. Inertial confinement devices contain small fuel pellets heated by a pulsed nanosecond laser or an ion beam. This leads to fusion and subsequent plasma expansion, limited by the particles' inertia. The size of inertial fusion plasma tends to be $1 - 100$ μm, the number density of the particles 10^{32} m^{-3}, and have a confinement time of $\sim 10^{-11}$ s [9].

Various magnetic confinement configurations exist. Linear devices based on magnetic mirror confinement rely on the so-called magnetic mirror effect in open magnetic field line topologies. In magnetic mirrors, the magnetic field is strongest at the device's edges, causing the reflection of charged particles. However, magnetic mirror devices suffer from significant plasma losses at the ends, plasma instabilities, challenges in maintaining the desired field configuration, particle drifts off field lines, non-isotropic confinement, and engineering complexities, and they typically operate at lower plasma pressures compared to other confinement methods [8, 10].

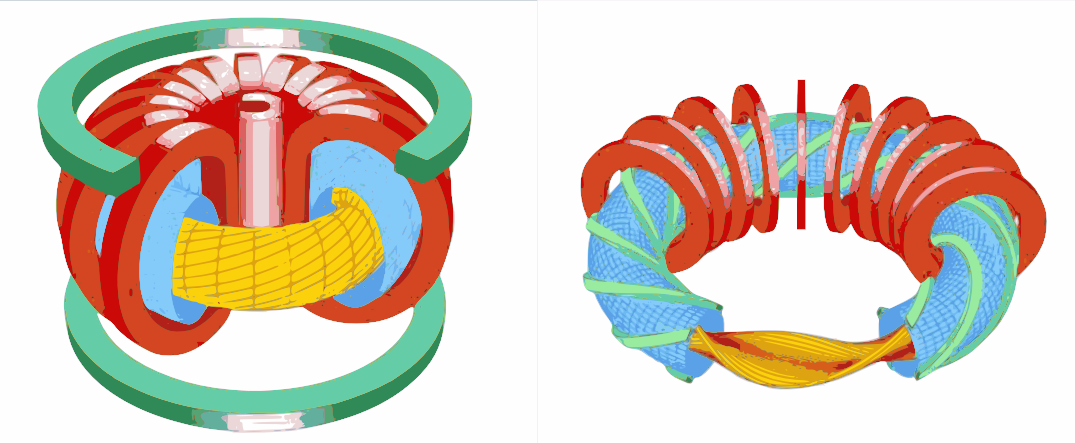

(a) *Tokamak.* **(b)** *Stellarator.*

Figure 1.2: *Illustration of a (a) Tokamak and (b) Stellarator.*

In toroidal magnetic field line configurations, such as the Tokamak or Stellarator, see Figure 1.2, the magnetic field lines follow the topology of a torus [8]. In a tokamak, a toroidal current flowing in a circular path around the major axis creates a poloidal magnetic field. A toroidal magnetic field is generated by external magnetic field coils. The superposition of the toroidal and poloidal magnetic fields creates a twisted configuration containing the plasma in the Tokamak, thus ensuring stable confinement. Without the poloidal magnetic field, the particles would drift in the vertical direction, perpendicular to the toroidal field, leading to a loss of the plasma. Therefore, driving a plasma current in the Tokamak is essential [11–13].

A Stellarator only relies on external magnetic fields to contain the plasma. This is achieved by twisting the external magnets so that the magnetic field in the Stellarator is inherently twisted without the need for a plasma current [14].

The viability of a fusion reactor depends to a large extent on the power gain Q, defined as the ratio between the power generated by the fusion processes' P_{output} and the heating power P_{input} used to sustain the fusion reaction:

$$Q = \frac{P_{\text{output}}}{P_{\text{input}}}. \tag{1.1}$$

For decades, reaching the breakeven point where $Q = 1$ has been a goal for scientists and engineers. In the following paragraph, some major magnetic fusion projects are listed.

Starting in the 1950s, significant strides were made in fusion research with the establishment of the Zero Energy Thermonuclear Assembly (ZETA) in the United Kingdom, aiming for controlled nuclear fusion [15]. In the 1960s, the Soviet Union introduced the Tokamak design, with the T3

Tokamak achieving its first plasma in 1968 [16]. In the 1970s, the USA launched the Tokamak Fusion Test Reactor (TFTR) at Princeton [17], setting several fusion records. The 1980s marked the initiation of the Joint European Torus (JET) Tokamak in the UK [18]. In the 1990s, the planning stage of the ITER Tokamak in France was initiated, aiming to demonstrate fusion's feasibility as a large-scale energy source, with construction beginning in 2007 [19]. Conceptual design for Demonstration Power Plant (DEMO) programs has been developed to facilitate the transition from experimental reactors to commercial power plants [20]. China's Fusion Engineering Test Reactor (CFETR) is part of the country's roadmap to achieving fusion energy and aims to bridge the gap between ITER and DEMO [21]. SPARC at Massachusetts Institute of Technology in the United States was announced in 2018 and will progress the development of compact, high-field Tokamaks [22]. The development of Stellarators has been advanced in experiments such as the Large Helical Device (LHD) in Japan [23] and Wendelstein 7-X in Germany [24]. Progress in inertial confinement fusion has been made mainly by the National Ignition Facility (NIF) in the United States [25].

Additionally, as of June 2023, 40 smaller-scale private enterprises have emerged, exploring alternative approaches to fusion and contributing to fusion research [26].

In these experimental facilities, a few common fusion reactions [12] with associated energy releases are:

$$\mathrm{D} + \mathrm{T} \longrightarrow {}^4\mathrm{He} + n + 17.6 \quad \mathrm{MeV}, \tag{1.2}$$

$$\mathrm{D} + \mathrm{D} \longrightarrow {}^3\mathrm{He} + n + 3.3 \quad \mathrm{MeV}, \tag{1.3}$$

$$\mathrm{D} + \mathrm{D} \longrightarrow \mathrm{T} + \mathrm{H} + 4.0 \quad \mathrm{MeV}, \tag{1.4}$$

$$\mathrm{D} + {}^3\mathrm{He} \longrightarrow {}^4\mathrm{He} + \mathrm{H} + 18.3 \quad \mathrm{MeV}. \tag{1.5}$$

For each reaction, the cross-section σ gives its probability to occur as a function of the center of mass energy. Figure 1.3 shows the cross-section σ for the D-D, D-T, and D-^{3}He reactions as a function of the center of mass energy. D-T fusion is often preferred over other reactions, such as D-D or D-^{3}He, because the D-T reaction has the highest cross-section at achievable energies, making it the most efficient for producing fusion energy. In comparison, the D-D and D-^{3}He reactions require higher energies or have lower cross-sections, posing greater technical challenges for achieving net positive energy output in current fusion devices [12].

A key performance indicator for fusion plasma is the so-called triple product, given by the product of ion density n, confinement time τ, and ion temperature T. Achieving high triple product values $nT\tau$ is essential for reaching the conditions necessary for sustained nuclear fusion,

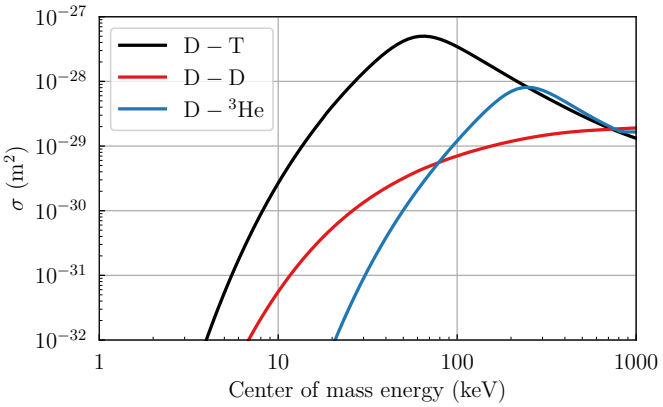

Figure 1.3: *Cross-section of* D-D, D-T, *and* D-^{3}He *reactions as a function of the center of mass energy. (Data from IAEA's Nuclear Data Section).*

as it indicates a high likelihood of particles overcoming the Coulomb barrier and undergoing fusion. The Lawson Criterion is defined by the minimum $nT\tau$ value required to produce a reaction with $Q > 1$ [27]. In addition, a higher boundary value for $nT\tau$ exists for each reaction, given by the Bremsstrahlung radiation, at which point the power of the plasma is radiated away.

Advances in technology and understanding of the underlying physics have improved the design of experimental devices. As of 2023, the fusion community has made significant strides towards nearing the Lawson criterion. The ITER project is expected to be the first Tokamak to reach $Q > 1$ [19].

1.3 External plasma heating systems in ITER

The ITER Tokamak, currently under construction in Cadarache, France, is the largest international nuclear fusion project to date. The ITER Members[1] have undertaken the collaborative effort to demonstrate the feasibility of fusion. The primary objectives of the ITER project are as follows [19]:

- To maintain internal fusion heating conditions within a deuterium-tritium plasma.
- To produce a fusion power output of 500 MW from 50 MW of input heating power.
- To showcase the integration of technologies that are vital for a future fusion power plant.
- To demonstrate the feasibility of Tritium breeding.

[1] China, the European Union, India, Japan, Korea, Russia, and the United States of America

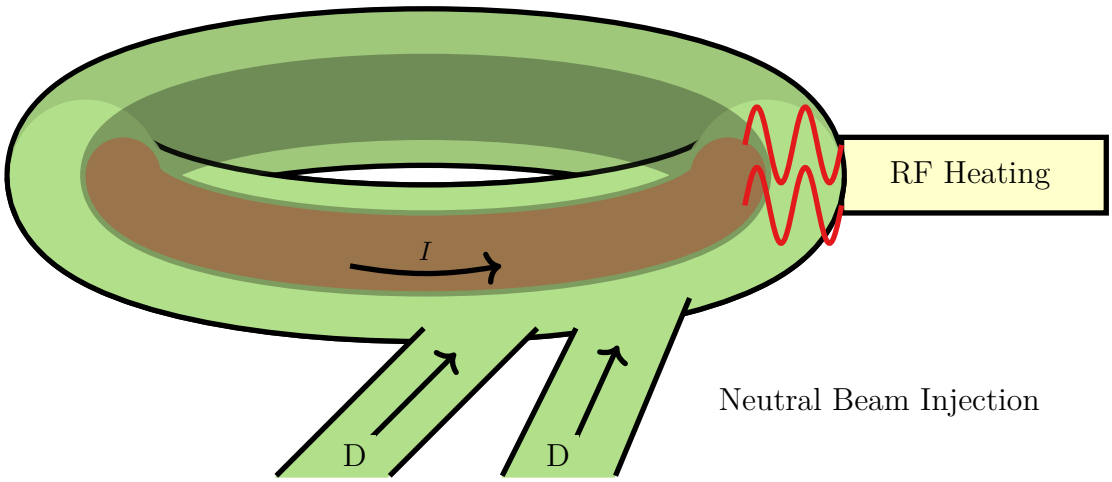

Figure 1.4: *Visual representation of the external heating techniques used in ITER, two NBI beamlines, and the generator waveguide for the RF are shown. The optional third beamline is omitted.*

- To demonstrate the safety protocols and standards for the safe operation of a fusion device.

To reach a sufficiently high temperature in the fusion plasma, external heating of the plasma is needed. In ITER, a combination of Neutral Beam Injection (NBI) and Radio Frequency (RF) heating will be used, as depicted in Figure 1.4.

- NBI works by heating the heavy plasma species by collisions with highly energetic neutral particles. It also provides the current drive of the poloidal magnetic field in the Tokamak devices.
- Electron Cyclotron Resonance Heating (ECRH) is an RF heating method that primarily heats the electrons in the plasma by the resonant energy transfer of electromagnetic waves matched with the gyro-frequency of the electrons.
- Ion Cyclotron Resonance Heating (ICRH) is an RF heating method, primarily used to heat the ions in the plasma using a similar working principle to ECRH, but with the resonant energy transfer to the ions.

NBI requires a beam of neutral particles since injecting a charged beam into the Tokamak is not possible due to the strong magnetic field. Since the direct acceleration of neutral particles is not feasible, the ITER NBI system necessitates generating, accelerating, and neutralizing ions. Negative Ions (NIs) are chosen since they have a substantially higher neutralization efficiency (60%) than positive ions (a few %) at the energies ($\sim$ 1 MeV) required for the ITER NBI [28, 29],

as will be described in Chapter 2, Section 2.1.3. The NIs for ITER are generated in RF-driven plasma sources, mostly by the conversion of atoms and positive ions [29, 30]. The NIs beamlets are extracted through a plasma-facing Plasma Grid (PG) and accelerated by electrostatic fields to a kinetic energy of up to 1 MeV through a multi-aperture multi-grid system. The first step of the extraction and acceleration system extracts particles from the ion source by an applied voltage of ~ 10 kV. Along with NIs, electrons are co-extracted from the plasma. The NIs are then neutralized into atoms before injection into the ITER tokamak. However, the electrons are unwanted since they can not contribute to the neutral beam and are instead dumped with a kinetic energy of ~ 10 keV by magnetic deflection onto the first grid of the acceleration system, the Extraction Grid (EG) [30]. The grid's ability to withstand the deposited power from co-extracted electrons represents a primary constraint in ion sources for fusion. Consequently, there's a crucial need to limit the number of these co-extracted electrons [30]. Additionally, for ITER NBI, strict requirements exist for the divergence of the extracted NI beamlets to ensure that the particles reach the end of the acceleration system without being lost on the grids [30]. The physics of the ion sources for the NBI, various test facilities, technical details, and the target values for the ITER NBI are extensively discussed in Chapter 2.

1.4 Outline of the thesis

This thesis aims to provide a comprehensive understanding of the extraction of NIs from RF-driven ion sources, integrating experimental observations with computational modeling to enhance the performance of fusion applications. The scope of the thesis is presented in Chapter 2, Section 2.8.

The outline of the thesis is as follows. Chapter 2 discusses the constraints and requirements of NI sources in fusion contexts, particularly the issues of co-extracted electrons during deuterium operations and beam divergence. Chapter 2 also provides a rationale for using 3D Particle-in-Cell (3D-PIC) modeling in studying ion extraction. The scope and research questions for the thesis are given in Section 2.8. Chapter 3 describes the numerical models that are used to simulate negative ion extraction in this thesis, detailing its computational constraints and advantages. Chapter 4 provides the validation of the flux-injection scheme developed during this thesis. Chapter 5 analyzes the dynamics of various plasma parameters and their impact on ion and electron extraction. Chapter 6 examines strategies to minimize co-extracted electrons, focusing on methods such as PG biasing and the implementation of electron fences, detailing their effects on NI extraction. Chapter 7 presents an analysis of ion beam optics, detailing the behavior of different ions upon extraction and implications for ion source performance.

Chapter 8 investigates how changes in the geometry of the PG can affect ion extraction, beam optics, and related phenomena. Finally, Chapter 9 provides a summary and conclusion of the work.

CHAPTER 2

Negative ion sources for fusion

Negative ion sources play an important role in fusion technology, especially within the NBI systems for plasma experiments. Beyond fusion, these sources have various applications, spanning from particle accelerators to space propulsion systems. This chapter describes the ITER NBI stages, highlighting the design of its ion sources, including two prototype versions at Max Planck-Institut für Plasmaphysik (IPP) Garching, Germany. The relevant plasma physics, including the production, extraction and acceleration of H^- ions, is discussed. This chapter also introduces diagnostic tools that offer insights into particle parameters used in the numerical simulations presented in this thesis. Finally, the scope and research questions of this thesis are presented in Section 2.8.

2.1 Neutral beam injection for ITER

2.1.1 Stages of the ITER NBI

The core principle behind plasma heating via NBI is energy transfer from neutral particles to the plasma particles in the fusion plasma. The neutral particles transfer their energy to the plasma through charge exchange collisions and ionization by electron or ion impact [31].

To accelerate the particles to sufficient energy, charged particles (positive or negative) are accelerated by electrostatic acceleration by direct current fields prior to their injection into the Tokamak in a grid system and then neutralized by charge exchange/electron stripping collisions with a background H_2/D_2 gas, this will be explained in Section 2.1.3.

The main stages of a NBI system are presented in Figure 2.1 and enumerated as follows.

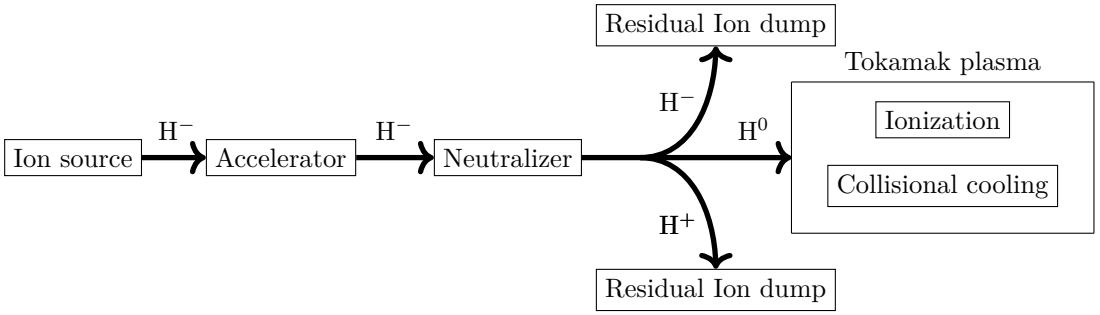

Figure 2.1: *Schematic overview of the main stages of an NBI system.*

1. **Ion Source**: Production of ions, positive or negative.

2. **Accelerator**: Acceleration of ions to the required energies using electrostatic grids.

3. **Neutralizer**: Conversion of high-energy ions to neutral particles, allowing for penetration into the plasma device. The conversion is only partial and the surviving ions (positive or negative) after the neutralizer are electrostatically deflected away from the energetic neutral path into a Residual Ion Dump (RID).

4. **Beamline**: Particle transport into the main plasma chamber.

5. **Plasma Injection**: Penetration of highly energetic neutral beams into the plasma, collisions (charge exchange and ionization by electron or ion impact) with plasma particles lead to heating and current drive.

ITER's NBI system requires two beams of H^- or D^- ions to achieve a heating power of 16.7 MW each, with 1 MeV of D or 0.87 MeV of H being directed to the plasma for a sufficient current drive [30]. The choice of hydrogen isotope will vary over the course of the ITER operation, during the initial, non-nuclear phases of the ITER operation, H will be used. For the later D-T operational phase, starting in 2035 according to the latest available official schedule of ITER, D will be used [30]. The Diagnostic Neutral Beams (DNB) operates by direct injection of neutral particles into the plasma to measure the He content in the plasma. Figure 2.2 shows the two ITER Heating Neutral Beams (HNB) beamlines (HNB1 and HNB2), the DNB, and the potential third NBI beamline (HNB3) [30]. The DNB will be used to measure the helium ash density which is produced by the D-T fusion reactions [32].

In the following sections, each stage of the NBI will be described.

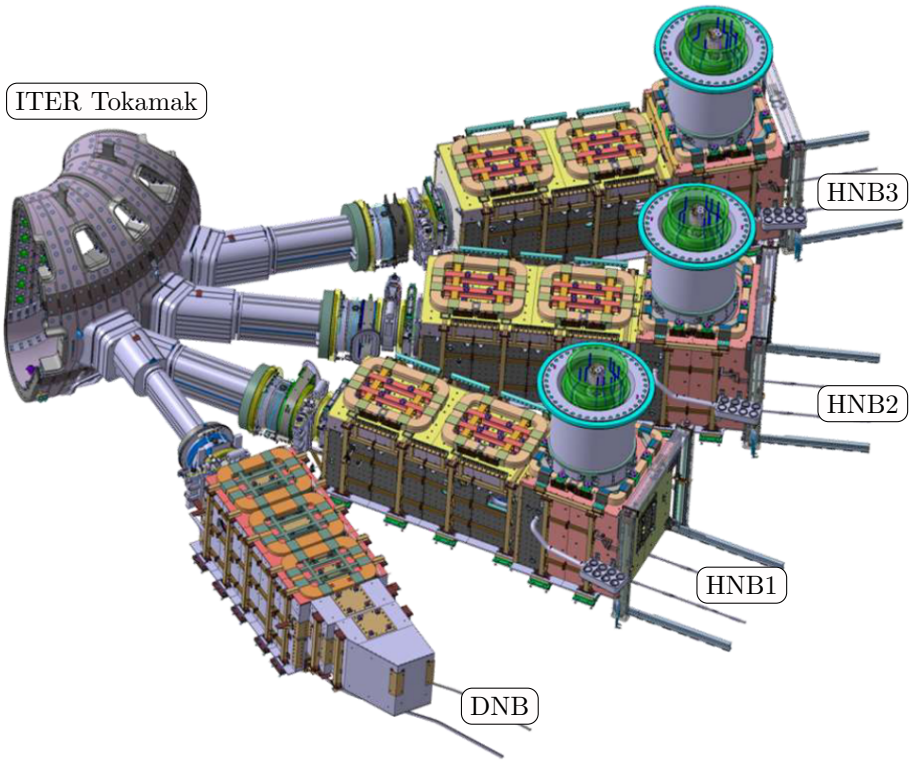

Figure 2.2: *Schematic view of ITER HNB and DNB. Adapted from [33].*

2.1.2 Ion sources for ITER

The first stage of each of the ITER NBI beamlines is an ion source. An ion source generates a partially ionized plasma from which charged ions are extracted. The plasma can be generated via various types of ion sources such as arc sources and RF sources. Arc sources use hot tungsten filaments to generate a low-pressure arc discharge in a gas-filled chamber. A cusp magnetic field can improve ionization rates and reduce plasma losses [34]. In contrast, RF sources utilize inductive coupling of RF power at $\sim$ 1 MHz to ignite and sustain the plasma [35]. Typically, cylindrical containers, so-called drivers, are mounted on the back of a larger source chamber and wounded with a coil, to which the RF power is applied [35].

The ions for the ITER NBI will be produced in large RF-driven ion sources. The RF design was chosen because it requires less maintenance due to the lack of filaments [36]. Two different accelerator concepts were considered for ITER NBI: the Multi-Aperture Multi-Grid (MAMuG), which was originally developed by Japan Atomic Energy Agency (JAEA) [37], and SINGle APerture - SINgle GAP (SINGAP), developed by CEA Cadarache [38], both designed for 40 A, 1 MeV D^- acceleration. The SINGAP concept uses a single acceleration step while the MAMuG

concept uses several grids which gradually accelerate the ions. The MAMuG design was chosen over the SINGAP design due to better voltage holding [39]. The ions are extracted through a system of 1280 apertures arranged in 16 groups of 5×16 apertures [39].

A schematic figure of an ion source for ITER is shown in Figure 2.3. The plasma is generated in the 8 drivers and diffuses into the expansion chamber. The extraction system consists of two grids, the PG which faces the expansion chamber, and the EG which is located at a 6 mm distance from the PG. A positive bias of $\sim$ 10 kV is applied between the two grids in order to extract NIs. The choice of extracting NIs instead of Positive Ions (PIs) is discussed in Section 2.1.3.

In low-temperature, low-pressure ion sources for NI based NBI, a horizontal Magnetic Filter Field ($\mathbf{B}_{\mathrm{FF}}$) with a typical field strength of several mT is used to decrease the electron temperature (from $\sim$ 10 eV to $\sim$ 2 eV) and density (from $\sim 10^{18}$ m^{-3} to $\sim 10^{17}$ m^{-3}) and thus reduce the destruction of NIs due to collisions with energetic electrons [35]. The latter process is known as Electron Detachment (ED):

$$e^- + \mathrm{H}^- \rightarrow \mathrm{H} + 2e^-. \tag{2.1}$$

Since the electron affinity of H is only 0.75 eV [40], destruction of the NIs is very efficient in plasmas with high electron temperature and density. The reduction in electron temperature and density is crucial for maintaining a high yield of NIs in the ion source. However, the transport of electrons and ions, generated in the drivers, towards the extraction region under the influence of the $\mathbf{B}_{\mathrm{FF}}$ leads to vertical asymmetries in plasma parameters between the top and bottom of the ion source due to plasma drift [41].

The Padova Research on ITER Megavolt Accelerator (PRIMA) test facility is located in Italy and houses Megavolt ITER Injector and Concept Advancement (MITICA), a full-scale prototype of the ITER NBI injector system, and Source for Production of Ion of Deuterium Extracted from RF Plasma (SPIDER), a prototype of the ITER NBI ion source [42–45]. The purpose of MITICA is to demonstrate the performance of each part of the NBI injector, from beam extraction, acceleration, and optics to neutralization at the ITER scale and parameters. SPIDER is an RF ion source of the same geometry as the ITER HNB, but with a maximum beam energy of 100 keV, an order of magnitude lower than foreseen in the ITER HNB. The purpose of SPIDER is to study the production of NI beams before the assembly of the high-voltage equipment in MITICA.

Figure 2.3 shows the ITER HNB acceleration system, including the RF ion source, PG, EG,

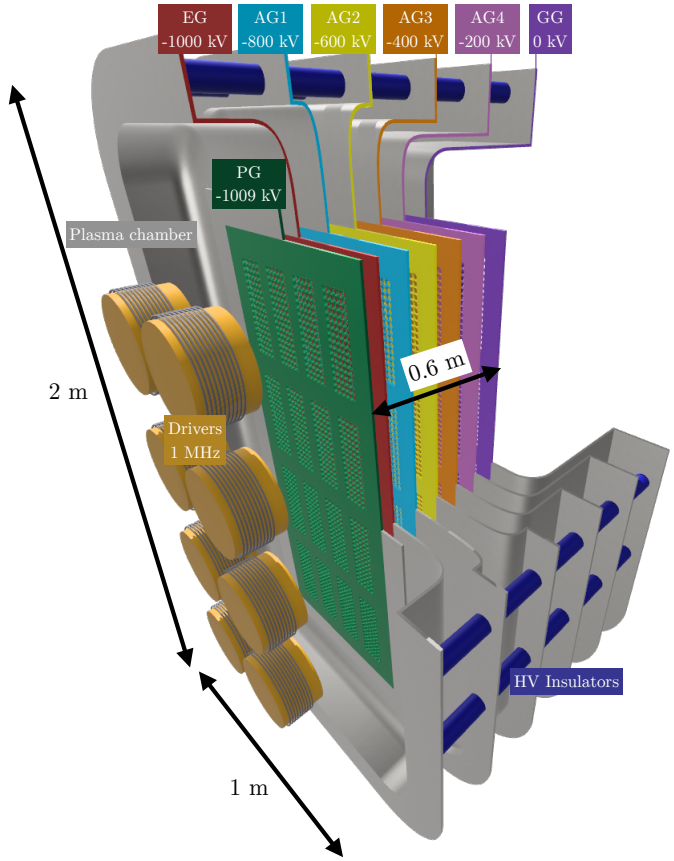

Figure 2.3: *Overview of the ITER HNB, including drivers, plasma chamber and the grid-system, adapted from [46].*

Acceleration Grid (AG) 1,2,3,4 and the Grounded Grid (GG). As described above, the total acceleration foreseen for ITER is 1 MeV, this is achieved by electrostatic acceleration over the grid system and the voltages for each grid are $\phi_{\mathrm{PG}} = -1009$ kV, $\phi_{\mathrm{EG}} = -1000$ kV, $\phi_{\mathrm{AG1}} = -800$ kV, $\phi_{\mathrm{AG2}} = -600$ kV, $\phi_{\mathrm{AG3}} = -400$ kV, $\phi_{\mathrm{AG4}} = -200$ kV, and $\phi_{\mathrm{GG}} = 0$ kV [42].

A schematic view of the ITER PG is shown in Figure 2.4. Each grid is comprised of 4×4 beamlet groups, each with 5×16 apertures [30]. The thickness of the PG is 9 mm and the apertures have a radius of 7 mm. The apertures are chamfered to increase the surface area of the PG. On the downstream side of the PG, facing the EG, the apertures are chamfered 2.5 mm in 45°. On the upstream side of the PG, facing the expansion chamber, the chamfer is 6.5 mm at a 40° angle to the normal of the PG. The deep chamfering of the upstream side gives the PG a so-called "egg-box" geometry, see Figure 2.4 (b) [30]. A detailed description of the aperture pattern for each grid is shown in [46].

The neutral hydrogen gas from the ion source diffuses past the expansion chamber and into the

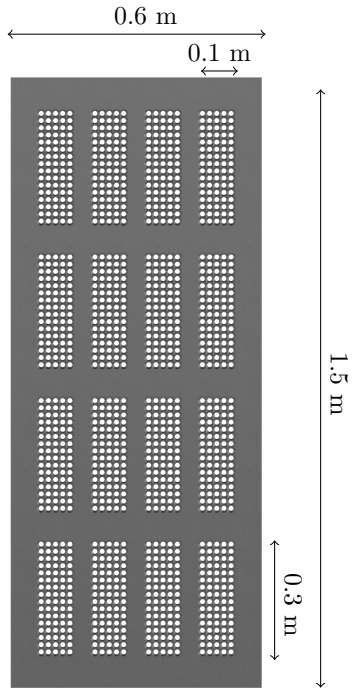

(a) *Upstream view*

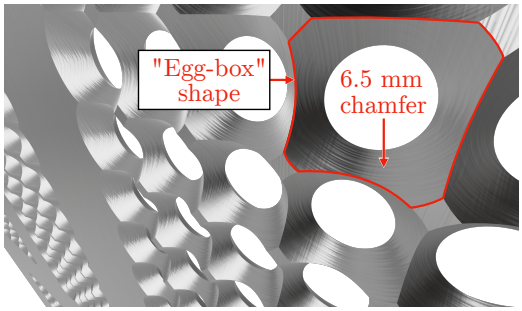

(b) *Upstream close-up.*

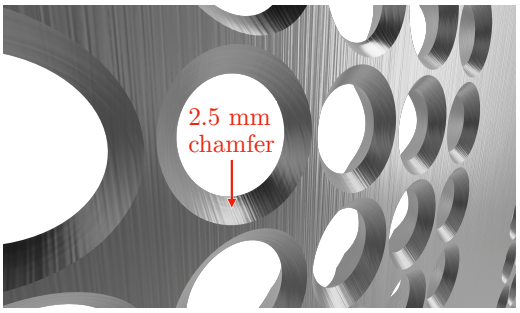

(c) *Downstream close-up.*

Figure 2.4: *Schematic figure of the PG geometry for ITER NBI, (a) shows the full upstream side of the grid, seen from the expansion chamber, (b) shows a close-up view of the apertures on the upstream side of the PG and (c) shows a close-up on the downstream side of the PG, facing the EG.*

extraction and acceleration stage of the NBI beamline. The extracted NIs undergo collisions with the hydrogen background gas.

In the extraction and acceleration region, electron stripping, see Equation (2.1), results in the creation of neutrals. This is not wanted since these neutrals are created with less energy than they would have if neutralization occurred after complete acceleration [30]. These neutrals are either lost on the acceleration grids or, if they pass through the acceleration system, their divergence frequently exceeds ITER specification (7 mrad) [30]. The NIs can be stripped of both electrons (double stripping), leading to the formation of PIs which are accelerated in the opposite direction of the NIs. These PIs can be accelerated back into the ion source and cause damage to the back-plate [30, 47, 48]. To limit the electron stripping of the extracted NIs to below 30%, the gas pressure must be kept below 0.3 Pa [49].

2.1.3 The gas neutralizer

The beam exiting the accelerator comprises mostly of NIs (H^-/D^-) [39]. In addition, some highly energetic e^-, H/D atoms, and H^+/D^+ ions are also present. The electrons are dumped

onto panels in the vicinity of the neutralizer. Divergent H/D from inside the accelerator hit the grids of the accelerator and do not enter the neutralizer. Some D^+ have enough kinetic energy in the downstream direction of the accelerator to overcome the retarding field and enter the neutralizer [39].

The neutralizer consists of four adjacent vertical channels along the columns of the aperture groups. Gas is introduced midway through the neutralizer channel via vertically aligned nozzles. The D^- beam is neutralized by the following reactions with D_2 [39]:

$$D^-_{\text{fast}} + D_2 \rightarrow D_{\text{fast}} + D_2 + e^- \quad \text{simple stripping.} \tag{2.2}$$

However, the simple stripping competes with the losses due to double stripping and re-ionization D_{fast} [39, 50]:

$$D^-_{\text{fast}} + D_2 \rightarrow {D^+}_{\text{fast}} + D_2 + 2e^- \quad \text{double stripping,} \tag{2.3}$$

$$D_{\text{fast}} + D_2 \rightarrow D^+ + D_2 + e^- \quad \text{ionization.} \tag{2.4}$$

Note that the reactions are shown for D^- and D_2, but equivalent reactions occur for H^- and H_2. An optimum thickness and gas density can be derived which produces the maximum fraction of neutrals in the beam exiting the neutralizer [49].

After the beam is neutralized, the remaining NIs, which are not neutralized, and the PIs produced via re-ionization, must be filtered out before injection into the Tokamak. The charged particles are removed from the beam by magnetic or electromagnetic deflection and dumped into a RID [51–54].

The choice of NIs for the ITER NBI is due to their higher neutralization efficiency, which is directly linked to the beam's energy. This relationship is shown for optimum target thickness in Figure 2.5, which compares the maximum achievable neutralization efficiency for both positive and NIs, based on [55]. An important observation is that the efficiency for PIs approaches zero for energies beyond 150 keV/amu, meaning that the use of NIs is a necessity in ITER. The neutralization efficiency of the NIs is higher due to the low (~ 0.75 eV) binding energy of the second electron [56].

However, the use of NIs presents some major drawbacks

- **Co-extraction of electrons**: When NIs are extracted from a source, electrons are inevitably co-extracted [35, 57–61].
- **Stripping of electrons**: Negative ions are more susceptible to losing their extra electron

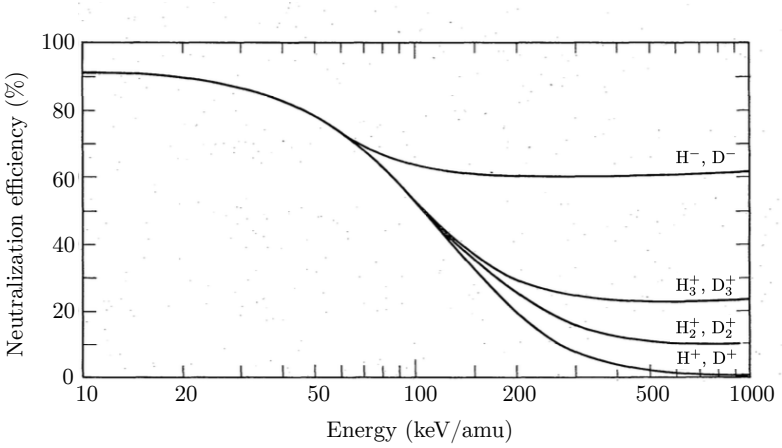

Figure 2.5: *Neutralization efficiency for negative and positive hydrogen ions at optimized target thickness. Adapted from [28].*

via stripping due to collisions with electrons and with the background gas [49].

- **Extracting high current**: The typical extracted NI current density (hundreds of Am^{-2}) is an order of magnitude lower than in PI sources (thousands of Am^{-2}) [62].
- **Beam optics**: Both applied magnetic fields deflect the extracted NI beamlets. This deflection of the NI beamlets must be compensated for [63, 64].
- **Production of NI**: Caesium (Cs) must be used to generate enough NI on the surfaces of the ion source [35]. This is described in Section 2.4.2.
- **Asymmetries**: Since the extracted current density is lower than in PI sources, the ion sources must be large. Therefore, achieving uniformity of the extracted beamlets is more difficult [57].

2.1.4 Parameters for ITER NBI

The requirements for the ITER NBI can be found in [30, 39, 65] and are summarized in Table 2.1. The ITER HNB system will deliver a total of 33 MW of energy from two beamlines delivering up to 16.7 MW each. The particle energies and pulse lengths will be 870 keV for 1000 s in the initial hydrogen phase and 1 MeV for 3600 s in the following deuterium operation. To ensure sufficient beam transport, the accelerated negative ion beam inhomogeneity must not exceed 10%. Additionally, due to power losses attributed to the neutralization of NIs and transmission losses throughout the beamline, the power of the accelerated NI beam must be $\sim$ 40 MW, which corresponds to a current of 46 A of hydrogen or 40 A of deuterium. For

Table 2.1: *Required parameters for the ITER HNB system [30, 39, 65].*

Parameter	Deuterium	Hydrogen
Power per beamline	16.5 MW	16.5 MW
Particle energy	1 MeV	0.87 MeV
Accelerated current density	200 Am^{-2}	230 Am^{-2}
Extracted current density	286 Am^{-2}	329 Am^{-2}
Co-extracted electron-ion ratio	≤ 1	≤ 1
Source filling pressure	≤ 0.3 Pa	≤ 0.3 Pa
Pulse length	3600 s	1000 s
Beam homogeneity	≥ 90 %	≥ 90 %
Beam divergence	≤ 7 mrad	≤ 7 mrad

an ITER-size ion source with 1280 apertures with 7 mm radii, this corresponds to accelerated current densities of 230 Am^{-2} and 200 Am^{-2} for hydrogen and deuterium, respectively. The stripping losses of negative ions are limited to below 30% by having a gas pressure of below 0.3 Pa. Factoring in the 30% stripping losses, an extracted NI current density of 329 Am^{-2} and 286 Am^{-2} is needed for hydrogen and deuterium, respectively. To limit the peak thermal load on the EG at a manageable level, the density of the co-extracted electron current must be maintained below that of the extracted negative ion current. Additionally, the extracted beam needs good beam optics for transport to the Tokamak, a homogeneity of 90% with a beam divergence (described in Section 2.5) below 7 mrad is required [66].

2.2 Prototype ion sources at IPP Garching

As an important step towards the development of ion sources for the ITER NBI systems, a series of prototype ion sources have been developed and tested. These sources represent a step-wise development approach, ensuring that technologies are matured at each stage before progressing to a larger scale. Situated at IPP in Garching, Germany, the BATMAN Upgrade (BUG) and Extraction from a Large Ion Source Experiment (ELISE) are important intermediate steps in this development process. These prototypes, along with the ITER size ion source SPIDER, as shown in Figure 2.6, follow a consistent design, ensuring scalability.

At BUG, an RF-driven ion source with a single driver and one grid segment with 14×5 apertures is used [68]. The facility allows for the acceleration of H^- ions and D^- ions. The main purpose of BUG is to advance the understanding of NI production and beam properties,

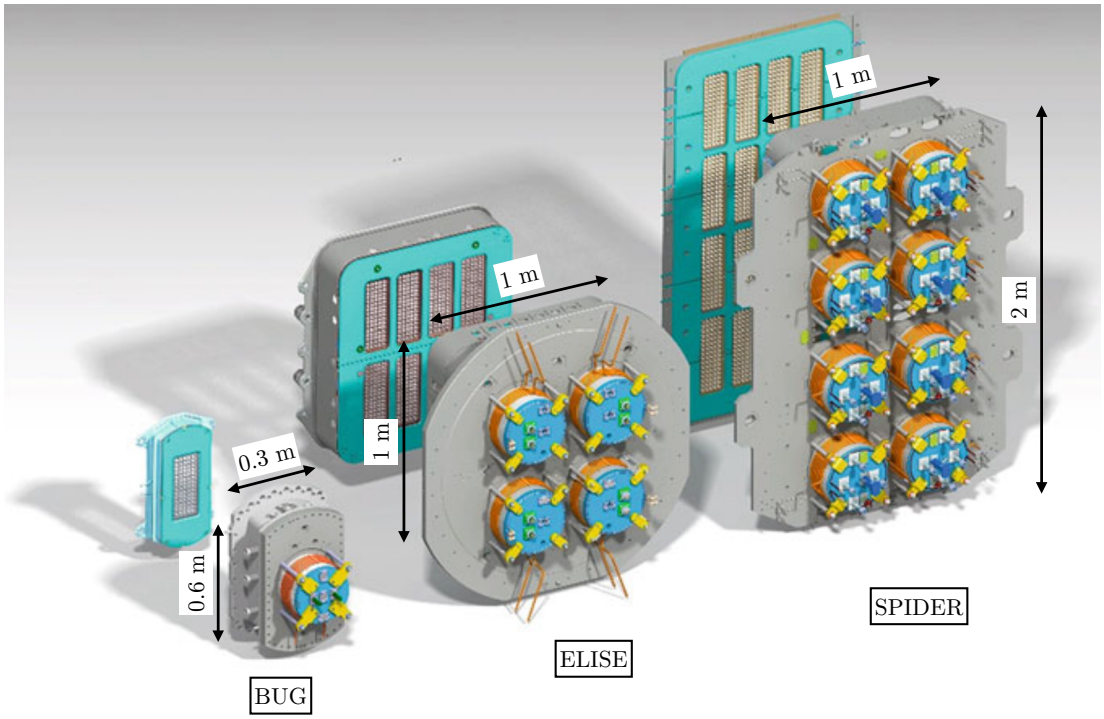

Figure 2.6: *The BUG, ELISE and SPIDER ion sources. Adapted from [67].*

and to demonstrate the achievement of ITER requirements in a smaller device. The study of beam properties can be done by masking the PG, which allows for studies with single aperture extraction [68].

The half-size ELISE test facility is designed to demonstrate the achievement of the ITER requirements in H^- and D^- as an intermediate step between BUG and the ITER ion sources [39]. The plasma in the ion source is generated in 2×2 cylindrical drivers by inductive coupling, described in Section 2.3.2, and the grids contain 640 apertures arranged in four groups with 16×5 aperture groups. The RF power is generated by two 1 MHz RF generators delivering up to 75 kW per driver [69].

The extraction and acceleration systems in BUG and ELISE are composed of three grids, the PG which faces the plasma, the EG, which is biased up to 10 kV with respect to the PG, and the GG at ground potential. The total acceleration over both EG and GG is up to 60 kV in ELISE and 50 kV in BUG. The relevant diagnostic tools in ELISE and BUG for this thesis are described in Section 2.6.

2.3 Plasma physics background in the context of negative ion sources

2.3.1 Basic properties of a plasma

Plasma physics is a well-studied field, and thorough descriptions can be found in a multitude of textbooks [70–72]. In this section, only a few important concepts are presented; in particular, the sheath formation between plasma and walls.

A plasma is defined in [7] as *"a quasineutral gas of charged and neutral particles which exhibits collective behavior"*, obeying the following three mathematical criteria:

$$\lambda_{\mathrm{De}} \ll L, \tag{2.5}$$

$$N_D \gg 1, \tag{2.6}$$

$$\omega_{pe}\tau > 1, \tag{2.7}$$

where λ_{De} is the Debye length, L is the length of the plasma container, N_D is the number of particles in a Debye sphere, ω_{pe} is the plasma frequency and τ is the mean time between collisions between electrons and neutrals.

A plasma is quasi-neutral, however, charge imbalances can be introduced, and can naturally occur in the boundary between the plasma and a solid surface, causing the development of electric fields. The Debye length is the characteristic length scale for the shielding of these electric fields, given by

$$\lambda_{\mathrm{De}} = \sqrt{\frac{\epsilon_0 k_{\mathrm{B}} T_e}{n_e e^2}}, \tag{2.8}$$

where ϵ_0 is the vacuum permittivity, k_{B} Boltzmann's constant, T_e the electron temperature, n_e the electron number density and e the unit charge. N_D can thus be understood as the number of plasma particles in a sphere with a volume of $\frac{4}{3}\pi\lambda_{\mathrm{De}}^3$. The plasma frequency ω_{pe} is given by

$$\omega_{pe} = \sqrt{\frac{e^2 n_e}{\epsilon_0 m_e}}, \tag{2.9}$$

where m_e is the electron mass.

The motion of a charged particle in an electromagnetic field is governed by the Lorentz force equation:

$$\mathbf{F} = q(\mathbf{E} + \mathbf{v} \times \mathbf{B}), \tag{2.10}$$

where $\mathbf{F}$ is the force on the particle, q is its charge, $\mathbf{E}$ is the electric field, $\mathbf{v}$ is the velocity of the particle, and $\mathbf{B}$ is the magnetic field. This leads to various drift motions, such as the $\mathbf{E} \times \mathbf{B}$ drift, denoted as $\mathbf{v}_{E\times B}$ and given by:

$$\mathbf{v}_{E\times B} = \frac{\mathbf{E} \times \mathbf{B}}{B^2}, \tag{2.11}$$

and the diamagnetic drift $\mathbf{v}_{\text{dia}}$, which can be expressed as:

$$\mathbf{v}_{\text{dia}} = -\frac{\nabla p \times \mathbf{B}}{qnB^2}, \tag{2.12}$$

where ∇p represents the pressure gradient. Furthermore, the Larmor radius r_L is the radius of gyration around magnetic field lines, and is given by:

$$r_L = \frac{mv_\perp}{|q|B}, \tag{2.13}$$

where m is the particle mass and $v_\perp$ the velocity component perpendicular to $\mathbf{B}$.

2.3.2 Plasma generation

Plasmas are formed by ionizing a neutral gas that naturally contains free electrons [71, 73]. The free electrons are accelerated by an electromagnetic field and ionize the neutrals in the gas through collisions. The ionizing collision leads to the formation of an electron-ion pair, and the new electron will also be accelerated by the electric field and ionize neutral particles [72]. The generation of the electromagnetic field can be done via two methods:

- **Capacitively Coupled Plasma (CCP)**: An electric field is generated by applying a potential difference across a neutral gas [74].
- **Inductively Coupled Plasma (ICP)**: An electromagnetic field is induced by an alternating current flowing through a coil located near the plasma. This generates a magnetic field that oscillates with the current, which in turn generates a circulating electric field due to Faraday's law [74].

2.3.3 Distribution functions

A plasma consists of a set of distinct groups of particles, called *species*, such as electrons, ions and neutrals. At thermal equilibrium, the velocity distribution of each species is described by

the Maxwell-Boltzmann distribution, given by:

$$f(\mathbf{v}) = n \left(\frac{m}{2\pi k_B T} \right)^{3/2} \exp\left(-\frac{m|\bar{\mathbf{v}}|^2}{2k_B T} \right), \tag{2.14}$$

where $f(\mathbf{v})$ is the number density function of particles with velocity $\mathbf{v}$, n is the total number density (number of particles per unit volume), m is the particle mass, T is the temperature, and k_B is the Boltzmann constant. The number density n can be verified by integrating $f(\mathbf{v})$ over all velocity space:

$$\int_{-\infty}^{\infty} f(\mathbf{v}) \mathrm{d}\mathbf{v} = n \tag{2.15}$$

The average kinetic energy E_{avg} of the particle species with a distribution function $f(\mathbf{v})$ is given by:

$$E_{\mathrm{avg}} = \frac{\int_{-\infty}^{\infty} \frac{1}{2} m \mathbf{v}^2 f(\mathbf{v}) \mathrm{d}\mathbf{v}}{\int_{-\infty}^{\infty} f(\mathbf{v}) \mathrm{d}\mathbf{v}} = \frac{3}{2} \cdot k_B T. \tag{2.16}$$

2.3.4 Low-temperature, low-pressure plasmas

The plasmas generated in the drivers of NI ion sources for fusion are characterized by a low density ($n_e \approx 10^{18}$ m^{-3}) due to the low gas pressure [30]. The energy transfer from the electrons to the ions is not as effective as in a plasma with higher density. Therefore, the temperature of the ions T_{i} and temperature of the neutrals T_{neutral} are low compared to T_e. Such plasmas are called *low-temperature, low-pressure plasmas*, with the following properties:

$$T_e \gg T_{\mathrm{i}} \approx T_{\mathrm{neutral}}, \quad \text{and} \quad 0.1 \text{ Pa} < p < 100 \text{ Pa}, \tag{2.17}$$

where p is the gas pressure [70, 74].

2.3.5 Plasma sheath formation

In the absence of externally applied voltages, a sheath forms at the boundary between the plasma and the wall to maintain quasi-neutrality and to ensure the electron and ion fluxes to the wall are equal, thereby preventing a net charge buildup in the plasma. The potential difference between the plasma and wall is determined by the electron temperature T_e, the mass ratio of ions to electrons ($m_{\mathrm{e}}/m_{\mathrm{ion}}$), and the ratio of ion and electron temperature (T_{i}/T_e),

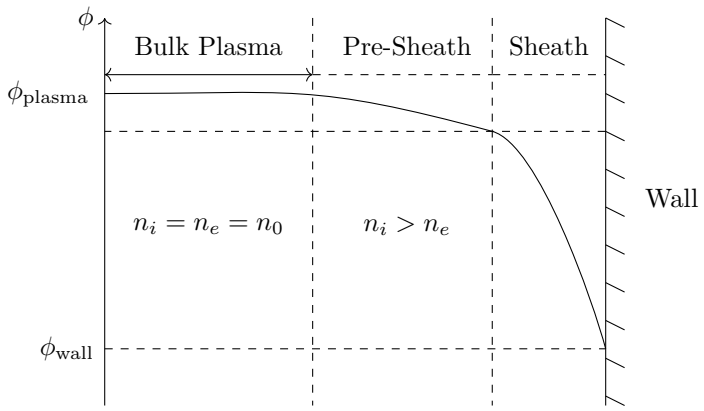

Figure 2.7: *Electrostatic potential close to the wall, including the bulk plasma, pre-sheath and sheath. Adapted from [74].*

according to the analytical models in [75, 76]:

$$\phi_{\text{plasma}} - \phi_{\text{wall}} = -\frac{k_{\text{B}} T_e}{2} \ln \left[2\pi \frac{m_{\text{e}}}{m_{\text{ion}}} \cdot \left(1 + \frac{T_{\text{i}}}{T_e} \right) \right], \tag{2.18}$$

where ϕ_{plasma} is the plasma potential at the sheath edge and ϕ_{wall} is the potential of the wall. The boundary region between the plasma and the wall, where electrostatic potential drops, is called a Debye sheath. Adjacent to the Debye sheath is the pre-sheath, which functions to pre-accelerate ions, a necessary step for ions to meet the so-called Bohm criterion. This criterion requires that ions enter the Debye sheath at or above a minimum speed, ensuring they have enough kinetic energy [77, 78]. Figure 2.7 shows a schematic figure of a Debye sheath and pre-sheath near a wall.

If a biased object is introduced into the plasma, it is shielded by the formation of a plasma sheath surrounding its surface. The properties of such a sheath depend on the bias and the size of the object. In the case that the object is small compared to the other surfaces, such as the tip of a Langmuir probe, it does not impact the overall potential of the plasma as long as the current leakage through this probe (or small object) remains negligible [78, 79].

As described in Section 2.2, the PG in both ELISE and BUG can be biased with respect to the source walls. This allows for the creation of a positive potential difference between the PG and the plasma ($\phi_{\text{plasma}} < \phi_{\text{PG}}$). The positive sheath forms a so-called electron sheath, or electron-attracting sheath, as opposed to the ion sheaths or ion-attracting sheath shown in Figure 2.7. Figure 2.8 shows an electron and ion sheath with the direction of the electric field indicated.

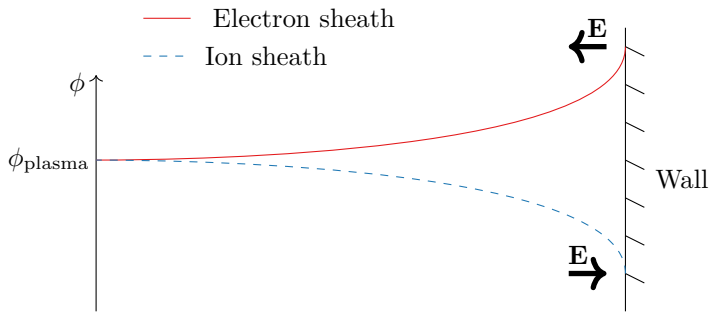

Figure 2.8: *Schematic figure of the potential profile for an ion and an electron sheath.*

2.4 Production and extraction of negative ions

In NI sources, H^- ions are produced by two separate mechanisms: Volume Production (VP) and Surface Production (SP). In the following sections, VP and SP will be described.

2.4.1 Volume Production

The formation of H^- ions in the plasma volume is achieved by dissociative attachment (DA) of electrons to hydrogen molecules. In general, DA are reactions of the type

$$e^- + AB \rightarrow AB^{-*} \rightarrow A^- + B \quad \text{or} \quad A + B^-, \tag{2.19}$$

where e^- is an electron colliding with a molecule AB. The electron becomes temporarily trapped in a resonant state of the molecule AB^{-*}. If the resonance is long-lived enough, then dissociation can occur. If not, the resonance auto-ionizes again and the ionized molecule emits one of its valence electrons. DA is the fundamental process governing VP in ion sources [80]. In the (prototype) ion sources for ITER, the Volume Produced H^- (H^-_{VP}) ions are produced by electrons colliding with hydrogen molecules in the volume of the plasma:

$$e^-_{\text{slow}} + H_2(v) \rightarrow H^-_{\text{VP}} + H, \tag{2.20}$$

where v is the vibrational level of the $H_2(v = 0, 1, 2, ...)$. To achieve a high collision frequency of Dissociative e^- Attachment (DA), a region with e^-_{slow} is needed. This is achieved as a secondary effect of the $\mathbf{B}_{\text{FF}}$. The $\mathbf{B}_{\text{FF}}$ increases the path length of the electron trajectories from drivers to PG, leading to an increased number of collisions with neutrals, which reduces the energy of the electrons [81, 82]. It was shown in [83] that the integral of the magnetic flux density from drivers to PG determines the electron cooling. As already mentioned, the magnetic filter thus separates the chamber into two regions with different plasma parameters, the driver region

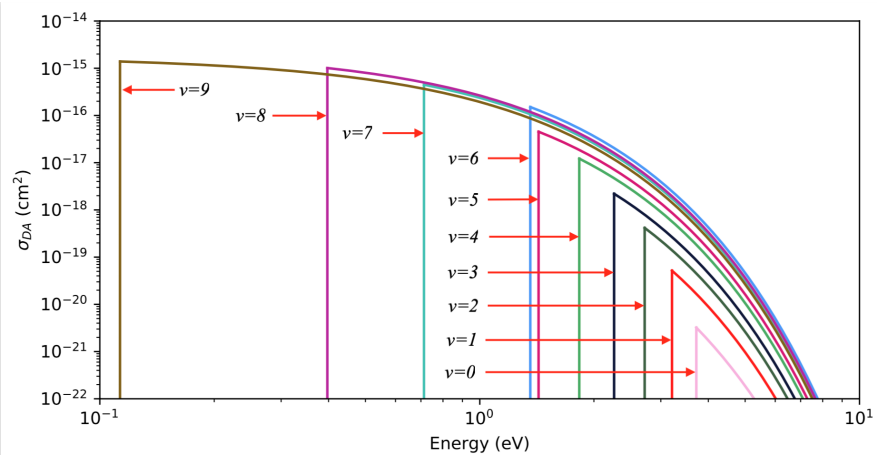

Figure 2.9: *Dissociative attachment cross-sections for vibrational states* $v = 0, 1, 2, .., 9$ *for* H_2.

and the extraction region. The full magnetic field topology in ELISE is shown in detail in [61, 84].

The vibrational level v of the target molecule determines the cross-section σ_{DA} for Equation (2.20) to occur. The cross-sections for H_2 and D_2 are given in [40, 85]. Based on values for $\sigma_v^{(0)}$ and $E_{th}(v)$, adapted from [40], Figure 2.9 shows the cross-sections σ_{DA} for the initial vibrational states $0-9$. The higher the vibrational level is, the larger the cross-section σ_{DA} is. For a plasma with a mean electron energy of ~ 2 eV, as is the case in front of the PG in ELISE and BUG, vibrational levels $v > 3$ dominate for H_2. The threshold energy for DA decreases and the peak value for σ_{DA} increases with increasing vibrational level v. The efficiency of reaction (2.20) can therefore be increased by vibrational excitement by collisions with energetic electrons:

$$\mathrm{e}^- + \mathrm{H}_2(v = i) \rightarrow \mathrm{H}_2(v = i + 1) + \mathrm{e}^-. \tag{2.21}$$

However, both vibrational excitement and de-excitement ($v = i \rightarrow v = i - 1$) are probable transition steps. In order to reach higher vibrational states ($v > 1$), multiple collisions are needed.

Additionally, higher vibrational states can be populated by radiative decay from singlet states ($\mathrm{H}_2^*(B, C, ...)$) [86–88]. These singlet states are formed by electron collisions of ground state molecules ($\mathrm{H}_2(X, v = 0)$) as follows:

$$\mathrm{e}^- + \mathrm{H}_2(X, v = 0) \rightarrow \mathrm{e}^- + \mathrm{H}_2^*(B, C, ...), \tag{2.22}$$

$$\mathrm{H}_2^*(B, C, ...) \rightarrow \mathrm{H}_2(X, v > 0) + h\nu, \tag{2.23}$$

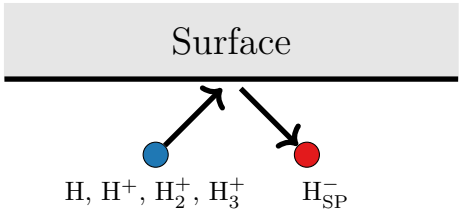

Figure 2.10: *Surface production of* H^- *ions.*

where h is Planck's constant and ν is the frequency of the emitted photon. The excitation process is effective for electrons with $T_e \geq 20$ eV [86].

2.4.2 Surface Production

Surface production of H^- ions is a process where neutral H atoms, or positively charged ions (H^+, H_2^+ and H_3^+) impinge on the PG with high energy and undergo charge transfer from the valence band of the surface. Theoretical models of Surface Produced H^- (H^-_{SP}) ion yield can be found in [89–93]. Figure 2.10 provides a schematic view of the process. For atomic H, this is achieved according to the following one-step process:

$$H + e^-_{wall} \rightarrow H^-_{SP}, \tag{2.24}$$

where e^-_{wall} is an electron in the valence band of the wall. In addition, positive H^+ ions approaching the metal surface can be neutralized with high probability. This conversion happens through a resonant charge transfer or an Auger process [90]. For molecular positive ions, H_2^+ and H_3^+, both dissociation and neutralization are likely to occur. The neutral H atoms are then free to gain an extra electron from the surface.

An illustration of the process is shown for a metal surface in Figure 2.11, where V_0 is the lowest level of the conduction band, φ is the work function, E_A is the electron affinity (energy spent when an electron is added to a neutral atom or molecule), ΔE is the shift of the affinity level and Γ is the level broadening of affinity. The work function W is defined by

$$W = -e\phi - E_F, \tag{2.25}$$

where e is the charge of an electron, ϕ is the potential near the wall, and E_F is the Fermi level in the material. For atoms near the surface, E_A is lowered due to the creation of a positive image charge in the metal.

Theoretical models for the H^- ion yield Y due to the backscattering of impinging ions or atoms

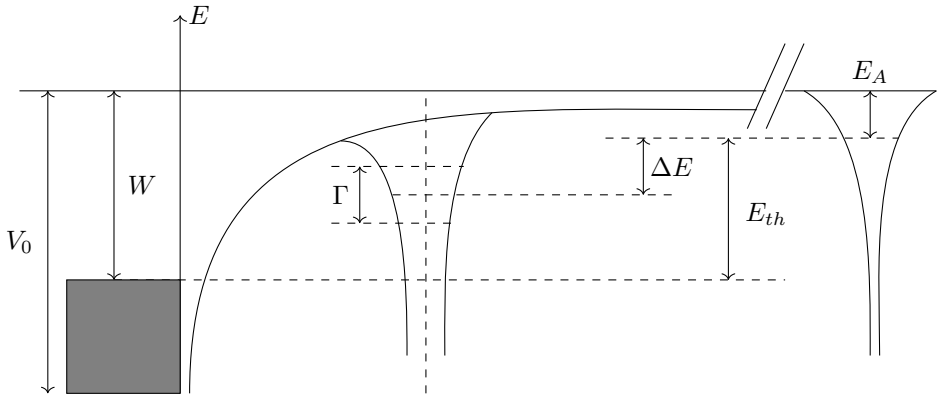

Figure 2.11: *Potential diagram close to the surface. Adapted from [90].*

have been developed by [92], among others. The relation between Y as a function of the incident energy of the atom or ion E_{in} can be expressed as

$$Y(E_{\text{in}}) = R_N \eta_0 \left[1 - \frac{E_{\text{th}}/R_E}{E_{\text{in}}}\right], \quad E_{\text{in}} \geq \frac{E_{\text{th}}}{R_N}, \tag{2.26}$$

where R_N is the fraction of reflected particles, η_0 is the electron transfer probability for H^-, E_{th} is the approximated threshold energy of the electron transfer probability and R_E is the energy reflection coefficient. The threshold energy E_{th} is approximated as the energy for an approximated step function of the electron transfer probability:

$$E_{\text{th}} = W - E_A. \tag{2.27}$$

For hydrogen, the electron affinity $E_A = 0.75$ eV [56, 94]. It is clear from Equations (2.26) and (2.27) that to increase the yield $Y(E_{\text{in}})$, the surface work function W should be decreased or the energy of the impinging particles E_{in} increased. To decrease the work function, an alkali metal, such as Cs in the case of ion sources for ITER, is deposited on the surface of the PG. The reason Cs is chosen is that it has the lowest work function of all stable elements of 2.0-2.1 eV [94]. However, the work function of a Cs-coated metal can be lowered to that below the value of bulk Cs by depositing less than one monolayer of Cs [95–97]. The minimum achievable work function ϕ_{min} for Cs is about 1.5 eV and is obtained with 0.5-0.7 monolayers. In environments with a vacuum and predominantly water vapor, ultra-low workfunction of $\sim 1.25 \pm 0.1$ eV have been measured [98].

In the context of NI sources, the use of Cs has been shown to significantly increase the amount of H^-_{SP} ions emitted from the surface [56, 99, 100]. Typically, the surface in ELISE and BUG

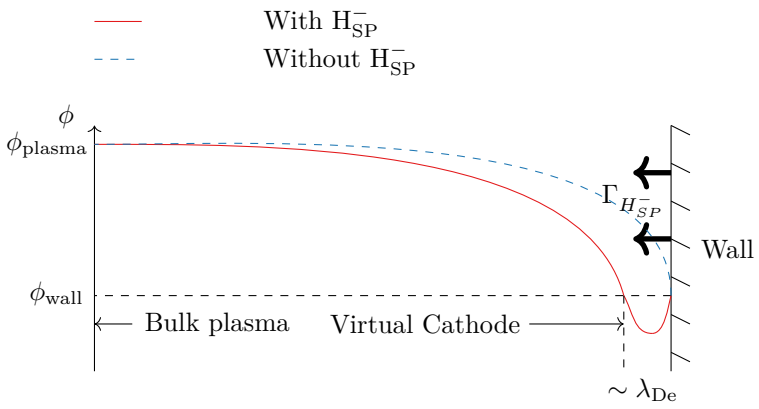

Figure 2.12: *The electrostatic potential and VC near a wall, with and without the emission of H^-_{SP} ions from the wall.*

is coated by Cs by evaporation from liquid Cs reservoirs by the use of a so-called Cs oven [96, 101–104]. It is shown in [105] that the NI density increases by a factor of 10, at a distance of 1 cm from the PG, during the caesiation due to increased emission of H^-_{SP} ions from the walls, and particularly from the PG. The presence of the H^- ions in the plasma, mostly due to surface production leads to the formation of an electronegative plasma, i.e., with $n_{H^-} \geq n_e$.

When H^- ions are produced at the surface of the wall, a double sheath with a local minimum of the potential near the wall can be formed due to the negative space charge from H^- ion accumulation close to the wall, commonly called a Virtual Cathode (VC) [106–108], see Figure 2.12. The VC limits the effective emission rate of H^-_{SP}, i.e., the number of NIs from the surface that can reach the plasma volume, by reflecting a fraction of ions back towards the wall. The depth and width of the VC depend on the plasma parameters, this is investigated in Chapter 5.

2.4.3 Collisional processes in the extraction region

In discharge plasmas, charged particles interact both via the generation of an electric field and via collisional interactions between the particles. In the context of NI production and extraction, collisional processes between NIs and the neutral background gas, collisions between negative and PIs, and collisions between e^- and the background gas are relevant.

Table 2.2 summarizes the most important collisional processes and Figure 2.13 the cross-section for these collisions. The most important destructive reaction is the stripping of electrons via ED. DA is the process governing the volume production of H^-, described in Section 2.4.1. Electron Elastic Collisions (eEC), is an elastic collision that does not impact the production or destruction of H^-, it does however impact the transport, which is of high importance when studying the co-extraction of electrons. Mutual Neutralization (MN) between H^- ions and H^+

Table 2.2: *Most relevant collision processes in the extraction region.*

Collision name	Process	Reference
Mutual neutralization (MN)	$H^- + H^+ \longrightarrow 2\,H$	[40, p. 24]
Associative detachment (AD)	$H^- + H \longrightarrow H_2 + e^-$	[40, p. 25]
Non-associative detachment (NAD)	$H^- + H \longrightarrow 2\,H + e^-$	[40, p. 25]
Charge exchange(CX)	$H^- + H \longrightarrow H + H^-$	[40, p. 26]
Dissociative e^- attachment (DA)	$e^- + H_2(\nu) \longrightarrow H + H^-$	[109, p. 207]
Electron detachment (ED)	$e^- + H^- \longrightarrow H + 2\,e^-$	[40, p. 23]
Electron elastic collision (eEC)	$e^- + H \longrightarrow e^- + H$	[40]

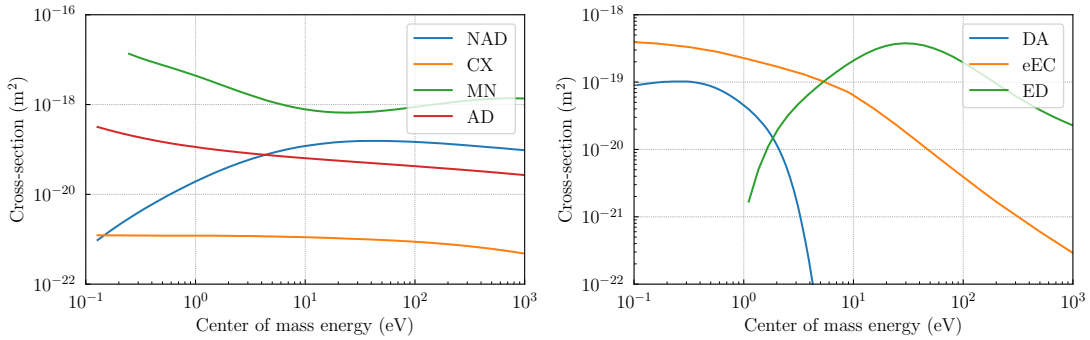

(a) **(b)**

Figure 2.13: *Cross-sections for collision processes in the extraction region as a function of the center of mass energy, (a) Non-Associative Detachment (NAD), Charge Exchange (CX), Mutual Neutralization (MN), Associative Detachment (AD), and (b) Dissociative e^- Attachment (DA), Electron Elastic Collisions (eEC), Electron Detachment (ED).*

ions, Associative Detachment (AD) and Non-Associative Detachment (NAD) cause destruction of H^- ions, out of which AD is the most relevant due to the high density of neutral H in the plasma ($n_H \sim 10^{19}$ m^{-3} and $n_{H^+} \sim 10^{17}$ m^{-3}). As mentioned above, Charge Exchange (CX) collisions between H^- ions and H do not reduce the amount of H^- ions in the plasma but may have an impact on their trajectories and extraction probability.

2.4.4 Extraction of negative ions and co-extraction of electrons

Extraction of H^- ions from the plasma chamber is achieved by applying an electric field between the PG and EG. At steady-state, an equipotential surface between quasi-neutral plasma on the source side of the PG, and the extracted ion beam, called plasma meniscus, is formed. Figure 2.14 shows the meniscus formation, VP, SP, extraction of NIs and the co-extraction of e^- in the extraction region near a PG aperture. The meniscus acts as an emission boundary, every negatively charged particle passing through the meniscus is accelerated out of the extraction

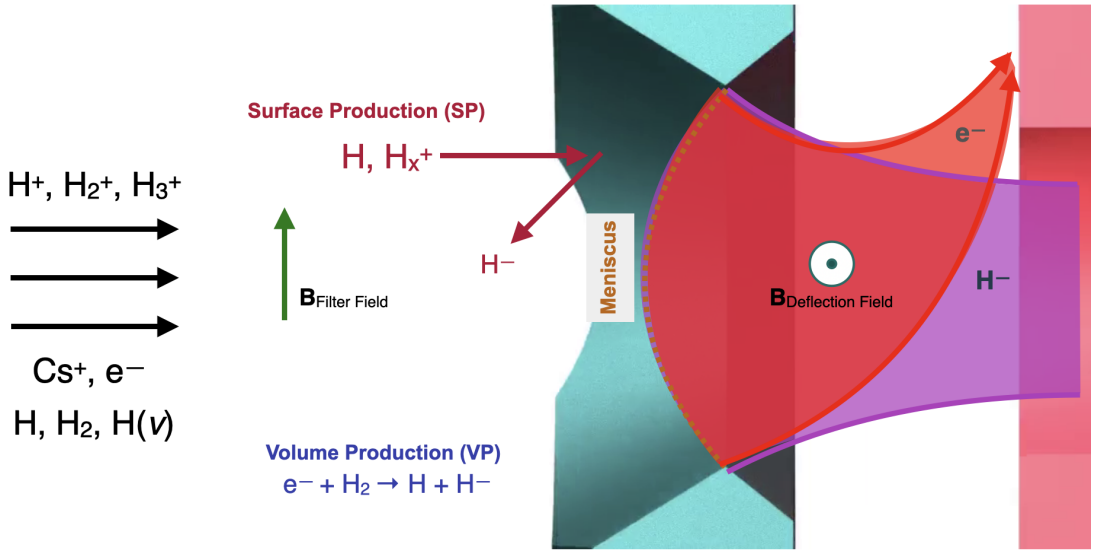

Figure 2.14: *Production of H^-_{VP} ions and H^-_{SP} ions in front of one aperture of the PG. The extraction of NIs and co-extraction of* e^- *are also shown.*

region while PIs are reflected. Therefore, the meniscus in this thesis is defined as the boundary where the PIs density is much lower than in the bulk plasma. Specifically, $n_{H^+} = 10^{13}$ m^{-3}, four orders of magnitude below the positive ion density in front of the PG, is chosen to define the meniscus.

The co-extracted electrons are separated from the NI beam by dumping them onto the EG by applying a Magnetic Deflection Field ($\mathbf{B}_{DF}$) with a major component in the vertical direction. The $\mathbf{B}_{DF}$ is generated by permanent magnets embedded inside the EG, placed in alternating directions for each row. The deflection field strength is up to 63 mT in the gap between the PG and EG, and $\sim$ 7 mT, at the central axial position 8 mm upstream of the PG aperture knife edge [108], i.e., in the plasma close to the meniscus.

One of the factors limiting the performance, i.e. the achievable extracted NI current is the amount of co-extracted electrons which needs to be limited below the power deposition threshold of the EG, which is 200 kW per grid segment [110]. This limits the amount of RF power and extraction voltage that can be used as well as the length of extraction pulses [111].

Figure 2.15 shows trajectories of H^-_{SP} ions. The ions are considered extracted when they cross the meniscus since the electric field after this meniscus surface strongly accelerates them through the grid system. The H^-_{SP} ions that are produced very close to the PG aperture are directly extracted from the plasma chamber (path *a*). Since the plasma is quasi-neutral and the H^-_{SP} ions traveling into the plasma chamber do not feel the electric field by the EG, there needs to be a physical process that causes the H^-_{SP} ions which travel deeper into the plasma to reverse

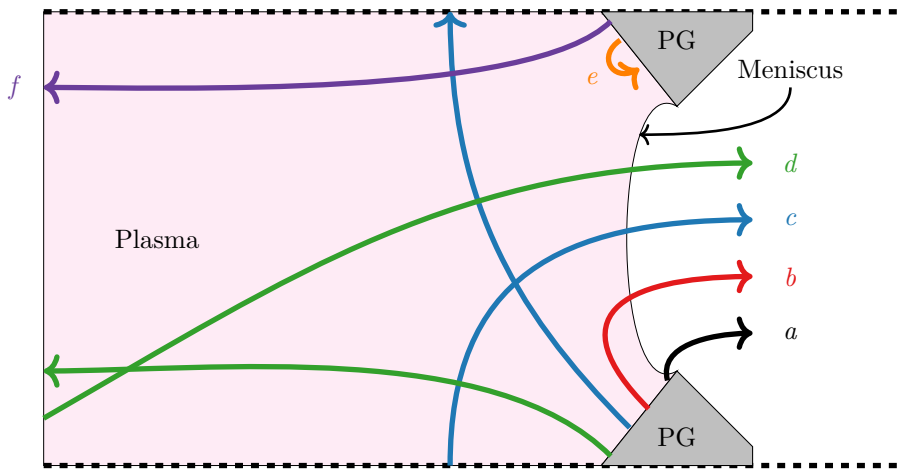

Figure 2.15: *Various possible trajectories of H^-_{SP} ions: (a) Direct extraction, (b) same-aperture indirect extraction, (c) neighbouring-aperture extraction, (d) extraction from bulk plasma, (e) H^-_{SP} ions reflected back to the PG by the VC, and (f) H^-_{SP} ions lost in the bulk plasma.*

their velocity for extraction to take place (paths b, c and d), such as collisions or bending of the trajectory by the magnetic field. The H^-_{SP} ions can travel between aperture rows or columns before extraction, following path c. A large fraction of the H^-_{SP} ions are never extracted, either due to reflection by the reversed field into the sheath back to the PG by the VC (path e), or they travel into the bulk plasma and are lost in the volume (path f) [62, 112].

2.4.5 Impact of biased surfaces on co-extraction of electrons

In both the ELISE and BUG ion sources, a Bias Plate (BP) is located on the plasma side of the PG and is electrically connected by U_{bias} to the source body but isolated from the PG. The BP is used to modify the potential distribution near the PG to limit the electron transport towards the apertures. It has been shown that biasing the PG positively with respect to the BP and source walls reduces the amount of co-extracted electrons [59, 105, 113].

Additionally, the introduction of a so-called Electron Fence (EF) to reduce co-extracted electron current has been studied. In the LHD, operated by National Institute for Fusion Science (NIFS) in Japan, experimental campaigns with an EF with a diameter of 5 mm, located at a distance of 5 mm and 7 mm from the PG, and oriented in the horizontal direction have been performed [114]. The idea of the EF is to intersect the trajectories of electrons following the field lines of the $\mathbf{B}_{DF}$, the EF is therefore placed in the horizontal direction. It was shown that the amount of co-extracted electrons was reduced when using the EF [114].

The electron temperature and density ($T_e \sim 10$ eV and $n_e \sim 10^{18}$ m^{-3} in the drivers) are reduced by an order of magnitude close to the PG via collisions with the gas enhanced by a

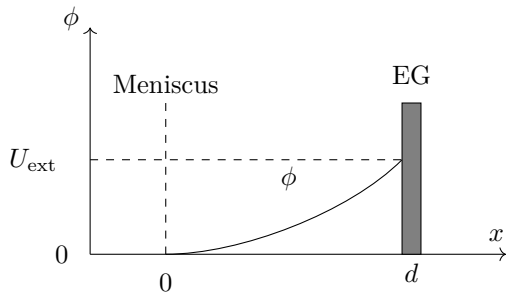

Figure 2.16: *Electrostatic potential in the space charge limit in 1D.*

horizontal $\mathbf{B}_{\text{FF}}$, which in ELISE is generated by a combination of driving a current I_{PG} of up to 5.3 kA through the PG and permanent magnets. This produces a magnetic field strength of around 5 mT close to the PG [66].

As the ITER NBI is designed for operating with both hydrogen, during the non-nuclear phases, and deuterium, during the D-T phase, investigations with both isotopes are needed. The effect of switching from operation in H to D has been investigated both in BUG and ELISE [57, 58, 111, 115, 116]. The ITER target of achieving a co-extracted electron current density that is lower than that of NIs has yet not yet been achieved during long pulse operation in deuterium in high-performance operation even with a higher $\mathbf{B}_{\text{FF}}$. During high-performance operation, the amount of co-extracted electrons increases strongly over time in deuterium, and with the RF power P_{RF}. To reduce the amount of co-extracted electrons, a stronger $\mathbf{B}_{\text{FF}}$ is generally used in D [57].

2.5 Negative ion acceleration and beam optics

There is a maximum extractable current density j_{SC} due to space charge limited emission [117]. To derive the space charge limit in 1D, one considers a case where the plasma meniscus and the EG electrodes are assumed to be two infinite, parallel, conducting plates with potential 0 V and U_{ext}, respectively. The plasma meniscus is located at $x = 0$ and the EG at $x = d$, see Figure 2.16. Assume that the particles crossing the meniscus have thermal velocity, this velocity is much lower than the velocity gained by the acceleration from $0 \rightarrow d$ ($\approx 1.385 \cdot 10^6$ m/s for H^- ions and 10 kV acceleration) and can be assumed to be 0 m/s.

Since all particles are assumed to flow uniformly, the electrostatic potential as a function of the x-position can be determined by solving the Poisson equation:

$$\frac{\mathrm{d}^2\phi}{\mathrm{d}x^2} = -\frac{\rho(x)}{\epsilon_0} \tag{2.28}$$

where x is the coordinate, $\phi(x)$ is the potential as a function of x, $\rho(x)$ is the charge density as a function of x, and ϵ_0 is the vacuum permittivity. The kinetic energy of the particles is proportional to $\phi(x)$

$$\frac{mv(x)^2}{2} = q\phi(x), \tag{2.29}$$

where $v(x)$ is the particle velocity in the x-direction as a function of x, m is the particle mass, q is the particle charge. The current density J of the extracted particles is assumed to be uniform and constant ($J = \rho(x)v(x)$) in the interval $[0, d]$. By integration by parts and using the Boundary Condition (BC) $\phi(0) = 0$ and $\phi'(0) = 0$ (the latter is true if one wants to find the space charge limited current $J = j_{\mathrm{SC}}$), one obtains

$$\phi(x)^{3/4} = \frac{3}{2}\left(\frac{j_{\mathrm{SC}}}{\epsilon_0}\right)\left(\frac{m}{2q}\right)^{1/4} x. \tag{2.30}$$

Using $\phi(d) = U_{\mathrm{ext}}$ gives

$$\phi(x) = U_{\mathrm{ext}}\left(\frac{x}{d}\right)^{4/3}, \tag{2.31}$$

and thus *Child-Langmuir's law*[7] is derived:

$$j_{\mathrm{SC}} = \underbrace{\frac{4}{9}\epsilon_0\left(\frac{2q}{m}\right)^{1/2}\frac{1}{d^2}}_{\Pi} U_{\mathrm{ext}}^{3/2} \equiv \Pi U_{\mathrm{ext}}^{3/2}, \tag{2.32}$$

where Π is called the Child-Langmuir *perveance*. Equation (2.32) gives the maximum current density that can flow between two parallel plates, the space charge limit. It is clear from the equation that in order to increase j_{SC}, one can either increase U_{ext}, or reduce d. The applicability of Child-Langmuir's law to ion source extraction systems depends on the degree to which the extracted beam is space charge limited, this is investigated in [118]. The normalized perveance in an experimental setting is the extracted current density j_{ex} as a fraction of the space charge limited emission j_{SC}:

$$\Pi_{\mathrm{normalized}} = \frac{j_{\mathrm{ex}}}{j_{\mathrm{SC}}}. \tag{2.33}$$

In the context of NBI systems, the width of the beamlet's angular distribution is of particular interest, since it largely determines the transmission of the beam through the beamline. A single Gaussian divergence θ_{stat} is calculated from the velocity component aligned with the beam axis

$v_{\parallel}$ and the velocity component in a direction perpendicular to the beam axis $v_{\perp}$ as:

$$\theta_{\text{stat.}} = \sqrt{2\langle \arctan\left(\frac{v_{\perp}}{v_{\parallel}}\right)^2 \rangle}. \tag{2.34}$$

The divergence can be calculated in the horizontal and vertical direction, but the distribution should be centered on the midpoint of the distribution before using Equation 2.34. When the local $v_{\parallel}$ is used, i.e., the $v_{\parallel}$ at a specific point in the grid system, the divergence decreases throughout the grid system as the beamlet is accelerated since the fraction $\frac{v_{\perp}}{v_{\parallel}}$ decreases. To avoid the effect that the specific amount of acceleration plays on the divergence, the final accelerated velocity is in this thesis used for $v_{\parallel}$, so that the divergence evolution is not obscured by the increase in velocity along the grid system.

The ITER NBI beamlines are designed under the assumption that the beam profile follows a Gaussian distribution [65]. The double-Gaussian consists of a core Gaussian with a smaller divergence θ_{core}, and a halo Gaussian with a larger divergence θ_{halo}. Adding the two components geometrically, weighted by their respective fractions f_{core} and f_{halo}, recovers the single Gaussian divergence $\theta_{\text{stat.}}$ as follows:

$$\theta_{\text{stat.}} = \sqrt{f_{\text{core}}\theta_{\text{core}}^2 + f_{\text{halo}}\theta_{\text{halo}}^2}. \tag{2.35}$$

Therefore, a single- or double-Gaussian can be fitted to the angular distribution.

Typically, the optimum perveance Π_{opt} is defined as the normalized perveance for which the beamlet divergence is minimized. For values below Π_{opt}, the beamlet is underperveant, and for values above Π_{opt}, the beamlet is overperveant; the beamlet perveance for the three cases is schematically shown in Figure 2.17. The beamlet profiles for the three cases are shown in Figure 2.18 for a three-grid system consisting of a PG, an EG and a GG.

The ion beamlets traveling through the grid system can be represented in phase space diagrams. A phase space diagram portrays the 6D space consisting of the particle coordinates (x, y, z) and momenta (x', y', z'). Figure 2.19 shows phase space diagrams in the x-direction for a particle beamlet traveling along a two-grid system in the z-direction that are diverging, converging, focused and almost parallel with the beam axis. The shape of the beamlet phase space is elliptical in this case, the width of the ellipse indicates that for a given particle position, there is a distribution of directions that the particles are traveling. In an idealized case, where each position x only corresponds to one momentum x', the ellipses would be replaced by lines. This is why the beam in Figure 2.19 is only *almost* parallel to the beam axis. The emittance ϵ of the beamlet is defined as the area of the beamlet in phase space and remains constant in conservative

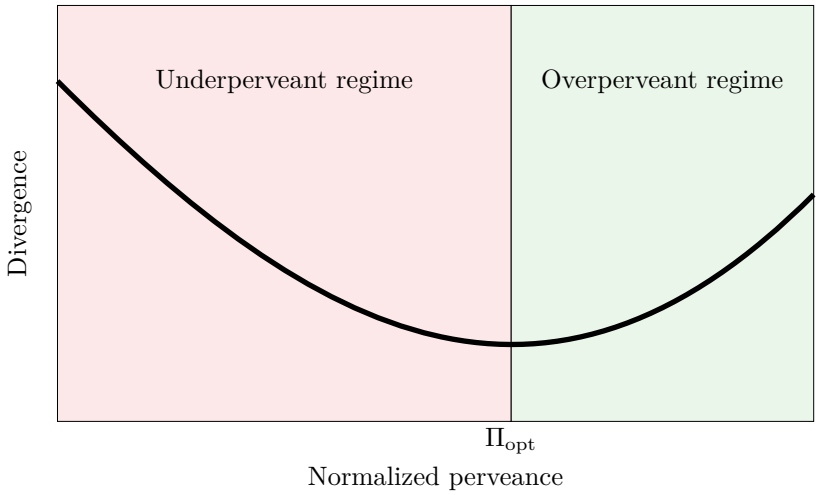

Figure 2.17: *Schematic representation of the beamlet divergence as a function of the normalized perveance.*

fields, the area of the particle ensemble in phase space thus remains constant throughout the grid system.

In general, non-linear optical effects, such as the shape of the meniscus, space charge repulsion or higher-order magnets, can cause the formation of a multi-component beam, with a separate beam halo and beam core [119–123]. Figure 2.20 (a) and (b) show phase space diagrams of a particle ensemble before and after having undergone non-linear effects. After the non-linear effect, the phase space diagram is S-shaped, and the beam halo component in the ensemble is portrayed by the extremities of the S-shape. Although the area (in red) of the two ensembles is conserved, the so-called emittance ellipse, drawn in dashed blue lines, is significantly larger after the non-linear effects. In addition, in Figure 2.20 (c), a particle ensemble is shown with an equal emittance ellipse as in Figure 2.20 (b). The choice of fitting an ellipse to the phase space diagram can be done under the assumption that the ion beam has a Gaussian distribution in x and x'. Multiple additional metrics (see Figure 2.21), such as the inclination angles α and β and their tangents x' and y' are defined for characterizing the emittance ellipse.

$$x' = \tan\alpha = \frac{p_x}{p_z}, \quad y' = \tan\beta = \frac{p_y}{p_z}. \tag{2.36}$$

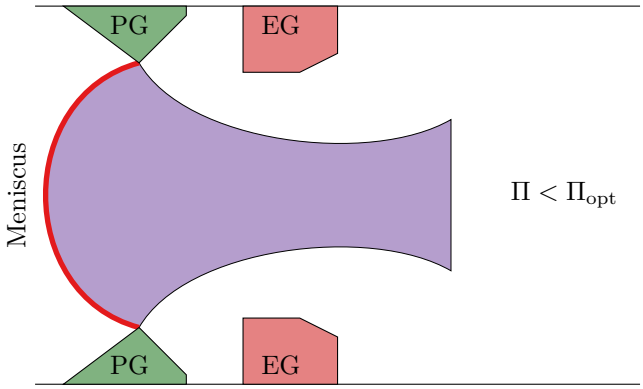

(a) *Underperveant beam.*

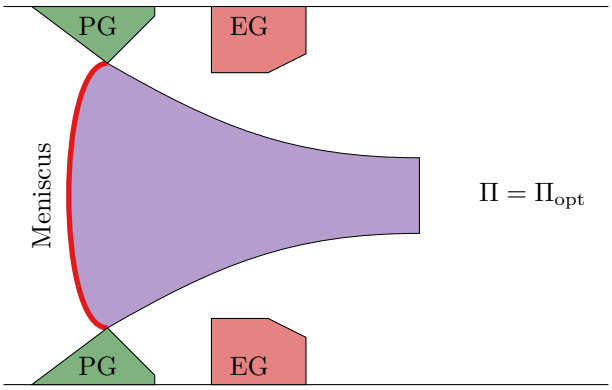

(b) *Beam in perveance optimum.*

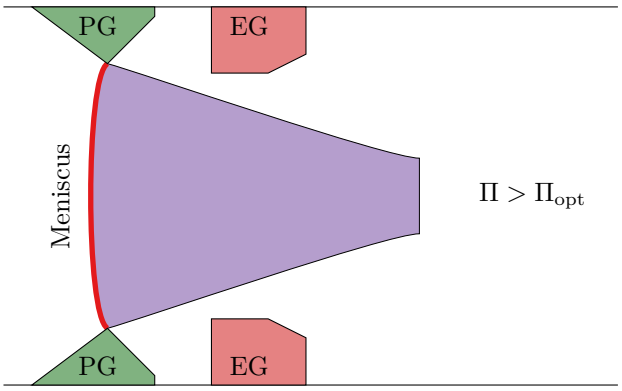

(c) *Overperveant beam.*

Figure 2.18: *Schematic view of the NI beamlet profiles for three extraction voltages showing the (a) underperveant regime, (b) perveance optimum and (c) overperveant regime.*

Moreover, from the ellipse equation, the following relations are given:

$$\gamma x^2 + 2\alpha x x' + \beta x'^2 = \epsilon, \tag{2.37}$$

$$\beta\gamma - \alpha^2 = 1, \tag{2.38}$$

$$A = \pi\epsilon = \pi R_1 R_2, \tag{2.39}$$

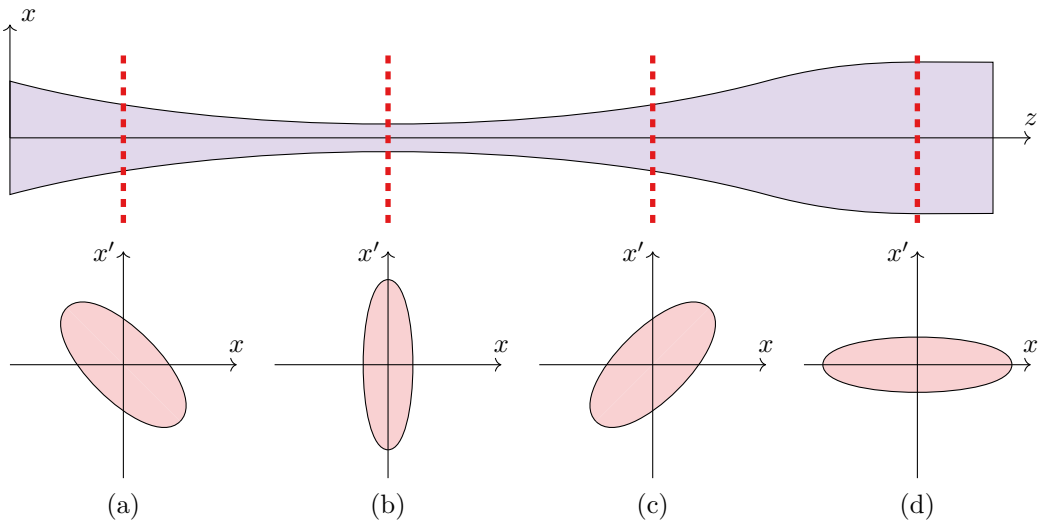

Figure 2.19: *Phase space diagrams of a (a) converging particle ensemble, (b) beamlet waist, (c) diverging particle ensemble and (d) particle ensemble that is almost parallel with the beam axis.*

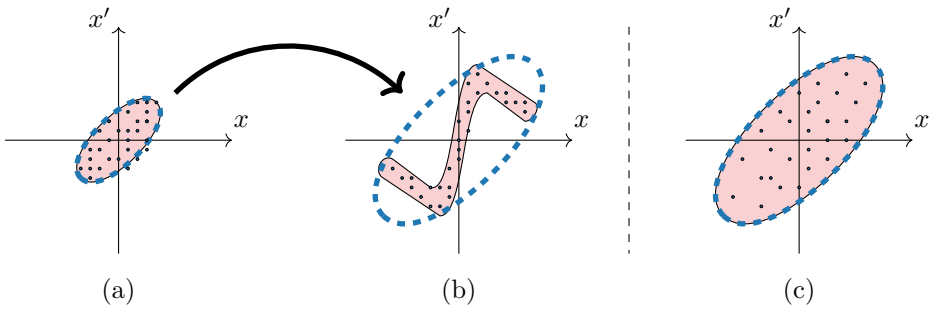

Figure 2.20: *Phase space diagrams of diverging particle ensemble (a) before and (b) after non-linear effects. Subfigure (c) has the same Twiss parameters as (b), but no beam halo.*

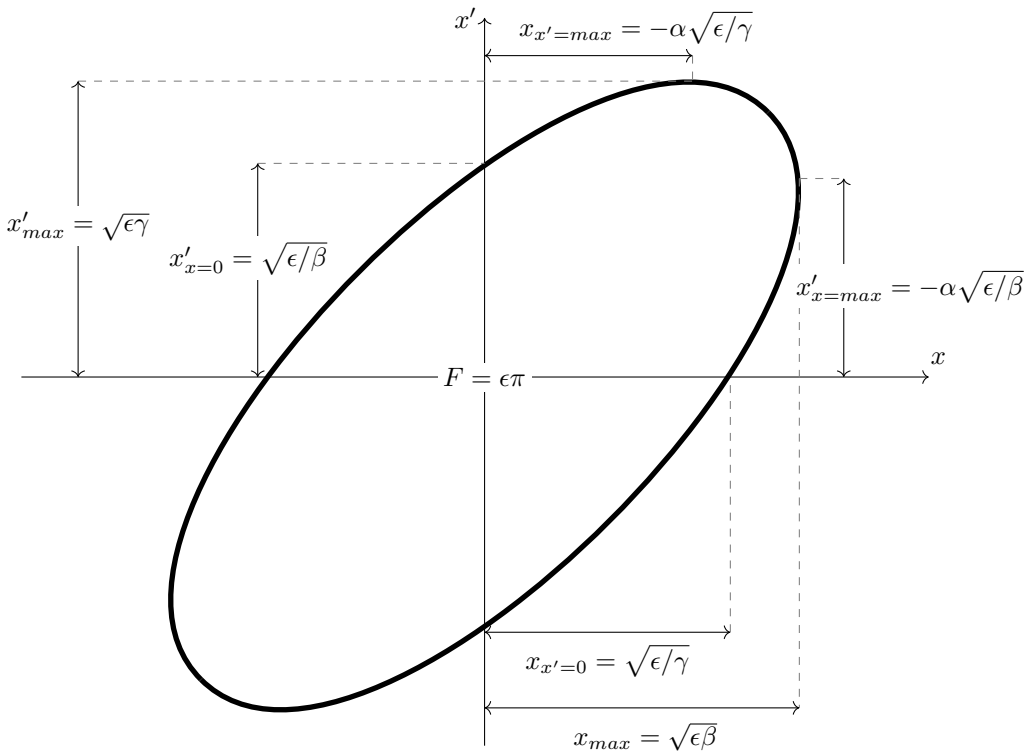

Figure 2.21: *Emittance diagram with derived twiss parameters. Adapted from [119].*

where α, β and γ as the so-called Twiss parameters, R_1 and R_2 are the major and minor radius of the emittance ellipse, respectively. Often, accelerator systems have a maximum allowed root-mean-square emittance:

$$\epsilon_{\mathrm{rms}} = \sqrt{\langle x'^2\rangle\langle x^2\rangle - \langle xx'\rangle^2}, \tag{2.40}$$

where $\langle X\rangle$ denotes the expected value of X. In the case of ITER, the demand on the beam optics is a beamlet divergence below 7 mrad. For an in-depth description of the characterization of beam transport in accelerator systems, the reader is referred to [119].

2.6 Diagnostic tools for the evaluation of source and beam performance

Monitoring and controlling the plasma parameters in the drivers and expansion chamber, as well as the extracted beam properties, is of crucial importance for understanding the relevant

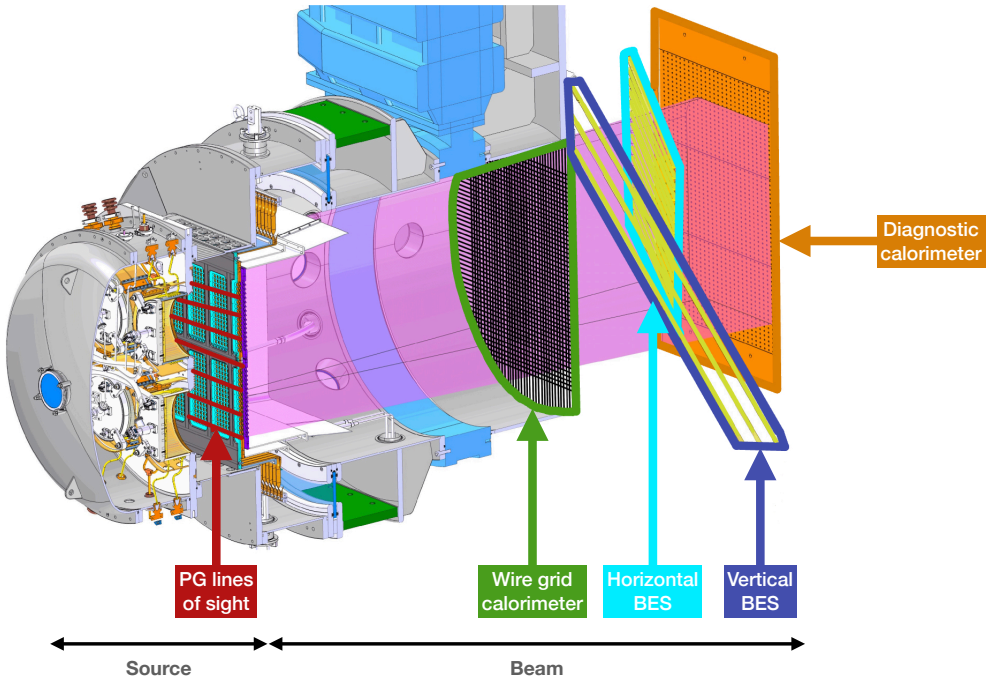

Figure 2.22: *Selected diagnostics in ELISE.*

physical processes and for identifying optimal operational conditions. The parameters are also used as input in numerical models used to study the ion source, which is of particular importance for this thesis.

Figure 2.22 and Figure 2.23 show examples of diagnostic tools and Line of Sight (LOS) used in ELISE and BUG, respectively. The diagnostics are categorized as source diagnostic tools (on the plasma side of the experiment) and beam diagnostic tools (on the beam side of the experiments). The main diagnostics will be explained in the following sections.

2.6.1 Source diagnostics

Two different plasma regimes exist in the ion source due to the impact of the already described $\mathbf{B}_{\mathrm{FF}}$ and the plasma expansion on the plasma parameters. In the driver, the plasma regime is characterized by higher plasma density ($n_e = n_i \sim 10^{18}$ m^{-3}) and electron temperature ($T_e \sim$ 10 eV). Inelastic electron collisions dominate for the population of the individual excitation states [124]. The density ratio of atoms to molecules is $\sim 0.3 - 0.5$ [115]. Diagnostics in the driver have to be adapted for these conditions by using non-invasive techniques. In the boundary layer near the PG, electron density and temperature are lower ($n_e < n_i \sim 10^{17}$ m^{-3}, $T_e \sim 2$ eV).

- **Optical Emission Spectroscopy (OES)** is based on the analyses of light emitted from

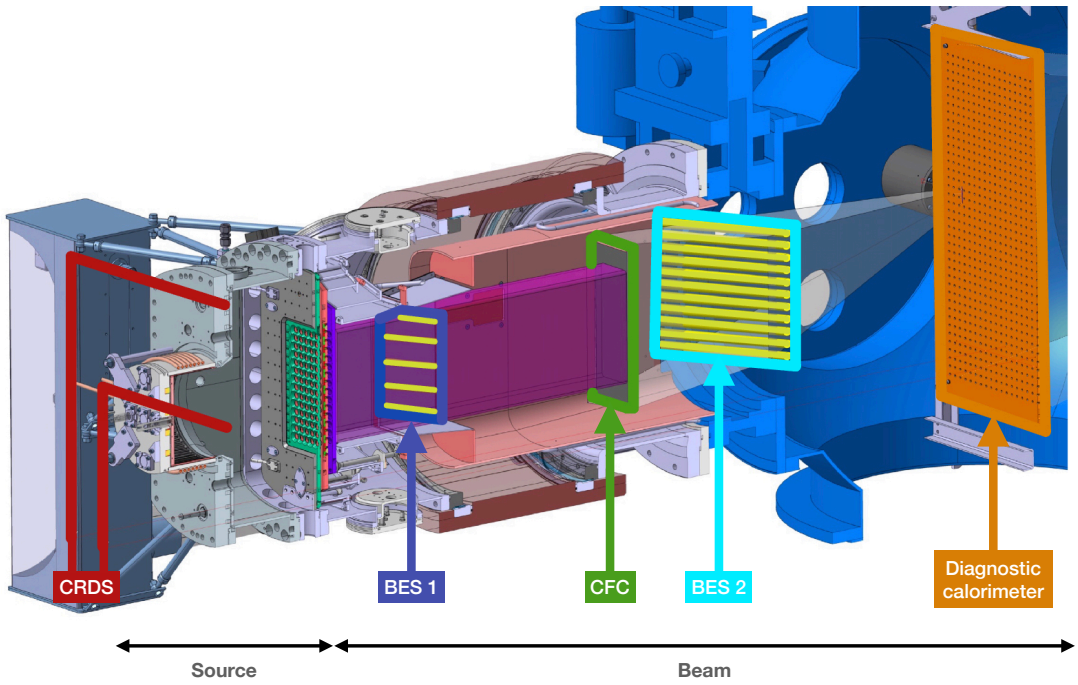

Figure 2.23: *Selected diagnostics in BUG.*

the plasma to determine different plasma parameters. The OES provides line-averaged measurements of the plasma parameters. The emissivity is determined for the Balmer lines (H_α, H_β, H_γ, ...), for the Fulcher band of H_2 ($d^3 \rightarrow a^3$), for the Cs line at 852 nm, and for impurities such as the atomic oxygen line, and three copper lines, the OH band and nitrogen. These measurements are used to detect impurities in the plasma, monitor the stability of pulses, and determine plasma parameters such as electron temperature T_e, plasma density, and vibrational and rotational temperatures [125].

- **Langmuir probes** are used for determining the plasma parameters, such as electron density, electron temperature, the floating potential ϕ_{floating} and plasma potential ϕ_{plasma} at the position in where the tip is placed. Langmuir probes consist of an electrode to which a variable biasing voltage can be applied. An I-V curve is used to determine the plasma parameters. A movable probe can determine the profile of the plasma, either in the axial direction (from driver exit to PG) or in the horizontal and vertical directions [35, 125].

- **Cavity Ring-Down Spectroscopy (CRDS)** is an absorption technique used to determine H^- ion density based on the photodetachment process of H^-. A short pulse of light is introduced into an optical cavity and is attenuated as it bounces between mirrors. The decay time of the light depends on the absorption of the particle species [126].

- **Tunable Diode Laser Absorption Spectroscopy (TDLAS)** is used to determine neutral Cs density. By passing a tunable diode laser through a medium and analyzing the absorbed light at specific wavelengths (852 nm for Cs), the concentration of the species can be determined [127].

2.6.2 Beam diagnostics

- **Electrical measurements** are performed to determine extracted NI current I_{ex}, co-extracted electron current I_e and the grounded grid current I_{gg} [125].
- **Tungsten wire calorimeter**, see Figure 2.22 is used to get an image of the extracted beam. The beam intersects the calorimeter, a grid of tungsten wires with a diameter of 0.2 mm, spaced by 20 mm, heating it to temperatures as high as 2600 K allowing it to emit visible light, representing an approximate shape of the beam [128].
- The **1D-Carbon Fiber Composite (CFC)**, see Figure 2.23, is a specialized calorimetric diagnostic tool designed specifically for assessing heat flux in beam diagnostics. The CFC consists of carbon fibers uniformly oriented in one direction (thereby 1D). The heat conduction along the wires is 20 times more effective than in the perpendicular direction. The wires are monitored with an Infrared (IR) camera from the rear side of the target. From the images, temperature profiles based on the 1D heat conduction can be derived, which can be used to determine the footprint and divergence of the beamlets [35, 129].
- **Beam Emission Spectroscopy (BES)** is based on the measurement of Doppler-shifted H_α radiation. It allows the measure of the intensity of the fully accelerated beam, the beam divergence, and the amount of negative hydrogen ions stripped in the accelerator [130–132]. Both ELISE and BUG are equipped with two BES setups. In ELISE, both BES locations are after the wire grid calorimeter, see Figure 2.22, 16 of the 20 optic heads are vertically arranged 5 cm apart for vertical beam profiling, while the remaining four are horizontally spaced 16 cm apart for horizontal profiling [133]. In BUG, the BES locations are before and after the 1D-CFC, both directed in the horizontal direction, see Figure 2.23. The first BES is close enough to the GG to detect signals from a single row of beamlets without beamlet mixing BES [131, 132].
- A **Diagnostic calorimeter** is a beam dump that allows the determination of the global beam power and the shape of the beam profile. The diagnostic calorimeter is shown both in the ELISE and BUG diagnostic setup in Figure 2.22 and Figure 2.23. An IR camera observes the diagnostic calorimeter and allows for studies of the beam homogeneity with a precision on the order of centimeters [35].

2.7 Numerical modeling of RF ion sources

2.7.1 Overview

Numerical models provide an important approach for studying complex processes in NI sources. In the context of beam formation processes of H^- ions, descriptions of the transport process of H^- ions and electrons through the plasma upstream of the meniscus to the extraction aperture are important to increase the H^- ion current, decrease the co-extraction of electrons, and control the beam optics. Generally, however, it is difficult to experimentally measure the detailed structure of the sheath or pre-sheath electric potential close to the extraction aperture and the resulting particle dynamics. To accurately describe the physics in the extraction region, the topology of the magnetic field, the interaction between particles, source walls, and the grid system need to be considered. These processes involve complex and intrinsically 3D physical behavior, strongly depending on the topology of the magnetic fields, but also the space charge distribution evolving in tight relation with the plasma source characteristics and the extraction field and the BCs. This renders experimental and analytical approaches untenable for a detailed study of the extraction mechanisms. Therefore, predictive numerical modeling and simulations are vital to understanding the extraction and beam formation processes.

Modeling the plasma generation process and the subsequent plasma expansion towards the plasma grid can be achieved through different types of models. Fluid models can be used for simulating the full ion source. The fluid modeling of the plasma source should ideally be electromagnetic, i.e., it solves the coupled Maxwell equations to include the inductive coupling of the RF to the plasma. However, a full Maxwellian distribution function is assumed, and thus microscopic quantities, such as the effect of applied electrostatic fields from the EG on the trajectories of single particles, are not resolved. Therefore, the formation of a plasma sheath towards the walls and the extraction of NIs are not treated.

Particle-In-Cell (PIC) models, described in Chapter 3 offer a first-principles-based approach for particle extraction and the formation of beamlets within the grid system. To simulate the extraction region close to the PG and the extraction and acceleration of NIs, 3D-PIC Monte Carlo Collisions (MCC) modeling [107, 134–139] is needed. These models include the meniscus formation, collisional processes, formation for the VC, VP and SP of NIs, extraction of NIs, co-extraction of e^-, and impact of both the $\mathbf{B}_{\mathrm{FF}}$ and $\mathbf{B}_{\mathrm{DF}}$ on the particle transport. However, these models can be computationally intensive due to numerical criteria imposed on the grid size, timestep, and number of simulated particles, described in Chapter 3, Section 3.2.5. Therefore, these simulations are generally constrained to a simulation domain consisting of one aperture

of the PG with periodic BCs. A review of PIC codes for the extraction region can be found in [140].

2.7.2 State of the art for PIC modeling of NI extraction

Dimensional reduction (from 3D to 1D or 2D) and scaling of physical parameters are the two main strategies used to reduce the high computational cost of PIC models of the extraction region in NI sources [140]. Simulations with a reduction of the spatial domain to 1D [81, 141–143] do not include the aperture of the PG and the extraction of NIs and co-extraction of e^-. Instead, the plasma formation in a slit domain is simulated, and H^-_{SP} ions may be emitted from one of the boundaries. These simulations can for example simulate Debye sheath formation and VC formation. 2D models include the geometry of the PG aperture [144]. However, the aperture is modeled as an infinite slit. The simulation domain typically covers one aperture. In both 1D and 2D simulations, magnetic fields may be included in the model. However, since not all three components of the magnetic field can be included, particle drifts (such as $\mathbf{E} \times \mathbf{B}$-drift and diamagnetic drift) are not fully described [140]. In the extraction region of ELISE and BUG, the $\mathbf{B}_{FF}$ and $\mathbf{B}_{DF}$ are perpendicular both to each other and to the beam axis. Therefore, the effects of drifts are important to the particle transport, which 2D models can not fully reproduce [140]. In 2.5D models [120, 136, 144, 145], the physical space is two-dimensional, but the vectors describing physical quantities such as the electric and magnetic fields, velocities, and forces have three components. This allows the simulation to capture some key aspects of three-dimensional behavior, such as out-of-plane magnetic field components or 3D particle motion, without the full computational cost of a 3D simulation. In 3D models [107, 121, 123, 137–139, 146–155], the PG aperture is modeled as a circular hole and a full 3D map of the magnetic field can be used as an input to the model. These models, however, require significantly more computation than 1D and 2D models and are therefore parallelized, as described in Chapter 3, Section 3.2.8, and usually simulated on computing clusters. Some 2D, 2.5D, and 3D models [107, 121, 136, 137, 139, 149, 156, 157] use scaled-down plasma parameters or physical constants to achieve reduced-size scaling or reduced-density scaling [137, 140, 157]. This makes the use of larger grid cells possible and thus allows for the simulation of a larger domain. However, scaling of physical quantities must be combined with appropriate scaling of physical constants, such as the vacuum permittivity, for the model to be applicable to experiments [140]. It has been shown that scaling of the plasma density does not change the properties, such as the plasma potential, of a quasineutral plasma [137]. However, in the Debye sheaths, where quasineutrality is not present, the physics are not fully reproduced, leading to an increased width of the sheath. In simulations with a small size domain, such as the simulations of SP and NI extraction, this can

have a significant impact on the particle transport [137]. Additionally, in magnetized plasmas, the ratio of the gyro radius and the sheath width is not preserved, which impacts the particle fluxes to the walls. For simulations where both plasma and beam are included, the extraction voltage must be scaled accordingly [137].

At the writing of this thesis, the following four 3D-PIC MCC models dedicated to the simulation of NI extraction and co-extraction of electrons exist.

- **Bari-Ex** was developed in CNR-Nanotec, Italy. It has been used for simulations of the extraction system of the NIO1 test bed, but with a grid size that is larger than the Debye length [146].
- **Fubiani et. al.** has developed a code at LAPLACE, Université de Toulouse, France. The code has been applied to various geometries, such as the extraction region in BAvarian Test MAchine for Negative ions (BATMAN). The code uses density scaling [137].
- **Keio-Beam Formation and eXtraction (Keio-BFX)** was developed at Keio University, Japan. Studies of meniscus and ion-ion plasma formation in the vicinity of one aperture have been performed. The code uses scaling of the domain size [107, 121, 139, 147–149].
- **Orsay Negative Ion eXtraction (ONIX)**: was developed at Laboratoire de Physique des Gaz et des Plasmas (LPGP), France [150–153] and extended in ITER Technology & Diagnostics (ITED), Germany [154, 158]. Studies of NI extraction from the ELISE and BUG ion sources have been performed. A typical simulation domain covers one extraction aperture, starting ~ 2 cm of the plasma on the upstream side of the PG up until the EG. The code does not necessitate the use of any scaling method for the plasma density or physical constants. A full 3D map of the magnetic field can be used as input, and the BC to the EG allows for a 2D plane. The code is written in Fortran and parallelized with Message Passing Interface (MPI) and scales well with increasing number of processor units, which allows for simulations with a grid size smaller than the Debye length with realistic plasma parameters [123, 138, 150–155].

Code-to-code benchmarking between Keio-BFX, Bari-Extraction (Bari-Ex) and ONIX has been published in [147]. There are still multiple open questions and physical effects that have not yet been included in these models. The most important ones are:

- Simulation with PG-biasing has not been performed. Generally, the simulated PG is on floating potential, meaning that a typical electron-repelling sheath is formed in its vicinity. This does not represent the sheath structure in the experiment, as described in

Section 2.4.5.

- Although H^-_{SP} ions are emitted from the PG surface, self-consistent simulation of H^-_{SP} ion accumulation in the plasma to the densities measured experimentally ($\sim 10^{17}$ m^{-3} [125]) has not been achieved.
- Due to the small computational domain, simulations of the NI transport throughout the beamlines have not been done, this makes comparisons between the simulated beamlet optics with experimental results impossible.

The ONIX code is used in this thesis to investigate these points among others. ONIX is an appropriate tool for the task since it does not rely on scaling and is still able to simulate the vicinity of an aperture in full-density.

The input parameters (particle temperatures and densities) of these codes are based on experimental measurements (see Section 2.6) or other numerical models. Asymmetries in both plasma density and extracted current density between the top and bottom segments are present in ELISE [57]. Additionally, line-averaged diagnostic techniques only represent the averages for each aperture row/column. Therefore, when using such values for inputs to 3D-PIC codes such as ONIX, or when using the global extracted current density for validation, one must consider the limitation that ONIX simulates the extraction process from a single aperture. This means ONIX does not account for global variations across different apertures. This discrepancy between local simulations and global measurements must be acknowledged for accurate interpretation and validation of the results.

2.8 Scope of the thesis

The work in this thesis revolves around the study of NI extraction, acceleration, and co-extraction of electrons from NI sources using the ONIX code. This thesis has two main themes, based on the open questions presented in Section 2.7.2. The first theme focuses on the physics of co-extracted electrons, and the second focuses on ion extraction and beam optics. The scope of the thesis can be summarized by seeking to answer the following questions:

- **Physics of the co-extracted electrons**
  - Which physical processes and parameters in the plasma determine the amount of co-extracted electrons?
  - How do biased surfaces in the ion source impact the co-extracted electron current and plasma properties near the PG?

  - Why are more electrons extracted during operation with deuterium than with hydrogen?
  - What are viable strategies for reducing the amount of co-extracted electrons?

- **Physics of ion extraction and beam optics**
  - Which plasma properties determine the accumulation of NI and formation of an ion-ion plasma near the PG in NI sources?
  - Which plasma properties determine the beam optics and what can be done to reduce the divergence of NI beamlets?
  - Which plasma grid geometries are the most favorable for extraction of NIs?

In order to approach these questions, the ONIX code has been improved by including a model for long-range effects of biased surfaces, electron losses along the magnetic field lines, and coupling with the ion-optics code Ion Beam Simulator (IBSimu) to extend the computational domain for investigations on beam optics.

CHAPTER 3

Modeling the extraction of negative ions with the 3D-PIC MCC code ONIX

In this manuscript, the 3D-PIC MCC [159] code ONIX [138] is used. It was developed to simulate NI extraction in sources that are dominated by surface production of NIs, which is the case for caesiated H^-/D^- sources [56, 80, 89]. The ONIX code self-consistently simulates particle transport in a hydrogen or deuterium plasma, including the effect of collisions and the influence of an external magnetic field. A detailed description of ONIX can be found in [138, 151–153] and validation in [138, 154].

This chapter provides a general overview of the PIC method and its implementation in ONIX. This is done in Sections 3.1-3.2.7. In Section 3.3, the specific implementation of ONIX for the simulation of the ELISE ion source geometry is presented.

During the course of the work conducted for this thesis, multiple improvements of the ONIX code have been implemented. The main contributions include the development of a new particle injection model, which improves on the previously used one to allow for a biasing of the PG, as outlined in Section 3.2.6. The ONIX code has been extended to include more complicated geometries, such as multi-aperture simulations and simulations of the BP or other biased objects. The ONIX code has also been coupled with the ion-optics code IBSimu, and an *a posteriori* particle tracking version of the coupled ONIX-IBSimu simulations has been developed, as outlined in Section 3.4.

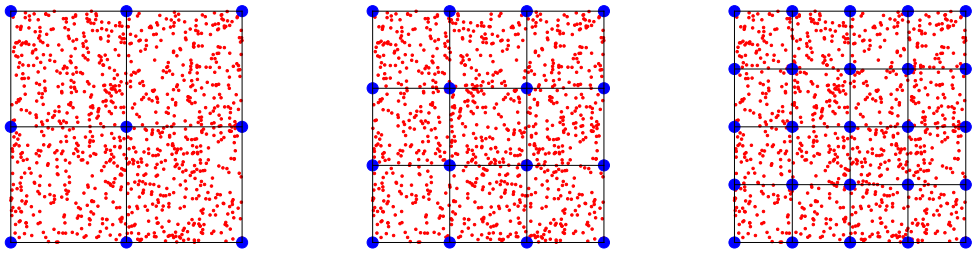

(a) (b) (c)

Figure 3.1: *A collection of macroparticles in a uniform mesh with (a)* 3×3*, (b)* 4×4*, and (c)* 5×5 *grid points.*

3.1 The Particle in Cell method

PIC modeling is a numerical method used extensively in plasma physics to solve self-consistent problems involving charged particles and electromagnetic fields. The computational domain is discretized into a grid or mesh on which the relevant field equations are solved. The particles interact with the field by interpolation from the grid points close to their locations. Figure 3.1 shows a collection of particles in a computational domain that has been discretized uniform grids of size 3×3, 4×4, and 5×5. The interaction between the particles and the fields forms the basis of the self-consistent problem.

In PIC simulations, macroparticles are used to reduce computational cost. Each macroparticle in the PIC simulation represents a statistical bunch of real particles with the same phase-space volume in the velocity distribution function. The Lorentz equation governs the motion of the particles, see Equation 3.1, and the trajectories of the simulated particles depend on the ratio of charge and mass. Therefore, a charged macroparticle will follow the same trajectory as a physical particle through the electric and magnetic fields. However, as is discussed in 3.2.5, the macroparticle density has to be sufficient for the solution for the fields to be satisfactory.

The plasma dynamics can be followed through its non-linear phase with PIC simulations. This is essential for many plasma phenomena, such as turbulence or the development of instabilities, which inherently involve non-linear processes. Unlike fluid-based codes, PIC simulations do not rely on specific assumptions about the plasma's state (such as assuming a Maxwellian distribution function), enabling them to capture these complex dynamics. One of the key benefits of PIC simulations is the dynamical range for the particle velocities, with no conditions imposed on their velocity distribution functions. This is critical in situations where non-Maxwellian distributions are present.

A full PIC cycle is summarised in Figure 3.2, each step described as follows

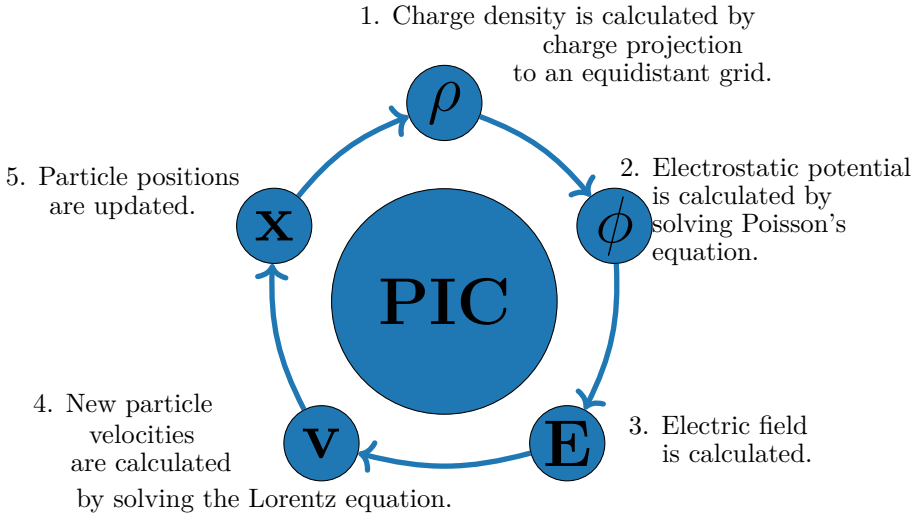

Figure 3.2: *The main steps in the PIC cycle.*

- **Initialization**: The particles and fields are initialized, particles are assigned initial positions, and velocities and BCs are defined.

- **Charge density extrapolation**: The charge density is calculated on a mesh.

- **Poisson solver**: Poisson's equation of the mesh is solved by using a numerical method, such as the Conjugate Gradient (CG) to compute the electrostatic potential at each mesh point.

- **Electric field solver**: The electric field is computed by taking the gradient of the electrostatic potential.

- **Field interpolation**: The electric and magnetic fields are interpolated from the mesh points onto the particle positions.

- **Particle pusher**: New particle velocities and positions are determined by solving the equations of motion.

- **Collisions**: Collisions are included by a MCC method, such as the Takizuka algorithm [160] or the Null Collision Method [161].

A comprehensive description of the PIC method can be found in [159, 162, 163]. Sections 3.2.1-3.3 describe the implementation of the PIC method in the 3D-PIC MCC code ONIX.

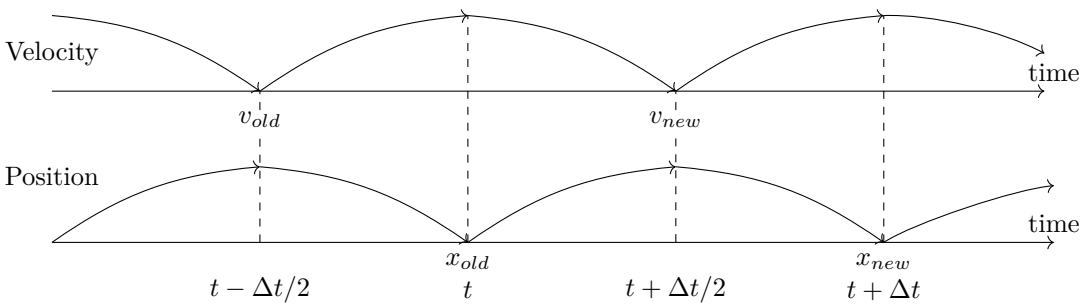

Figure 3.3: *Leapfrog timestepping.*

3.2 Overview of the ONIX code

3.2.1 Particle pusher

The motion of the ions and electrons is determined by Newton's second law and the Lorentz equation as follows:

$$\frac{\mathrm{d}\mathbf{x}}{\mathrm{d}t} = \mathbf{v}, \quad \frac{\mathrm{d}\mathbf{v}}{\mathrm{d}t} = \frac{q}{m}\left(\mathbf{E} + \mathbf{v} \times \mathbf{B}\right), \tag{3.1}$$

where $\mathbf{x}, \mathbf{v}, q$ and m are the position, velocity, charge and mass of the particle, and $\mathbf{E}$ and $\mathbf{B}$ are the electric and magnetic field at the particle position, respectively. The equations of motion are discretized according to the Boris-Buneman Leapfrog method since it has excellent long-term stability and preserves the phase space volume [159, 164]. The method relies on updating the velocity and position in staggered time steps, where the particle positions are defined at integer time steps ($t = \Delta t$, $2\Delta t$, $3\Delta t$, ...) and particle velocities at half-integer time step ($t = 0.5\Delta t$, $1.5\Delta t$, $2.5\Delta t$, ...), see Figure 3.3. Given the velocity at time step $k - 1/2$ (v_{old}), the velocity at time step $k + 1/2$ (v_{new}) is given by:

$$\mathbf{v}_{k+1/2} = \frac{\mathbf{x}_{k+1} - \mathbf{x}_k}{\Delta t}, \tag{3.2}$$

and

$$\frac{\mathbf{v}_{k+1/2} - \mathbf{v}_{k-1/2}}{\Delta t} = \frac{q}{m}\left(\mathbf{E}_k + \frac{\mathbf{v}_{k+1/2} + \mathbf{v}_{k-1/2}}{2} \times \mathbf{B}_k\right), \tag{3.3}$$

where $\mathbf{x}_k$, $\mathbf{v}_k$, $\mathbf{E}_k$ and $\mathbf{B}_k$ are the position, velocity, electric field and magnetic field at the k-th time-step, respectively. The particle position $\mathbf{x}_{k+1}$ is obtained as follows

$$\frac{\mathbf{x}_{k+1} - \mathbf{x}_k}{\Delta t} = \mathbf{v}_{k+1/2} \quad \Leftrightarrow \quad \mathbf{x}_{k+1} = \mathbf{v}_{k+1/2}\Delta t + \mathbf{x}_k \tag{3.4}$$

Using the Boris-Buneman definition of half-acceleration, $\mathbf{v}_{k+1/2}$ can be obtained by separating the rotation terms in Equation (3.3) into two intermediate velocities $\mathbf{v}^-$ and $\mathbf{v}^+$:

$$\mathbf{v}^- \equiv \mathbf{v}_{k-1/2} + \frac{q\mathbf{E}_k}{2m}\mathbf{D}, \tag{3.5}$$

$$\mathbf{v}^+ \equiv \mathbf{v}_{k+1/2} - \frac{q\mathbf{E}_k}{2m}\Delta t. \tag{3.6}$$

The following two relations directly follow from the definitions of $\mathbf{v}^-$ and $\mathbf{v}^+$:

$$\mathbf{v}_{k+1/2} + \mathbf{v}_{k-1/2} = \mathbf{v}^- + \mathbf{v}^+, \tag{3.7}$$

$$\frac{\mathbf{v}_{k+1/2} - \mathbf{v}_{k-1/2}}{\Delta t} = \frac{\mathbf{v}^+ - \mathbf{v}^-}{\Delta t} + \frac{q\mathbf{E}_k}{m}. \tag{3.8}$$

Thus, $\mathbf{v}_{k+1/2}$ and $\mathbf{v}_{k-1/2}$ can be substituted in Equation (3.3) to obtain the rotation by the Lorentz force:

$$\frac{\mathbf{v}^+ - \mathbf{v}^-}{\Delta t} = \frac{q}{2m}(\mathbf{v}^+ + \mathbf{v}^-) \times \mathbf{B}_k. \tag{3.9}$$

The Boris method is implemented by first obtaining $\mathbf{v}^-$ from Equation (3.5) which represents half of the acceleration, then performing a full rotation according to Equation (3.9) to obtain $\mathbf{v}^+$. Lastly, the new velocity $\mathbf{v}_{k+1/2}$ is obtained via Equation (3.6).

3.2.2 Projection to numerical grid points

The particle density at each gridpoint is calculated by projecting the charge of the particle onto the neighboring gridpoints using linear interpolation. The dimensionality of the projection can be of any degree, however here the 2D case is used for illustration. For the sake of clarity, let the grid be a uniform grid where each cell is formed by the four nearest gridpoints in a rectangle, see Figure 3.4. The area A_{cell} of such a cell is given by:

$$A_{cell} = \Delta x \Delta y, \tag{3.10}$$

where Δx and Δy are the width and height of the cell, respectively. For each particle in the cell, the cell is divided into four areas. Given a particle at position (x_p, y_p) as follows:

$$A_1 \equiv A_{i,j} = (\Delta x - l)(\Delta y - m), \tag{3.11}$$

$$A_2 \equiv A_{i+1,j} = l(\Delta y - m), \tag{3.12}$$

$$A_3 \equiv A_{i,j+1} = (\Delta x - l)m, \tag{3.13}$$

$$A_4 \equiv A_{i+1,j+1} = lm, \tag{3.14}$$

where the lengths l and m are defined as:

$$l \equiv x_p - x_i, \tag{3.15}$$

$$m \equiv y_p - y_i, \tag{3.16}$$

illustrated in Figure 3.4. Next, the total charge density to be distributed from a particle with charge q to the four nearest gridpoints is given by:

$$\rho_{cell} = \frac{q}{A_{cell}}. \tag{3.17}$$

The added charge density to each gridpoint ρ_i is given by

$$\rho_1 \equiv \rho_{i,j}, \tag{3.18}$$

$$\rho_2 \equiv \rho_{i+1,j}, \tag{3.19}$$

$$\rho_3 \equiv \rho_{i,j+1}, \tag{3.20}$$

$$\rho_4 \equiv \rho_{i+1,j+1}. \tag{3.21}$$

The projected charge density $\rho_{k,l}$ to each gridpoint in the cell is given by the following linear interpolation:

$$\rho_i = \rho_{cell}\frac{A_i}{A_{cell}}, \quad i = 1, 2, 3, 4. \tag{3.22}$$

In 3D, the analogous cell volume V_{cell} is given by:

$$V_{cell} = \Delta x \Delta y \Delta z. \tag{3.23}$$

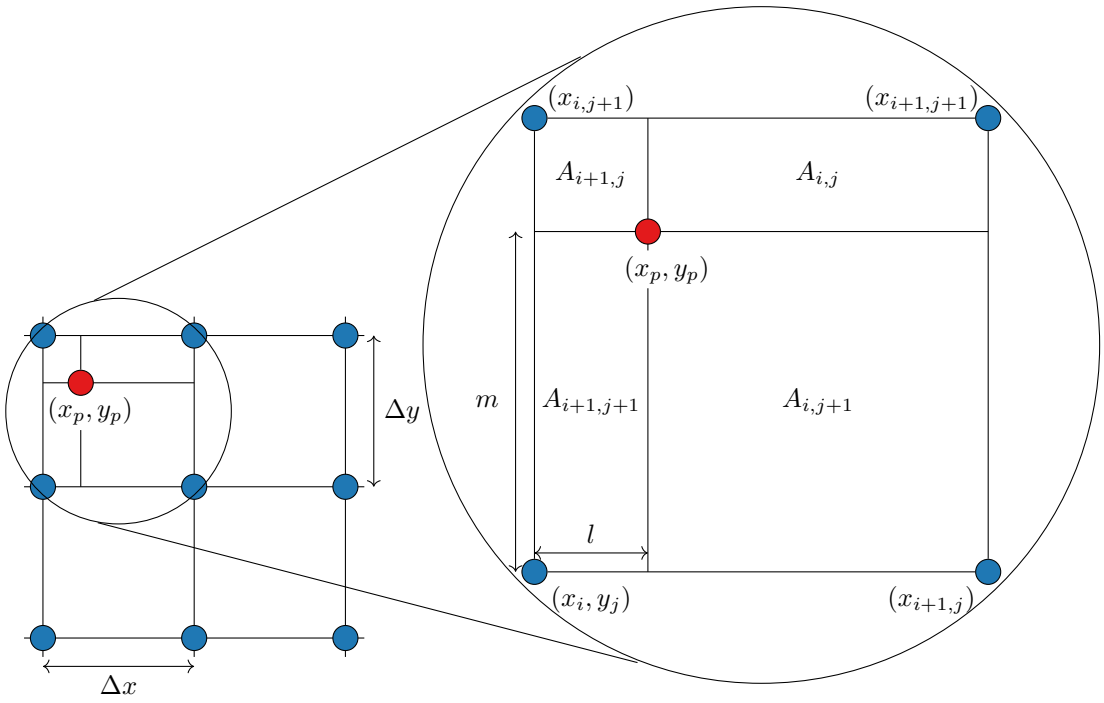

Figure 3.4: *4-point projection of particle charge on a 2D grid.*

In the same manner as in the 2D case, it is useful to define the volumes V_k and projected charge densities ρ_k^{3D}, $k = 1, 2, ..., 8$ for clarity, see Figure 3.5 for a visualization of the 8 volumes.

$$V_1 \equiv V_{i,j,k} = (\Delta x - l)(\Delta y - m)(\Delta z - n), \qquad \rho_1^{3D} \equiv \rho_{i,j,k}, \tag{3.24}$$

$$V_2 \equiv V_{i+1,j,k} = l(\Delta y - m)(\Delta z - n), \qquad \rho_2^{3D} \equiv \rho_{i+1,j,k}, \tag{3.25}$$

$$V_3 \equiv V_{i,j+1,k} = (\Delta x - l)m(\Delta z - n), \qquad \rho_3^{3D} \equiv \rho_{i,j+1,k}, \tag{3.26}$$

$$V_4 \equiv V_{i,j,k+1} = (\Delta x - l)(\Delta y - m)n, \qquad \rho_4^{3D} \equiv \rho_{i,j,k+1}, \tag{3.27}$$

$$V_5 \equiv V_{i+1,j+1,k} = lm(\Delta z - n), \qquad \rho_5^{3D} \equiv \rho_{i+1,j+1,k}, \tag{3.28}$$

$$V_6 \equiv V_{i+1,j,k+1} = l(\Delta y - m)n, \qquad \rho_6^{3D} \equiv \rho_{i+1,j,k+1}, \tag{3.29}$$

$$V_7 \equiv V_{i,j+1,k+1} = (\Delta x - l)mn, \qquad \rho_7^{3D} \equiv \rho_{i,j+1,k+1}, \tag{3.30}$$

$$V_8 \equiv V_{i+1,j+1,k+1} = lmn, \qquad \rho_8^{3D} \equiv \rho_{i+1,j+1,k+1}. \tag{3.31}$$

The total charge density ρ_{cell}^{3D} to be distributed is given by:

$$\rho_{cell}^{3D} = \frac{q}{V_{cell}}. \tag{3.32}$$

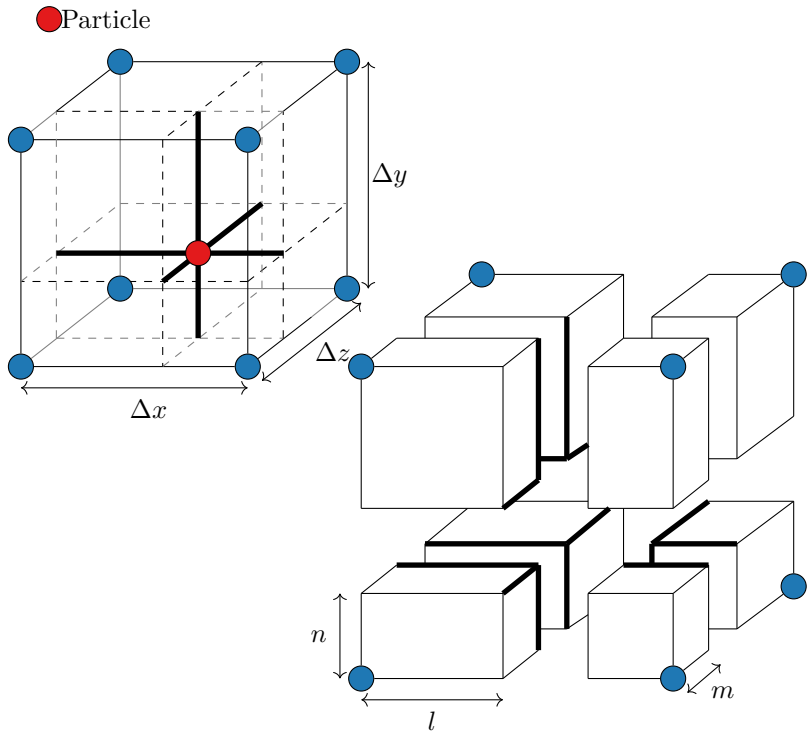

Figure 3.5: *8-point projection of particle charge.*

Finally, the charge distributed to each gridpoint is given by the following linear interpolation:

$$\rho_i^{3D} = \rho_{cell}^{3D} \frac{V_i}{V_{cell}}. \tag{3.33}$$

In ONIX, a second-order charge projection scheme is used, meaning that the charge from each particle is distributed to the nearest 64 mesh points using a second-neighbor linear interpolation technique. A detailed description is given in [150].

3.2.3 Poisson solver

To calculate the electrostatic potential ϕ, the Poisson equation is solved:

$$\nabla^2 \phi = -\frac{\rho}{\epsilon_0}, \tag{3.34}$$

where ρ is the charge density and ϵ_0 is the vacuum permittivity. In cartesian coordinates, the equation can be written:

$$\left(\frac{\partial^2}{\partial x^2} + \frac{\partial^2}{\partial y^2} + \frac{\partial^2}{\partial z^2} \right) \phi(x, y, z) = -\frac{\rho}{\epsilon_0}. \tag{3.35}$$

Equation (3.35) is discretized as follows:

$$\frac{\phi_{i-1,j,k} - 2\phi_{i,j,k} + \phi_{i+1,j,k}}{\Delta x^2} + \frac{\phi_{i,j-1,k} - 2\phi_{i,j,k} + \phi_{i,j+1,k}}{\Delta y^2} + \frac{\phi_{i,j,k-1} - 2\phi_{i,j,k} + \phi_{i,j,k+1}}{\Delta z^2} = -\frac{\rho_{i,j,k}}{\epsilon_0}.$$

Given that $\Delta x = \Delta y = \Delta z$, this can be rewritten as:

$$\phi_{i-1,j,k} + \phi_{i+1,j,k} + \phi_{i,j-1,k} + \phi_{i,j+1,k} + \phi_{i,j,k-1} + \phi_{i,j,k+1} - 6\phi_{i,j,k} = -\frac{\rho_{i,j,k}}{\epsilon_0} \cdot \Delta x^2. \quad (3.36)$$

The matrix equation can be written as:

$$\mathbf{A}\phi = \mathbf{b}, \quad (3.37)$$

where

$$A = \begin{bmatrix} -6 & 1 & 1 & 1 & 1 & 0 & 0 & \dots \\ 1 & -6 & 1 & 1 & 0 & 0 & 0 & \dots \\ 1 & 1 & -6 & 1 & 1 & 1 & 0 & \dots \\ 0 & 1 & 1 & -6 & 1 & 1 & 1 & \dots \\ \vdots & \vdots & \vdots & \vdots & \vdots & \vdots & \vdots & \vdots \\ \dots & 0 & 0 & 1 & 1 & 1 & -6 & 1 \\ \dots & 0 & 0 & 0 & 1 & 1 & 1 & -6 \end{bmatrix}, \quad b = -\frac{\Delta x^2}{\epsilon_0} \begin{bmatrix} \vdots \\ \rho_{i,j,k} \\ \vdots \end{bmatrix}. \quad (3.38)$$

In ONIX, equation (3.37) is solved on each grid point using the CG method. The CG method is an iterative method for solving systems of linear equations on the form

$$\mathbf{A}\mathbf{x} = \mathbf{b}, \quad (3.39)$$

where $\mathbf{A}$ is a sparse, square, symmetric, positive-definite matrix, $\mathbf{b}$ is a known vector and $\mathbf{x}$ is the solution, in the case of the Poisson equation, $\mathbf{x}$ represents the ϕ in vector form. The quadratic form is a function $f(\mathbf{x})$ defined by:

$$f(\mathbf{x}) = \frac{1}{2}\mathbf{x}^T A\mathbf{x} + \mathbf{b}^T\mathbf{x} + \mathbf{c}, \quad (3.40)$$

where $\mathbf{x}$ is a vector with elements x_i with respect to some basis and the elements $a_{i,j}$ of A are constants [165]. It can be shown that if $\mathbf{A}$ is symmetric then the gradient of $f(\mathbf{x})$ can be written as:

$$f'(\mathbf{x}) \equiv \begin{bmatrix} \frac{\partial f(\mathbf{x})}{\partial x_1} \\ \frac{\partial f(\mathbf{x})}{\partial x_2} \\ \vdots \\ \frac{\partial f(\mathbf{x})}{\partial x_n} \end{bmatrix} = \mathbf{A}\mathbf{x} - \mathbf{b}. \tag{3.41}$$

Since $\mathbf{A}$ is positive definite ($\mathbf{x}^T A\mathbf{x} > 0$), follows that $f(\mathbf{x})$ is minimized by $f(\mathbf{x}) = \mathbf{A}\mathbf{x}$. Therefore $\mathbf{A}\mathbf{x} = \mathbf{b}$ can be solved by finding an $\mathbf{x}$ that minimizes $f(\mathbf{x})$ [165]. An extensive description of the CG method is available at [166] and the implementation in ONIX can be read in [150]. Additionally, in ONIX, Poisson's equation is solved using Dirichlet BCs and second-order interpolation for grid points near curved surfaces, using correction factors based on the simulation's geometry. This methodology ensures that the potential on the grid points near surfaces is accurate. A detailed description is given in [150, 167].

3.2.4 Electric field solver

To determine the electric field $\mathbf{E}$ in the PIC simulation, the gradient of the electrostatic potential ϕ is calculated:

$$\mathbf{E} = -\nabla\phi. \tag{3.42}$$

In the discretized version, the electric field is calculated only at each node in the grid by taking the gradient of the potential. Given a cartesian grid, the electric field at each node is given by $\mathbf{E}_{i,j,k} = (E_x, E_y, E_z)_{i,j,k}$ is given by:

$$\mathbf{E}_{i,j,k} = \left(\frac{\phi_{i+1,j,k} - \phi_{i-1,j,k}}{2\Delta y}, \frac{\phi_{i,j+1,k} - \phi_{i,j-1,k}}{2\Delta x}, \frac{\phi_{i,j,k+1} - \phi_{i-1,j,k-1}}{2\Delta z} \right), \tag{3.43}$$

where E_x, E_y and E_z are the components of $\mathbf{E}_{i,j,k}$ along each axis. Next, the electric field at each particle position $\mathbf{E}_p$ is calculated by linear interpolation:

$$\mathbf{E}_p = \frac{1}{V_{cell}} \sum_{i=1}^{8} V_i \mathbf{E}_i, \tag{3.44}$$

where $E_i, i = 1, 2...8$ are given by:

$$\mathbf{E}_1 \equiv \mathbf{E}_{i,j,k}, \tag{3.45}$$

$$\mathbf{E}_2 \equiv \mathbf{E}_{i+1,j,k}, \tag{3.46}$$

$$\mathbf{E}_3 \equiv \mathbf{E}_{i,j+1,k}, \tag{3.47}$$

$$\mathbf{E}_4 \equiv \mathbf{E}_{i,j,k+1}, \tag{3.48}$$

$$\mathbf{E}_5 \equiv \mathbf{E}_{i+1,j+1,k}, \tag{3.49}$$

$$\mathbf{E}_6 \equiv \mathbf{E}_{i+1,j,k+1}, \tag{3.50}$$

$$\mathbf{E}_7 \equiv \mathbf{E}_{i,j+1,k+1}, \tag{3.51}$$

$$\mathbf{E}_8 \equiv \mathbf{E}_{i+1,j+1,k+1}. \tag{3.52}$$

This is the linear derivative calculation of the electric field, but also higher-order derivative can also be used. The implementation of the electric field solver in ONIX is described in detail in [138].

3.2.5 Stability conditions

In order to resolve physics at the Debye scale and avoid numerical plasma heating, the following restriction of the cell width Δx can be calculated [168],

$$\Delta x < 3.4\lambda_{\mathrm{De}}, \tag{3.53}$$

where λ_{De} is the Debye length. When setting up the parameters for a PIC simulation, the user must therefore consider the highest value that the electron density takes in the simulation domain, and the lowest temperature, since $\lambda_{\mathrm{De}} \propto \sqrt{T_e/n_e}$. Figure 3.6 shows the λ_{De} as a function of T_e and n_e. As is discussed in Section 3.5, in the vicinity of an extraction aperture in the ELISE ion source $T_e = 2$ eV and $n_e = 6 \cdot 10^{16}$ m^{-3}, which is equivalent to a Debye length of $4.3 \cdot 10^{-5}$ m.

To resolve the electron plasma frequency in an explicit electromagnetic plasma simulation, the following requirement on the time step is necessary [159]:

$$\Delta t \leq 0.1/\omega_{pe}. \tag{3.54}$$

In order to meet the requirement defined by Equation (3.54), $\Delta t \leq 7.2 \cdot 10^{-12}$ s. In addition,

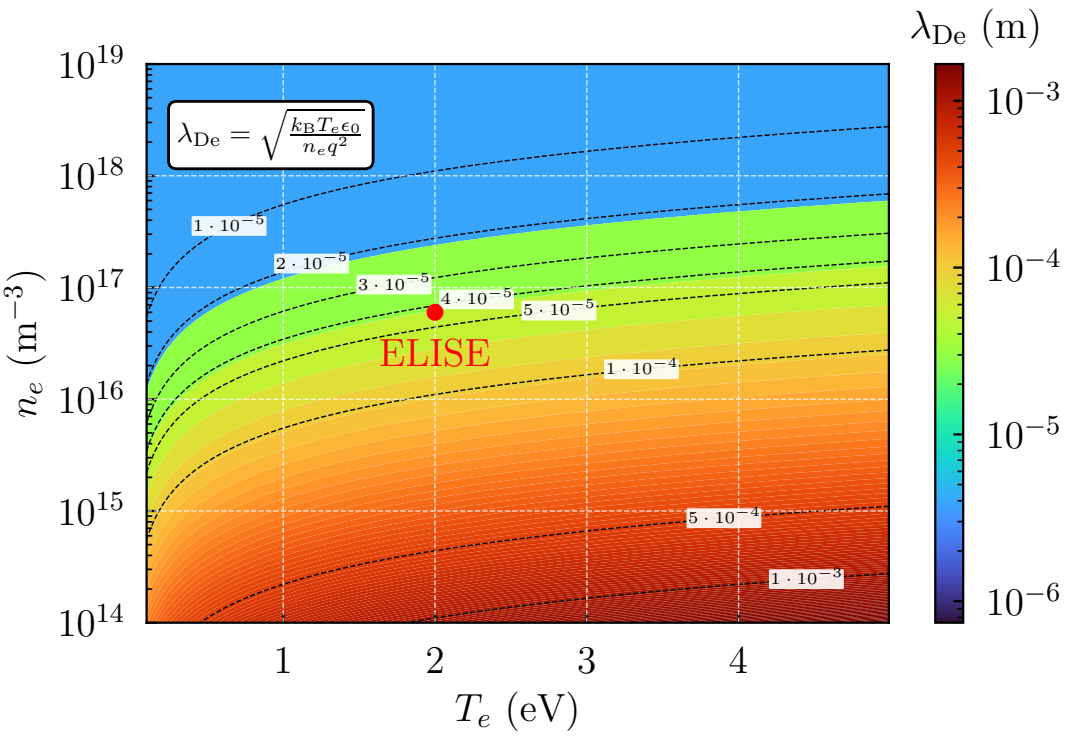

Figure 3.6: *The Debye length λ_{De} as a function of T_e and n_e.*

the time step must satisfy the Courant-Friedrichs-Lewy (CFL) condition [159]:

$$\Delta t < \Delta x / c, \tag{3.55}$$

where $\Delta x \sim \lambda_{\mathrm{De}}$, and c is the velocity of the fastest particles [169]. To determine the relevant CFL condition for the 3D-PIC simulations in this thesis, the following steps are taken. In a plasma with electrons with $T_e = 2.0$ eV, the 99th percentile of particle velocities is $c > 1801000$ m/s, which for $\Delta t = \lambda_{\mathrm{De}}/c$ translates to a $\Delta t < 2.4 \cdot 10^{-11}$ s. Figure 3.7 shows how ω_{pe}, $0.1/\omega_{pe}$ and λ_{De}/c changes with n_e when $T_e = 2.0$ eV. For the plasma parameters in the vicinity of an extraction aperture in ELISE, $n_e = 6 \cdot 10^{16}$ m^{-3} and $T_e = 2.0$ eV is marked with a gray dashed line. To satisfy both, the requirement based on Equation (3.54) and (3.55), the timestep must be chosen below both red lines in the graph.

3.2.6 Particle (re-)injection

Multiple particle injection and re-injection methods can be used in PIC simulations. Typically, a pair-injection model, see Figure 3.8 (a), is used. In pair-injection, the simulation starts with a uniform distribution of electrons and ions injected in a limited volume, a so-called injection

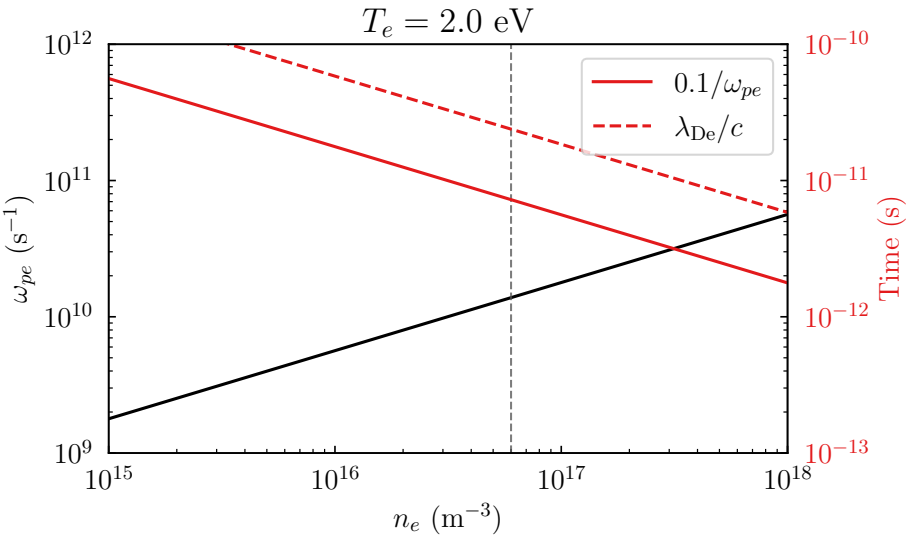

Figure 3.7: *ω_{pe}, $0.1/\omega_{pe}$ and λ_{De}/c as a function of n_e, $T_e = 2.0$ eV. The electron density $n_e = 6 \cdot 10^{16}$ m^{-3} is marked with a gray dashed line.*

zone. H^-_{VP} ions are re-injected when exiting the simulation domain, and positive ions are re-injected together with an electron when exiting the simulation domain. Electrons and H^-_{SP} ions are lost when exiting the simulation domain. The pair-injection scheme is the standard injection scheme used in ONIX.

The pair-injection scheme allows the user of the code to define the plasma density in the injection zone at the start of the simulation. Since the number of positive ions is kept constant while the plasma spreads out in the simulation domain, the overall density in the simulation domain will be lower than the value used as the initial density in the injection zone. However, as a direct consequence of the pair-injection model, the fluxes across its boundaries can not be imposed, which restricts the ability of the user to simulate plasmas with biased surfaces. In addition, to avoid electron cooling in the pair-injection model, i.e. the non-physical loss of high-energy electrons to one of the boundaries of the simulation domain, electrons are artificially thermalized in the injection zone to keep T_e stable over the course of a simulation, as described in [154].

The second method of particle injection involves injecting electrons, NIs, and positive ions from an injection plane, adapting the 1D implementation in [142]. The development of the flux-injection model is one of the main topics of this thesis. Two versions of the flux-injection model are used: the two-sided flux-injection model, see Figure 3.8 (b), where the particles are injected in both perpendicular directions to the injection plane, and one-sided flux-injection, where the particles are only injected in one direction, and the injection plane boundary coincides with the

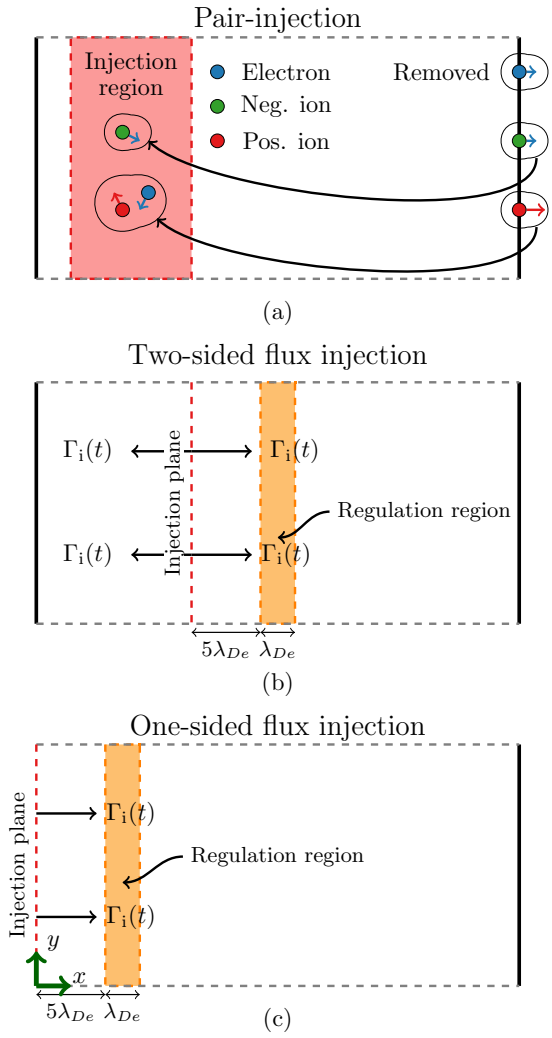

Figure 3.8: *The ONIX simulation domain for (a) pair-injection, (b) two-sided flux-injection, and (c) one-sided flux-injection.* Γ_i *is the flux of particle species i (PIs, NIs, or electrons).*

boundary of the simulation domain, see Figure 3.8 (c). To keep the charge density continuous across the boundary of the one-sided flux-injection scheme, mirrored particles on the left side of the injection plane are used when calculating the charge density. Positive ions passing through the boundary are deleted, while electrons are reflected and thermalized. To simulate a condition near floating potential with the one-sided injection scheme, one boundary of the simulation (ϕ_w) is set to 0 V and the other to ϕ_{pl}, as given in Equation (2.18).

The flux-injection method allows for a larger self-consistent region of the simulation domain since there is no injection zone where electrons are thermalized. Additionally, the fluxes of charged particles across the boundary plane can be altered to ensure the plasma conditions required by the user so that the transition from the bulk plasma to the simulation region is

more realistic.

The influx of positive ions $\Gamma_{\mathrm{PI}}(t)$ in the flux-injection model is regulated by a Proportional-Integral-Derivative (PID) [170],

$$\Gamma_{\mathrm{PI}}(t) = \underbrace{P \cdot e(t)}_{\Gamma_P} + \underbrace{I \cdot \int_0^t e(t)\mathrm{d}t}_{\Gamma_I} + \underbrace{D \cdot \frac{\mathrm{d}e(t)}{\mathrm{d}t}}_{\Gamma_D}, \tag{3.56}$$

where P, I, D are constants and $e(t)$ is the error at time t, given by

$$e(t) = n_{\mathrm{PI}}(t) - n_{\mathrm{PI},SS}, \tag{3.57}$$

where $n_{\mathrm{PI}}(t)$ is the density of positive ions in the regulation zone at time t, and $n_{\mathrm{PI},SS}$ is the input value for the steady-state density of positive ions. The densities are taken in a regulation zone located $5\lambda_{\mathrm{De}}$ from the injection point, see Figure 3.8. The distance $5\lambda_{\mathrm{De}}$ is used to ensure that the regulation region is far enough from the injection plane so that it is located in a flat plasma region, but close enough so that the influx of particles can be regulated within a short response time. The influx of negatively charged particles equals that of PIs, with the electron-to-NIs ratio set according to the input parameters; typically, a distribution of $0.7 : 0.3$ of electrons to ions is used.

Although the particles are injected from an injection plane, as ONIX is a 3D-3V PIC code, each particle has velocity components in three directions. The velocity components parallel to the injection plane are sampled from an ordinary Maxwellian distribution while the axial velocity of each species i is selected by random sampling from a Maxwellian flux velocity distribution

$$f_i(v) = |v| \cdot \left(\frac{m_i}{k_{\mathrm{B}} T_i}\right) \cdot \exp\left[\frac{-m_i v^2}{2 k_{\mathrm{B}} T_i}\right], \tag{3.58}$$

where v is the velocity, m_i and T_i are the mass and temperature of the species, respectively. A physical validation of the flux-injection model in ONIX is presented in Chapter 4.

3.2.7 Collisions

In plasmas, charged particles interact both via the generation of an electric field and collisional interactions with the gaseous species in the volume, including charged particles. Thus, particles interact with the neutral background gas, which is not directly simulated using PIC. To simulate the collisional processes taking place in the plasma, various MCC techniques can be used.

In short, the MCC technique works by determining the collision frequency for the relevant interactions that dominate in the plasma kinetics, iterating over the simulated macroparticles and using random numbers to determine whether a collision is taking place. The MCC technique can be used for all kinds of collisions, elastic and inelastic. Interactions with "background" particles that are not directly simulated allow for momentum transfer and thus total momentum conservation is not preserved. This can be contrasted with the Direct Simulation Monte Carlo (DSMC), where all particles involved in the collision are included as macroparticles directly in the simulation. Since DSMC requires pairing of particles to collide, the computational time and memory requirements for such algorithms are more costly. However, in cases where the background density is orders a magnitude higher than that of the simulated species, the MCC assumption of particles not having a large effect on the background holds. The probability of a collision using the MCC method is given by [159]

$$P_{\text{collision}} = 1 - \exp\left(-\nu \Delta T\right) = 1 - \exp\left(-n\sigma v_{\text{rel}} \Delta T\right), \tag{3.59}$$

where n is the density of the background, σ is the cross-section of the collision, v_{rel} is the relative velocity and ΔT the real-time between two calls to the collision subroutine. It is required that $\exp\left(-\nu \Delta T\right) \ll 1$ so that the probability has a physical meaning. In ONIX, $\Delta T = 10\Delta t$, where Δt is the timestep used in the simulations. Using factor 10 ensures that the collision subroutine is called often enough for the collisions to be physical, but rarely enough to significantly reduce the computational time needed to iterate over each particle. This technique is called sub-cycling.

Moreover, the collision processes included in ONIX pertain to the generation and elimination of NIs, and elastic collisions between electrons and neutrals. MN, AD, NAD, CX, eEC, see Table 2.2 and Figure 2.13 for the cross-sections. Coulomb collisions are implemented in ONIX using the Takizuka algorithm [160]. This method involves pairing particles within a mesh cell and rotating their relative velocity in the rest frame of the incident particle. The implementation in ONIX can be read in [158]. Due to the low density of the ion sources studied in this thesis, the impact of Coulomb collisions on the simulation results remains small.

3.2.8 Parallelization

Parallelization of 3D-PIC simulations is crucial due to the massive computational resources required for these types of calculations. Since the 3D-PIC method necessitates a large number of simulated macroparticles, typically ~ 30 per cell, and a grid size that obeys the requirements presented in Section 3.2.5, simulations quickly become computationally demanding, both in

terms of processing time and memory usage. By dividing the computation across multiple Processing Elements (PEs), parallelization allows for faster computation time and the handling of larger, more complex and realistic simulations.

Parallelization can be implemented in the 3D-PIC code using multiple approaches, among the following:

- **Domain Decomposition**: The computational domain is divided into smaller subdomains, each assigned to a different PE. Communication between PEs is needed when particles move from one subdomain to another. This method is highly scalable but requires careful load balancing to ensure all PEs have a similar amount of work [150, 171].
- **Particle Decomposition**: The particles are divided among the PEs rather than the spatial domain. Each PEs is responsible for advancing a subset of the particles and then updating the total field quantities on the grid. Particle decomposition is easier to implement than domain decomposition since each PE calculates the electrostatic field independently, but the field solver therefore does not scale with the number of PEs [172].

The choice of parallelization method depends on the specifics of the PIC simulation, the available hardware, and the trade-off between development complexity and execution efficiency. Regardless of the method used, parallelization is a key aspect of performing large-scale, detailed 3D-PIC simulations. ONIX has been parallelized by the domain decomposition method using MPI; the spatial domain is decomposed into equally sized subdomains which are each assigned to one PE that handles the movement of the particles and stores the local fields. A detailed description of the parallelization is given in [150].

The simulations in this thesis are performed on the MARCONI-FUSION [173] and SuperMUC [174]. A typical simulation (at plasma density $\sim 10^{17}\mathrm{m}^{-3}$) requires approximately 774000 CPU hours. This is distributed on 96 nodes with 48 MPI processes each. This gives an approximate wall-clock time of 7 days per simulation.

3.3 3D-PIC modeling of the ELISE extraction system

In this section, the application of ONIX for the simulation of NI extraction in ELISE is presented. The domain layout, visualized from an overhead perspective, is depicted in Figure 3.9. The ion source comprises several integral parts, such as the BP, PG, EG, and GG, as presented in the schematic. The domain size is $30 \times 20 \times 20$ mm and ends at the upstream surface of the EG. The PG geometry is based on the ITER extraction systems, where the radius of the PG apertures are 7 mm and the edges are chamfered in 40° on the plasma-facing side and 45° on the

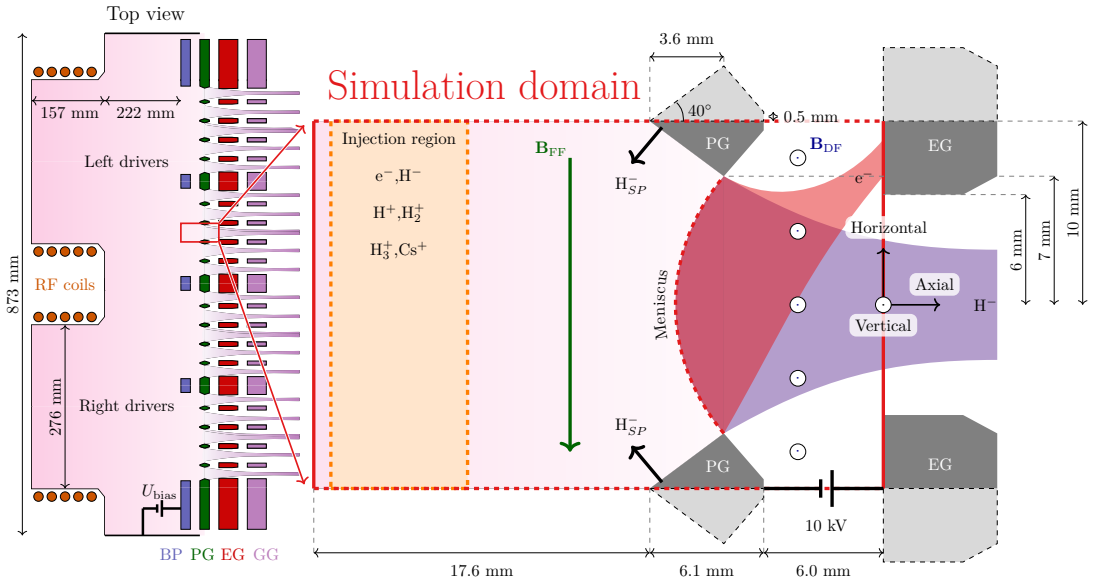

Figure 3.9: *Left side: schematic figure of the ELISE ion source, including the BP, PG, EG and GG, seen from above. The simulation domain used in this thesis covers one aperture in the PG, marked with a red rectangle on the left side and enlarged on the right side. The aperture is taken as the central aperture in one of the aperture groups. The injection zone of the particles is marked with dashed red lines, and the two magnetic fields, the* $\mathbf{B}_{\mathrm{FF}}$ *and* $\mathbf{B}_{\mathrm{DF}}$ *are indicated. Surface-produced ions are uniformly emitted from the plasma-facing side of the PG. The extracted* H^- *ion beam (in light purple) begins from the meniscus (red dashed line) and is extracted through the nearest EG aperture, and the electron beam is deflected to the left due to the upwards-directed* $\mathbf{B}_{\mathrm{DF}}$*. The origin of the coordinate system is located in the center of the downstream boundary plane.*

beam-facing side. In simulations with the pair-injection scheme, the BCs for the potential are $\phi_{\mathrm{bulk}} = \phi_{\mathrm{PG}} = 0$ V, where ϕ_{bulk} is the boundary towards the plasma and ϕ_{PG} is the boundary of the PG, which neglects the biasing of the PG.

The boundary towards the EG ϕ_{EG} is taken as the vacuum solution from the particle tracking code IBSimu [175], described in Section 3.4, with an extraction voltage of 10 kV. The magnetic field was calculated in Ansys for the geometry of the ELISE ion source with a 2.5 kA current drawn through the PG [176]. The potential is periodic in the horizontal and vertical boundaries. The periodic boundaries in the horizontal and vertical directions imply that particles are reinjected from the opposing wall but with equal velocity, meaning that the simulation in effect, represents an infinite grid of apertures. In the ONIX simulations for the ELISE ion source, the simulation domain has been limited to only one aperture due to the large computational cost of the simulations. The aperture is taken as the center aperture in one of the aperture groups, far from the source walls, with periodic BCs in the horizontal and vertical directions. A schematic 3D view, including the magnetic field components and aperture geometry, is shown in Figure 3.10.

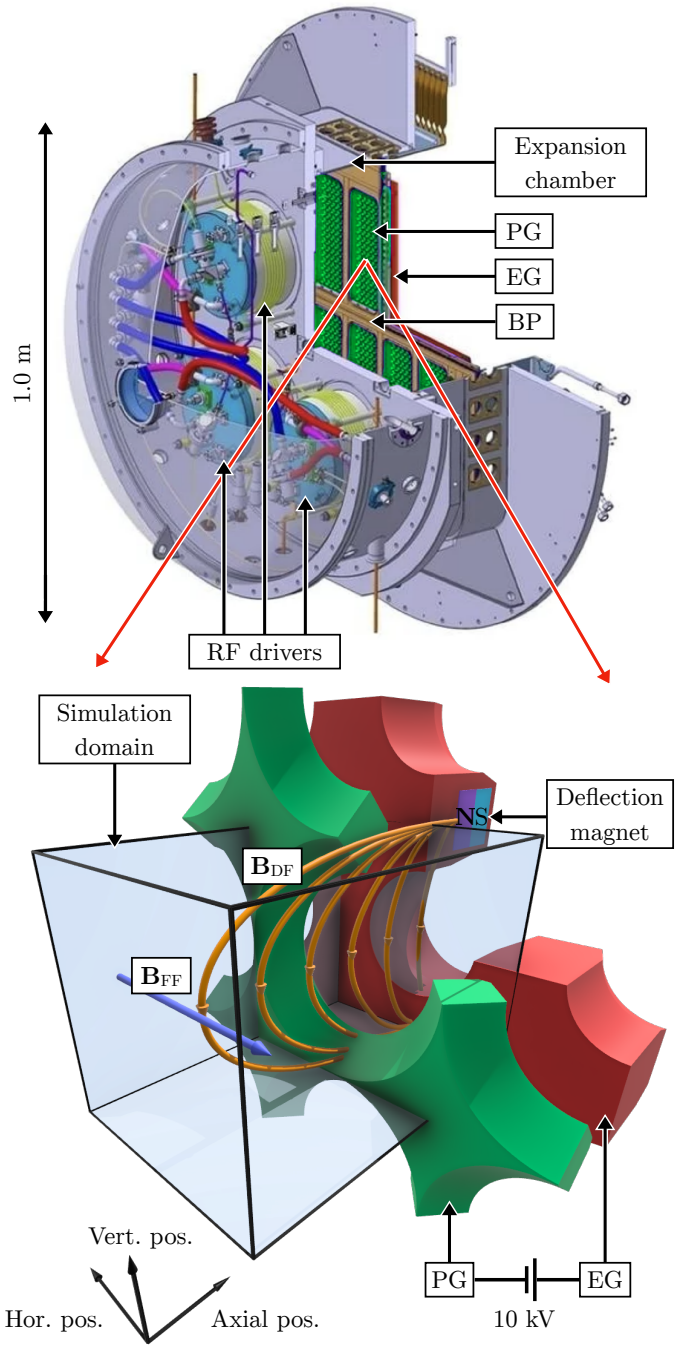

Figure 3.10: *(top) Schematic view of the ELISE ion source and (bottom) 3D-view of the ONIX simulation domain for simulation of one PG and EG aperture in ELISE.*

An initial uniform distribution of particles with Maxwellian velocities is injected in a 7 mm wide region marked in dashed lines in Figure 3.9. H^-_{SP} ions are uniformly emitted from the plasma-facing side of the PG. The plasma then self-consistently evolves according to the PIC algorithm. The simulation is stopped when the extracted NI current density is steady (varies

on the order of 1 Am^{-2}) and the electron current density fluctuates around a stationary value with an amplitude of ~ 10 Am^{-2}.

3.4 Beam optics simulations

In this thesis, ONIX is coupled with the ion-optics code IBSimu (described in Section 3.4.1) to extend the simulation domain and simulate beam transport through the grid system.

An alternative approach is to simulate the full grid system with 3D-PIC-MCC modeling, in a similar manner as is done in ONIX. One such code is Orsay Negative ion ACceleration (ONAC), which can not only simulate the acceleration of NI with different initial conditions, but it includes the space charge effect on the field distribution inside the accelerator and all the species as well as collisions of the beam particles (NI and co-extracted electrons) with the residual neutrals [177]. In this thesis, the ONIX+IBSimu coupling scheme is compared to extending the 3D-PIC-MCC modeling domain via coupling ONIX with ONAC.

The drawback of 3D-PIC modeling approach is the high computational cost, which practically limits the number of simulations and domain size. The typical simulation domain using ONAC does not include the plasma side of the PG. Due to the small computational domain, beamlet properties after the full grid system including acceleration stages cannot be directly calculated for particles self-consistently generated in the plasma. Gun-type codes, such as the ion-optics codes BEAMORBT [178], SLACCAD [179, 180], Kobra3D [181], Opera3D [182], and IBSimu[119, 175], make more approximations and only track NIs explicitly, but are many orders of magnitude faster. Although this leaves out many physical processes, such as plasma generation, sheath formation and production of H^-_{SP} ions, it is a common approximation that was successfully used in the design of many positive and NI extraction systems [44, 183–185].

In a standalone IBSimu simulation, the full grid system is contained, starting 2 mm upstream of the PG, up to 10 mm past the GG. The flowchart for an IBSimu simulation is shown in Figure 3.11. IBSimu includes the modification of the electric field by the beam itself through the space charge of the previous iteration, which is used in the solution of the Poisson equation. IBSimu only tracks the beam particles explicitly; a thermal charge density with a temperature of typically 0.8 eV compensates for the space charge of the beam particles in the plasma region. Collisions are neglected. The compensating positive ions in the plasma are approximated by an analytical charge density, and the collisional behavior of the particles in the plasma is mimicked by locally suppressing the magnetic field in the plasma region.

The beam is initialized on a plane 2 mm before the PG, meaning that all the injected particles

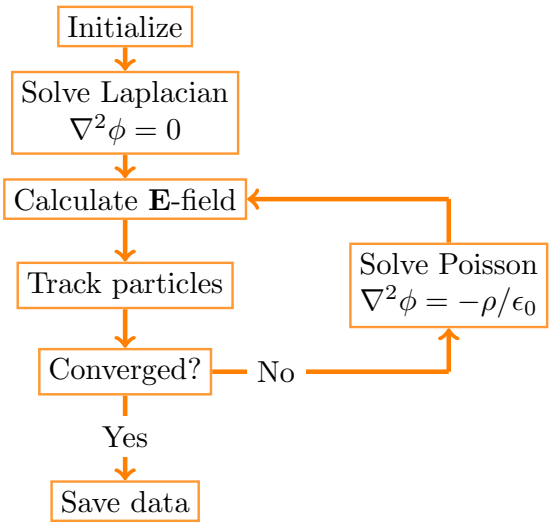

Figure 3.11: *Numerical schema for an IBSimu simulation.*

are effectively H^-_{VP}. The particle transport in the plasma is not included, the magnetic field is suppressed in the plasma region so that the particle trajectories are straight and the aperture is evenly illuminated, which in particular is not the case for H^-_{SP}, see Figure 2.15. Effects of the magnetic field on the NIs in the plasma is a possible reason for differences between simulations that neglect such effects and measurements [186]. Because the physics of plasma creation and wall losses is not included, the plasma potential and the sheath at the PG do not follow from the model: the potential is 0 V in the plasma region. The current density is an input parameter. To enable the particles to cross the field-free region upstream of the PG, they are provided with a starting energy (of typically 3 eV) in the beam direction. The particles are created with a perpendicular temperature $T_\perp$, typically of ~ 1 eV (close to the temperature of negative ions and atoms), which provides an initial divergence of $\sqrt{T_\perp/U_{tot}}$ [64, 187, 188].

3.4.1 Coupling of 3D-PIC and ion optics simulations

In this thesis, ONIX is coupled with IBSimu to extend the simulation domain for efficient and detailed beam transport simulations through the grid system, self-consistently including the effects of space charge on the potential in both the plasma and beamlet. This coupling balances computational efficiency with the need for accuracy, allowing for the simulation of phenomena such as sheath formation and SP. The approach uses iterative boundary condition adjustments, which will described in this section.

By extending the computational domain, the accelerated beamlet properties can be calculated for particles from a 3D-PIC simulation, and directly compared to gun-type electrostatic

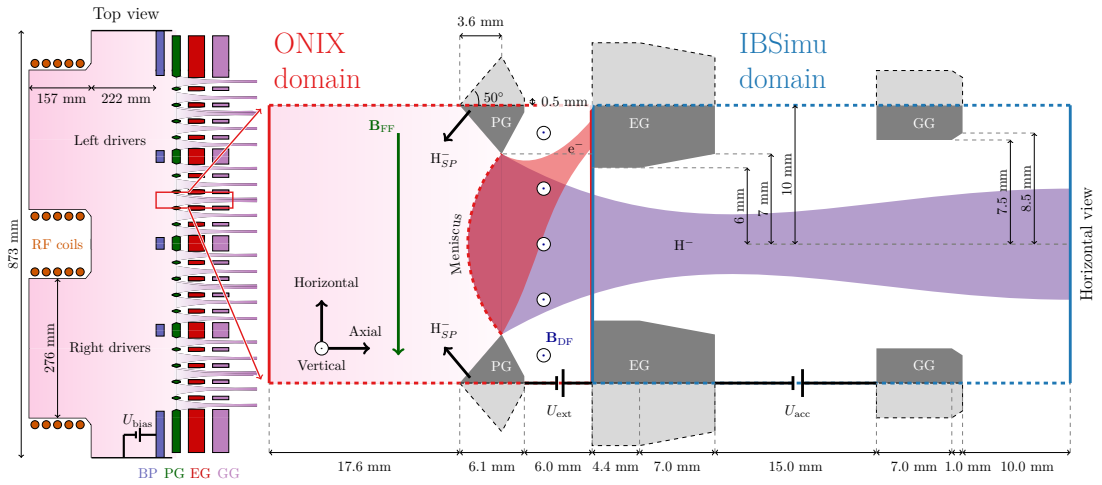

Figure 3.12: *Schematic horizontal section of the ELISE ion source and the ONIX/IBSimu simulation domains, marked in red and blue, respectively. In the ELISE source, the plasma generated in the drivers expands onto the grid system. The ONIX domain contains the extraction region of a single aperture, whereas the IBSimu domain includes the extraction and acceleration stages. The deflection magnets inside the EG are not visible in this horizontal section, but the magnetic field direction is indicated.*

simulations to assess the impact of the approximations made in those simulations. In a coupled ONIX-IBSimu simulation, the IBSimu simulation domain starts at the axial plane where the ONIX domain ends, i.e. at the upstream EG surface. The axial positions are given with respect to the boundary plane between the IBSimu and ONIX simulation domains, see Figure 3.12. Particles exiting the downstream boundary of the ONIX domain are accumulated over 100 timesteps (so that enough particles are collected) and then further tracked in IBSimu. At the EG boundary, the particles exit the ONIX domain and are further tracked in IBSimu, self-consistently treating the space charge of the beam with a mean-field approach.

However, since the ONIX simulation is initially run until steady-state with the vacuum BC, denoted as $\phi_{x=0}^{\text{vacuum}}$, on the boundary of plane B, see Figure 3.13, the space charge effect of the beam is not taken into account. In order to obtain a non-vacuum potential that can be used as a BC (which accounts for the effect of space charge at Plane B, the particles and potential map are first exported from ONIX at Plane A. This potential at Plane A contains the space charge effects of the extracted particle beam.

Next, Plane A is used as a BC in an IBSimu simulation. This allows for the tracking of the exported particles from Plane A through the grid system.

Following this, a new boundary potential at Plane B is produced, denoted as $\phi_{x=0}^{\text{non-vacuum}}$. This boundary contains the space charge contributed by the particles, and this boundary is used as a BC within ONIX. This process is done iteratively until convergence of the potential boundary is

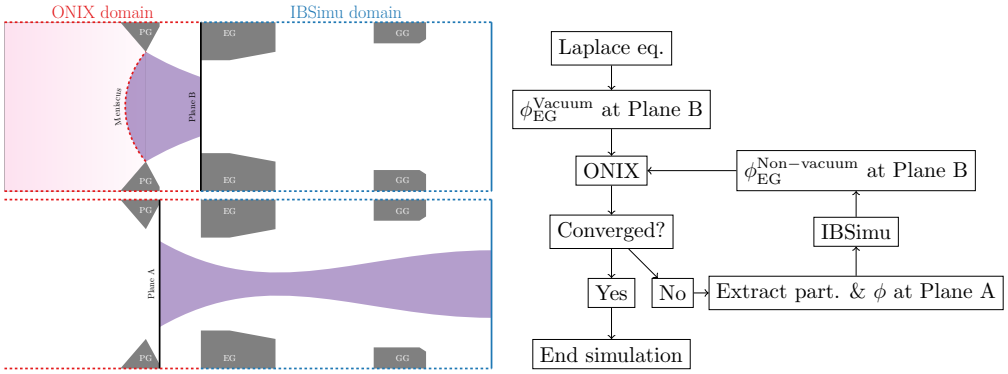

(a) **(b)**

Figure 3.13: *The ONIX+IBSimu coupling scheme, including the A and B coupling planes.*

reached. Very few iterations are required, typically 3 to obtain the whole convergence between the two simulation domains. Figure 3.13 illustrates this coupling scheme, and a validation of this scheme can be found in Chapter 4.

3.4.2 *A posteriori* particle tracking

Finally, the potential maps from the ONIX and ONIX-IBSimu simulations were extracted and stitched together for the *a posteriori* analysis. Negative ions from the volume and the surface of the PG were tracked until the end of the grid system, 10 mm past the GG.

Since the ONIX simulation only stores particle properties at the current timestep, the history of the particles is lost, and it is not possible to link specific particle properties at the exit of the grid system to upstream phenomena. To enable this type of analysis, diagnostic particles are tracked *a posteriori* through the combined ONIX-IBSimu fields. In the *a posteriori* analysis, the H^-_{VP} ions and electrons are injected at the upstream boundary, 15 mm upstream of the PG, and the H^-_{SP} ions are produced uniformly on the conical surface of the PG with a cosine-distribution and an initial temperature of 0.6 eV, equal to the value used in ONIX. These parameters are the same as in the ONIX simulation. The number of tracked particles is on the order of millions to obtain data with a high resolution. The fields are interpolated on a 0.1 mm mesh so that the sheath is resolved. Since full trajectories are followed, this allows linking upstream to downstream particle properties so that e.g. the impact of the initial velocity distribution on the divergence can be studied [123].

It is important to determine how particle parameters on the meniscus are correlated with particle parameters in the accelerated beamlet. In the context of *a posteriori* simulations, the meniscus surface is chosen based on the potential gradient since the positive ion density is not

included in the model; in the plasma, the potential is ∼0 V but after the transition through the meniscus rapidly increases. Because of the large potential gradient in the extraction gap, the choice of the meniscus potential has little impact on the spatial position when chosen in a reasonable range: at 10 kV extraction potential, there is approximately a 70 V increase per grid cell. To avoid incorrectly assigning the meniscus position based on statistical fluctuations of the potential, the 30 V surface is taken as the meniscus, which corresponds well with the meniscus based on positive ion density.

3.5 Parameters

The choices of input parameters are important for simulating a plasma with properties close to those observed in experiments. ONIX can simulate e^-, H^-, H^+, H_2^+, H_3^+ and Cs^+ ions. For each species, an initial temperature and density must be specified. In the flux-injection case, the density is used as a basis for setting the injected flux of each species, according to Equation (3.56). The H and H_2 densities are set to constant values and only used for the collision module in ONIX.

Previously published ONIX simulations, such as [108, 138, 154], used input parameters based on measurements done in test facilities using permanent magnets for generation of the filter field (described in the next section), such as in BATMAN test facility [189]. In the ELISE/BUG case, the electron temperature is a factor two higher and electron density a factor two lower than in the BATMAN case at the typical working point of the ion source [190, 191]. Additionally, the previous publications used an emission rate of NIs from the PG (550 Am^{-2}) based on the optimum work function, corresponding to a submonolayer of Cs.

This thesis's full-scale 3D-PIC MCC simulations are based on two sets of input parameters. The High Density/Low Temperature (HD/LT) case corresponds to measurements [190] obtained from operation in the BATMAN test facility operating with permanent magnets [189] and the Low Density/High Temperature (LD/HT) case are based on conditions in ELISE and BUG, where the $\mathbf{B}_{\mathrm{FF}}$ is generated by a current I_{PG} through the PG. Table 3.1 shows the input parameters used in the simulations for the two cases. The main differences between the HD/LT case and LD/HT case are indicated with yellow in Table 3.1.

Based on Langmuir probe measurements performed close to the PG at the prototype source, the electron density is $0.6 \cdot 10^{17}$ m^{-3} with an error bar of $\pm 0.3 \cdot 10^{17}$ m^{-3} [35]. The latter measurements also provide a reference value for the electron temperature in the extraction region of 2 eV with an error bar of ±1 eV. The injected NI density at the start of the simulation

in both cases was chosen to equal the value of electron density.

In order to ensure that the NI density increases to this level in the simulation, a distribution of NIs is injected in the volume at the start of the simulation (this has not yet been achieved self-consistently in 3D-PIC simulations for NI extraction). If this initial injection is not done, the simulation does not self-consistently reach the NI density measured in the bulk plasma. These ions are labeled as H^-_{VP} ions in the present thesis, but in experimental studies, it has been shown that the majority of H^- ions originate from the surface [105]. The starting density of NIs in the injection zone is chosen based on cavity ring-down spectroscopy measurements performed at the ELISE test facility in the proximity of the plasma grid [126].

The Cs^+ density is estimated based on measurement of neutral Cs density obtained by absorption spectroscopy [192] and considering an average ionization degree of Cs close to the PG of around 70% [101]. The density of the background gas, i.e. molecular and atomic hydrogen is calculated by considering the source filling pressure of 0.3 Pa (i.e. the pressure of the molecular hydrogen injected in the source before the plasma is ignited) [39]. The density of the positive hydrogen ion species, i.e. H^+, H_2^+, H_3^+ is then calculated to ensure quasi-neutrality and considering a ratio of 40:40:20 respectively, as measured at a positive ion source with plasma conditions similar to the ones present in the NI source under investigation [193].

By using the ideal gas law and a density ratio of atomic to molecular hydrogen of 0.3, resulting from spectroscopy measurements [87, 191, 194], the density of H_2 ($n_{H_2} = 3.2 \cdot 10^{19}$ m^{-3}) and H ($n_H = 9.5 \cdot 10^{18}$ m^{-3}) have been estimated. The gas temperature for H_2 ($T_{H_2} = 0.1$ eV) can be obtained by the Fulcher emission [87] close to the PG, while the atomic gas temperature ($T_H = 0.8$ eV) results from [195]. The temperature of the H^+ and H^-_{VP} ions was assumed the same as the one of the atomic hydrogen, while the temperature of H_2^+, H_3^+ was the same as the molecular hydrogen.

As for the H^-_{SP} ions, the emission rate was calculated by considering the conversion of atomic hydrogen onto the PG surface. The conversion yield of H into H^- is $Y_{H\rightarrow H^-} = 3.9\%$ when assuming a work function equal to the one of the bulk Cs and $T_H = 0.8$ eV [89, 92]. The impinging atomic flux on the PG is thus given by:

$$\Gamma_H = \frac{1}{4} n_H \bar{v}_H = \frac{1}{4} n_H \sqrt{\frac{8 k_B T_H}{\pi m_H}} = 3.49 \cdot 10^{22} \quad \text{s}^{-1}\text{m}^{-2}. \tag{3.60}$$

The emission rate $\Gamma^{emission}_{H\rightarrow H^-}$ can then be estimated as

$$\Gamma^{emission}_{H\rightarrow H^-} = \Gamma_H Y_{H\rightarrow H^-} \approx 200 \quad \mathbf{Am}^{-2}. \tag{3.61}$$

Table 3.1: *Input parameters for the HD/LT and the LD/HT case. Marked in yellow are the most important differences between the two simulations.*

	HD/LT case		LD/HT case	
Species	**Temp. (eV)**	**Density (m^{-3})**	**Temp. (eV)**	**Density (m^{-3})**
e^-	1.0	$1.8{\cdot}10^{17}$	2.0	$0.9{\cdot}10^{17}$
H^-_{VP}	0.8	$1.8{\cdot}10^{17}$	0.8	$0.9{\cdot}10^{17}$
H^+	0.8	$1.5{\cdot}10^{17}$	0.8	$0.71{\cdot}10^{17}$
H^+_2	0.1	$1.5{\cdot}10^{17}$	0.1	$0.71{\cdot}10^{17}$
H^+_3	0.1	$0.47{\cdot}10^{17}$	0.1	$0.36{\cdot}10^{17}$
Cs^+	0.1	$0.16{\cdot}10^{17}$	0.1	$0.02{\cdot}10^{17}$
H	0.8	$1.0{\cdot}10^{19}$	0.8	$0.95{\cdot}10^{19}$
H_2	0.1	$3.1{\cdot}10^{19}$	0.1	$3.2{\cdot}10^{19}$
Species	**Temp. (eV)**	**Γ (Am^{-2})**	**Temp. (eV)**	**Γ (Am^{-2})**
H^-_{SP}	0.6	550	0.6	200

In the HD/LT case, an emission of 550 Am^{-2} was used, this corresponds to a work function of 1.6 eV. The initial temperature of the H^-_{SP} ions is set to 0.6 eV, as is used in [108, 154].

During operation with the deuterium isotope, 25% more atoms are present compared to hydrogen [196]. At the same pressure and temperature as in hydrogen, equivalent derivations for the densities of n_{D_2} and n_D after dissociation can be made. This results in $n_{D_2} = 3.1 \cdot 10^{19}$ m^{-3} and $n_D = 1.2 \cdot 10^{19}$ m^{-3}. The emission rate of D^- from the surface of the PG is scaled by the mass ratio between hydrogen and deuterium, resulting in an emission rate of $\Gamma^{emission}_{D \to D^-} \approx 175$ Am^{-2} for the same yield.

It is important to note that in 3D-PIC simulations of this type, matching a required plasma density is difficult, since the particle densities are self-consistently evolving until reaching a steady state. When using pair-injections, the initially injected densities, given in Table 3.1, were therefore set to be 50% higher in order for the density at steady state to reach values close to the desired values.

The numerical parameters defining the time step and size are set in accordance with the requirements outlined in Section 3.2.5. For the HD/LT and LD/HT simulations, the parameters are given in Table 3.2.

Table 3.2: *Numerical parameters used in the ONIX simulations.*

Parameter	**Value**
$\Delta_{\text{axial}}, \Delta_{\text{horizontal}}, \Delta_{\text{vertical}}$	35 μm
$N_{\text{axial}}, N_{\text{horizontal}}, N_{\text{vertical}}$	864, 576, 576
Δt	$5 \cdot 10^{-12}$ s

CHAPTER 4

Validation of the flux-injection model

This chapter presents an investigation of the effect of the flux-injection schemes presented in Chapter 3. To perform studies with reduced calculation time ($\sim$ 1 h per simulation on a single node) and in a simple case without the impact of the 3D-magnetic field, a so-called "slab-domain" is used, see Figure 4.1. The width and height (L_y and L_z) of the slab-domain are 52 μm, while the length L_x is typically 500 μm or larger. In the x-direction, the BCs are Dirichlet conditions, typically with a potential of 0 V on both the left wall ($\phi_{\mathrm{lw}} = 0$ V) and the right wall ($\phi_{\mathrm{rw}} = 0$ V). In the y- and z-directions, the BCs are periodic, effectively making the domain 1D. The slab-domain geometry can be used with any of the particle injection schemes presented in Chapter 3: pair-injection, two-sided flux-injection or one-sided flux-injection.

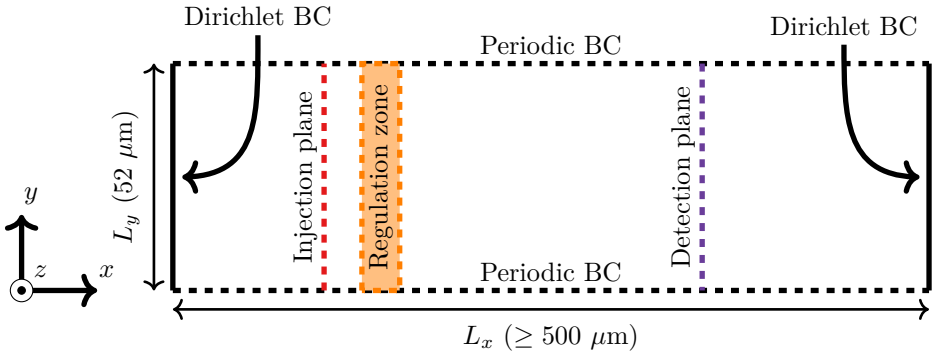

Figure 4.1: *Geometry of the slab-domain simulations.*

4.1 Flux-injection in the slab-domain

Some basic results of a simulation of electrons and H^+ ions in an electropositive plasma, i.e., H^- ions are neglected, using the two-sided flux-injection are depicted in Figure 4.2. The temperatures T_e and T_{H^+} are 1 eV and 0.8 eV, respectively, and the steady-state positive ion density $n_{+,SS}$ is $5 \cdot 10^{17}$ m^{-3} ($\lambda_{De} = 15$ μm). The figure shows time traces over the first 100,000 iterations, equivalent to 0.5 μs for the PID components: Γ_P, Γ_I, and Γ_D (top), the error in the density $e(t)$ for both electron and H^+ ions (middle) and the total number of macroparticles for both electrons and H^+ (bottom).

The impact of the derivative component in Equation (3.56) is set to zero ($D = 0$) to avoid noise amplification. However, the integral term, which integrates past errors, counteracts system oscillations and facilitates convergence to the setpoint. The proportional term tends to zero as $n_+(t)$ approaches $n_{+,SS}$, meaning $\Gamma_I >> \Gamma_P$. The system comes to equilibrium after 0.05 μs, at which point Γ_I and Γ_P are constant.

At the start of the simulation, the system begins from an unpopulated state, resulting in $e(t) = 100\%$ for both species. After approximately 0.05 μs, the error stabilizes, approaching near 0%, implying that the simulated state converges towards the desired system state. This stabilization of the error function is mirrored in the Γ_P component, which also approaches zero after 0.05 μs.

Despite an equal injection rate of electrons and H^+ ions, the total number of H^+ ions surpasses that of electrons. This discrepancy is due to the positive space charge in the Debye sheath, caused by the higher mobility of electrons compared to that of the H^+ ions. This leaves an excess of H^+ ions in the simulation domain, and thus the plasma potential is proportional to T_e, as in Equation (2.18). Stability is reached after 0.075 μs, with a slight delay after the flux is stable since more time is needed for the particles to spread out across the full simulation domain.

Figure 4.3 shows the axial, horizontal, and vertical components ($E^x_{kin}, E^y_{kin}, E^z_{kin}$) of the kinetic energy (averaged over 5000 iterations) for electrons and H^+ ions after 0.5 μs in the "detection plane", located between the injection plane and the right-hand side wall, see Figure 4.1. The sign of each kinetic energy component is preserved in the distribution, such that $E^x_{kin}, E^y_{kin}, E^z_{kin}$ are defined as follows,

$$E^{dir}_{kin} = \text{sgn}(v_{dir}) \cdot m v^2_{dir}, \tag{4.1}$$

where sgn is the sign function and v_{dir} is the velocity component in one direction (x, y or

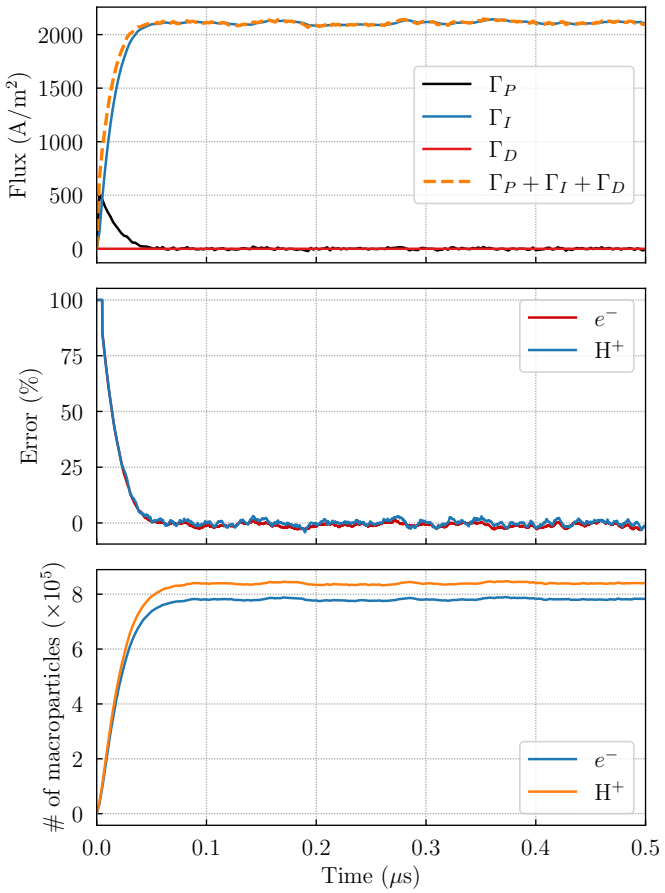

Figure 4.2: *Visualization of the flux-injection scheme over 100,000 iterations, equivalent to 0.5 μs. Subfigure (top) shows the PID components' evolution, Γ_P, Γ_I, and Γ_D (D is set to 0). The middle subfigure depicts $e(t)$ for both species. The bottom subfigure shows the total number of macroparticles for both species.*

z). For the electrons, the y- and z-components of the Velocity Distribution Function (VDF) correspond well to a Maxwellian distribution of 1 eV, indicating that neither numerical heating nor cooling has occurred. In the x-direction, the distribution is cut at -2.5 eV which corresponds to the plasma potential ϕ_{pl}; the electrons with higher energy in the x-direction will overcome the potential barrier in the plasma sheath and be collected on the right side. For the H^+ ions, the horizontal and vertical components of the VDF also correspond well to a Maxwellian distribution of 0.8 eV. A drifting Maxwellian is observed in the x-direction, which is caused by the acceleration of the H^+ ions by the so-called "source sheath" between the plasma and the injection plane [76, 142]. The source sheath forms due to the difference in mobility between electrons and H^+ ions and has a theoretical depth $\Delta_{\text{source sheath}} = 0.5T_e$ [76], this corresponds well to the drift observed in the simulation. All H^+ ions on the right-hand side of the injection plane will be collected at the wall. Therefore, $E^x_{\text{kin}} > 0$ for all H^+ ions to the right of the

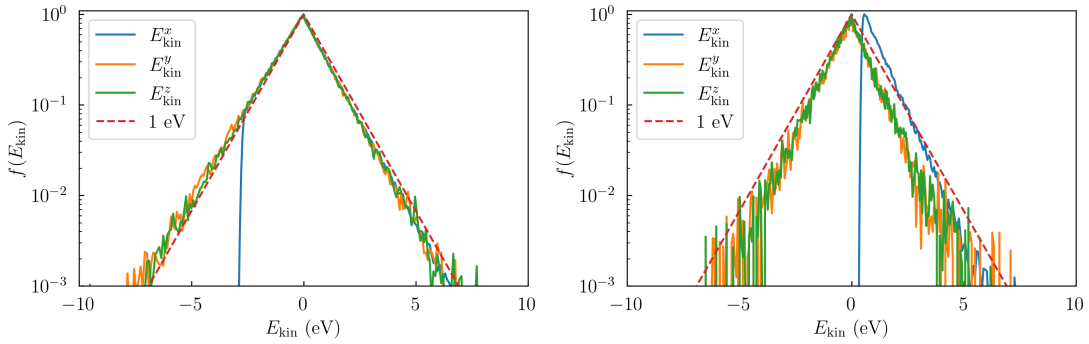

(a) e^- **(b)** H^+

Figure 4.3: *Distribution of the x, y, and z-components of kinetic energy* ($E^x_{\mathrm{kin}}, E^y_{\mathrm{kin}}, E^z_{\mathrm{kin}}$) *for (a) electrons and (b* H^+ *ions in the center of the plasma simulation volume (at* $x = 0.36$ *mm).*

injection plane. In summary, the flux-injection scheme correctly reproduced a Maxwellian velocity distribution in the plasma.

4.2 Variation of plasma parameters and code-to-code benchmarking

The ONIX flux-injection particle injection scheme was benchmarked by comparison with the 1D3V-PIC code BACON [142], which uses a similar particle-injection method as in the flux-injection developed for ONIX. The two codes were used with the same parameters for a variation of electron temperature and density. Figure 4.4 shows the impact of electron density on the normalized plasma potential ϕ_{pl}/T_e for ONIX using flux- and pair-injection and for BACON using flux-injection, for the electron temperature $T_e = 2$ eV. For ONIX with pair-injection, the plasma potential increases from 2.4 V/eV at 10^{15} m^{-3} to 2.9 V/eV at 10^{18} m^{-3}, which is not in accordance with Equation (2.18). For the pair-injection case, both the size and thermalization rate of the region will affect the plasma potential since it limits the velocity distribution of electrons that are allowed to pass through it without being thermalized. The thermalization rate for the electrons is kept constant ($f = 10^9$ s^{-1}) while varying the density, which impacts the rate at which electrons leave the thermalization region. For the flux-injection model, the plasma potential is constant for electron densities up to 10^{17} m^{-3}. In conclusion, the flux-injection scheme accurately reproduces the theoretical plasma potential over a wide range of particle densities.

Figure 4.5 shows the impact of electron temperature on ϕ_{pl}/T_e for ONIX using flux- and pair-injection and for BACON using flux-injection at a constant electron density of $n_e = 5{\cdot}10^{17}$ m^{-3}.

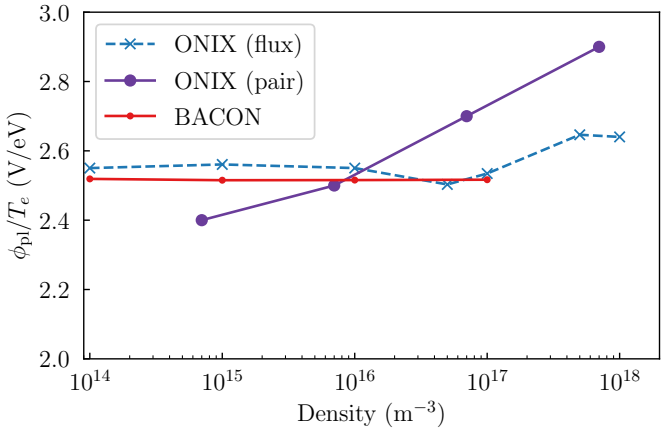

Figure 4.4: *Normalized plasma potential as a function of electron density for ONIX simulations with flux- and pair-injection compared with BACON with flux-injection.* $T_e = 2.0$ *eV.*

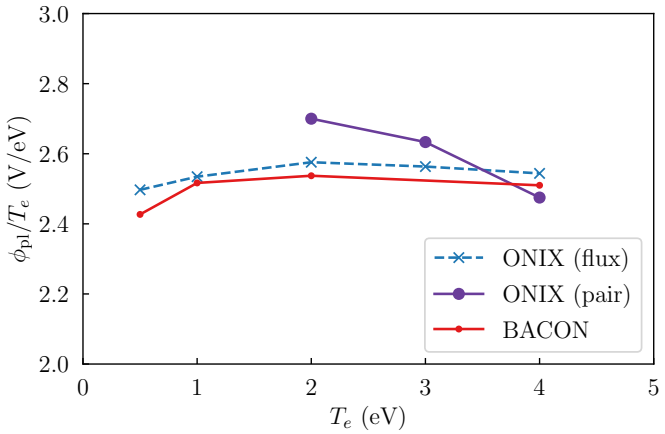

Figure 4.5: *Normalized plasma potential as a function of* T_e *for ONIX simulations with flux- and pair-injection compared with BACON with flux-injection.* $n_e = 5 \cdot 10^{17}\ m^{-3}$

The normalized plasma potentials for ONIX and BACON with flux-injection correspond well to the theoretical values with increasing T_e ($\phi_{\mathrm{pl}} = 2.5T_e$) by Stangeby [75]. However, for ONIX with pair-injection, a dropoff of normalized plasma potential of ≈ 0.3 V/eV occurs between 2 eV and 4 eV.

Equation (2.18) shows the influence of the ratio $\frac{m_e}{m_{\mathrm{ion}}}$ on the plasma potential; with an increased ion mass, the ion flux towards the walls decreases, in turn, to balance the fluxes of ions and electrons, ϕ_{pl} increases. To further validate the flux-injection model against Equation (2.18), the mass of the positive ion was varied from 0.15 amu to 20 amu. Figure 4.6 shows the normalized plasma potential as a function of the positive ion mass for ONIX with flux-injection and Equation (2.18) for $T_e = 2$ eV. The normalized plasma potential increases with the mass of the positive ion, closely following the theoretical prediction.

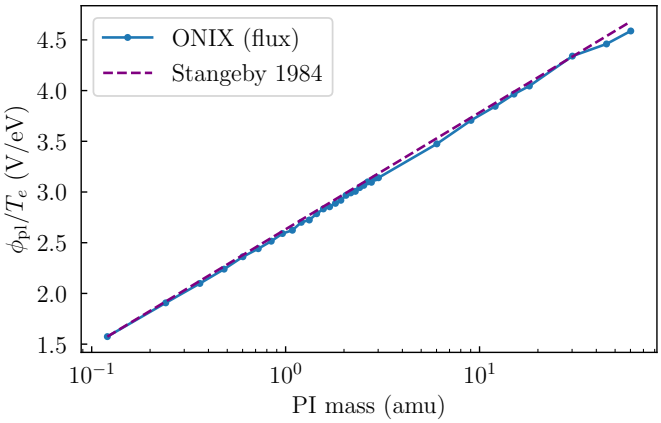

Figure 4.6: *Normalized plasma potential in ONIX as a function of PI mass from 0.15 to 20 amu, compared to theoretical values by Stangeby [75]. $T_e = 2$ eV.*

In more complex simulations, such as for the plasma in close vicinity to an extraction aperture of a source for NI production, such as ELISE, multiple species of PIs are present. In such cases, the plasma potential depends on the combined fluxes to the walls by each species. Additionally, the presence of NIs has a large impact on the plasma potential since they have a lower mobility than the electrons and thus decrease the flux of negatively charged particles toward the walls. To demonstrate that the flux-injection scheme can also simulate such scenarios, simulations with ion species of varying mass were performed.

For simulations with multiple positive ion species, the total injected positive ion flux in the flux-injection scheme is kept equal to the injected electron flux in both directions, i.e., $\Gamma^+ = \Gamma^-$. However, the desired ratios of PIs (user inputs) were obtained by controlling the relative flux of each positive ion species by a PID. Figure 4.7 (a) shows the influx of each particle species and Figure 4.7 (b) shows the error throughout a simulation with mixed positive ion species with a ratio of 40:40:20 of H^+:H_2^+:H_3^+. The ratio was chosen based on measurements at a positive ion source with plasma conditions similar to the ones present in the NI source under investigation [193]. Since the total flux Γ^+ is determined by Equation (3.56), the total flux of PIs is stabilized quicker than the individual ratio of each species. This is reflected in the error in electron density, which reaches a low error quicker than for the positive ion species.

4.3 Removal of the source sheath

As one of the goals of the flux-injection model is to allow for simulations with variations of the PG bias while keeping the plasma potential fixed, a smooth transition in the potential from the simulation domain to the bulk plasma must be obtained. The first step towards this is to

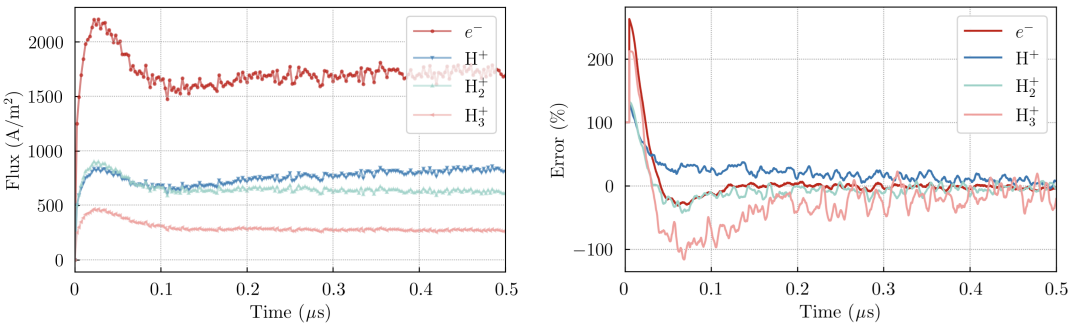

(a) (b)

Figure 4.7: *Illustration of particle species influx and the corresponding error over a simulation involving mixed positive ion species with a target ratio of 40:40:20. (a) shows the positive ion flux and (b) shows the error in electron and positive ion densities.*

modify the injection scheme to remove the source sheath. This has previously been done in the BACON [142] code. Equation (3.58) is modified by giving the PIs an additional push ΔE in the axial direction, which is equivalent to the acceleration they would otherwise get from the source sheath.

Figure 4.8 shows the potential profile for one simulation with $\Delta E = 0$ eV and one with $\Delta E = 0.5$ eV for a constant electron temperature $T_e = 2$ eV. In the $\Delta E = 0$ eV case, a source sheath with a depth of $\Delta_{\text{source sheath}} = 0.5$ V is formed around the injection plane, which corresponds to theory [76]. However, in the $\Delta E = 0.5$ eV case, the source sheath has been fully removed, while keeping the plasma potential the same as in the $\Delta E = 0$ eV case ($\phi_{\text{pl}} = 2.5$ V). By removing the source sheath, the transition of the potential from the injection plane to the simulation domain is smooth and has no gradient (no electric field is present close to the injection plane). This enables calculations for biasing of the PG, i.e., defining a potential difference between the bulk plasma and PG, as will be shown in Chapter 6. Such calculations have previously been impossible in 3D-PIC simulations since the plasma potential increases equally to the PG potential with the pair-injection model.

4.4 Flux-injection in the ELISE geometry

4.4.1 Impact on the plasma properties

For a case of comparison between simulations with the flux-injection scheme and the pair-injection scheme for NI extraction, two 3D-PIC simulations were performed with the LD/HT parameters, presented in Chapter 3. In one case, the one-sided flux-injection model was used with a removed source sheath, with a PG potential of 0 V, and with an upstream boundary

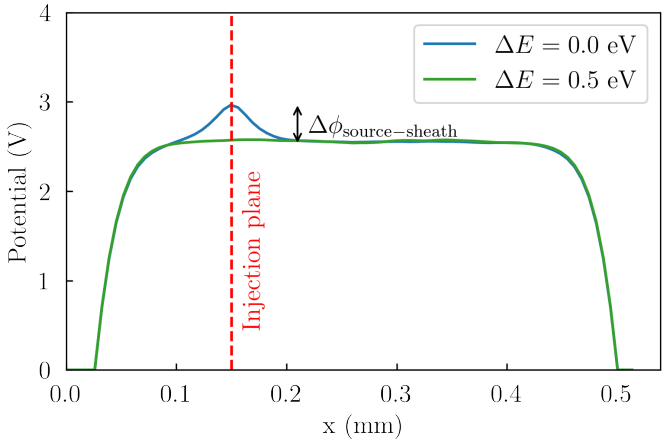

Figure 4.8: *Potential profiles for $\Delta E = 0$ eV and $\Delta E = 0.5$ eV for the two-sided flux-injection scheme.*

potential of 5 V for the ELISE PG geometry. The potential difference between the upstream boundary and the PG is chosen to be 5 V to correspond to the floating potential obtained from Equation (2.18) for an electron temperature of 2 eV. This simulation was compared to an equivalent simulation with the pair-injection model, where both the PG potential and upstream boundary potential were set to 0 V. In the resulting figures, the potential is shown with respect to the PG potential, which is denoted as 0 V in both cases.

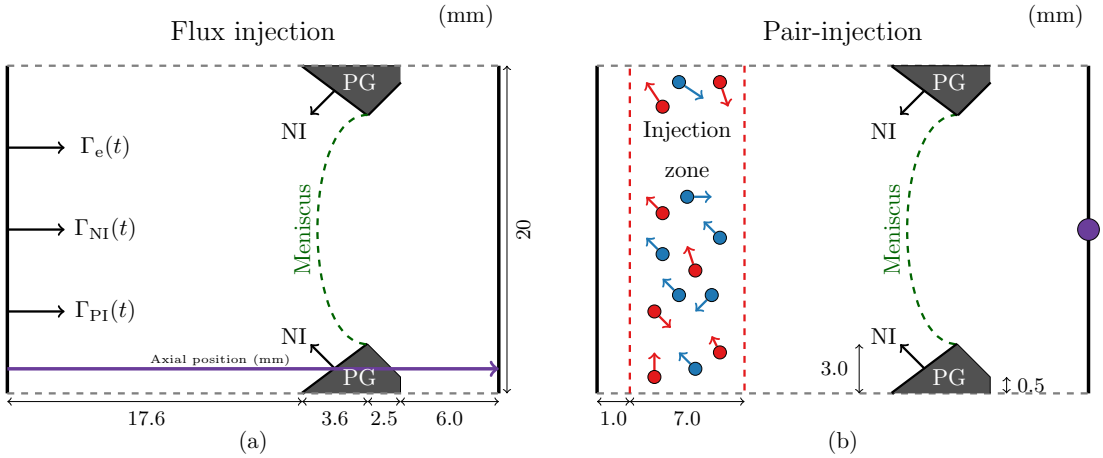

Figure 4.9: *The ONIX simulation domain for simulation of the extraction of NIs in the ELISE ion source using (a) Flux-injection and (b) Pair-injection. The length measures are given in mm.*

Figures 4.9 (a) and (b) show the axial-vertical slices of the 3D simulation domain for the flux- and pair-injection simulations, respectively, based on the ELISE geometry. The origin of the coordinate system is marked with a purple dot. For the pair-injection case, the particles are

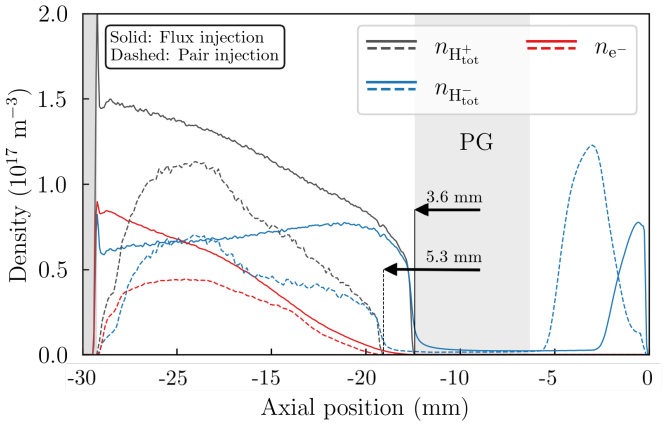

Figure 4.10: *Particle density along the center-line for the flux-injection case and the pair-injection case using the input parameters for the LD/HT case. The penetration of the meniscii from the PG knife are marked with black arrows.* U_{ext}*=10 kV,* U_{acc}*=55 kV.*

injected in a 7 mm wide injection zone. The simulation boundary at -30 mm and the PG potential ϕ_{PG} are set to 0 V, this is equivalent to assuming that there is no plasma after the upstream boundary. Instead, in the one-sided flux-injection case, there is an influx from the upstream boundary of electrons, NIs, and PIs, denoted by Γ_e, Γ_{NI}, and Γ_{PI}, respectively.

Figure 4.10 shows the sum of all PIs ($n_{H^+_{tot}}$), NIs ($n_{H^-_{tot}}$) and electrons (n_{e^-}) at steady state along the axial center line for the flux-injection case and the pair-injection simulations. The particle densities in the pair-injection case have their maxima in the injection zone, and decrease towards the PG and the upstream boundary. The reason is that the thermalization of the electrons in the injection zone interrupts the particle trajectories, which keeps the density of both PIs and NIs high in the injection zone to satisfy quasi-neutrality. In the flux-injection case, the electron and PI density have their maxima at the upstream boundary and decrease towards the PG, while the density of NIs is approximately equal throughout the simulation domain until reaching the meniscus.

In the flux-injection case, the PIs and NIs approach the meniscus with a direct flux from the bulk plasma, while in the pair-injection case, all ions travel in a random direction in the injection zone, including toward the bulk plasma. In terms of particle fluxes, the flux-injection scheme thus gives a more accurate representation of the ion source [197].

The extracted current densities for both injection schemes are summarized in Table 4.1. The main differences between the two scenarios are as follows: In the flux-injection scenario, j_e is 15 Am^{-2} higher, $j_{H^-_{VP}}$ is 53 Am^{-2} higher, and $j_{H^-_{SP}}$ is 16 Am^{-2} lower compared to the pair-injection LD/HT scenario. Since the flux-injection case results in a higher plasma density

Table 4.1: *Extracted current densities for the flux-injection and pair-injection LD/HT simulations.* U_{ext}*=10 kV,* U_{acc}*=55 kV.*

	$j_{H^-_{\mathrm{VP}}}$	$j_{H^-_{\mathrm{SP}}}$	j_{ex}	j_{e}	$j_{\mathrm{e}}/j_{\mathrm{ex}}$
Simulation	A/m^2	A/m^2	A/m^2	A/m^2	
Flux-injection	88	57	146	108	0.74
Pair-injection	35	73	108	93	0.86

close to the meniscus (approximately by a factor of 2), the meniscus penetrates less into the plasma (3.6 mm in the flux-injection case compared to 5.3 mm in the pair-injection case), see Figure 4.10. The less penetrating meniscus reduces the extracted $\mathrm{H^-_{SP}}$ ion current density since fewer $\mathrm{H^-_{SP}}$ ions are directly extracted. Additionally, with flux-injection, $j_{\mathrm{H^-_{VP}}}$ is higher compared to the case pair-injection due to the higher plasma density near the meniscus.

This shows that even for simulations where the particle parameters are equal in the bulk plasma, the particle injection scheme plays a critical role in the meniscus penetration and extracted current densities. While both injection schemes produce extracted current densities that are well below the ITER target of 329 Am^{-2}, the flux-injection scheme allows for a higher current density to be extracted from the bulk plasma ($j_{\mathrm{H^-_{VP}}}$) due to the more realistic particle fluxes in the simulation. It is important to note, however, that reaching the ITER target of 329 Am^{-2} has not yet been achieved in 3D-PIC simulations of the ELISE ion source.

Figure 4.11 shows the electrostatic potential along the axial direction, 2 mm from the bottom of the simulation domain for the pair-injection and flux-injection simulations, both with T_e = 2.0 eV. In both cases, a VC of $\sim$ 1 V is formed in front of the PG due to the emission of $\mathrm{H^-_{SP}}$ ions. With the pair-injection scheme, a sheath towards the left-hand side of the simulation domain is formed. This sheath does not exist in the real ion source and is only a numerical remnant from the injection scheme that has been used. This sheath impacts the simulation in two main ways. It accelerates positive ions from the injection zone towards the upstream boundary of the simulation and reflects electrons and NIs. In particular, the $\mathrm{H^-_{SP}}$ ions are accelerated towards the upstream boundary by the Debye sheath formed in front of the PG, but the sheath formed on the upstream side of the simulation domain reflects these $\mathrm{H^-_{SP}}$ ions, which does not correctly represent the ion transport in the real ion source. This will occur for any pair-injection model with an upstream Dirichlet BC since the sheath towards the boundary reflects approaching $\mathrm{H^-_{SP}}$ ions. In contrast, the flux-injection scheme instead produces a plasma potential closer to what is taking place in the real ion source, with a flat transition from the simulation domain to the bulk plasma.

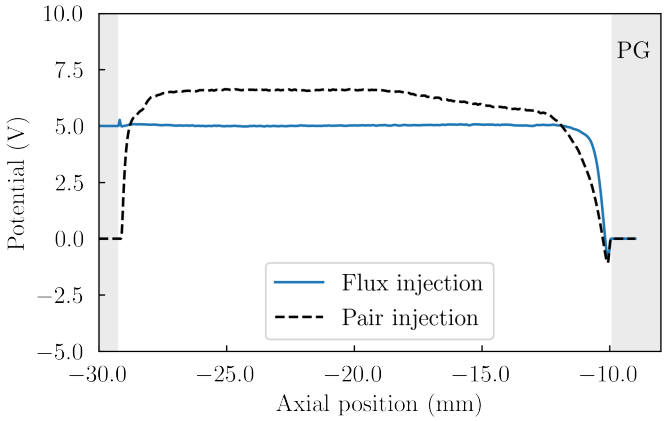

Figure 4.11: *Potential along the axial direction, 2 mm from the bottom of the simulation domain for the flux-injection and pair-injection (LD/HT) simulations.* $T_e = 2$ *eV.*

4.4.2 Electron transport

Generally, in negative ion sources, the transport of electrons in the axial direction is reduced due to the perpendicular magnetic fields (both $\mathbf{B}_{\mathrm{FF}}$ and $\mathbf{B}_{\mathrm{DF}}$), leading to a reduction of electron density from the bulk plasma towards the aperture. At 5 mm upstream of the PG, the total field strength is 7.7 mT in the simulations, this corresponds to the combined field from the $\mathbf{B}_{\mathrm{DF}}$ and $\mathbf{B}_{\mathrm{FF}}$ generated by a current $I_{\mathrm{PG}} = 1.7$ kA through the PG [108].

In the simulation with the pair-injection scheme, the thermalization of electrons interrupts the particle orbits around the magnetic field lines. Since the electrons are magnetized by the $\mathbf{B}_{\mathrm{FF}}$ and $\mathbf{B}_{\mathrm{DF}}$ in the vicinity of the extraction apertures, the impact of the thermalization plays an important role in the pair-injection case. Figure 4.12 shows sample trajectories of electrons using the electrostatic potential obtained from the flux-injection simulation with the thermalization turned on (top) and off (bottom), the particle tracking was done using the *a posteriori* particle tracking described in Chapter 3. The trajectories of electrons follow the typical banana orbits of the $\mathbf{B}_{\mathrm{DF}}$ in the axial-vertical plane, see Figure 3.10. However, inside the thermalization region, the trajectories are interrupted by the thermalization and do not follow the magnetic field lines, as they would do in the real ion source. Thermalization will also have an impact on the co-extraction of electrons by introducing an artificial electron transport between field lines.

To show the effect that each injection method plays on the formation of an ion-ion plasma in front of the meniscus, Figure 4.13 shows the fraction of ions to electrons for the flux- and pair-injection simulations. Due to thermalization in the pair-injection case, the electron trajectories are interrupted and the transition to an ion-ion plasma is abrupt. The thermalization region

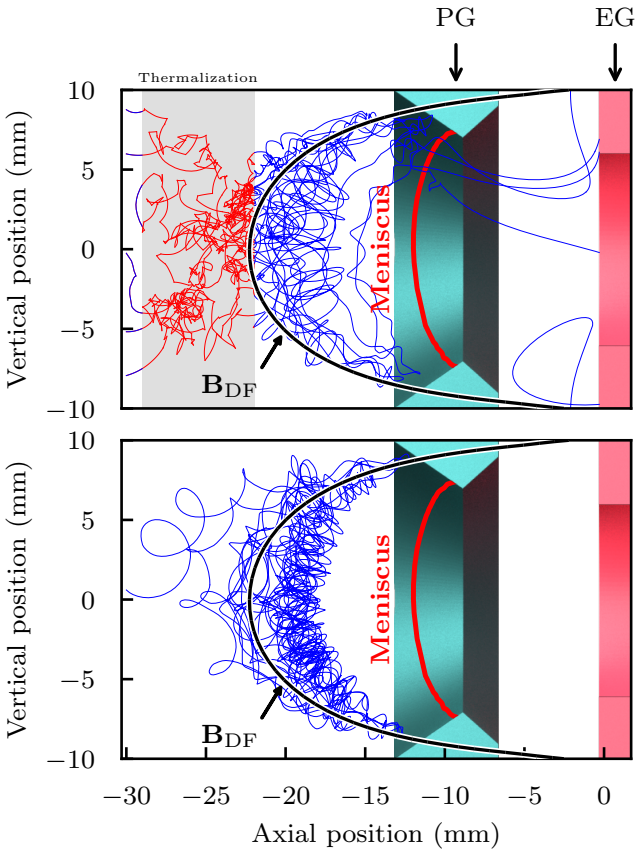

Figure 4.12: *Electron trajectories with (top) and without (bottom) thermalization. The thermalization zone is marked with a gray box, the meniscus is shown with a red line and one field line of the* $\mathbf{B}_{\mathrm{DF}}$ *(∼ 7.7 mT 5 mm from the PG) is shown (black line).* U_{ext}*=10 kV,* U_{acc}*=55 kV.*

is not placed far enough from the aperture to give electrons sufficient space for self-consistent redistribution. In the axial-vertical plane, the electron density is higher than the negative ion density at the top and bottom of the simulation domain until the sheath and VC form since the NIs accumulate in the VC. The reason why the higher electron fraction reaches closer to the PG in the axial-vertical plane than in the axial-horizontal plane is that the electrons are magnetized by the $\mathbf{B}_{\mathrm{DF}}$ which has field lines going from the top to the bottom of the aperture, see Figure 3.10. To minimize the effect of the thermalization region on the electron trajectories, the simulation domain for the pair-injection must be enlarged to make room for the self-consistent formation of the plasma separated from the $\mathbf{B}_{\mathrm{DF}}$ near the PG, which would increase the computational requirements due to more particles and more grid elements.

Another effect of the thermalization is the impact on the electron transport along the $\mathbf{B}_{\mathrm{FF}}$. The long-range electron transport is represented by the accumulated horizontal and vertical distance which the electrons travel, which can be tracked by saving the global coordinate $\mathbf{x}_{\mathrm{global}}(t)$ at time

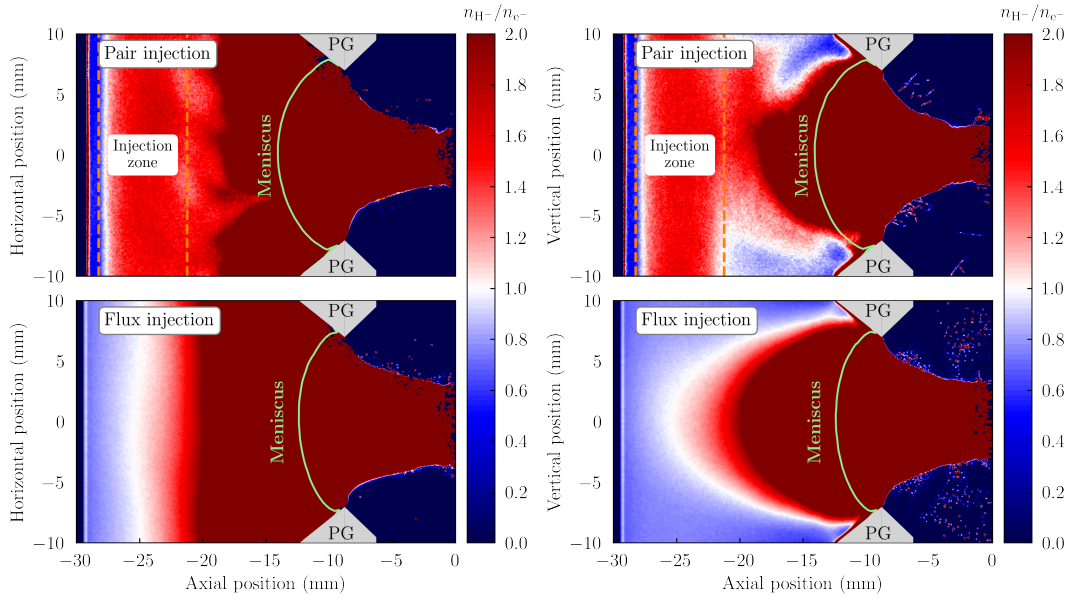

Figure 4.13: *2D profiles of ion to electron ratios for the (top) pair-injection and (bottom) flux-injection simulations in the (a) axial-horizontal plane and (b) axial-vertical plane. LD/HT, U_{ext}=10 kV, U_{acc}=55 kV.*

t for each particle over the course of its trajectory, including laps across the periodic boundaries of the simulation. To investigate the effect that thermalization plays in electron transport, *a posteriori* simulations were performed where the electrons were (a) not thermalized, and (b) thermalized with a frequency of $f = 10^9$ s^{-1}, as is used in [154], and (c) thermalized with a frequency of $f = 2 \cdot 10^9$ s^{-1}, as is used in [137]. The polarization of the $\mathbf{B}_{\text{DF}}$ was flipped between each aperture row. Figure 4.14 shows a histogram of the global coordinates of the electrons when passing through the meniscus in the horizontal-vertical plane. The electrons are injected in the injection zone between -10 mm and 10 mm, marked in red in Figure 4.14. For the case without thermalization, where $f = 0$ s^{-1}, 29.2% of the electrons are extracted through the same aperture as where they are injected, meaning that a majority of electrons are moving to neighboring apertures by crossing at least one periodic boundary. For the two cases with thermalization, higher percentages, 45.7% and 45.8%, respectively, are extracted from the same aperture as the injection zone. In all three cases, the distance traveled is higher in the horizontal direction than in the vertical direction due to the travel along the $\mathbf{B}_{\text{FF}}$ field lines, which span over all aperture columns. In contrast, the electron trajectories along the $\mathbf{B}_{\text{DF}}$ follow the typical banana orbits. This indicates that vertical electron transport does not play a large role near the PG apertures (further investigated in Section 4.5). The profiles for the two cases with electron thermalization are almost equal, indicating that a thermalization

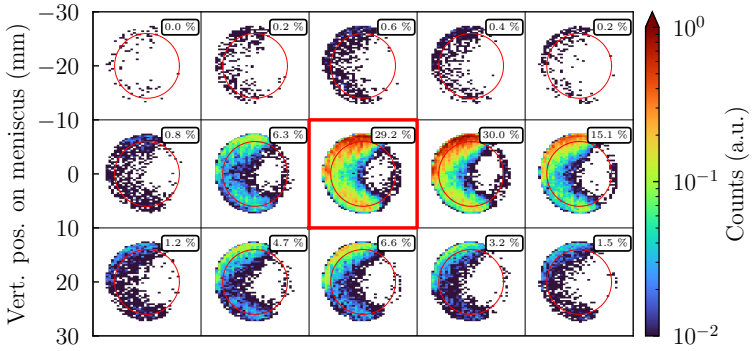

(a) *No thermalization*

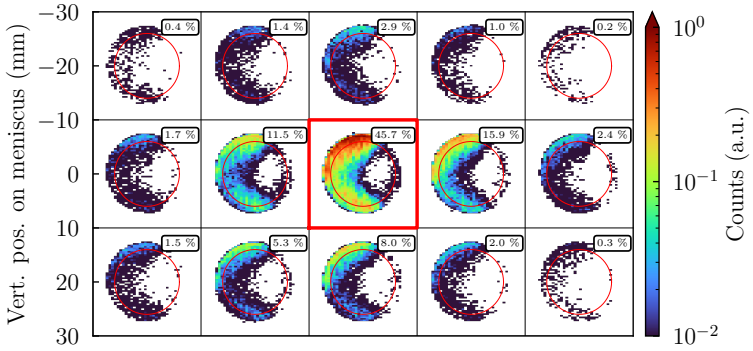

(b) $f = 10^9\ s^{-1}$

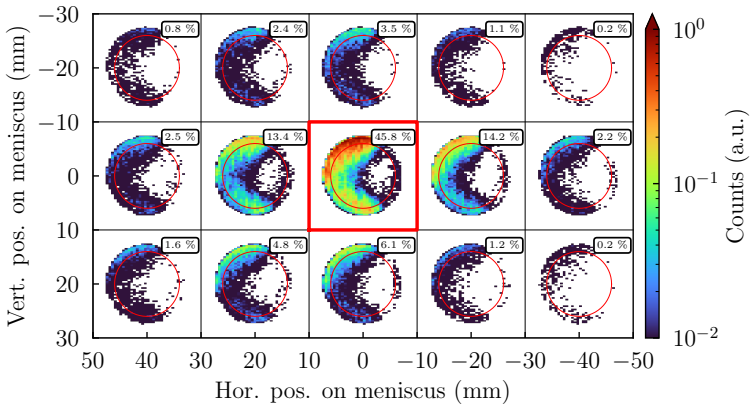

(c) $f = 2 \cdot 10^9\ s^{-1}$

Figure 4.14: *Histograms of global electron positions on the meniscus. All electrons are started in the injection box of the central aperture, where horizontal and vertical positions are between -10 mm and 10 mm, marked with a red square. (a) No thermalization, (b)* $f = 10^9\ s^{-1}$*, and (c)* $f = 2 \cdot 10^9\ s^{-1}$*. The size of the apertures is shown with red circles.*

rate of 10^9 s^{-1} is sufficient to hinder the horizontal transport of the electrons along the filter field lines. In conclusion, the electron transport along the $\mathbf{B}_{\mathrm{FF}}$ is better represented by the flux-injection scheme than the pair-injection scheme due to the thermalization of electrons in the latter.

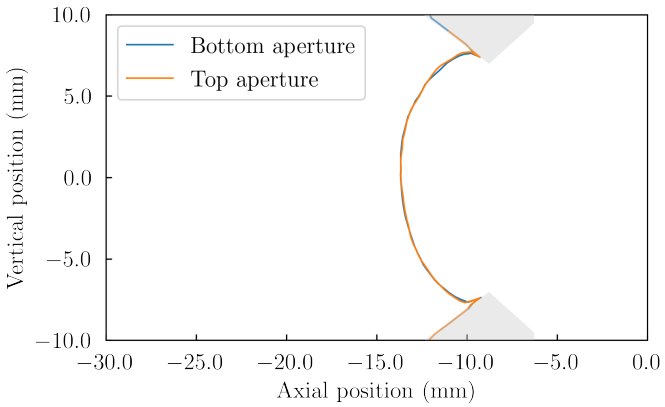

Figure 4.15: *Meniscus shape for the top and bottom apertures in the double-aperture simulation.*

4.5 Double aperture simulations

3D-PIC simulations of NI extraction typically simulate a single aperture with periodic BCs along both vertical and horizontal axes to reduce the need for computational resources, this common approach neglects the influence of the alternating $\mathbf{B}_{\mathrm{DF}}$ polarization. To check the validity of this approach, a two-aperture simulation is necessary as it is the minimal setup that accurately represents both polarities of the $\mathbf{B}_{\mathrm{DF}}$.

The impact of the alternating row-wise polarizations of the $\mathbf{B}_{\mathrm{DF}}$ on particle dynamics and meniscus formation was investigated using a simulation with two vertically aligned apertures using the one-sided flux-injection model. The flux-injection scheme is used to avoid the impact of the electron thermalization with the pair-injection scheme. The plasma density was set at 1×10^{16} cm^{-3}, which is lower than the LD/HT parameters to save calculation time, and with an electron temperature of $T_e = 2$ eV.

Figure 4.15 shows the meniscus profiles in the axial-vertical plane for the top and bottom apertures, with no significant differences in the meniscus shape and penetration. Similarly, the extracted current densities showed little variation, with the total extracted negative ion current density at 12.3 Am^{-2} for the top aperture and 12.6 Am^{-2} for the bottom aperture. The co-extracted electron current density is 7.1 Am^{-2} for the top aperture and 6.6 Am^{-2} for the bottom aperture. The extracted current densities are significantly lower than in the full-density simulations presented in Section 4.4.1, which is expected due to the lower plasma density.

In conclusion, the simulation indicated minimal asymmetry between the top and bottom apertures, supporting the findings shown in Figure 4.14 that the majority of the electrons are ex-

tracted from the same aperture row where they are injected. This suggests that the alternating polarity of the $\mathbf{B}_{\mathrm{DF}}$ has a small impact on row-wise asymmetries, affirming that single-aperture models are a good approximation and will therefore be used for the remainder of the simulations presented in this thesis.

4.6 Conclusions

This chapter has investigated the physics of the flux-injection scheme in a slab-domain geometry using a wide range of plasma parameters and for the ELISE PG geometry using both flux- and pair-injection. The plasma potential corresponds well to the analytical values based on Equation (2.18). In addition, the flux-injection scheme successfully regulates the influx of particles so that the solution converges to a state with the desired particle density of each species. By shifting the Maxwellian of the injected PIs, the source-sheath can be removed, which allows for a flat potential from the injection plane to the plasma. The slab-domain geometry effectively simplifies the complex plasma behavior for a more focused analysis where the impact of the 3D-magnetic field does not play a role. Therefore, the slab-domain simulations using the flux-injection scheme are well-suited for basic parametric variation, this is done in Chapter 5 to study $\mathrm{H}^-_{\mathrm{SP}}$ ion accumulation in the plasma.

The flux-injection scheme provides several improvements to the study of plasma physics, including the ability to simulate electron losses along field lines. It also allows for a more realistic simulation of particle fluxes compared to the pair-injection model. Using *a posteriori* particle tracking, it is shown that the thermalization method used in the pair-injection significantly reduces the transport of the electrons along the $\mathbf{B}_{\mathrm{FF}}$; without thermalization, 29.2% of the electrons were extracted through the same aperture where they were injected into the model, while when thermalization is activated, 46% of electrons are extracted through the same aperture where they are injected.

Furthermore, minimal effects were observed from the alternating polarity of the $\mathbf{B}_{\mathrm{DF}}$ in a two-aperture setup, which shows that a single-aperture simulation domain is a good approximation that allows for reducing the computational resources while preserving the relevant physics. Therefore, the single-aperture geometry will be used for the remainder of the simulations presented in this thesis.

CHAPTER 5

Towards self-consistent modeling of negative ion extraction with realistic parameters

This chapter explores the influence of basic plasma parameters, such as plasma density, temperature, emission of H^-_{SP}, and isotope on the plasma development, meniscus formation, ion extraction, and co-extraction of electrons.

The impact of altering parameters from the HD/LT case (representing the BATMAN setup with a filter field from permanent magnets) to the LD/HT case (based on the ELISE and BUG setups with a filter field induced by a current through the PG) was investigated. Both cases are detailed in Table 3.1. Since the HD/LT scenario differs from the LD/HT scenario in terms of plasma parameters (particle temperatures and densities), including the emission rate of H^-_{SP}. Full-density simulations were carried out for both the HD/LT and LD/HT parameters. Furthermore, to distinguish effects due to changes in plasma parameters from those arising from variations in the emission of H^-_{SP} from the PG, the emission rate value was modified for both the HD/LT and LD/HT parameters. The emission rate of H^-_{SP} ions was varied from 100 Am^{-2} to 550 Am^{-2}.

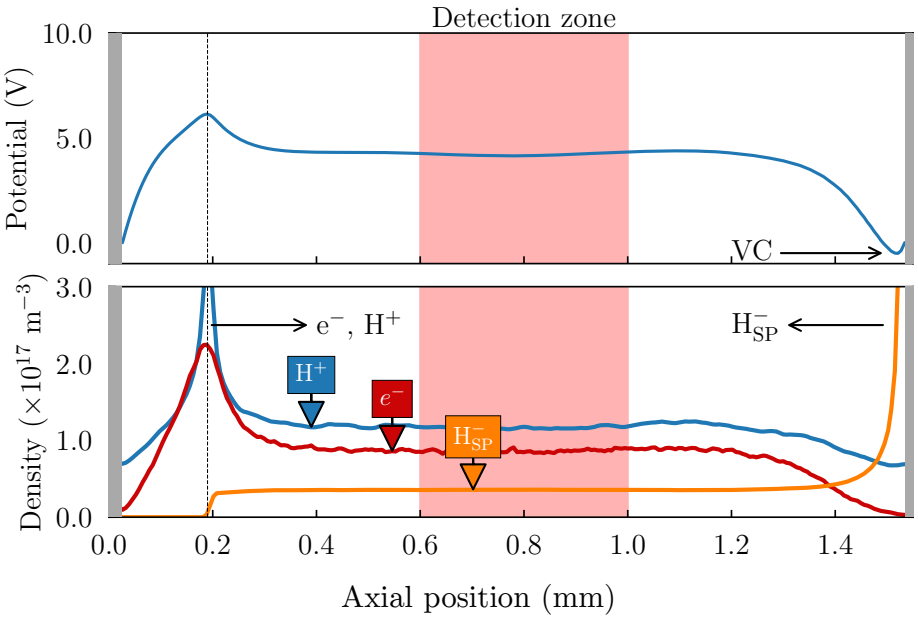

Figure 5.1: *Particle densities and electrostatic potential for a slab-domain simulation with* $n_{H^+} = 1.2 \cdot 10^{17}$, $T_{H^+} = 0.8$ *eV*, $T_e = 2.0$ *eV*, $T_{H^-_{SP}} = 0.6$ *eV and* $\Gamma_{H^-_{SP}} = 200$ Am^{-2}. *The injection plane is marked with a dashed black line.*

The primary inquiries addressed concern the influence of plasma parameters on:

1. Accumulation of H^-_{SP} in the plasma,
2. Meniscus formation and shape,
3. Extracted currents of H^-_{VP} and H^-_{SP},
4. Co-extraction of electrons.

To analyze the impact of plasma properties on the accumulation of H^-_{SP} ions, a slab domain was used, neglecting the other three effects (2-4) listed before. This renders the typically complex 3D simulations with ONIX into practically 1D simulations, which is useful for studying the behavior of the plasma without the complications of the ELISE geometry, particle extraction, and magnetic fields. The PIC parameters are given in Table 5.1. In this simulation setup, the e^- and H^+ ions were injected with the two-sided flux-injection particle scheme. Figure 5.1 showcases particle densities and the electrostatic potential for a slab-domain simulation. H^-_{SP} ions are injected from one wall of the simulation domain and are removed upon crossing the injection plane, located at 0.195 mm, so that only H^-_{SP} ions approach the plasma from the wall they are emitted from. The impact of H^-_{SP} ion reflection on the other boundary is thus mitigated. Only H^-_{SP} (no H^-_{VP}) are thus simulated. Particle density, temperature, and the emission rate of H^-_{SP} were varied in distinct parametric changes.

Table 5.1: *PIC parameters for a slab-domain simulation.*

Parameter	Value
N_x, N_y, N_z	240, 10, 10
$\Delta x, \Delta y, \Delta z$	6.5 μm, 6.5 μm, 6.5 μm
L_x, L_y, L_z	1.56 mm, 65 μm, 65 μm
Δt	5 ps

5.1 Investigation of H^-_{SP} accumulation in the slab-domain

In experimental investigations, it has been shown that H^-_{SP} ions represent about 90% of the total current of extracted NIs, and the density of NIs in the vicinity of the extraction apertures. The accumulation of H^-_{SP} ions in the plasma has, however, previous 3D-PIC simulations did not reach the density measured in experiments. Therefore, it is commonplace to inject additional H^- ions in the bulk of the plasma to artificially make up for the lack of NIs in the simulated plasma. This method can increase the total density of H^- ions, but not replicate the velocity and spatial distribution of H^-_{SP} ions. Therefore, for a correct representation of the H^- ions in the plasma, it is important to study the accumulation of H^-_{SP} ions in the plasma, so that the accumulation can be self-consistently accounted for. The accumulation of H^-_{SP} ions in the plasma depends on the formation of the VC, which limits the fraction of H^-_{SP} ions that can enter the plasma. Studies of the formation of the VC in a simplified domain are thus vital for understanding which physical parameters have the greatest impact on the accumulation of H^-_{SP} ions in the plasma.

5.1.1 Plasma density variations

Simulations in the slab-domain with H^+ density varied from 10^{15} m^{-3} to $5 \cdot 10^{17}$ m^{-3} were performed. Table 5.2 presents the plasma parameters used. Each simulation ran until saturation (a plateau) of $n_{H^-_{SP}}$, but since the density greatly affects the calculation time, the simulations with lower density ran for more timesteps.

Figure 5.2 shows the time trace of $n_{H^-_{SP}}$ in the detection zone over the course of two simulations, one with $n_{H^+} = 1.0 \cdot 10^{17}$ m^{-3} and one with $n_{H^+} = 2.0 \cdot 10^{17}$ m^{-3}. In both cases, $n_{H^-_{SP}}$ is saturated after 0.4 μs, i.e. the simulation has reached equilibrium. However, the density of H^-_{SP} $3.0 \cdot 10^{16}$ m^{-3} in the case with $n_{H^+} = 1.0 \cdot 10^{17}$ m^{-3} and $4.0 \cdot 10^{16}$ m^{-3} in the case with $n_{H^+} = 2.0 \cdot 10^{17}$ m^{-3}. The difference in $n_{H^-_{SP}}$ can be attributed to the formation of the

Table 5.2: *Simulation parameters for slab-domain with varied* H^+ *density*

Parameter	Value
T_e	2 eV
T_{H+}	0.8 eV
$T_{H^-_{SP}}$	0.6 eV
Γ_{SP}	200 A/m^2

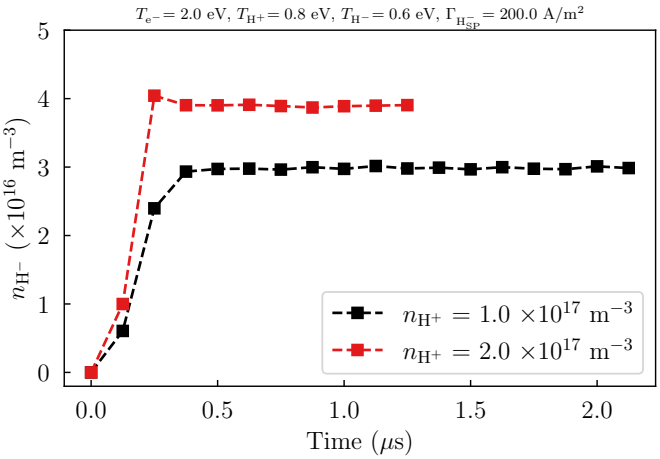

Figure 5.2: *Time trace of* $n_{H^-_{SP}}$ *in the detection zone over the course of two simulations with different* n_{H^+}.

VC, which plays a vital role in the H^-_{SP} accumulation in the plasma. Specifically, a higher plasma density offers space charge compensation near the wall, reducing the depth of the VC. Consequently, a larger proportion of the H^-_{SP} ions can overcome the VC barrier and penetrate the plasma. This behavior is illustrated in Figure 5.3, which depicts the depth of the VC and the fraction of H^-_{SP} ions that are repelled by the VC as a function of the n_{H^+}.

At $n_{H^+} \approx 15 \cdot 10^{16}$ m^{-3}, the depth of the VC is 0 V, indicating the VC has been fully offset by the PIs in the plasma. Thus, all H^-_{SP} ions will reach the plasma. This point signifies saturation of the H^-_{SP} density. Figure 5.4 shows the relationship between the density $n_{H^-_{SP}}$ as a function of n_{H^+}. The same saturation point can be observed. To increase the accumulation of NIs in front of the extraction apertures, it is therefore highly important for a plasma with sufficiently high density to be present in front of the PG, where the H^-_{SP} are emitted.

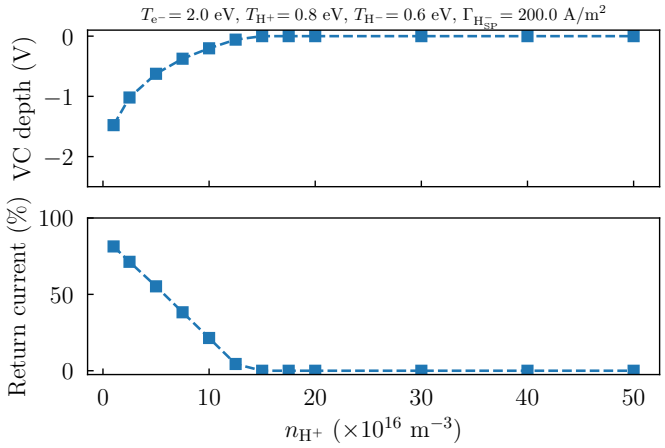

Figure 5.3: *VC depth (top) and the fraction of H^-_{SP} ions repelled by the VC (bottom) as a function of the n_{H^+} in the plasma.*

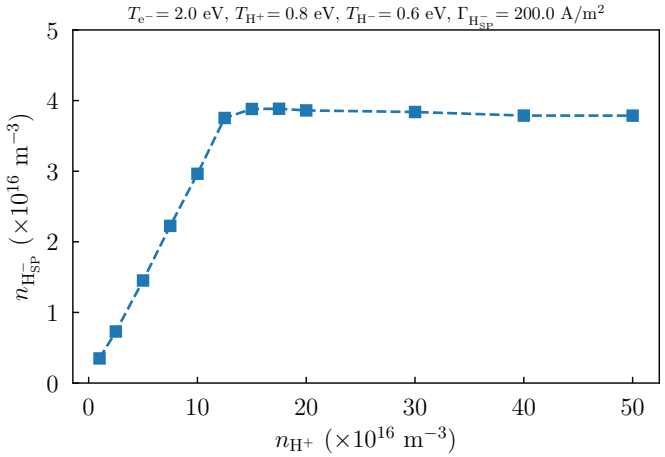

Figure 5.4: *$n_{H^-_{SP}}$ as a function of n_{H^+}*

5.1.2 Specificities of negative ion emission

Simulations in the slab-domain with Γ_{SP} varied from 0 Am^{-2} to 3000 Am^{-2} were performed to investigate the sensitivity of Γ_{SP} on the H^-_{SP} ion accumulation in the plasma. Table 5.3 presents the plasma parameters.

Figure 5.5 shows the time trace of $n_{H^-_{SP}}$ over the course of three simulations, with $\Gamma_{H^-_{SP}} = 50$ Am^{-2}, $\Gamma_{H^-_{SP}} = 200$ Am^{-2}, and $\Gamma_{H^-_{SP}} = 2000$ Am^{-2}, respectively. In each case, $n_{H^-_{SP}}$ is saturated after 0.4 μs. For the $\Gamma_{H^-_{SP}} = 50$ Am^{-2} case, $n_{H^-_{SP}}$ saturates at $0.9 \cdot 10^{16}$ m^{-3}, while both the $\Gamma_{H^-_{SP}} = 200$ Am^{-2} and $\Gamma_{H^-_{SP}} = 2000$ Am^{-2} cases saturate at an identical value of around $3.7 \cdot 10^{16}$ m^{-3}.

Table 5.3: *Particle parameters for the slab-domain simulations with varying* $\Gamma_{H^-_{SP}}$.

Parameter	Value
T_e	2 eV
T_{H+}	0.8 eV
$T_{H^-_{SP}}$	0.6 eV
n_{H+}	$1.2 \cdot 10^{17}$ m^{-3}

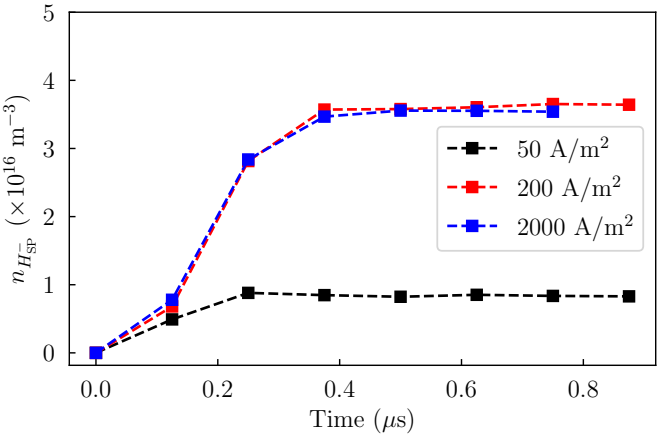

Figure 5.5: *Time trace of* $n_{H^-_{SP}}$ *over the course of three simulations with different* $\Gamma_{H^-_{SP}}$ *values.*

Figure 5.6 shows the depth of the VC and the return current as a function of $\Gamma_{H^-_{SP}}$. Both the depth of the VC and the return current increase with $\Gamma_{H^-_{SP}}$, meaning that a higher fraction of H^-_{SP} is reflected back towards the emitting surface. As shown in Figure 5.4, the density of the plasma affects to what degree space charge compensation of the VC can take place. In this case, the mechanism is the same, but instead of finding the minimum density for which complete space charge compensation of the VC occurs, the maximum emission rate for the given plasma density compensates the VC can be found. In this case, the VC starts forming when $\Gamma_{H^-_{SP}} = 200$ Am^{-2}.

Figure 5.7 shows the relationship between the density of $n_{H^-_{SP}}$ as a function of $\Gamma_{H^-_{SP}}$. Figure 5.7 also shows an equivalent variation of $\Gamma_{H^-_{SP}}$, but for $2.5 \cdot 10^{17}$ m^{-3}. The higher plasma density leads to a higher current necessary to reach the saturation point, e.g., for $2.5 \cdot 10^{17}$ m^{-3}, saturation is reached at 400 Am^{-2}.

In the parameters for the previously shown simulations and for the standard set of parameters used for simulations of the ELISE, the temperature for the injected H^-_{SP} ions is assumed to

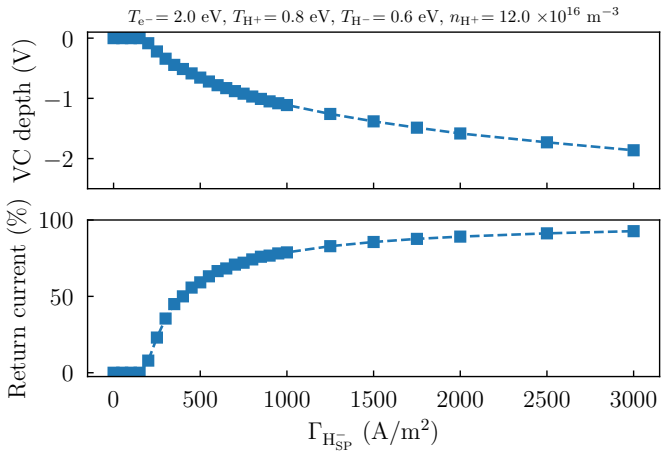

Figure 5.6: *Depth of the VC (top) and the NI return current (bottom) as a function of* $\Gamma_{H^-_{SP}}$.

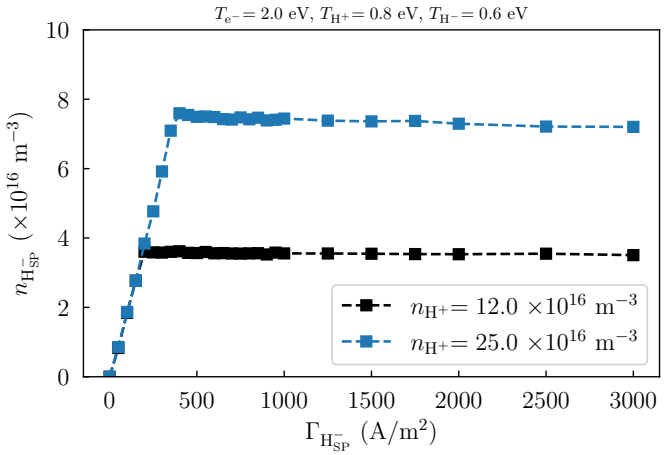

Figure 5.7: *Density of* H^-_{SP} *as a function of* $\Gamma_{H^-_{SP}}$.

be 0.6 eV, based on the atomic temperature of H. However, recent studies have indicated the possible existence of a hot component of atomic hydrogen [198]. Therefore, a variation of the $T_{H^-_{SP}}$ was performed in the slab domain.

Figure 5.8 shows the time trace of $n_{H^-_{SP}}$ over the course of three simulations, with $T_{H^-_{SP}} = 0.5$ eV, $T_{H^-_{SP}} = 3.0$ eV, and $T_{H^-_{SP}} = 5.0$ eV, respectively. The other plasma parameters are $T_e = 2.0$ eV, $T_{H^+} = 0.8$ eV, $n_e = 12 \cdot 10^{16}$ m^{-3}, and $\Gamma_{H^-_{SP}} = 500$ Am^{-2}. In each case, $n_{H^-_{SP}}$ is saturated after 0.4 μs. As expected, the density of H^-_{SP} increases for a hotter temperature of the emitted H^-_{SP} ions from the wall. Figure 5.9 shows the depth of the potential well (a) and the return current (b) as a function of $T_{H^-_{SP}}$; the higher temperature of H^-_{SP} leads to a deepening of the potential well, but the return current decreases, leading to an increased accumulation of H^-_{SP} in the plasma. Lastly, Figure 5.10 shows $n_{H^-_{SP}}$ as a function of $T_{H^-_{SP}}$; no saturation of $n_{H^-_{SP}}$

is observed in the studied interval up to $T_{H^-_{SP}} = 5$ eV. This means that if the temperature of the impinging H atoms, and consequently H^-_{SP} ions, are higher than the estimated 0.6 eV, then significantly more NIs would be present in the plasma volume.

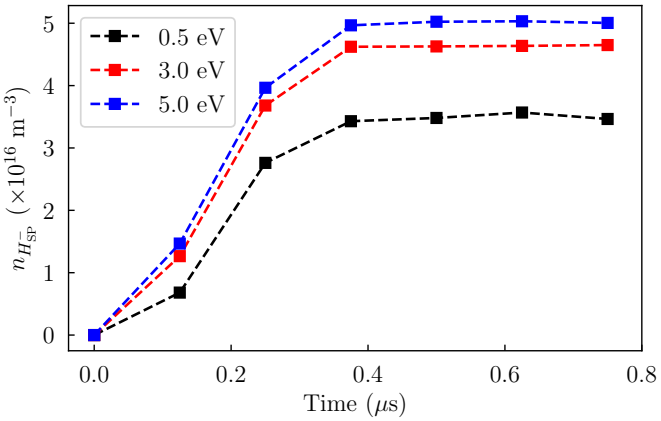

Figure 5.8: *Time trace of $n_{H^-_{SP}}$ over the course of three simulations with different $T_{H^-_{SP}}$ values.*

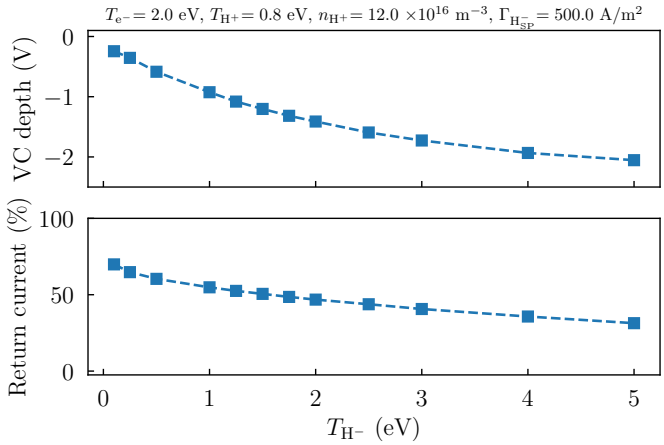

Figure 5.9: *Depth of the potential well and the return current as a function of $T_{H^-_{SP}}$.*

5.1.3 Study on the impact of the ion mass

To study the effect of the ion mass on the H^-_{SP} accumulation in the plasma, simulations in the slab domain were performed with varying ion mass. The composition of the plasma remained the same as in the parametric variations with hydrogen, except that the mass of both H^+ and H^-_{SP} was altered numerically. Table 5.4 shows the parameters used in the simulations.

Figure 5.11 shows the time trace of $n_{H^-_{SP}}$ throughout three simulations, where the mass of both positive and NIs have been set to 1 amu, 2 amu and 3 amu, corresponding to the three isotopes of hydrogen: protium, deuterium, and tritium. In each case, $n_{H^-_{SP}}$ is saturated after 0.4 μs,

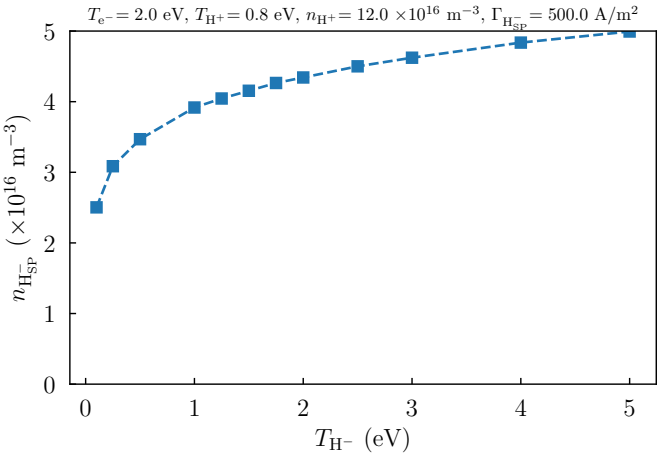

Figure 5.10: *$n_{H^-_{SP}}$ as a function of $T_{H^-_{SP}}$.*

Table 5.4: *Particle parameters for the slab-domain simulations with varying ion masses.*

Parameter	Value
T_e	2 eV
T_{H^+}	0.8 eV
$T_{H^-_{SP}}$	0.6 eV
n_{H^+}	$1.0 \cdot 10^{17}$ m^{-3}

0.5 μs and 0.6 μs, respectively. The time until saturation differs between the cases due to the mass difference between the species; since the temperature of the injected species is kept constant, the species with higher mass are slower, and thus it takes more timesteps for the simulation to reach convergence.

Figure 5.12 shows the depth of the VC and the return current as a function of the ion masses. Here, intermediate mass values between the physically existing species are also used to establish the trend. With increased mass, the depth of the VC grows, leading to a higher fraction of emitted H^-_{SP} that are reflected back to the surface. Thus, more NIs penetrate the plasma in the simulations with the lowest ion mass, they are, however, lost quicker since their velocity is higher. In the hypothetical case with $m_H = 0.5$ amu, the VC is not formed. Nevertheless, the differences in $n_{H^-_{SP}}$ between the simulated cases are small. The differences in the plasma parameters between H and D are therefore not explained singularly by the mass.

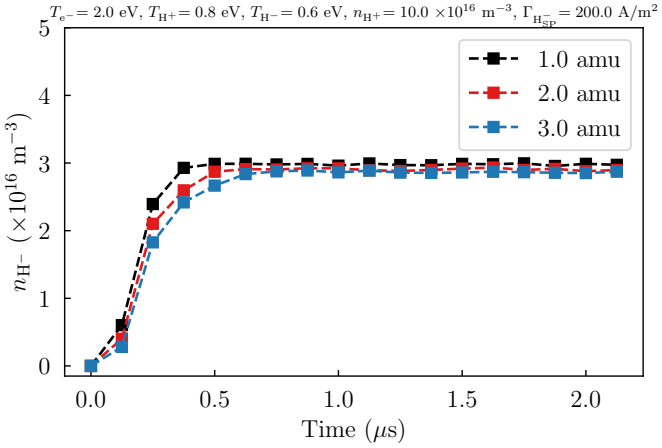

Figure 5.11: *Time trace of $n_{H^-_{SP}}$ throughout three simulations with varying ion masses.*

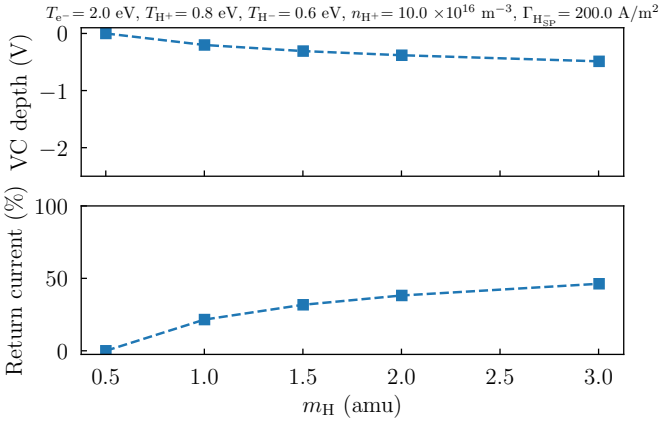

Figure 5.12: *Depth of the VC (top) and the return current (bottom) as a function of the ion mass.*

5.2 Analysis of plasma parameters in the extraction region in 3D ELISE simulations

5.2.1 Impact of electron temperature and density on the extraction of negative ions and electrons

The two full-density ONIX simulations (HD/LT and LD/HT) ran for 320, 000 timesteps, equivalent to 1.6 microseconds, for steady-state to be reached. At this point, the potential distribution and extracted NI current were not changing in time, and a stable meniscus was formed. The j_e oscillates on the order of ~ 10 Am^{-2}. Figure 5.13 shows the particle density of H^-_{VP} and H^-_{SP} ions and meniscus in the horizontal-axial plane for the HD/LT and LD/HT cases, respectively,

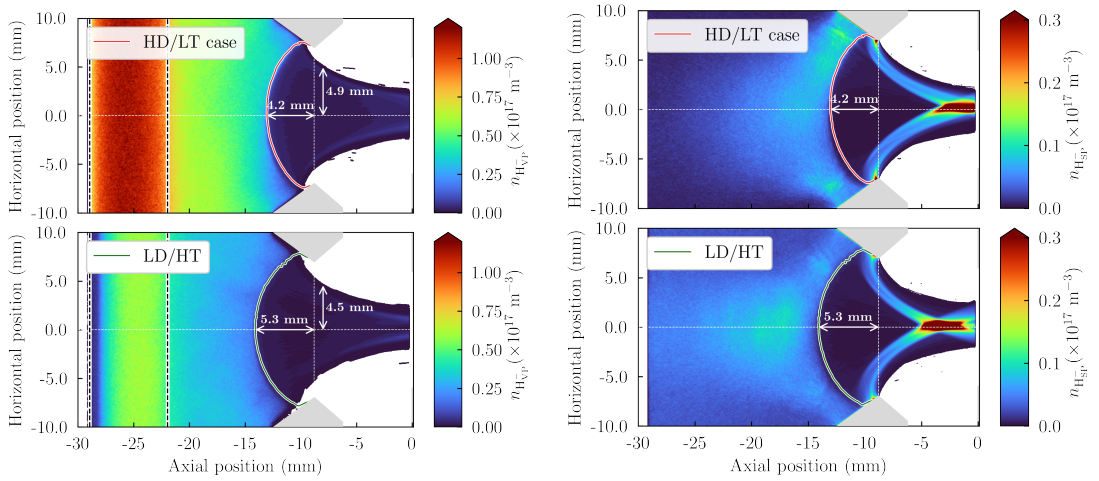

Figure 5.13: *Particle density map of (a) H^-_{VP} and (b) H^-_{SP}, for the HD/LT case (top) and the LD/HT case (bottom). The meniscus profiles are given with red and green lines. The axial distance from the PG knife is indicated. The injection zone for the H^-_{VP} ions is marked with black dashed lines. Note that the color scales in (a) and (b) are not the same as the H^-_{VP} density in the plasma is much larger than the H^-_{SP} density.*

at the end of the simulation, averaged over 10000 iterations.

The extracted current densities of NIs from the volume and surface, as well as of co-extracted electrons are given in Table 5.5. Most notably, j_e is significantly increased in the LD/HT case compared to the HD/LT case. This is primarily due to the higher electron temperature, which increases the electron flux towards the meniscus and leads to a higher co-extracted electron current. Additionally, the impact of the meniscus penetration on the j_e is discussed in Section 5.2.2.

The extracted NI current j_{ex} is reduced in the LD/HT case compared to the HD/LT case due to the reduced H^-_{VP} ion density, see Table 3.1, leading to a reduction of extracted H^-_{VP} current $j_{H^-_{VP}}$. Additionally, the transport of NIs close to the meniscus is changed, both due to the higher plasma potential (caused by the higher electron temperature) and the 1.1 mm deeper penetrating meniscus (caused by a lower plasma density for the same extraction voltage), see Figure 5.13 (b). Although the emission rate is 64% lower than in the HD/LT case, the extracted H^-_{SP} current $j_{H^-_{SP}}$ is only reduced by 11%. The interplay between the plasma parameters and the meniscus location impacts the extraction mechanisms of NIs and thus the total extracted current density.

Table 5.5: *Extracted current densities for the HD/LT and LD/HT cases.*

	$j_{H^-_{VP}}$ (Am^{-2})	$j_{H^-_{SP}}$ (Am^{-2})	j_{ex} (Am^{-2})	j_e (Am^{-2})	j_e/j_{ex}
HD/LT	74	82	156	22	0.14
LD/HT	35	73	108	93	0.86

5.2.2 Meniscus profile and H^- ion beam optics

The effect of the meniscus shape on the extracted H^- ions can be seen in Figure 5.13. The meniscus is marked for each case, the center position of the meniscus penetrates 1.1 mm deeper in the LD/HT case compared to the HD/LT case and the edges of the meniscus attach closer to the PG knife in the HD/LT case. This is expected, since when decreasing the plasma density, while keeping the extraction potential the same, the external electric field penetrates deeper into the plasma due to the decreased Debye shielding by the plasma.

Since the meniscus acts as an electrostatic lens for the extracted NIs, its shape and position have a large impact on the divergence of the extracted NI beam. In particular, the ratio between the beam core (mainly from H^-_{VP}) and the beam halo (mainly from H^-_{SP}) is highly dependent on the meniscus penetration. Due to the flatter meniscus in the HD/LT case, the extracted beam of H^-_{VP} ions is wider, as shown in Figure 5.13. At the axial position 1 mm downstream of the PG knife, the radius of the H^-_{VP} beam in the LD/HT case is 4.5 mm, while it is 4.9 mm in the HD/LT case. In order to study the downstream effect on the beam divergence caused by this shift, coupling of the ONIX code with a beam tracking code such as IBSimu is needed [175], this is further discussed in Chapter 7.

The extracted H^-_{SP} beam has two clear components, NIs extracted from the plasma through the center of the meniscus, and directly extracted ions through the edges of the meniscus, forming a beam halo. The majority of the extracted H^-_{SP} ions are directly extracted through the edges of the meniscus while H^-_{SP} ions entering the plasma are rarely extracted. However, since the potential of the upstream boundary to the bulk plasma $\phi_{bulk} = 0$ V (at axial position -30 mm), a plasma sheath is formed towards this boundary. This sheath reflects NIs produced at the PG, allowing them to reverse their trajectories and be extracted through the center of the meniscus. The 1.1 mm deeper penetrating meniscus allows for a larger fraction of H^-_{SP} to be directly extracted without entering the plasma, therefore, even though the emission rate of H^-_{SP} is lower in the LD/HT case (200 Am^{-2}) than in the HD/LT case (550 Am^{-2}), the fraction of H^-_{SP} in the halo is similar. The beam of directly extracted H^-_{SP} is wider in the LD/HT case

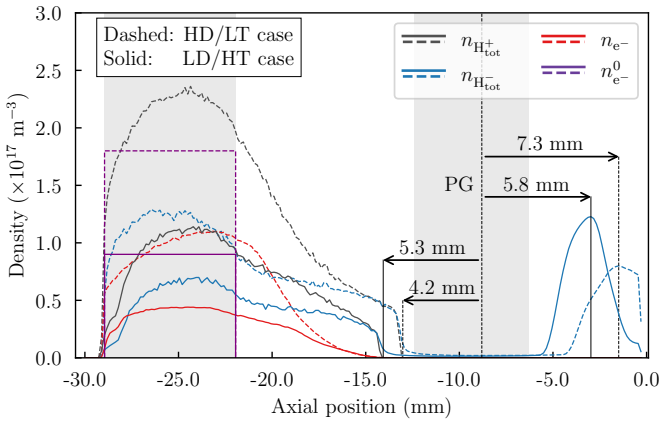

Figure 5.14: *Densities of PIs, NIs, and electrons along the central axis of the simulation domain for the HD/LT case and LD/HT case. The injection zone is represented by the gray box to the left. The initial electron density $n^0_{e^-}$ is indicated with purple lines. The distance from the knife of the PG to the meniscus position and the peak of the extraction H^- beam are indicated with arrows for the two simulations.*

and has a focus point that is moved backward by 1.5 mm while the meniscus moved deeper into the plasma by only 1.1 mm, compared to the HD/LT case. This leads to a lower perveance in the LD/HT case, which means a lower extraction voltage should be used to produce a beam with the same divergence as in the HD/LT case.

Figure 5.14 shows an axial density profile along the center of the simulation domain of the sum of all PIs ($n_{H^+_{tot}}$), NIs ($n_{H^-_{tot}}$) and electrons (n_{e^-}) at steady state and the initial density of electrons ($n^0_{e^-}$) along the axial center line of the simulation domain for the two standard cases. In both cases, the maximum plasma density is located in the injection zone, after which the densities drop off until reaching the center of the meniscus. Although the initial distributions of electrons and H^-_{VP} contain the same number of macro particles, the electron density is decreased with respect to the set value in both cases due to collisions with H_2, extraction, collisions with the PG and loss towards the bulk plasma boundary, see Figure 5.14. The shape of the axial electron density profile in the HD/LT case and LD/HT case is similar.

In both the HD/LT and LD/HT cases, $n_{H^-_{tot}}$ decreases by $\approx 50\%$ from the boundary of the injection zone, until 1 mm in front of the meniscus. Due to their higher mass, the NIs are not magnetized and therefore do not decrease in density as much as the electrons. It is the H^- density in the region close to the meniscus which is directly correlated with the extracted NI current, and this explains the difference in $j_{H^-_{VP}}$ given in Table 5.5.

For the electrons, on the other hand, the situation is more complex. The electrons in the simulation domain are magnetized and follow the field lines of $\mathbf{B}_{DF}$ and $\mathbf{B}_{FF}$, this slows down

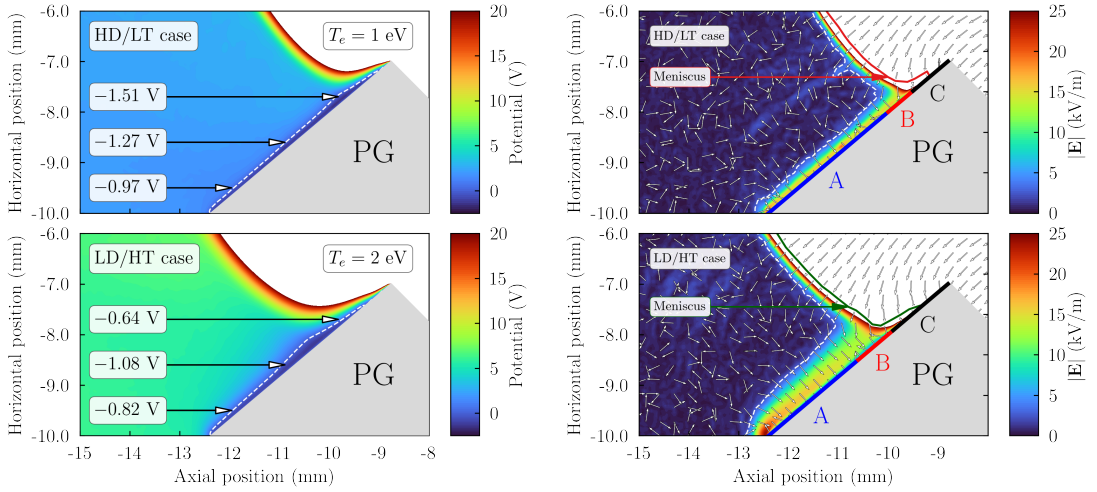

Figure 5.15: *Close-up view of the chamfered region of the PG. (a) Electrostatic potential in the axial-horizontal plane near the PG for the HD/LT case (top) and LD/HT case (bottom). The $\phi = 0$ V contour line is marked with a dashed white line and the arrows (at horizontal positions -9.5 mm, -8.6 mm and -7.7 mm) indicate the deepest position of the VC along that axial line. (b) Absolute magnitude of the electric field in the axial-horizontal plane near the PG for the HD/LT case (top) and LD/HT case (bottom). The direction of the arrows indicates the direction of the electric field. The $|\mathbf{E}| = 2.5$ kV/m is marked with a dashed white line. The color for $|\mathbf{E}| > 25$ kV/m is set to white so that the meniscus can be seen. The meniscus is indicated in dashed red (HD/LT) and green (LD/HT) lines.*

the diffusion of electrons along the axial direction and causes a reduction of n_e. While the electron density is higher in the injection zone in the HD/LT case ($n_e = 12{\cdot}10^{16}$ m^{-3}) compared to the LD/HT case ($n_e = 6 \cdot 10^{16}$ m^{-3}), it decreases to a similar density ($n_e = 1.4 \cdot 10^{15}$) at the axial −15 mm, see Figure 5.14. Therefore, although the electron density is similar at this axial position, j_e is $\sim$ 4 times higher in the LD/HT case, partly due to the 1.1 mm deeper penetrating meniscus.

5.2.3 Sheath structure in the extraction region

For H^-_{SP}, the sheath between the plasma and the PG, as well as the shape of the meniscus, impacts their trajectories. To clarify how the plasma parameters play a role in the extraction of H^-_{SP}, the electrostatic potential near the right-hand side of the simulation domain for the HD/LT and LD/HT cases are shown in Figure 5.15 (a). The electron temperature is 1 eV in the HD/LT case and 2 eV in the LD/HT case, which increases the plasma potential from $\sim$ 2.5 V to $\sim$ 6 V. Due to the emission of H^-_{SP} from the PG, a VC is formed close to the PG. The $\phi = 0$ V contour line is marked with a dashed white line, delineating the boundary of the VC (where $\phi < 0$). The depth of the VC depends both on the plasma parameters and the emission rate of

H^-_{SP}, as shown in Sections 5.1.1 and 5.1.2. In lower density plasma, the VC is wider and deeper due to decreased Debye shielding, see Figure 5.15 (a). However, a decreased emission of H^-_{SP} from the PG produces a less deep VC, as was shown in Section 5.1.2. As the LD/HT case has both lower density and lower emission rate than the HD/LT case, these effects counteract each other; for the LD/HT case, the deepest point of the VC is ≈ 1.1 V while the deepest point of the VC in the HD/LT case is ≈ 1.5 V. In both cases, the deepest position of the VC is located ≈ 0.5 mm from the meniscus. To directly compare the effect of the plasma parameters, one can compare the LD/HT case with the HD/LT case for the same emission rate of H^-_{SP}, namely $550\,\mathrm{Am}^{-2}$. In this case, a deeper VC develops in the LD/HT case. Furthermore, as can be seen in Figure 5.15 (a), the deepest position of the VC in the HD/LT case (-1.51 V) is located at the position of the top arrow (horizontal position -7.7 mm), while in the LD/HT case, the deepest position can be found further away from the PG knife. For H^-_{SP} not to be reflected towards the PG, they need sufficient energy to overcome this barrier, the extraction probability is thus non-uniform over the PG [108] and also overall lower in the HD/LT case.

Figure 5.15 (a) shows that the shape, width and depth of the VC, clearly depend on the distance from the knife of the PG, and the position of the meniscus. The deepest position of the VC tends to be close to the meniscus since $n_{H^+_{Tot}}$ is lower in this region than further away from the meniscus. In the LD/HT case, there is not enough space for a quasi-neutral plasma with a flat potential to be formed in the area between the meniscus and PG. This can be seen in 5.15 (b), which shows the magnitude and direction of the **E**-field near the right-hand side of the simulation domain for the LD/HT and HD/LT cases. The dashed white line indicates the contour line where $|\mathbf{E}| = 2.5$ kV/m, approximately delineating the quasi-neutral plasma from the sheath and the meniscus. In the LD/HT case, the sheath towards the PG is ~ 0.4 mm wider due to the higher Debye length of electrons, and the meniscus penetrates deeper. Additionally, the field lines connecting the PG directly with the meniscus reach toward the plasma side of the PG in the LD/HT case. In the HD/LT case, the contour line is closer to the PG surface, meaning the sheath is narrower. In the region downstream of the meniscus (region C in Figure 5.15 (b)), the vast majority of H^-_{SP} are directly extracted, following the electric field lines. For the H^-_{SP} ion produced upstream of the meniscus (region A), most ions are accelerated towards the quasi-neutral plasma by the sheath. However, in an intermediate region (region B), H^-_{SP} ions produced upstream of the meniscus, but sufficiently close to it, can be guided by the electric field lines toward the meniscus surface without crossing the white dashed line. Using Figure 5.15 (b), since the H^-_{SP} travel along the field lines of the electric field lines, one can see that more H^-_{SP} ions are directly extracted without crossing the dashed white line in the LD/HT case compared to the HD/LT case.

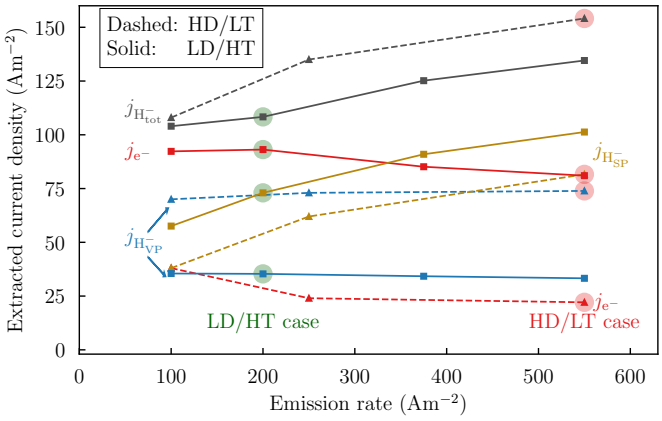

Figure 5.16: *Extracted current densities for the LD/HT case and HD/LT case for a variation of H^-_{SP} emission rate varying from 100 to 550* Am^{-2}*. The extracted current densities for the two standard cases are marked by purple circles for the LD/HT case and red circles for HD/LT case.*

In conclusion, both the plasma density, which determines the penetration of the meniscus, the depth of the VC, and the electron temperature, which determines the plasma sheath near the PG have a large impact on the particle transport of H^-_{SP} from PG to the meniscus. The plasma density balances the fraction of NI extracted from the volume and from the surface of the PG.

5.2.4 Variation of negative ion emission rate

In order to isolate the effect of the change in plasma parameters (from the HD/LT case to the LD/HT case) on the extracted current densities, the results of a variation of the NI emission rate from the PG from 200 to 550 Am^{-2} for both cases are shown in Figure 5.16, as mentioned before. In addition to the conclusions from the emission rate variation in the slab domain, this parametric variation provides insights into the effect on the extracted current densities.

In the simulations with an emission rate of 550 Am^{-2}, the total extracted H^- current decreased from 156 Am^{-2} to 135 Am^{-2} when going from high to low density, however, as previously mentioned, the H^-_{VP} and H^-_{SP} are impacted in opposite ways. Since the NI flux of H^-_{VP} across the meniscus is directly correlated with the NI density close to the meniscus, the lower NI density at this position in the LD/HT case ($\sim 2.5 \cdot 10^{16}$ m^{-3}) compared to the HD/LT case ($5 \cdot 10^{16}$ m^{-3}) lead to a 58% reduction of $j_{H^-_{VP}}$, from 74 Am^{-2} to 31 Am^{-2}. For the extracted H^-_{SP}, on the other hand, the current increased from 82 Am^{-2} to 101 Am^{-2} due to the deeper penetration of the meniscus, which allows for more H^-_{SP} to be directly extracted without entering the plasma, as is shown in Figure 5.13 (b).

When decreasing the emission rate of NIs from the plasma grid from 550 Am^{-2} to 100 Am^{-2}, $j_{H_{SP^-}}$ decreases by 43 Am^{-2} for both the LD/HT and HD/LT case while $j_{H_{VP^-}}$ decreases by 2 Am^{-2} in both cases. The decreased NI current is correlated with an increase in extracted electrons. However, the reduced NI current is not fully substituted by a proportional electron current since a significant fraction of the NIs are directly extracted through the edges of the meniscus, and thus do not affect the charge balance close to the remaining surface of the meniscus.

As is discussed in Section 5.1.1, the co-extracted electron current is significantly increased in the LD/HT case compared to the HD/LT case due to the higher electron temperature. This result is consistent in all simulations regardless of the H^-_{SP} emission rate. However, the electron current is slightly reduced with an increasing emission rate due to more negative space charge from the ions in the vicinity of the meniscus.

5.3 Extraction of negative deuterium ions in 3D simulations

To study the effect of the ion mass on the co-extraction of electrons in the ion source, ONIX simulations at three different densities were performed with varying ion mass. Low-density simulations at $n_{H^+} = 7 \cdot 10^{14}$ m^{-3}, medium-density simulations at $n_{H^+} = 6 \cdot 10^{15}$ m^{-3}, and high-density simulations at the standard parameters presented in Table 3.1. The low-density simulations allow for parameter surveys using 3D-PIC MCC modeling of an extraction aperture. Medium-density simulations require longer calculation time to perform but are useful since they are closer to realistic operating parameters and are fast enough to reach plasma densities that are very well-matched from simulation to simulation so that the simulations are directly comparable. The high-density simulations are resource-intensive and are thus used to confirm whether the trends from the low and medium-density cases hold true in high-density.

5.3.1 Mass variation in a low-density plasma

ONIX simulations in 3D were conducted in low-density, $n_{H^+} = 7 \cdot 10^{14}$ m^{-3}. As discussed in Section 5.2.1, the meniscus's penetration significantly impacts the co-extraction of electrons. Therefore, the extraction potential was scaled down to 500 V so that the penetration of the meniscus and perveance of the beam would remain comparable to the full-density simulations (this was done by trial and error while staying close to the scaling strategy in [137]). The parameters are given in Table 5.6. The one-sided flux-injection scheme was used so that the

Table 5.6: *Particle parameters used for the low-density 3D ONIX simulations.*

Parameter	Value
T_e	2 eV
T_{H^+}	0.8 eV
n_{H^+}	$7 \cdot 10^{14}$ m^{-3}
Γ_{SP}	0 A/m^2
U_{ext}	500 V

plasma density could be set to equal value while changing the mass of the ions from 1 amu to 10 amu. Negative ions were injected into the bulk plasma, but surface production was not included to avoid making additional assumptions about the emission rate. In order to compare all simulations at a floating potential, the PG potential was changed in each simulation in response to the influx of species onto its surface until a steady state where the net current density across the PG was 0 Am^{-2}.

Due to the deuterium's higher mass than Protium, the ions are slower, and thus a higher density is needed to match the extracted NI current j_{ex}. One simulation with the deuterium isotope was therefore made with a higher density by a factor $\sqrt{2}$, i.e. $n = \sqrt{2} \cdot 7 \cdot 10^{14} \approx 10 \cdot 10^{14}$ m^{-3} in order to match the j_{ex} (≈ 0.52 Am^{-2}) with the protium case.

Figure 5.17 shows the density of e^- and H^+ ions along the axial center-line for 1 amu, 2 amu, 10 amu, and a simulation with 2 amu (deuterium) where the extracted current density is matched to the extracted current density for 1 amu. The density is only shown on the plasma side of the PG knife. The drop-off of the H^+ ion density indicates the penetration of the meniscus, which is similar for the $m_{\mathrm{H}} = 1$ amu and $m_{\mathrm{H}} = 2$ amu cases, for $m_{\mathrm{H}} = 10$ amu, the penetration of the meniscus is ≈ 1 mm less. However, the most prominent effect on the extracted current densities comes from the higher density in the $m_{\mathrm{H}} = 2$ amu (current matched) case, which is shown in Figure 5.18.

Figure 5.18 shows each ion mass's extracted electron and ion currents, including the current-matched deuterium simulation. The j_{ex} drops off by the square root of the mass ratio between the species and for Protium, while the co-extracted electron current density is approximately the same. The ratio $j_{\mathrm{e}}/j_{\mathrm{ex}}$ strongly increases with the mass of the ion as a direct effect of the ion mass, the drastic increase of j_{e} which is observed experimentally when changing the isotope from Protium to deuterium [58] is not observed for the low-density simulation.

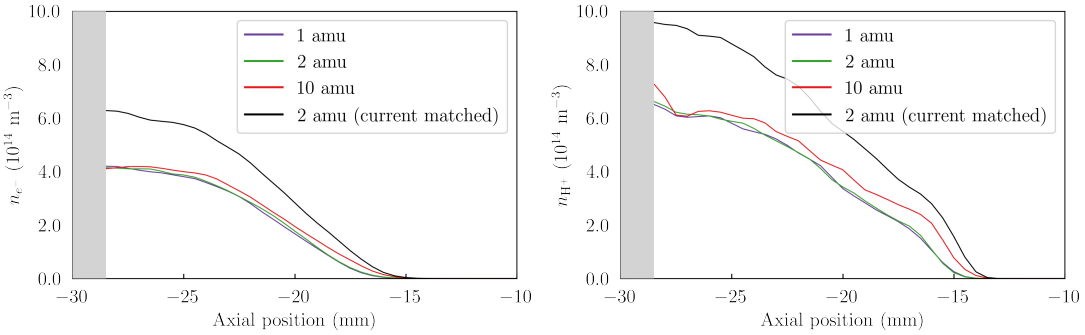

(a) **(b)**

Figure 5.17: *Comparison of particle density in low-density settings: (a) Electron and (b)* H^+ *ion density distribution along the center line of the simulation domain.*

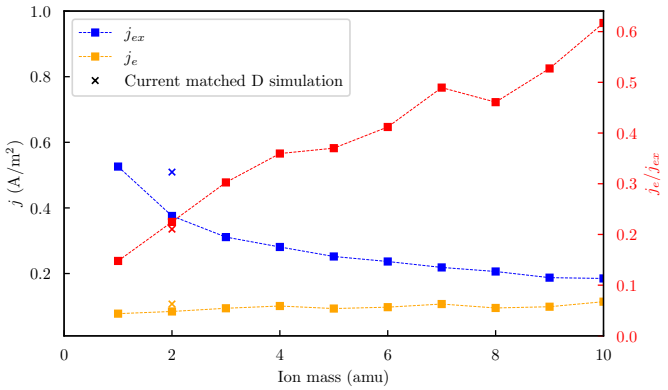

Figure 5.18: *Extracted electron and ion currents for each ion mass in low-density settings.*

5.3.2 Mass variation in a medium-density plasma

Two simulations with medium plasma density were performed. The particle parameters are given in Table 5.7 and the extraction voltage was 1 kV to keep the meniscus penetration similar to the low-density cases. The ion mass was set to 1 amu and 2 amu, respectively, and the PG was set to floating potential. Table 5.8 shows the extracted ion current, electron current, and their ratio for the hydrogen and deuterium simulations.

Figure 5.19 shows the electron to NI fraction for the two simulations. In both cases, the electrons dominate the negative space charge in the bulk plasma, but due to the $\mathbf{B}_{\mathrm{DF}}$, the electron density rapidly tapers off, and near the meniscus, the NIs dominate. Additionally, there is

There is, however, a difference in where the electrons are clustered near the meniscus. In the deuterium simulation, there are more electrons near the meniscus edges of the meniscus, which leads to a higher co-extracted electron current. This is seen in Figure 5.20, which shows the

Table 5.7: *Particle parameters used for the medium-density 3D ONIX simulations.*

Parameter	Value
T_e	2 eV
$T_{\mathrm{H+}}$	0.8 eV
$n_{\mathrm{H+}}$	$6 \cdot 10^{15}$ m^{-3}
Γ_{SP}	0 A/m^2
U_{ext}	1 kV

Table 5.8: *Extracted ion current density, electron current density, and their ratio for the hydrogen and deuterium simulations in medium-density settings.*

Simulation	j_{ex} (Am^{-2})	j_{e} (Am^{-2})	$j_{\mathrm{e}}/j_{\mathrm{ex}}$
Hydrogen	3.0	1.4	0.5
Deuterium	2.5	2.7	1.1

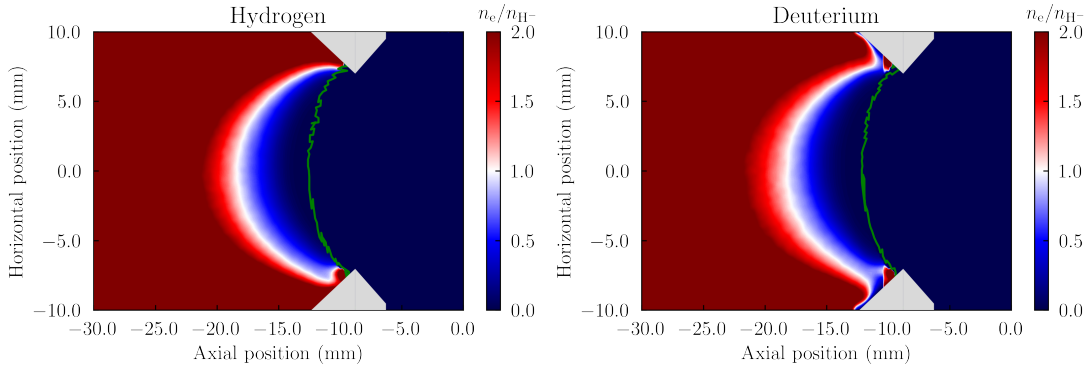

(a) **(b)**

Figure 5.19: *Electron to NI fraction for the (a) hydrogen and (b) deuterium simulations.*

fraction of electrons in the deuterium simulation with respect to the hydrogen simulation. The difference in the electron distribution near the meniscus between the hydrogen and deuterium simulations can be partly attributed to the deeper Debye sheath towards the PG in the deuterium case, due to the higher ion mass. A lower electron flux toward the PG leads to more electrons near the meniscus and, thus, more co-extracted electrons.

Figure 5.21 shows the flux of electrons in the hydrogen and deuterium simulations in the axial-horizontal and axial-vertical planes. In both cases, the electrons follow the $\mathbf{B}_{\mathrm{FF}}$ lines in the axial-horizontal plane and the $\mathbf{B}_{\mathrm{DF}}$ lines in the axial-vertical plane. In the deuterium case, the

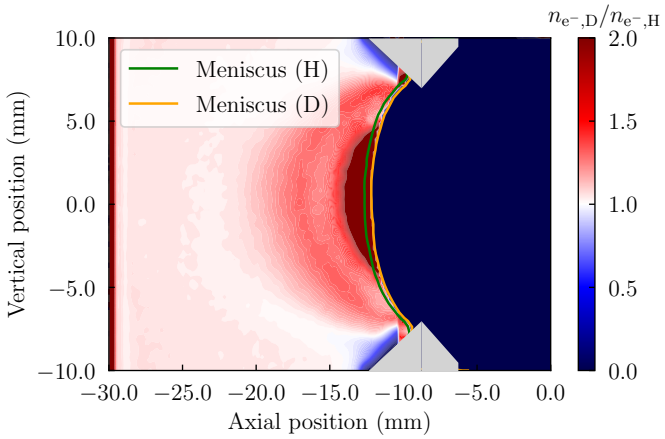

Figure 5.20: *Fraction of electrons in the deuterium simulation with respect to the hydrogen simulation near the meniscus.*

flux of electrons from the bulk plasma is higher than in hydrogen; both in the axial-horizontal and axial-vertical planes, the red high flux regions reach closer to the meniscus, which leads to a higher j_e.

5.3.3 Mass variation in a high-density plasma

As a final step, to compare directly with the LD/HT hydrogen simulation, a deuterium simulation is made where the mass of the NIs was increased, while keeping the plasma parameters equal ($n \approx 10^{17}$ m^{-3}). Due to the large number of macro particles and narrow grid size of the two parameter sets, matching the particle densities exactly with the flux-injection scheme is not feasible in the simulation time since it is much more costly than for the low- and medium-density cases. Therefore, the pair-injection scheme is used in the comparison.

Figure 5.22 shows the meniscus shape for the hydrogen and deuterium case. As in the low-density case, the shapes of the menisci are similar, and the difference in particle densities mainly determines the differences. However, the zoom of the region where the meniscus intercepts the PG in Figure 5.22 shows a slight shift of the meniscus position when deuterium is used instead of hydrogen. Additionally, the meniscus is symmetric in the hydrogen case while in the deuterium case, the meniscus is slightly asymmetric.

Table 5.9 shows the extracted ion current, electron current, and their ratio for the hydrogen and deuterium simulations. The deuterium simulation has a lower ion current density by a factor of $\approx \sqrt{2}$ and a higher ratio of j_e/j_{ex} compared to the hydrogen simulation. This is consistent with the results observed in the low and medium-density simulations, where the deuterium simulations also showed a lower ion current density and a higher ratio of electron

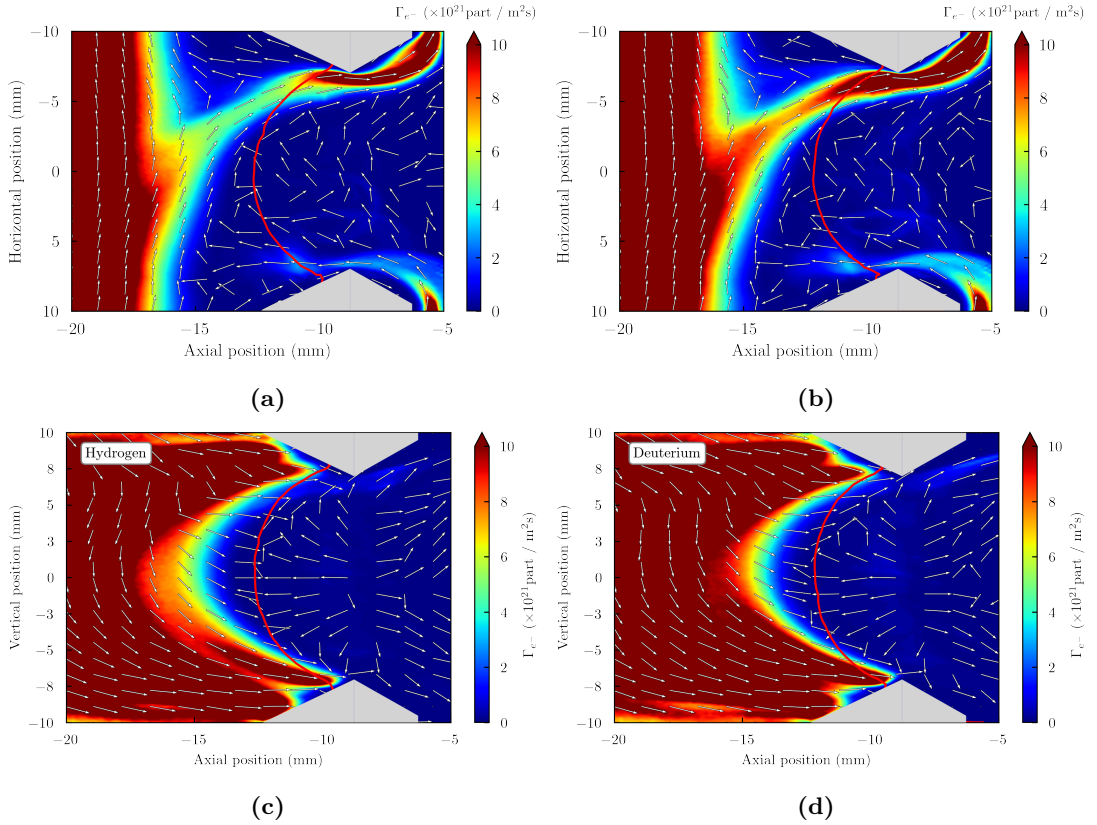

Figure 5.21: *Electron flux in the hydrogen (left) and deuterium (right) simulations. The top row shows the flux in the axial-horizontal plane, while the bottom row shows the flux in the axial-vertical plane. The meniscus is marked with a red line for each case.*

current density to ion current density. However, $j_e/j_{ex} = 2.8$ in the deuterium case, which is ~ 2.5 times higher than in the medium-density case. This shows that full-density simulations are needed to capture the physics of the co-extracted electrons. Additionally, these results capture the trend of experimental findings [58, 111, 115].

5.4 Conclusions

The study of plasma density and emission of H^-_{SP} ions in slab-domain simulations revealed several key findings.

- A higher plasma density offers space charge compensation near the wall, reducing the depth of the VC and allowing a larger proportion of the H^-_{SP} ions to penetrate the plasma.
- At a certain plasma density, the VC is fully offset by the PIs in the plasma, leading to saturation of the H^-_{SP} ion density.

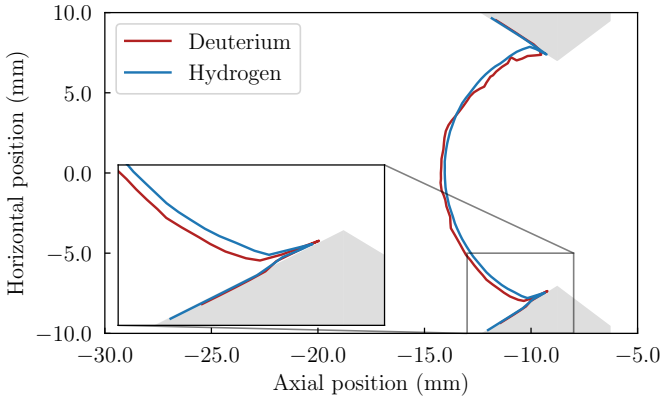

Figure 5.22: *Meniscus shape for the high-density deuterium and hydrogen simulations.*

Table 5.9: *Extracted ion current density, electron current density, and their ratio for the hydrogen and deuterium simulations.*

Simulation	j_e (Am^{-2})	$j_{H^-_{VP}}$ (Am^{-2})	$j_{H^-_{SP}}$ (Am^{-2})	j_{ex} (Am^{-2})	j_e/j_{ex}
Hydrogen	93	35	73	108	0.86
Deuterium	200	20	52	72	2.8

- The depth of the VC increases with $\Gamma_{H^-_{SP}}$, which leads to a higher fraction of H^-_{SP} ions that are reflected towards the emitting surface.

- By increasing the temperature of the emitted H^-_{SP} ions from 0.6 eV to 5 eV, the density of H^-_{SP} ions in the plasma ($n_{H^+} = 12{\cdot}10^{16}$ m^{-3}) increases from $3.5{\cdot}10^{16}$ m^{-3} to $5.0{\cdot}10^{16}$ m^{-3}. This shows that the temperature of the H^-_{SP} ions plays an important role in the H^-_{SP} ion accumulation in the plasma.

To show the impact that changing plasma density, electron temperature and emission rate of H^-_{SP} ions has on the extracted current densities, meniscus formation and plasma potential, two cases have been compared using the typical ONIX simulation volume. The first case is based on parameters in the BATMAN ion source, with a filter field generated by permanent magnets (the HD/LT case), and the second case is based on operational parameters in the ELISE and BUG ion sources, with a filter field generated by passing a current through the PG. The main differences were a higher electron temperature by a factor 2, lower particle density by a factor 2 and lower emission of H^-_{SP}. The conclusions are as follows.

- The penetration of the meniscus is 1.1 mm deeper in the LD/HT case compared to the HD/LT case due to decreased Debye shielding with lower density.

- Due to higher electron temperature (2 eV compared to 1 eV) and the 1.1 mm deeper penetrating meniscus in the LD/HT case, the co-extracted electron current density is 4 times higher than in the HD/LT case.
- Even though the emission rate is reduced by 64% in the LD/HT case, $j_{H^-_{SP}}$ is only reduced by 11% due to 1.1 mm deeper penetration of the meniscus in the LD/HT case. This means that most of the $j_{H^-_{SP}}$ are directly extracted H^-_{SP} ions.
- Both the VC and plasma sheath are non-uniform along the PG, and the deepest point depends on the plasma parameters and the meniscus shape. For the LD/HT case, the maximum depth of the VC is ≈ 1.1 V while in the HD/LT case it is ≈ 1.5 V. The deepest position of the VC is for both cases located ≈ 0.5 mm from the meniscus.
- The reduced plasma density ($n_e = 6 \cdot 10^{16}$ m^{-3} compared to $n_e = 12 \cdot 10^{16}$ m^{-3}) and increased electron temperature (2 eV compared to 1 eV) in the LD/HT case widens the Debye sheath by ≈ 0.4 mm and increases the plasma potential by ≈ 3 V. Consequently, the H^-_{SP} ions that enter the plasma are accelerated toward the bulk plasma by an additional ≈ 3 eV, which decreases their extraction probability.
- The effect of the plasma parameters on the extracted current densities can be seen when comparing the HD/LT case to the LD/HT case for a given emission rate of NIs from the PG. In the LD/HT case, $\approx 25\%$ more H^-_{SP} ions and $\approx 300\%$ more electrons and 50% fewer H^-_{VP} ions are extracted when setting the emission 550 Am^{-2} in both cases. This is a consequence of the deeper meniscus penetration and higher electron temperature, as mentioned above.

The increased co-extracted electrons and reduced extracted ions during deuterium operation can be effectively studied using 3D-PIC modeling. When operating in deuterium, the floating plasma potential is higher due to the higher mass of the deuterium isotope. An elevated plasma potential is related to a reduced electron flux directed towards the PG, leading to an increased accumulation of electrons in front of the meniscus. This phenomenon provides a partial explanation for the observed rise in co-extracted electron current.

CHAPTER 6

Impact of biased surfaces on the electron dynamics in NI sources

This chapter provides an examination of injection methods and BCs in 3D-PIC modeling, primarily focused on their influences on their application for the simulation of the PG bias. The simulation domain in 3D-PIC MCC typically only covers one of the PG apertures, the boundaries are thus far from the source walls, which can not be directly included in a 3D-PIC simulation. Previous PIC studies, such as described in [134–139] have neglected the effect of biasing the PG with respect to the source walls by treating the PG boundary and the upstream plasma-side boundary as walls with Dirichlet conditions. Simulations in 1D using a Neumann condition on the plasma-facing side of the domain have been performed [141]; however, PG biasing has not been incorporated in 3D-PIC simulations.

In addition to studying the effect that biasing the PG has on the co-extraction of electrons, the so-called electron fence is introduced in simulations with ONIX. The geometry is based on the one used in NIFS [114], which was shown to reduce the amount of co-extracted electrons. Since the PG geometry in NIFS is not the same as the one used at IPP, simulations with both PG geometries are done to investigate whether the EF has the same impact in both PG configurations.

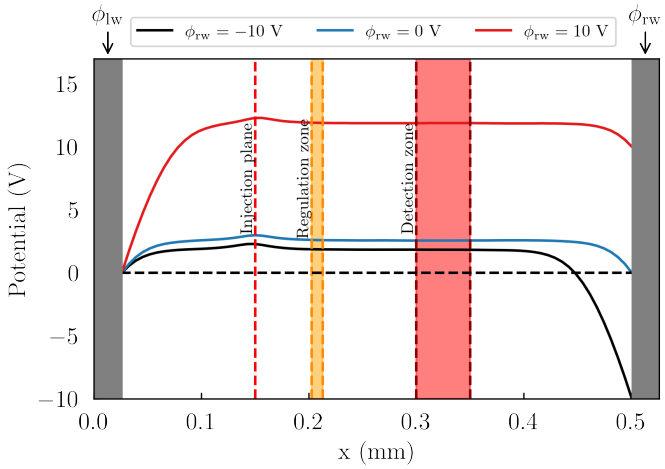

Figure 6.1: *Electrostatic potential for simulations with varying ϕ_{rw}. The injection plane is marked with a dashed red line, the regulation zone is marked with an orange box and the detection zone where the plasma potential is evaluated is marked with a red box.*

6.1 PIC modeling of biased walls

6.1.1 Biasing in a slab-domain

The impact of biasing of the right wall on the plasma potential was investigated by simulating a plasma with $T_e = 1$ eV, $T_{\mathrm{H}^+} = 0.8\ eV$ and $n_{+,SS} = 10^{17}$ m^{-3} for varying bias of the right wall ϕ_{rw} between -10 V and +10 V. The potential of the left wall ϕ_{lw} was 0 V in all cases.

Figure 6.1 shows the potential profiles for three simulations with ϕ_{rw} set to -10 V, 0 V and +10 V, respectively. The injection plane, regulation zone and detection zone are indicated. On each side of the simulation domain, a Debye sheath is formed towards the wall. When both walls are set to $\phi_{\mathrm{lw}} = \phi_{\mathrm{rw}} = 0$ V, the sheath is equally deep on both sides, approximately 2.5 V, as given in Equation (2.18). The ϕ_{rw} has a large impact on ϕ_{pl}, in particular when biasing the wall positively with respect to the floating potential, as this increases ϕ_{pl} almost by an equal amount since the area of the left and right walls are equal [78].

The differences between plasma potential ϕ_{plasma} and the potentials on the left wall and right wall are shown in Figure 6.2 as a function of ϕ_{rw}. For a right-hand side bias below -2.5 V, $\phi_{\mathrm{pl}} - \phi_{\mathrm{lw}}$ is unaffected. As the right-hand side bias approaches and passes 0 V, the $\phi_{\mathrm{pl}} - \phi_{\mathrm{lw}}$ compensates the potential and follows the increase of the ϕ_{rw} bias. In simulations where the particles are injected into the plasma, and not from the wall, the fluxes towards the boundaries adjust to ensure flux balance and quasi-neutrality. Thus, the bias between the PG and plasma observed experimentally can not be simulated with a two-sided injection scheme. For the PG

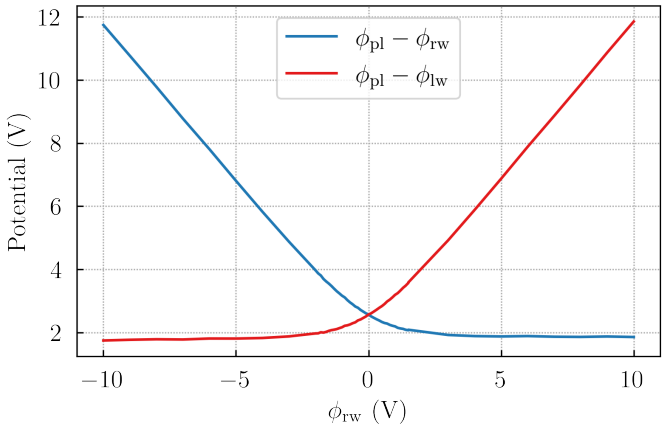

Figure 6.2: *Difference between plasma potential and the potential on the left and right walls as a function of* ϕ_{rw}.

biasing simulations in Section 6.1.2, the one-sided pair-injection is therefore used.

6.1.2 PG biasing by 3D-PIC modeling in the ELISE geometry

The flux-injection scheme permits a seamless transition of the plasma potential from the bulk plasma on the upstream side of the simulation domain to the simulated plasma. Biasing of the PG is achieved by modifying the potential difference between the bulk plasma and the PG, treating it as an adjustable input parameter for the simulation. The PG bias ranged from -5 V to +1 V relative to the plasma potential using the plasma parameters of the LD/HT case and U_{ext}=10 kV, U_{acc}=55 kV.

Figure 6.3 shows the potential profiles for varying PG bias along the axial direction near the bottom of the simulation domain. The plasma potential for simulations with −5 V and −3 V are unchanged. However, when increasing the potential to −1 V and +1 V, the potential of the plasma also increases. This potential increase is not proportional to the increase in PG potential, which explains why a further reduction of co-extraction of electrons is observed. The depth of the VC is equal (0.8 V) for the -5 V, -3 V, and -1 V cases, and 0.7 V for the +1 V case.

In the specific scenario where the PG bias is −5 V, the sheath close to the PG is strongly electron-repelling. Consequently, electrons from the plasma are unlikely to reach the PG and are thus more likely to be extracted. The co-extracted electron current density is approximately 110 Am^{-2} for an extraction voltage of 10 kV. Increased PG potential leads to more e^- that can overcome the potential barrier, decreasing electron density in the vicinity of the aperture, and in turn, a decrease of the co-extracted electron current. A strong reduction in the co-extracted

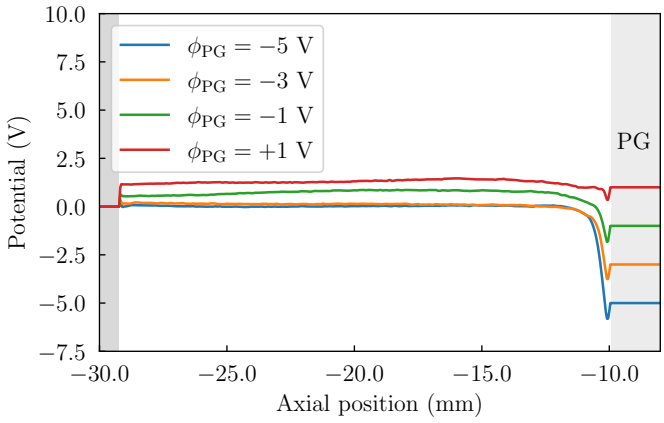

Figure 6.3: *Potential profiles along the axial direction for varying PG bias, taken 2 mm from the bottom of the simulation domain.* U_{ext}*=10 kV,* U_{acc}*=55 kV.*

electron current density is observed, see Table 6.1. This reduction exceeds a factor of 4, which follows the trend shown in experimental investigations [105].

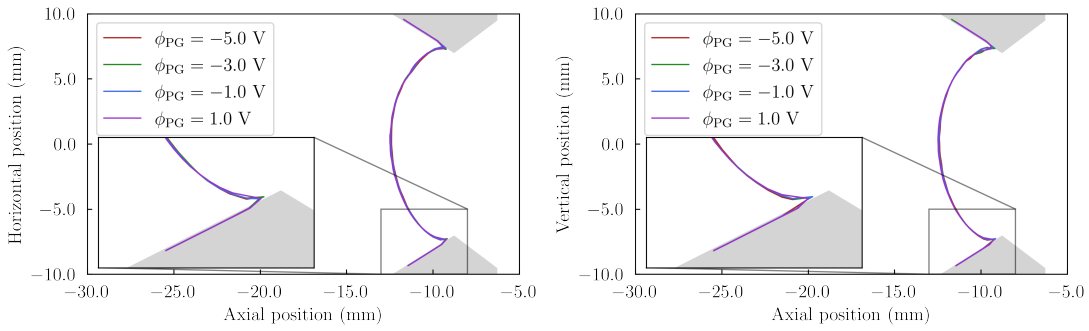

(a) **(b)**

Figure 6.4: *Meniscus shape for varying PG bias in the (a) horizontal and (b) vertical plane.* U_{ext}*=10 kV,* U_{acc}*=55 kV.*

Table 6.1: *Extracted currents for varying PG bias.* U_{ext}*=10 kV,* U_{acc}*=55 kV.*

ϕ_{PG}	$j_{H^-_{VP}}$	$j_{H^-_{SP}}$	j_e	j_{ex}	j_e/j_{ex}	VC
V	A/m^2	A/m^2	A/m^2	A/m^2	A/m^2	V
−5 V	88	57	108	146	0.74	0.8
−3 V	89	57	79	147	0.54	0.8
−1 V	91	55	68	148	0.46	0.8
+1 V	93	56	23	151	0.15	0.7

Figure 6.5 depicts the two-dimensional density distribution of H^-_{SP} ions in the horizontal plane, showing the influence of different PG biases. The greatest H^-_{SP} ion density is achieved for a PG bias of -5 V. Under this specific bias condition, the H^-_{SP} ion concentration reaches its peak value

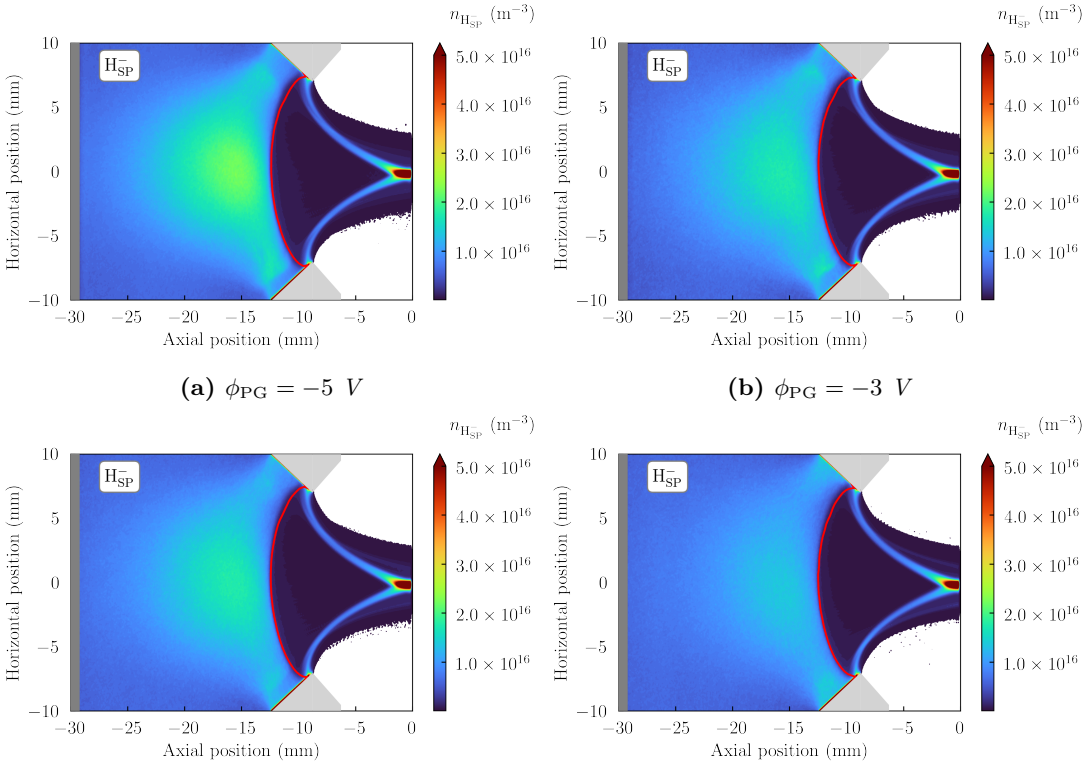

(a) $\phi_{PG} = -5\ V$ **(b)** $\phi_{PG} = -3\ V$

(c) $\phi_{PG} = -1\ V$ **(d)** $\phi_{PG} = +1\ V$

Figure 6.5: *H_{SP}^- ion density for varying PG biases. U_{ext}=10 kV, U_{acc}=55 kV.*

in front of the meniscus. However, since the trajectories of the ions are predominantly towards the bulk plasma, away from the meniscus, the higher population of H_{SP}^- ions in the system is not reflected in a higher extracted current density of H_{SP}^-, as shown in Table 6.1. Additionally, the extracted H_{VP}^- ion current density increased from 88 Am^{-2} for $\phi_{PG} = -5$ V to 93 Am^{-2} for $\phi_{PG} = +1$ V.

To bias the PG positively with respect to the plasma without increasing the plasma potential, the number of injected negative charges via the flux-injection scheme was increased. This was done by increasing the influx of electrons until the bump of the electrostatic potential on the upstream side of the simulation domain was removed with a positive PG bias of +1 V. This allows for a higher electron current to be drawn by the PG. Figure 6.6 shows the potential for the two simulations with positive PG bias, with and without adjustment of the influx of electrons. When the number of electrons is adjusted, the influx of negative species is higher than the influx of positive species ($\Gamma_- > \Gamma_+$) so that the potential in the plasma is reduced.

Table 6.2 shows the extracted current densities for the standard injection case where $\Gamma_- = \Gamma_+$ and increased electron injection case where $\Gamma_- > \Gamma_+$. Although more electrons are injected

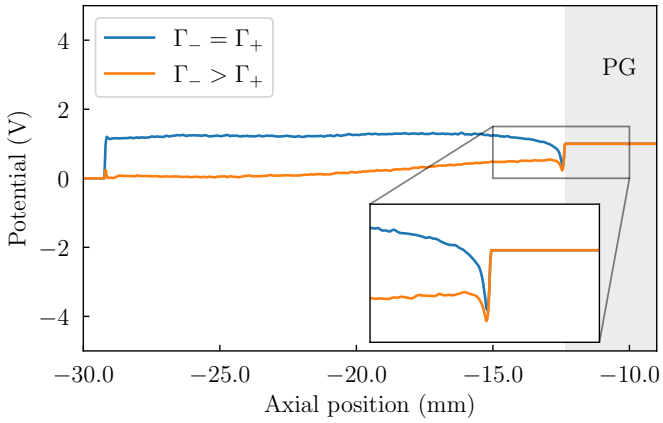

Figure 6.6: *Potential along the axial direction, 2 mm from the bottom, using flux-injection with $\Gamma_- = \Gamma_+$ (standard case) and increased electron injection case with $\Gamma_- > \Gamma_+$. The bias of the PG is +1 V w.r.t the plasma.*

into the simulation domain, this is not reflected in a higher amount of co-extracted electrons. Instead, the electrons are collected by the PG, since an electron-attracting sheath is formed, and thus the co-extracted electron current density is 12.6 Am^{-2} in the $\Gamma_- > \Gamma_+$ case, compared to 23.2 Am^{-2} in the $\Gamma_- = \Gamma_+$ case. The VC in the case with $\Gamma_- > \Gamma_+$ is 0.7 V towards the PG, which is 0.3 V less than in the $\Gamma_- = \Gamma_+$ case. This represents the first steps towards simulations of a PG bias above floating potential, showing that such simulations are possible with 3D-PIC modeling.

Table 6.2: *Extracted currents for the standard injection case where $\Gamma_- = \Gamma_+$ and increased electron injection case where $\Gamma_- > \Gamma_+$. The bias of the PG is +1 V w.r.t the plasma.*

	$j_{H^-_{VP}}$	$j_{H^-_{SP}}$	j_e	j_{ex}	j_e/j_{ex}	VC
	A/m^2	A/m^2	A/m^2	A/m^2		V
$\Gamma_- = \Gamma_+$	93	56	23.2	151.1	0.2	0.7
$\Gamma_- > \Gamma_+$	99	55	12.6	155.0	0.1	1.0

6.2 Influence of an electron fence on co-extraction of electrons and negative ion production

Simulations were conducted to study the interaction of an Electron Fence (EF) with the charged particles in the extraction region. The geometry of the EF used in the simulations is based on the EF used in NIFS [114]. The geometries of the IPP PG and NIFS PG are shown in Figure 6.7. The PG geometry used in NIFS [199] is thinner and has a larger angle of the conical surface compared to the PG used in ELISE [110], here referred to as the IPP PG. Since

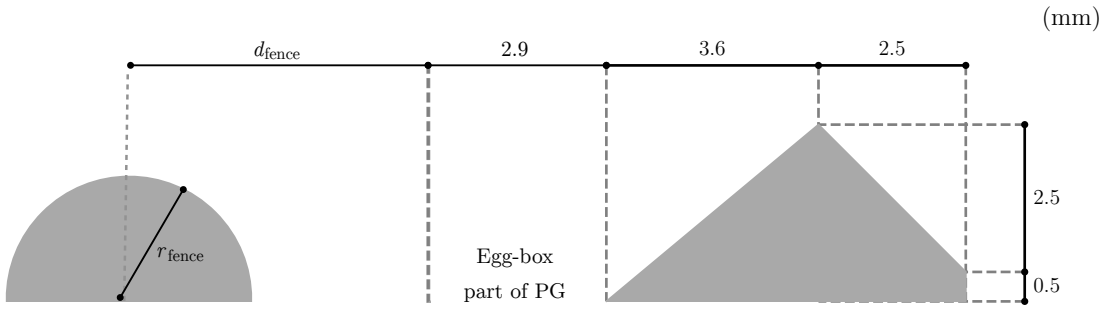

(a) *IPP PG fence configuration.*

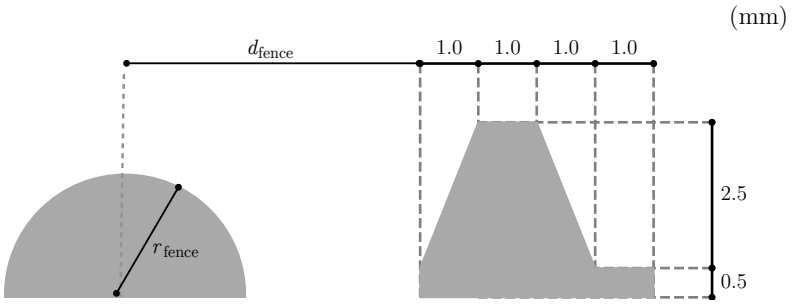

(b) *NIFS PG fence configuration.*

Figure 6.7: *Schematic representation of the (a) IPP PG geometry and (b) NIFS PG geometry, including the positioning of the EF in each case.*

the PG geometry in NIFS differs from the one used at IPP, simulations with the fence were done for both PG geometries. Notably, the egg-box shape of the IPP PG, see Figure 2.4, limits the minimum distance that can be maintained between the PG and the EF. The distance between both PGs and the EGs was kept equal (6 mm from the downstream side of the PG to the downstream side of the EG). The impact of the EF was studied in two orientations, horizontal (corresponding to EF rods placed between each aperture row) and vertical (corresponding to EF rods placed between each aperture column). When the EF is oriented in the horizontal direction, the trajectories along the $\mathbf{B}_{\text{DF}}$ are interrupted. However, when the EF is oriented in the vertical direction, it interrupts the electron trajectories along the $\mathbf{B}_{\text{FF}}$. This means that the EF can reduce the co-extraction of electrons while being oriented in both directions. The impact on both the surface production of NIs and co-extracted electron current density was studied under a variation of the EF bias.

6.2.1 Impact on the co-extraction of electrons

Simulations in low-density and reduced extraction voltage were performed to study the effect of the EF on the co-extraction of electrons for a large number of cases. The simulations were done using the flux-injection method, but with a constant influx of electrons, H^+ ions and H^- ions

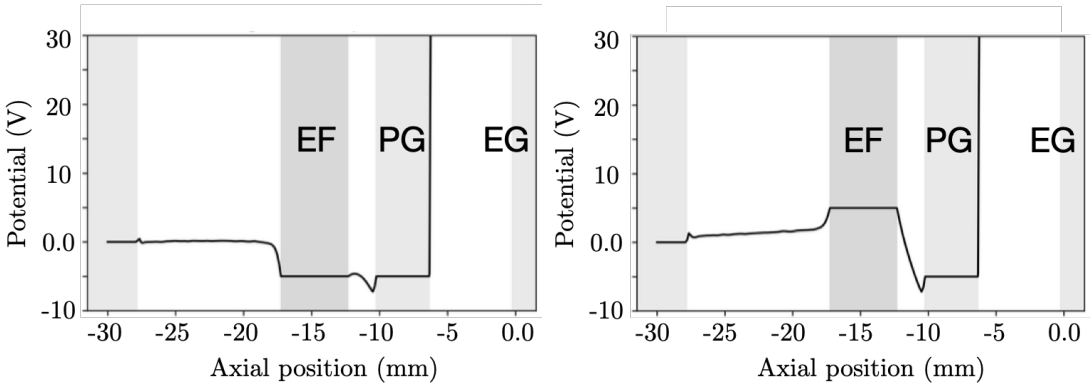

(a) $\phi_{\text{Fence}} = -5$ *V.* **(b)** $\phi_{\text{Fence}} = +5$ *V.*

Figure 6.8: *Potential profile 2 mm from the bottom along the axial direction for (a)* $\phi_{\text{Fence}} = -5$ *V and (b)* $\phi_{\text{Fence}} = +5$ *V using the NIFS PG geometry. The fence geometry is* $d_{\text{fence}} = 5$ *mm,* $r_{\text{fence}} = 2.5$ *mm in both cases.*

with $\phi_{\text{pl}} = 0$ V. The bias of the EF, ϕ_{Fence}, was varied between -5 V to +5 V, with respect to the plasma potential while the bias of the PG was kept close floating potential ($\phi_{\text{PG}} = -5$ V). The cases with $\phi_{\text{Fence}} = -5$ V and $\phi_{\text{Fence}} = 5$ V are shown in Figure 6.8. For the $\phi_{\text{Fence}} = -5$ V case, the plasma potential is not disturbed by the EF, which has the same bias as the PG and an electron-repelling sheath is formed in front of the EF. For the $\phi_{\text{Fence}} = 5$ V case, the plasma potential increases slightly due to the accumulation of electrons on the EF and an electron-attracting sheath is formed in front of the EF. Since the EF has a relatively small area compared to the PG, biasing it positively with respect to the plasma can be done without a large impact on the plasma potential [78]. This means that the EF can remain electron-attracting with a higher positive bias than the PG.

Figure 6.9 (a) shows the co-extracted electron current density for the NIFS and IPP fence configurations with a $r_{\text{fence}} = 2.5$ mm as a function of ϕ_{Fence}. For the NIFS fence configuration, simulations with the EF in both the horizontal and vertical directions are shown. For comparison, the co-extracted electron current density for the IPP configuration without an EF is shown with a black dashed line. The more electrons that are collected by the EF, the fewer are co-extracted. In all cases, the co-extracted electron current density decreases with ϕ_{Fence} up until ≈ 0 V. For $\phi_{\text{Fence}} > 0$ V, every electron approaching the EF is collected, and therefore there is no further reduction of the co-extracted electron current density.

Figure 6.9 (b) shows the co-extracted electron current density for the NIFS configuration as a function of the fence radius, with the bias 0 V. The co-extracted electron current density decreases with the radius of the fence, both in the configuration with the fence in horizontal and vertical orientation. However, the vertical fence is more efficient for a radius of 2 mm or

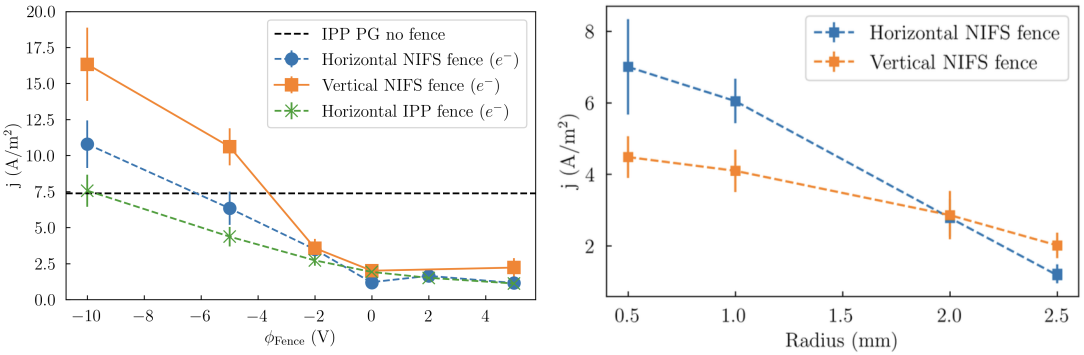

(a) *Distance from PG: 5 mm, fence radius: 2.5 mm.* **(b)** *Distance from PG: 5 mm,* $\phi_{\text{Fence}} = 0$ *V.*

Figure 6.9: *Co-extracted electron current density (a) as a function of* ϕ_{Fence} *and (b) as a function of the fence radius.*

smaller since it effectively stops the horizontal transport of electrons along the $\mathbf{B}_{\text{FF}}$. For a radius of 2 mm or larger, the electrons following the $\mathbf{B}_{\text{DF}}$ field lines are also collected, which reduces the co-extracted current to below that of the vertical fence.

6.2.2 Impact on negative ion production

One of the concerns of installing an EF is that it could reduce the extraction of NIs. In particular, a large EF may shield a significant component of the PG and reduce the amount of H^-_{SP} ions produced on its surface by decreasing the number of H atoms and H^+ ions reaching te PG. Since the electrons travel many orbits before extraction, placing the EF on every second row may have a similar impact as placing it on every row. Placing it on every second row would shield a smaller area of the PG. For an initial estimation of the impact, a ray tracing simulation using IBSimu was performed by tracking H atoms emitted from the driver of a simplified single-driver ion source geometry with the IPP PG configuration and driver radius 120 mm. The BP was not included, which means that the whole upstream side of the PG was facing the plasma. The trajectories of these atoms follow straight lines in a random direction from an emission plane bordering the driver. The trajectories are depicted in Figure 6.10 in the axial-horizontal and axial-vertical plane, along with EF, PG, EG and GG. It can be seen that the EF shields the PG from a fraction of the trajectories of H atoms in red.

Figure 6.11 shows the shielding effect of the EF as a function of its radius. Two configurations are analyzed: with an EF between every aperture row and a fence on alternate rows. For an EF with a radius of $r_{\text{fence}} = 2.5$ mm at a distance of $d_{\text{fence}} = 5$ mm from the PG, the amount of H atoms reaching the PG is reduced by 28%. For the configuration with an EF on every second row, the amount of H atoms is reduced by 14%. These percentages are not

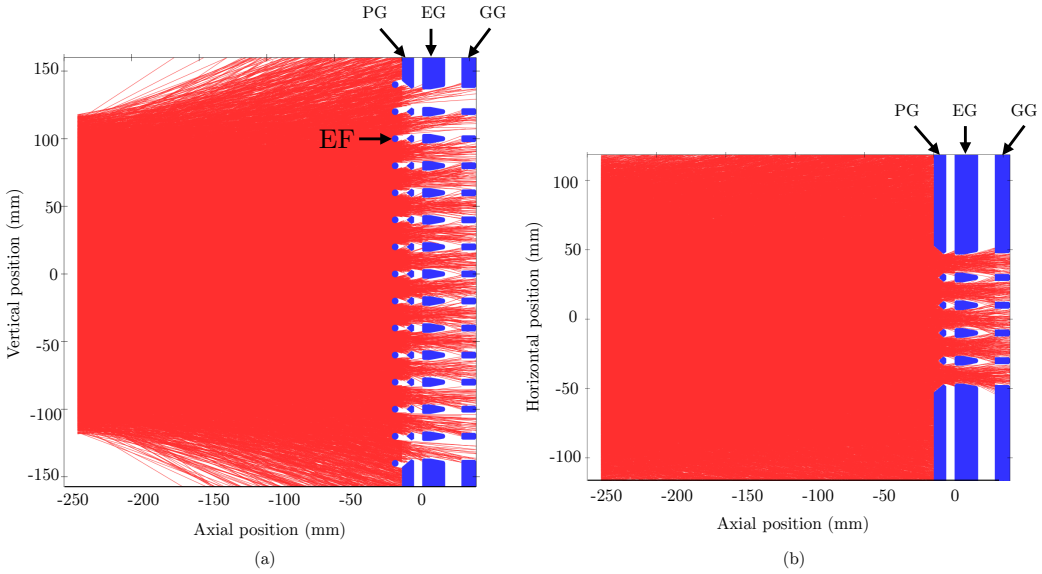

Figure 6.10: *(a) Trajectories of* H *atoms in the presence of an EF, in the (a) axial-vertical plane and (b) axial-horizontal plane.*

necessarily proportional to the amount of extracted NIs for multiple reasons. Firstly, NIs are produced by both atomic hydrogen and PIs, the latter would react to the disturbance in the electrostatic potential that the EF causes in a more complicated fashion. Secondly, the degree of caesiation may be altered by the EF, leading to a change in NI production. Thirdly, the EF itself would be caesiated and thus its surface would contribute to the emission area of H^-_{SP}. These effects, however, would require a more sophisticated model to study and are left out of the analysis.

In conclusion, it has been shown that an EF can significantly reduce the amount of co-extracted electrons, but with the cost that the production of NIs will likely decrease. Experimental investigations are therefore needed.

6.3 Conclusions

Biasing of the PG was performed in 3D-PIC simulations using flux-injection for the first time. Both negative biases from -5 V, close to floating potential, to positive biases up to +1 V with respect to the plasma were performed. A similar tendency as observed in experiments was obtained, namely a substantial reduction in the co-extracted electron current.

Experiments using PG biasing in ONIX have shown a reduction in the co-extracted electron current density by an approximate factor of 4. The introduction of the EF has yielded significant

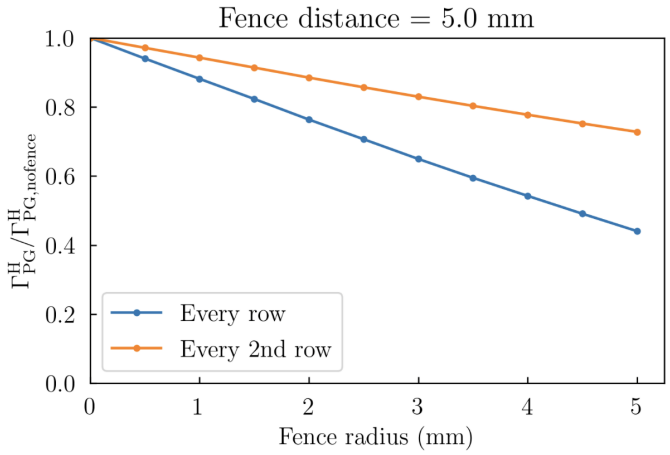

Figure 6.11: *The shielding of the EF of* H *atoms from the driver as a function of the radius of the fence. The graph contrasts two scenarios: a configuration where the EF is present on every aperture row versus one with the EF on every second aperture row. Distance from PG: 5 mm.*

reductions. The EF effectively reduces the co-extracted current density across both the IPP PG and NIFS PG geometries. The combined effect of both PG biasing and the EF remains to be explored. An EF placed on every second row may reduce the co-extracted electron current density to a similar degree as an EF on every row, but shield the PG less from approaching H atoms. Simulations with an EF on alternate rows remain to be done. However, to do this, a two-aperture simulation would be needed.

CHAPTER 7

Coupling of 3D-PIC and ion optics simulations

The 3D-PIC computational domain used in ONIX is extended by coupling with the ion-optics code IBSimu, as described in Section 3.4. The method, presented in Figure 3.13, allows for self-consistently including the effects of space charge on the extracted NI beam at the EG plane. This chapter presents the validation of the coupling scheme and evaluation of beam optics for both H^-_{VP} and H^-_{SP} ions. Lastly, the *a posteriori* particle tracking method is used to show the statistical impact of particle parameters in the plasma on the particle parameters in the beam and the probability of extraction.

7.1 Evaluation of the coupling

As an initial BC, the vacuum solution of the Poisson equation at the interface between the two domains simulation domains was used. Since no space charge effect is included on the boundary, an unphysical discontinuity in the electric field appears on the boundary between the ONIX and IBSimu simulation domains (Plane B in Figure 3.13).

The further towards the meniscus from B, the less the vacuum potential has an impact on the beam at that location. To show the impact that the lack of space charge on the boundary has on the beam formation, particles were extracted from an ONIX simulation with vacuum boundary from 9 locations at axial positions between -7.5 mm and 0 mm. In addition, the solution for the electrostatic potential was extracted from each position. The particles, along with the potential plane are used as inputs for IBSimu simulations. Figure 7.1 shows the axial-

vertical beam profiles of the H^- ions for starting positions (a) -7.6 mm, (b) -3.6 mm, and (c) 0 mm. To evaluate the impact the starting position has on the beamlet formation, Figure 7.2 shows the particle energy at the EG plane as a function of the initial starting location. For a fully converged coupling of the two codes, there should not be a spatial dependence since both field solvers should give the same solution for the electric field. However, the further away from the EG plane the particles are started, the lower their energy is since the impact of the vacuum boundary decreases. For particles started at axial position -7.6 mm, the average energy is 7.25 keV at the EG plane, while for particles starting on the EG plane (where the potential is given by the vacuum solution), the average kinetic energy is 8.0 keV.

For the coupling process, -6 mm (Plane A) is chosen since it is sufficiently upstream such that the effect of the vacuum BC is negligible while still being outside the plasma. Particles were started from this boundary in IBSimu and tracked through the grid system. The non-vacuum potential, including the effect of space charge at the EG-plane $\phi_{x=0}^{\mathrm{non-vacuum}}$ was exported from IBSimu and used as an updated BC in ONIX. Subsequently, particles and the potential map were exported from ONIX to be used as BCs in IBSimu. This process was done iteratively until convergence of the potential boundary was reached, the coupling scheme is shown in Figure 3.13.

The resulting on-axis potentials for the coupled ONIX+IBSimu simulations, along with the vacuum potential and the ONIX and IBSimu simulations using the vacuum plane as a BC, are shown in Figure 7.3 (a). On the boundary plane, the ONIX potential with vacuum BC (in red) and the IBSimu potential with vacuum BC (in blue) are equal to the vacuum potential obtained without any space charge. Since there is no space charge effect included on the boundary, the gradient of the potential (the electric field) has an unphysical discontinuity on the boundary. To remove this discontinuity, the model must include the space charge from the NI beamlet on the boundary. This is obtained in the ONIX+IBSimu simulation (in green), where the electric field is continuous across the boundary. The contour lines in the horizontal plane, shown in 7.3 (b), illustrate the effect of space charge on the potential and demonstrate that 6 mm is sufficiently far upstream. The penetration and shape of the meniscus (corresponding to the 30 V contour) are virtually unchanged.

The on-axis potential at the EG surface changes by almost 1 kV when including the effect of space charge on the boundary instead of the vacuum solution. In Figure 7.4 (a) the difference between the vacuum potential and the potential after one iteration is shown, Figure 7.4 (b) shows the difference between the potential after two iterations. The additional iteration between the two models (ONIX and IBSimu) yields a change of only a few Volts, indicating that no

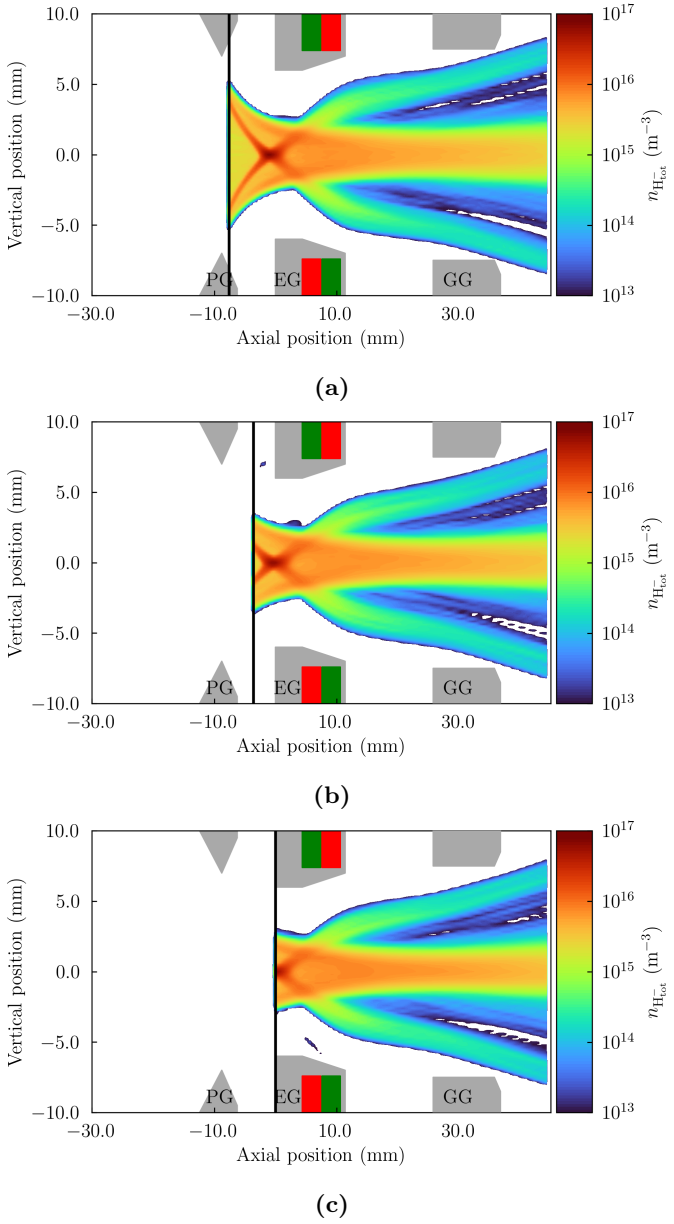

Figure 7.1: *Vertical cross-section of the H^- density in the beamlet formation and acceleration regions throughout the ELISE grid system for H^- ions injected on axial position (a) -7.6 mm, (b) -3.6 mm, and (c) 0 mm. The embedded deflection magnets are represented by the red/green boxes.*

additional iterations with an updated non-vacuum field are necessary.

The extended computational domain allows linking 3D-PIC simulated extraction scenarios to beamlet properties. A coupled ONIX-IBSimu simulation is simulated with $U_{\mathrm{ext}} = 10$ kV and an acceleration voltage $U_{\mathrm{acc}} = 55$ kV, close to the ELISE design operating potentials, and the same parameters as used for the standalone ONIX simulations. The particle parameters are

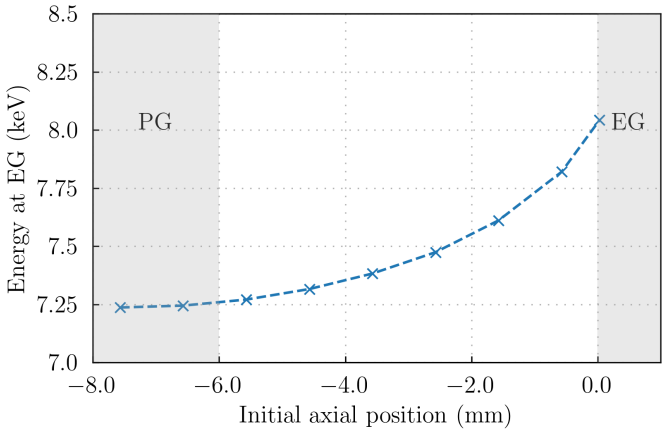

Figure 7.2: *Average particle kinetic energy at the EG plane as a function of the starting position for the initial ONIX simulation with a vacuum boundary.* U_{ext}*=10 kV,* U_{acc}*=55 kV.*

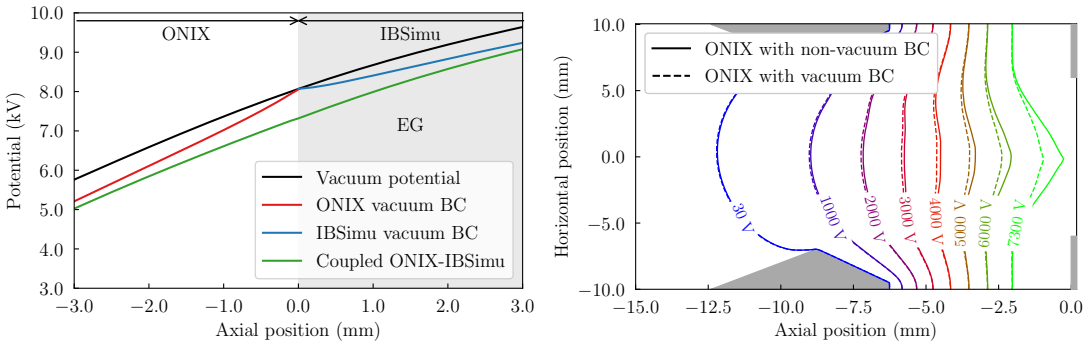

(a) **(b)**

Figure 7.3: *(a) On-axis electrostatic potential near the boundary between the ONIX/IBSimu coupling plane and (b) electrostatic potential in a horizontal cross-section of the ONIX domain for the non-vacuum and vacuum BC. The 30 V contour corresponds to the meniscus.* U_{ext}*=10 kV,* U_{acc}*=55 kV.*

given by the LD/HT parameters in Table 3.1. In addition, a standalone IBSimu simulation with matched extracted current density is performed.

Figure 7.5 shows a comparison between the coupled ONIX+IBSimu simulation and a standalone IBSimu simulation, illustrating the vertical distribution of NI density across the simulation domains. The PG, EG, and GG are marked in gray, while the deflection magnets are represented by green and red boxes. In the coupled ONIX+IBSimu simulation (Figure 7.5 (a)), a distinct beam halo is formed due to the extraction of H^-_{SP} ions. This halo effect is absent in the standalone IBSimu simulation (Figure 7.5 (b)), which results in a more uniform and focused ion beam distribution since no H^-_{SP} ions are simulated.

To show the impact that the extraction voltage plays on the meniscus formation, and by ex-

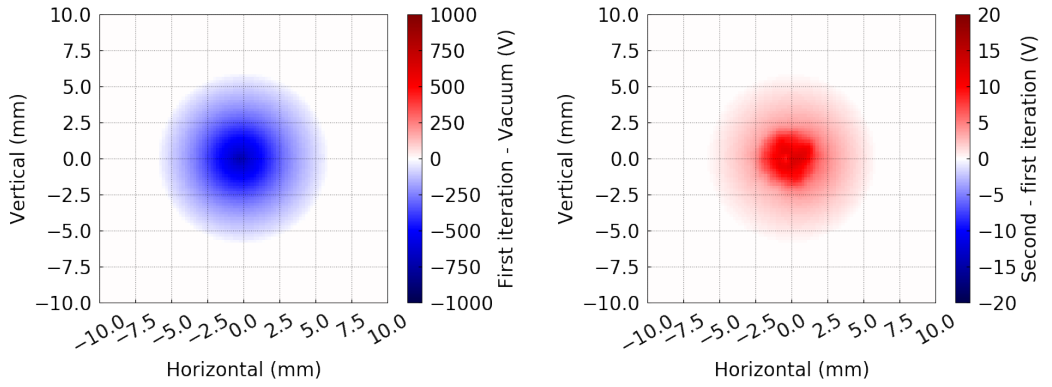

(a) **(b)**

Figure 7.4: *Difference in electrostatic potential between the vacuum potential after (a) the first and (b) the second iteration.*

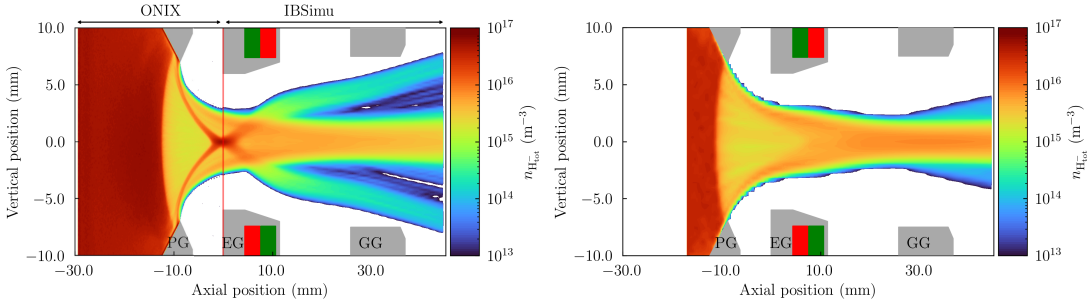

(a) *ONIX+IBSimu* **(b)** *Standalone IBSimu.*

Figure 7.5: *Vertical cross-section of the H^- density in the beamlet formation and acceleration regions throughout the ELISE grid system for (a) the coupled ONIX+IBSimu simulation and (b) the standalone IBSimu simulation. The embedded deflection magnets are represented by the red/green boxes in (a) and (b).*

tension, the beamlet formation of H^- ions, an additional coupled ONIX+IBSimu simulation was done with $U_{\text{ext}} = 5$ kV and $U_{\text{acc}} = 27.5$ kV, so that the ratio of $U_{\text{acc}}/U_{\text{ext}}$ is equal in both simulations. Figure 7.6 shows a vertical slice of the NI density throughout both simulation domains, with H^-_{VP} and H^-_{SP} ions separated. The PG, EG, and GG are indicated in gray and the deflection magnets are indicated with green/red boxes. Although the H^-_{VP} and H^-_{SP} overlap spatially in the extraction gap in the ONIX+IBSimu simulation, the H^-_{SP} ions have a different angular distribution than the H^-_{VP}, which will be shown later. Many of the extracted H^-_{SP} ions are directly extracted near the knife edge of the PG without entering the plasma, as illustrated by trajectory (a) in Figure 2.15. The directly extracted H^-_{SP} ions form a beam halo that is spatially separated from the H^-_{VP} at the end of the grid system.

For H^-_{SP} ions, which are extracted through the edge of the meniscus, the meniscus curvature in

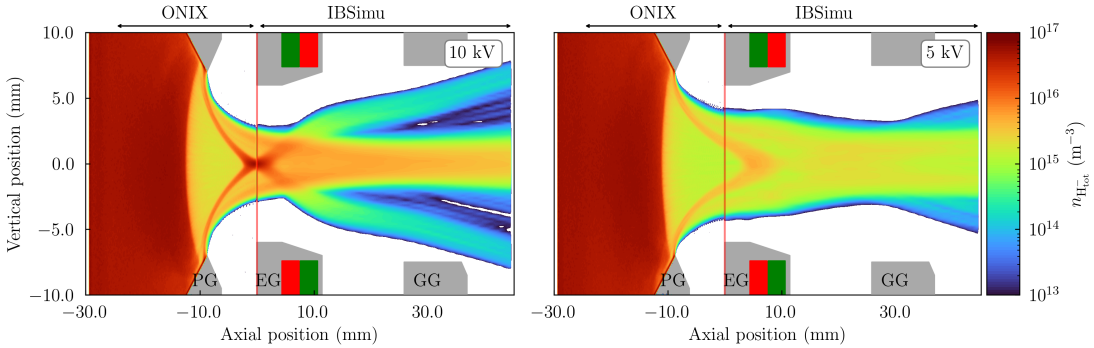

(a) $U_{ext} = 10$ *kV and an* $U_{acc} = 55$ *kV.* **(b)** $U_{ext} = 5$ *kV and an* $U_{acc} = 27.5$ *kV.*

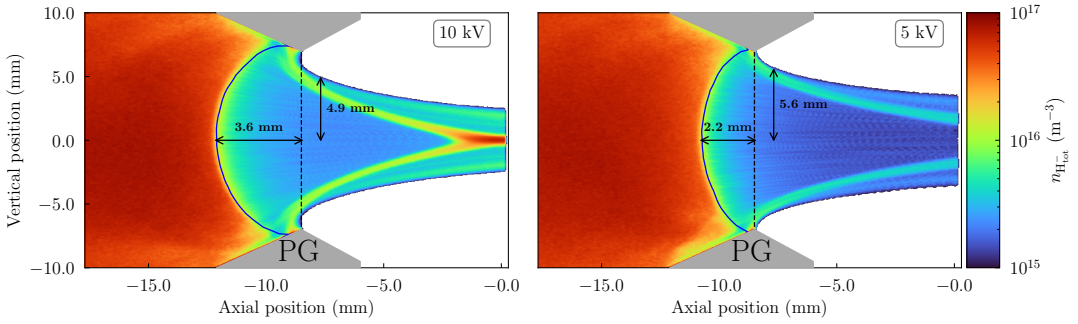

(c) $U_{ext} = 10$ *kV and an* $U_{acc} = 55$ *kV.* **(d)** $U_{ext} = 5$ *kV and an* $U_{acc} = 27.5$ *kV.*

Figure 7.6: *Vertical cross-section of the* H^- *density in the beamlet formation and acceleration regions throughout the ELISE grid system for (a) and (c):* $U_{ext} = 10$ *kV and (b) and (d):* $U_{ext} = 5$ *kV. Subfigures (a) and (b) show the coupled simulation domains, and (c) and (d) show the meniscus region of the ONIX domain. The deflection magnets are represented by the red/green boxes.*

the aperture center is less important than for H^-_{VP} ions, which are mostly extracted through the center of the meniscus. The final beam properties depend on the shape of the meniscus, where the meniscus particles are extracted, and the particle properties at this location.

Figure 7.7 shows particle trajectories of H^-_{VP} and H^-_{SP} tracked with the *a posteriori* model, colored by the kinetic energy of each test particle during its flight path. To match the parameters in the ONIX+IBSimu simulation (with $U_{ext} = 10$ kV), the H^-_{VP} are injected with a temperature of 0.8 eV and H^-_{SP} with a temperature of 0.6 eV. The trajectories of the H^-_{SP} and H^-_{VP} ions match well with the particle density from the coupled ONIX+IBSimu simulation shown in Figure 7.5 (a). The energy of the H^-_{SP} is higher than that of the H^-_{VP} in the plasma due to the initial acceleration by the plasma sheath towards the PG. In addition to NIs, electrons can also be tracked using the *a posteriori* model.

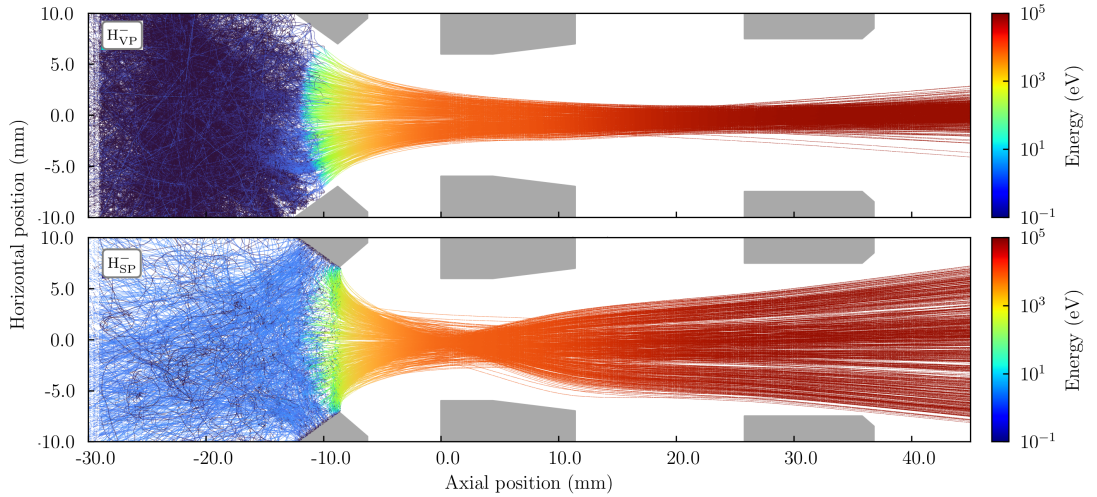

Figure 7.7: *Trajectories of H^-_{VP} and H^-_{SP} and tracked a posteriori, colored by the kinetic energy. U_{ext}=10 kV, U_{acc}=55 kV.*

7.2 Code-to-code benchmark

In addition to the coupled ONIX+IBSimu simulation, an additional coupling was done between ONIX and ONAC (described in Chapter 3, Section 3.4) to verify that the coupling scheme is code-independent and works well for both coupling 3D-PIC with ion optics codes and other 3D-PIC codes. The particles from ONIX were exported and transferred to ONAC in the same fashion and with the same properties as in the ONIX+IBSimu coupling with $U_{ext} = 10$ kV and $U_{acc} = 55$ kV.

ONAC results presented here neglect the effect of collisions (such as stripping, double stripping etc.) on the beam transport, in order for the results to be comparable with the IBSimu simulation. Figure 7.8 shows the angular distribution of H^-_{SP} at axial position 45 mm for ONIX-IBSimu coupling and ONIX-ONAC coupling and the *a posteriori* simulation. The angular distribution is similar for all three cases, both for H^-_{SP} ions and H^-_{VP} ions (not shown). The H^-_{SP} ions do not have a Gaussian distribution, as already indicated by Figure 7.6. This can be seen in Figure 7.8 by observing the highly divergent peaks at the edges of the distributions. A separation between the two beam components, beam core and beam halo, as in [200], is observed. Since both coupled simulations produce similar beam profiles, it is concluded that the coupling method works well both for coupling 3D-PIC codes and coupling 3D-PIC with ion optics codes such as IBSimu. The angular distribution of the *a posteriori* run also agrees well with the angular distribution of the coupled ONIX-IBSimu and ONIX-ONAC runs, showing that equivalent results can be derived using the *a posteriori* approach.

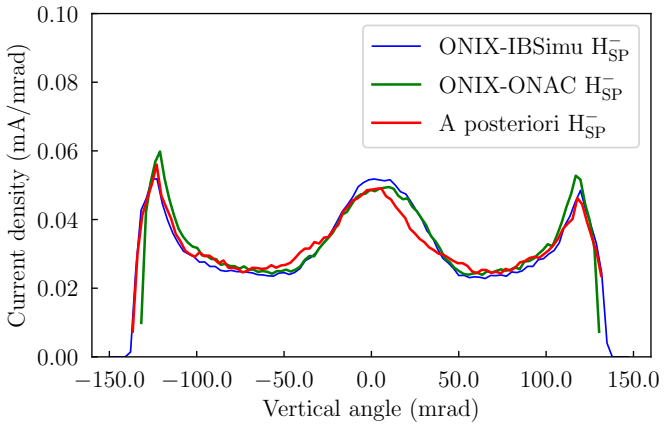

Figure 7.8: *Vertical angular distribution at axial position 45 mm for the coupled ONIX-IBSimu H^-_{SP} ions, coupled ONIX-ONAC H^-_{SP} ions, and H^-_{SP} ions from the a posteriori analysis. U_{ext}=10 kV, U_{acc}=55 kV.*

7.3 Extraction probability and current density profiles

The NIs produced in the ion source (both via VP and SP) are either lost by collision with some surface, lost via destructive collision, or extracted. For a given production rate of H^-_{SP} and H^-_{VP} ions, the extraction probability $P_{extraction}$ is what determines the total extracted current density of H^- ions. Here, $P_{extraction}$ is studied for NIs injected in the ONIX simulation domain. A baseline investigation was conducted using the *a posteriori* analysis to study the extraction probability and the resulting current density profile of the NIs. The potential map from the U_{ext}=10 kV, U_{acc}=55 kV case is used in this section for the analysis since it most closely corresponds to the ITER NBI extraction potential. Although the simulations are run at ITER-relevant voltages, the results are not in the perveance optimum since j_{ex} is too low, and thus the divergence is far above the 7 mrad required for ITER. At higher j_{ex}, the beam halo fraction and divergence would be significantly reduced.

Approximately 95% of the extracted H^-_{SP} ions are extracted in the aperture where they are generated, as opposed to moving one or more aperture rows or columns before extraction. Furthermore, the average flight distance from injection to crossing the meniscus was 4 mm. The extraction probability of the H^-_{VP} depends on the injection location of the particles: moving the injection location further upstream increases the fraction extracted by neighboring apertures. The H^-_{VP} ions were injected uniformly on the upstream horizontal-vertical boundary, 71% of the particles were extracted through the same aperture as the domain in which they were injected, and their average flight distance until crossing the meniscus was 26 mm.

The initial location, energy and depth of the VC have a large impact on the extraction prob-

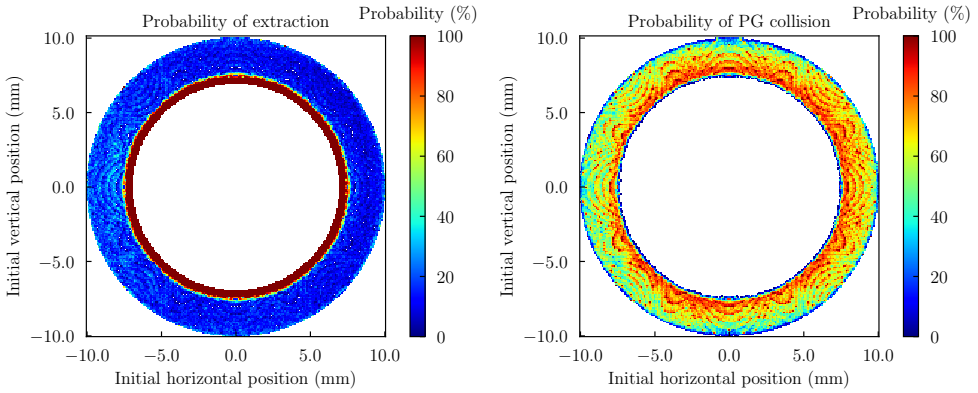

(a) **(b)**

Figure 7.9: *Probability of (a) extraction and (b) hitting the PG as a function of the starting position of H^-_{SP} on the PG.*

ability of the H^-_{SP} ions. The *a posteriori* analysis shows that although the overall extraction probability is $\sim 20\%$, nearly all H^-_{SP} ions are directly extracted when starting close to the PG knife edge, where no VC is present. This is shown in Figure 7.9, which shows the extraction probability and probability for collision with the PG for H^-_{SP} ions depending on their starting position on the PG. The H^-_{SP} ions that start further from the PG knife edge need to overcome the VC, resulting in a lower extraction probability at lower energies. For an initial energy below approximately 1 eV, the majority of the H^-_{SP} ions return back to the PG since the kinetic energy is too low to traverse the VC, which is ≈ 1 V.

The effect of the VC on the extraction probability can be seen in Figure 7.10, which shows the probabilities for various outcomes for test particles of H^-_{SP} ions as a function of their initial energy E_0. The depth of the VC is ~ 1 V, thus H^-_{SP} ions with initial energy lower than ~ 1 eV are immediately reflected back towards the PG. The overall extraction probability of H^-_{SP} ions is 18% for E_0 close to 0 eV (see the green line in Figure 7.10). However, this is predominantly due to the direct extraction of H^-_{SP}, which do not need to overcome the VC to be extracted. The blue line in Figure 7.10 represents H^-_{SP} ions produced at a radial position $R_0 \geq 8$ mm, which is 1 mm away from the radial position of the tip of the PG. These ions are not directly extracted and therefore only 2% of them are extracted with E_0 close to 0 eV. The depth of the VC is not uniform over the PG, so the probability of extraction depends both on the initial location and initial energy of the H^-_{SP} ions. In [201], a tendency of reduced extraction probability for higher H^-_{SP} energy was shown. However, the effects of the VC and electric field in the plasma were neglected.

H^-_{SP} which enter the plasma are accelerated by the plasma sheath ($\approx 2.5T_e = 5$ V) [75] are

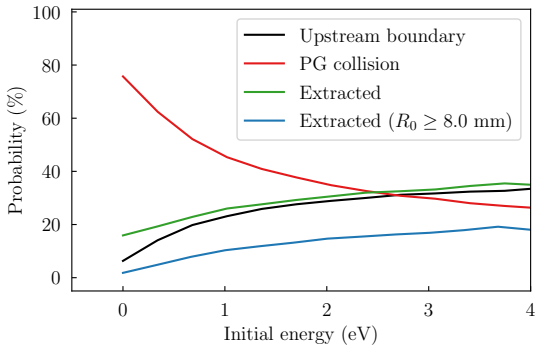

Figure 7.10: *Probability of various outcomes for H^-_{SP} ions as a function of their starting energy. U_{ext}=10 kV, U_{acc}=55 kV.*

therefore rarely extracted, instead they exit the simulation domain on the upstream boundary. 5% of the extracted H^-_{SP} are extracted after passing through the periodic boundary. This is likely a lower bound, since a fraction of the H^-_{SP} ions that are lost on the bulk plasma side of the simulation domain may in reality return to the region near the extraction apertures [201].

Figure 7.11 (a) shows a side and front view of the meniscus colored by the current density of H^-_{SP} and H^-_{VP} ions penetrating the meniscus, and a standalone IBSimu simulation. Since the meniscus penetrates past the knife edge of the PG, the axial position of the meniscus varies in the horizontal-vertical plane. The current densities in the side view are high since the plots are line-integrated. For both ONIX and standalone IBSimu, the meniscus penetrates 3.6 mm into the plasma from the PG knife edge. There is a difference in the distribution of current through the meniscus for the three cases. In the case of the full 3D-PIC simulation using ONIX, the directly extracted H^-_{SP} ions can be seen in Figure 7.11 (a) as a ring of increased current density close to the PG knife edge. In the case of H^-_{VP} ions, the effect of the plasma sheath towards the PG can be seen, i.e. the H^-_{VP} ions do not reach the PG. Since the sheath is not included in the IBSimu standalone run, the NIs are able to cross the meniscus at larger radii close to the PG.

Figure 7.11 (b) and 7.11 (c) show the average current density as a function of the horizontal/vertical position on the meniscus for H^-_{SP} and H^-_{VP} ions, and the meniscus from the IBSimu standalone simulation. The averaged current density is calculated using the radius of the meniscus, which is 7.5 mm (0.5 mm wider than the radius of the PG aperture). Due to the sheath formation toward the PG, the H^-_{VP} current density decreases near the edge of the meniscus. The IBSimu standalone simulations can not take the sheath formation into account self-consistently, and thus the current density over the meniscus is uniform. For the H^-_{SP} ions, a clear peak can be observed for horizontal position ±7 mm, which corresponds to the directly extracted parti-

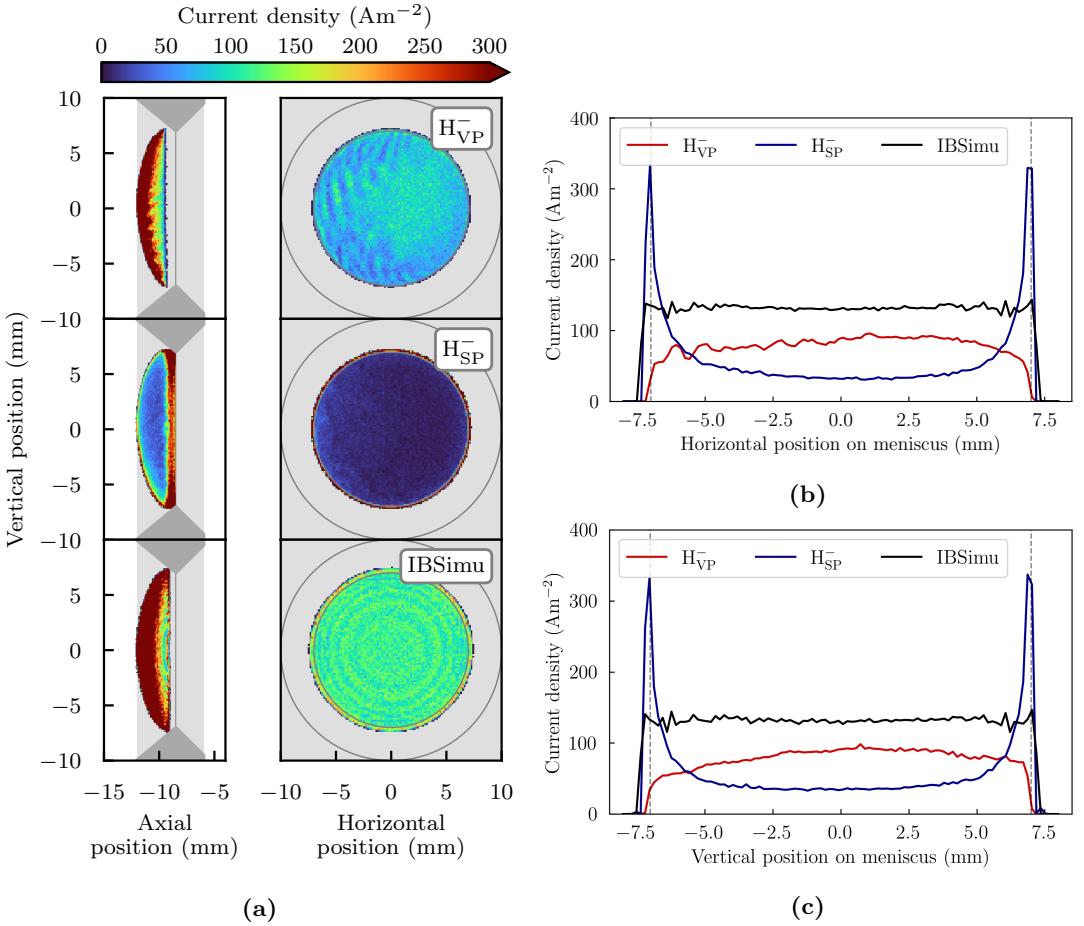

Figure 7.11: *(a) Histogram of the locations where the (top) H^-_{VP}, (center) H^-_{SP} and (bottom) IBSimu particles cross the meniscus. Left: Axial-vertical plane and right: horizontal-vertical plane. The average current density of a posteriori H^-_{VP} and H^-_{SP} ions and IBSimu ions crossing the meniscus along the (b) horizontal and (c) vertical position on the meniscus. The vertical dashed lines correspond to the edges of the PG aperture. U_{ext}=10 kV, U_{acc}=55 kV.*

cles close to the aperture edge, the majority of H^-_{SP} is extracted from this region. The current density distribution over the meniscus influences the properties of the accelerated beamlet, as will be shown in Section 7.4.

7.4 Beamlet properties

Figure 7.12 shows the horizontal divergence, calculated with Equation (2.34), throughout the grid system. H^-_{VP} and H^-_{SP} ions are shown for the two coupled ONIX-IBSimu simulations, along with standalone IBSimu simulations with the matched extracted current density. The value and slope of the divergence match well on the boundary between the coupled simulation domains. Here the final accelerated velocity is used for $v_{\parallel}$, so that the divergence evolution is

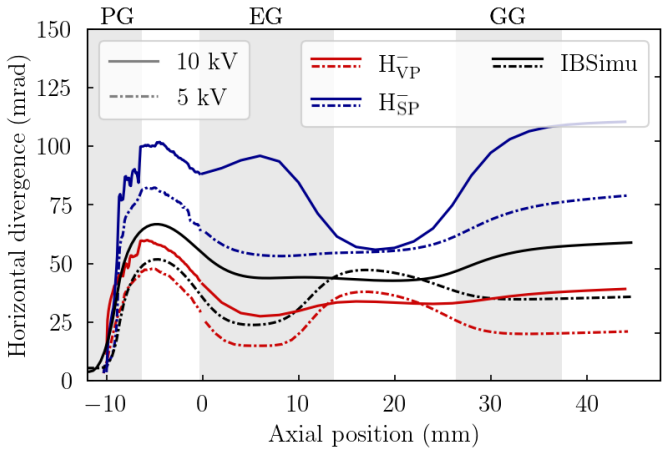

Figure 7.12: *Horizontal beam divergence for H^-_{VP}, H^-_{SP} and IBSimu standalone particles as a function of the axial position for $U_{ext} = 5$ kV and $U_{ext} = 10$ kV.*

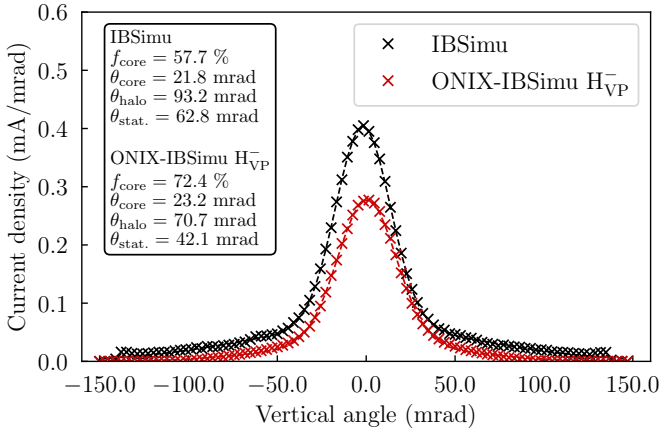

Figure 7.13: *Vertical angular distribution of the coupled ONIX-IBSimu H^-_{VP} ions and a standalone IBSimu simulation. The beam profiles for the H^-_{VP} and IBSimu particles are fitted with a double Gaussian (dashed lines). U_{ext}=10 kV, U_{acc}=55 kV.*

not obscured by the increase in axial velocity due to the acceleration through the grid system. For more insight into the shape of the angular distribution, a double Gaussian is fitted: a core Gaussian with a smaller divergence θ_{core}, and a halo Gaussian with a larger divergence θ_{halo}. Adding the two components geometrically, weighted by their respective fractions f_{core} and f_{halo}, recovers the single Gaussian divergence $\theta_{stat.}$. The current density translates to a normalized perveance of 0.10, far below the design value of approximately 0.26 for the divergence optimum of this grid system [201].

Upstream of the meniscus, in the plasma region, the ONIX beamlet is more divergent than the standalone IBSimu beamlet, which simply has the $\sqrt{T_\perp/U_{tot}}$ contribution to the divergence. The H^-_{SP} ions are more divergent than the H^-_{VP} ions, which are qualitatively similar to a

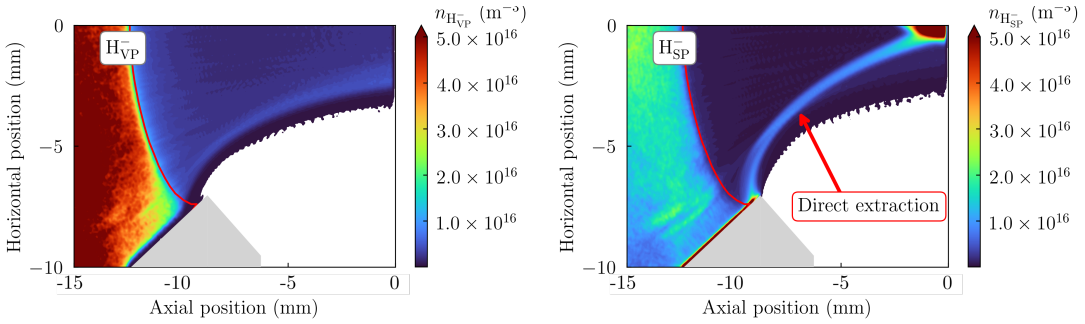

Figure 7.14: *Particle density of (a) H^-_{VP} and (b) H^-_{SP} ions. The meniscus is marked with a red line and the directly extracted H^-_{SP} ions are marked with a red arrow. U_{ext}=10 kV, U_{acc}=55 kV.*

standalone IBSimu simulation. The divergence in the ONIX simulations follows from a self-consistent evaluation of the plasma region, whereas in IBSimu the divergence depends on the user-selected perpendicular temperature $T_\perp$.

The divergence determination (Equation 2.34) assumes that the angular distribution is a single Gaussian; large particle angles heavily bias the divergence value. Figure 7.13 shows the angular distribution and the divergence values at the end of the grid system at an extraction potential of 10 kV for the volume produced ONIX particles simulated with ONIX+IBSimu, and for the standalone IBSimu simulation. The ONIX+IBSimu H^-_{VP} and standalone IBSimu angular distributions are not strictly single Gaussians; a double Gaussian is a better fit to the distribution. The H^-_{VP} ions have a similar core divergence θ_{core} in ONIX+IBSimu (23.2 mrad) and standalone IBSimu (21.8 mrad), which represents a fraction f_{core} of the distribution. The halo divergence θ_{halo} of H^-_{VP} ions is lower in the ONIX+IBSimu simulation (70.7 mrad) than in the IBSimu standalone simulation (93.2 mrad). The higher single Gaussian divergence $\theta_{stat.}$ for the IBSimu standalone calculation (62.8 mrad) compared to the ONIX+IBSimu H^-_{VP} simulation (41.1 mrad) is mostly caused by the different amount and width of the halo component since the core divergences are similar.

7.5 From meniscus to accelerated beamlet

The *a posteriori* analysis is used to link the particle properties at the meniscus to particle properties in the accelerated beamlet. The position where the particles cross the meniscus largely determines the particle angle with respect to the beamlet normal (final angle) at the end of the grid system, as shown in Figure 7.15 for (a) H^-_{VP} and (b) H^-_{SP}. As shown in Figure 7.11 (a), most H^-_{VP} ions are extracted through the center of the meniscus, which results in a lower

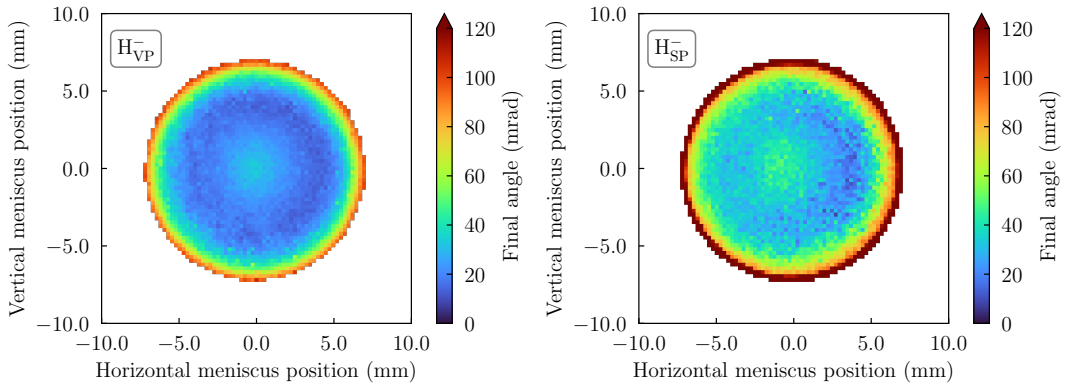

(a) **(b)**

Figure 7.15: *Final angle of the extracted (a) H^-_{VP} and (b) H^-_{SP} as a function of the position where they cross the meniscus in the horizontal-vertical plane. U_{ext}=10 kV, U_{acc}=55 kV.*

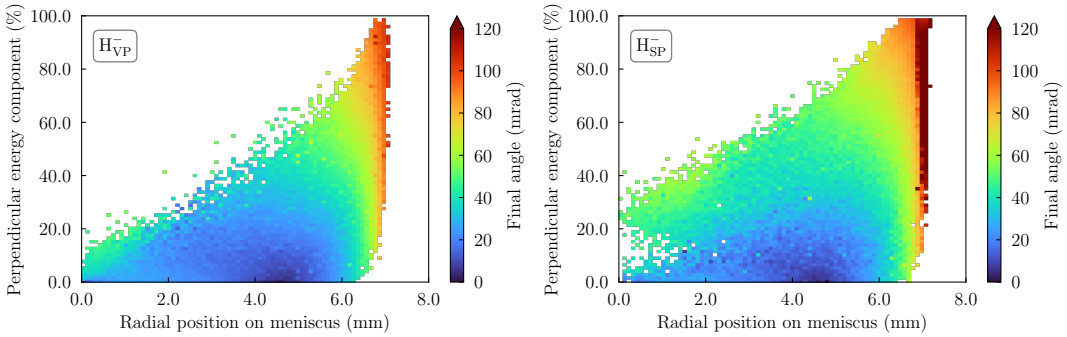

(a) **(b)**

Figure 7.16: *The angle after the grid system as a function of the radial position on the meniscus and the perpendicular energy component on the meniscus surface for (a) H^-_{VP} and (b) H^-_{SP} ions. U_{ext}=10 kV, U_{acc}=55 kV.*

angle at the end of the grid system. The directly extracted ions are extracted through the outer edge of the meniscus, resulting in a final angle of > 100 mrad. The H^-_{SP} ions that are extracted through the center region of the meniscus (either by transport to a neighboring aperture or extraction through the center of the aperture in which they were created) have a much smaller final angle.

Figure 7.16 shows the final angle as a function of the radial crossing point on the meniscus and the perpendicular energy on the meniscus for H^-_{VP} and H^-_{SP} ions. For an ion traveling directly in the direction of the beam axis, the perpendicular energy is 0%. The total magnitude of the energy is ≈ 30 eV, since the meniscus is taken to be the surface with $\phi = 30$ V. The H^-_{VP} and H^-_{SP} plots are qualitatively similar, which is expected since for identical radial positions, the particles roughly have experienced identical electrostatic potential along their trajectories. Particles with

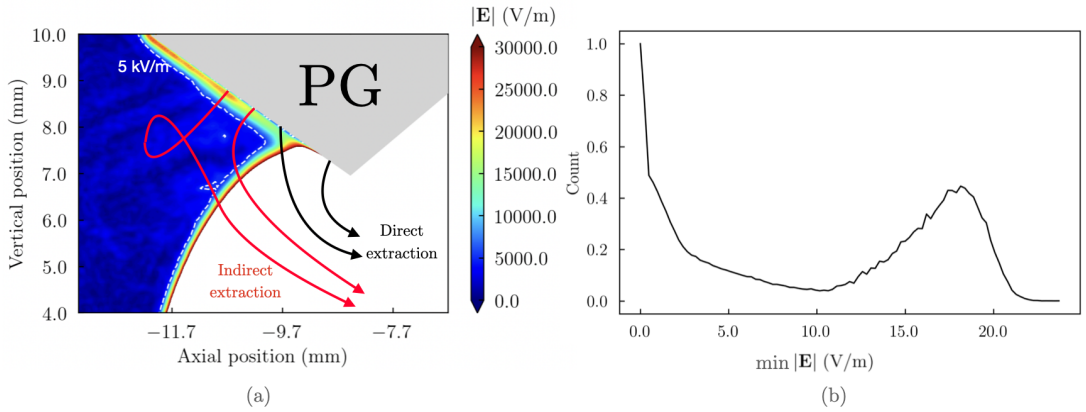

Figure 7.17: *(a) Electric field strength and particle trajectories near the PG. The 5 kV/m contour line is marked with a dashed white line. (b) Distribution of the minimum electric field in the trajectories of extracted H^-_{SP} test particles. U_{ext}=10 kV, U_{acc}=55 kV.*

the highest final angle are extracted at the largest radial meniscus position, almost independent of their initial perpendicular energy. Particles going through the central region of the meniscus tend to have a low angle at the end of the grid system. For H^-_{SP} ions, there are more particles at the meniscus with perpendicular energy above 5 eV for radial positions below 4 mm. These particles are accelerated by the PG sheath and travel almost perpendicular to the meniscus until extraction; for H^-_{VP}, such an extraction path is highly unlikely. Repeating this analysis for the standalone IBSimu simulation gives the same qualitative picture. Since the sheath is not included in the IBSimu standalone simulations, NIs are able to cross the meniscus close to the knife edge of the PG. These observations show that the Debye sheath that forms in front of the plasma grid has an impact on the extraction of H^- ions and that neglecting it has an impact on the extracted beam.

7.6 Quantification of direct extraction of negative ions

To separate direct from indirect extraction of H^-_{SP} quantitatively, the electric field that is felt by the particle during its trajectory is considered. Figure 7.17 (a) shows the magnitude of the electric field in the vicinity of the PG, with the 5 kV/m contour line marked with a dashed white line.

In 7.17 (b), the distribution of the minimum electric field in the trajectories of extracted H^-_{SP} test particles started uniformly over the PG is shown. Two peaks can be seen, one for low values of the minimum electric field, which corresponds to particles that have traveled for a longer distance through the plasma where the typical value is $\sim$ 1 kV/m, and one for values

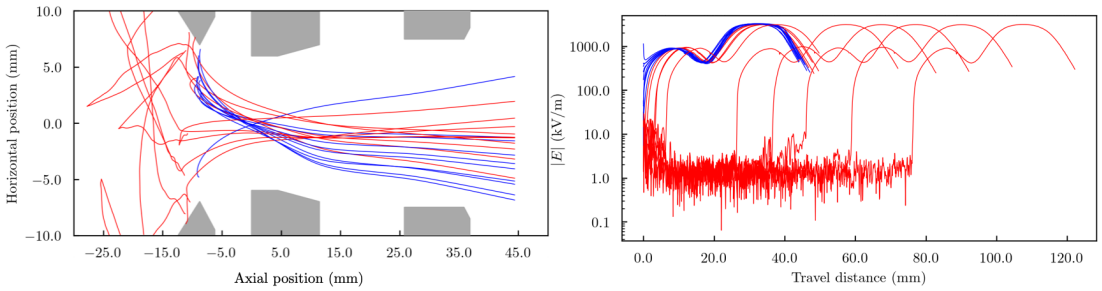

Figure 7.18: *(a) Particle trajectories of directly extracted H^-_{SP} in blue and indirectly extracted H^-_{SP} ions in red. (b) The magnitude of the electric field felt by each particle as a function of their travel distance.*

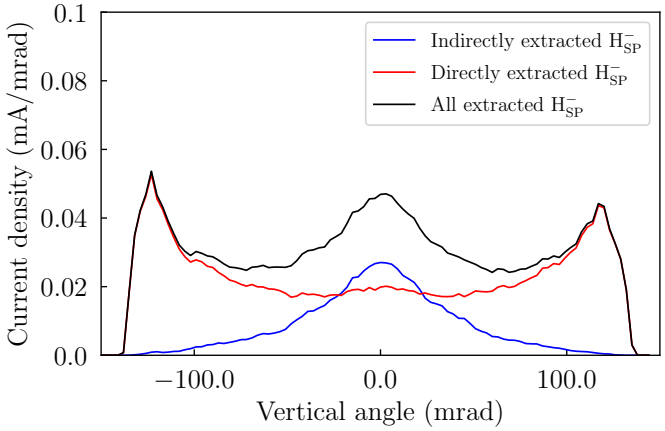

Figure 7.19: *Angular distribution of directly and indirectly extracted H^-_{SP} ions.*

with a maximum at 18 kV/m, which is a typical value in the Debye sheath. The extracted H^-_{SP} can be categorized as directly or indirectly extracted based on whether they passed through a location with a sufficiently weak electric field.

Figure 7.18 shows a sample of extracted test particle trajectories started on the PG and the magnitude of the electric field felt by each particle during the flight path. The point of extraction can clearly be seen in Figure 7.18 (b), as this is where the value for the electric field rapidly increases to thousands of kV/m. In Figure 7.19, which shows the angular distribution of the H^-_{SP} ions, 2.5 kV is used as the delineation between indirect and direct extraction. The halo caused by the H^-_{SP} can be identified with the directly extracted H^-_{SP} ions, while the distribution for the indirectly extracted H^-_{SP} ions is more similar to the H^-_{VP} distribution.

Figure 7.20 shows the final radial position and angle as a function of the total flight distance of H^-_{VP} and H^-_{SP} ions. The shortest possible trajectories are the trajectories of directly extracted H^-_{SP}, which end up at the end of the grid system both with a large final radial position and

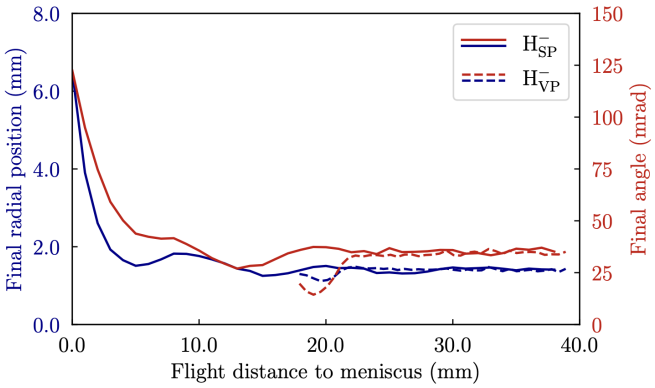

Figure 7.20: *The final radial position and angle as a function of the total flight distance of H^-_{VP} and H^-_{SP} ions from their origin until crossing the meniscus.*

angle. As the distance the H^-_{SP} ions travel in the plasma before crossing the meniscus increases, the final radial position and angle decrease since the H^-_{SP} travel from the PG to a location of the meniscus closer to the center. For the H^-_{VP} ions, the shortest possible distance to the meniscus is ≈ 18 mm, which is only possible if the H^-_{VP} is injected at the center of the injection plane and travels straight toward the center of the meniscus. For H^-_{VP}, the dependence on travel distance on the final radial position and angle is less pronounced. Interestingly, for a travel distance of > 22 mm, the H^-_{SP} behave as H^-_{VP} in that their final radial position and angle are equal and constant. In conclusion, this means that H^-_{SP} ions that travel at least one aperture row before extraction are likely to produce equivalent beam optics as H^-_{VP} ions approaching from the bulk plasma.

7.7 Conclusions

The ONIX code was coupled with the ion-optics code IBSimu to extend the computational domain to contain the plasma and the full grid system, a prerequisite for calculating the properties of the accelerated beamlet. With an *a posteriori* approach, trajectory data was obtained, which enables connecting particle properties in the accelerated beamlet with upstream phenomena.

The ONIX input parameters are based on experiments, but the extracted current densities are below the ITER target, resulting in a highly divergent beamlet in the simulations with a core divergence of 23.2 mrad for the H^-_{VP} ions. The results presented in this chapter provide insights into the effect of including a physical plasma model and surface production of NIs on the beam optics. Particles extracted through the edge of the aperture end up highly divergent in the accelerated beamlet, independent of the perpendicular energy when crossing the meniscus.

However, the perpendicular energy does increase the final divergence of the particles extracted through the center of the aperture. The H^-_{SP} ions are highly divergent at the end of the grid system because they are mostly directly extracted near the edge of the aperture. The angular distribution of the H^-_{SP} ions is not Gaussian, instead, a core component and two highly divergent peaks ($\gtrsim$ 100 mrad) are observed. However, for H^-_{SP} ions that travel $>$ 22 mm inside the plasma before extraction, the angle at the end of the grid system is equal to that of H^-_{VP} ions, this shows that H^-_{SP} ions that travel into the bulk plasma or between apertures before extraction have equal divergence as the H^-_{VP} ions. The H^-_{VP} ions are extracted more evenly over the aperture, but the repelling Debye sheath around the PG decreases the current density at the edges; IBSimu simulations that neglect sheath physics and H^-_{SP} ions have a flat current density profile over the aperture. The different extracted current density profiles have an impact on the accelerated beamlet, which in both cases is well described by a double Gaussian. Although the core divergence of H^-_{VP} ions matches well between ONIX-IBSimu and standalone IBSimu simulations, there is a smaller core fraction in the standalone IBSimu simulation (57.7%) compared to the coupled ONIX-IBSimu simulation (72.4%) since more particles are extracted through the edge.

CHAPTER 8

Investigations of negative ion extraction in different geometries

The optics of the extracted NI beam are influenced to a large degree by H^-_{SP} ions. It is shown in Chapter 7 that the meniscus is deeply penetrating under standard simulation conditions with the IPP PG geometry since the extracted NI current density does not match the extraction voltage of 10 kV. As a result, the extracted NI beamlets are highly underperveant in the simulations. It is also shown that the position on the meniscus through which the H^- ions are extracted has a large impact on the final divergence of the beam, and directly extracted H^-_{SP} ions were observed to create a highly divergent beam halo. To evaluate the impact of grid geometry on the meniscus formation, plasma properties, beam optics of NI ions, and co-extraction of electrons, variations of the PG geometry are investigated in this chapter using the flux-injection model.

The LD/HT plasma parameters and BCs were kept the same in the bulk plasma for each simulated case. The one-sided flux-injection scheme was used with the PG potential at -5 V with respect to the plasma potential and $U_{ext} = 10$ kV, $U_{acc} = 55$ kV. The emission rate of H^-_{SP} ions is 200 Am^{-2} in each simulation.

8.1 Flattening of the PG knife edge

To investigate how the meniscus penetration depends on the PG knife edge of the PG geometry, the IPP PG is compared to two PG geometries with flattened knife edges. The grid geometries are given in Figure 8.1. The first geometry is the PG geometry used in the neutral beam test

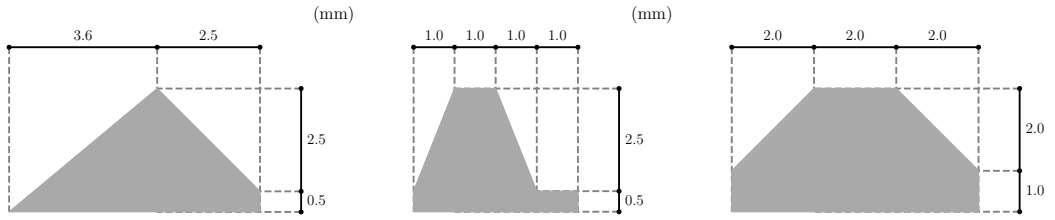

(a) *IPP PG* **(b)** *NIFS PG* **(c)** *Oct. PG*

Figure 8.1: *Simulated grid geometry for the IPP PG, NIFS PG, and Oct. PG. The distance from the downstream side of the PG to the EG is kept at 6 mm in each simulation.*

stand at the NIFS [199]. Compared to the IPP PG, the NIFS PG is thinner and has a larger angle of the conical surface (the conical surface of the PG refers to the plasma-facing chamfered surface). The distance between both PGs and the EG was kept equal (6 mm). An additional PG geometry was investigated with a similar conical angle as the IPP PG, but which also has a chamfered flat part at the knife of the PG, just as for the NIFS PG. This PG shape is called Octagon PG (Oct. PG). The reason to simulate the Oct. PG is to investigate whether a larger flat section of the PG affects the position at which the meniscus attaches to the PG and if fewer directly extracted NIs contribute to the beam halo. Since the penetration of the NIFS PG into the plasma is lower than that of the IPP PG and the Oct. PG PG, the $\mathbf{B}_{\mathrm{DF}}$, which penetrates into the plasma, is stronger near the PG for the NIFS PG, this may additionally affect the electron transport. This chapter aims to investigate the effect on both ions and electrons.

Table 8.1 shows the extracted current densities for the three simulations, one with each of the three PG geometries. The highest total extracted current densities of NIs were obtained for the IPP PG (146 Am^{-2}), mostly due to the higher extraction probability of $\mathrm{H}^-_{\mathrm{SP}}$ ions with poor optics. For the NIFS PG, more $\mathrm{H}^-_{\mathrm{VP}}$ ions were extracted (97 Am^{-2}) than for the IPP PG (88 Am^{-2}), while for the Oct. PG, both fewer $\mathrm{H}^-_{\mathrm{SP}}$ (17 Am^{-2}) and $\mathrm{H}^-_{\mathrm{VP}}$ (74 Am^{-2}) ions were extracted. The co-extracted electron currents were similar for the IPP and NIFS PG (108 Am^{-2} and 109 Am^{-2}, respectively), but about 20 Am^{-2} higher for the Oct. PG (125 Am^{-2}). In conclusion, the choice of PG geometry (among the ones tested) does impact the extracted current densities of NIs mainly by the number of directly extracted $\mathrm{H}^-_{\mathrm{SP}}$ ions.

Figure 8.2 (a) shows the outline of the menisci and Figure 8.2 (b) shows the particle densities along the central axis for the three cases. The penetration of the meniscus is equal in all three cases, however, the total surface area of the meniscus for the Oct. PG cases is smaller since the inner corner of the PG is at a lower axial position and thus cuts off the outermost part

Table 8.1: *Extracted currents for the IPP PG, NIFS PG, and Oct. PG. U_{ext}=10 kV, U_{acc}=55 kV.*

Simulation	$j_{H^-_{VP}}$	$j_{H^-_{SP}}$	j_e	j_{ex}	j_e/j_{ex}
	Am^{-2}	Am^{-2}	Am^{-2}	Am^{-2}	
IPP PG	88	57	108	146	0.7
NIFS PG	97	26	109	118	0.9
Oct. PG	74	17	125	87	1.4

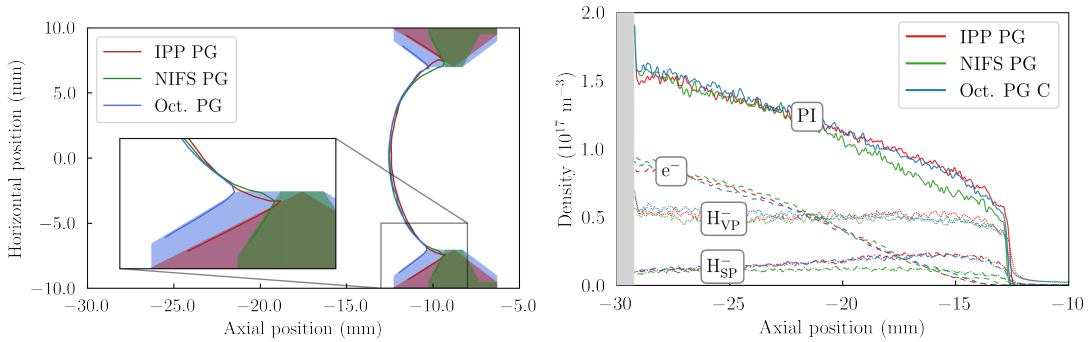

(a) **(b)**

Figure 8.2: *(a) Meniscus shapes and (b) particle densities along the central axis for the IPP PG, NIFS PG, and Oct. PG.*

of the meniscus. Compared to the IPP PG, the surface area of the meniscus in the Oct. PG case is ≈ 15% lower, which corresponds well to the $j_{H^-_{VP}}$, which is also 15% lower. The particle densities for the PIs, electrons and H^-_{VP} ions are similar for all three simulations inside the plasma. Although the H^-_{SP} ion density is equal in all three cases near the bulk plasma, the H^-_{SP} ion density close to the meniscus is lower in the NIFS PG case than for the IPP PG and Oct. PG due to the shallower angle of the PG chamfer. In terms of extracted current density, this leads to the highest $j_{H^-_{VP}}$ (92 Am^{-2}) out of the three cases, since less of the negative space charge near the meniscus is taken up by H^-_{SP}.

For all three cases, the H^-_{SP} ions that overcome the VC are accelerated by the Debye sheath towards the plasma. Figure 8.3 shows particle trajectories of H^-_{SP} ions started on the conical surface of the IPP PG, NIFS PG and Oct. PG, colored blue if they are extracted and red if not. The H^-_{SP} ions in the NIFS PG case travel predominantly upstream, away from the beam direction, while for the IPP and Oct. PG, the NIs from the opposing sides of the PG overlap in the region where the axial position is > -20 mm. This leads to a reduced indirect extraction probability of H^-_{SP} ions. However, due to the direct extraction of H^-_{SP}, the $j_{H^-_{SP}}$ is higher in the NIFS PG case (26 Am^{-2}) than in the Oct. PG case (17 Am^{-2}).

Figure 8.4 shows the H^-_{SP} ion and electron density in the vertical-axial plane for each PG

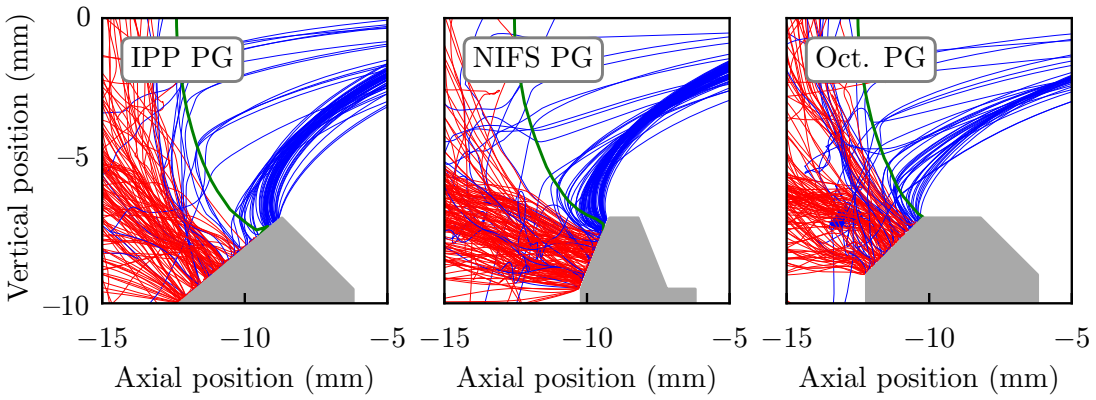

Figure 8.3: *Particle trajectories for extracted (in blue) and not extracted (in red) H^-_{SP} ions injected on the surface of the conical surface of the IPP PG, NIFS PG, and Oct. PG.*

geometry. The electron density is similar for each case, however, the electron density for the NIFS grid is lower near the PG since the $\mathbf{B}_{DF}$, which penetrates into the plasma, causes the orbits of the electrons to bounce between the top and bottom of the PG further away from the PG. For the IPP PG and the Oct. PGs, the H^-_{SP} ion density close to the meniscus is $\sim 2 \cdot 10^{16}$ m^{-3} while for the NIFS PG, the density is $\sim 1 \cdot 10^{16}$ m^{-3}. Additionally, the higher amount of directly extracted H^-_{SP} ions for IPP PG and NIFS PG can be seen in the highly divergent components of the beam.

To study the effect of the PG shape on the direct extraction of H^-_{SP}, *a posteriori* simulations with each PG geometry were performed. Table 8.2 shows the fraction of indirectly extracted H^-_{SP} ions ($j^{\text{Indirect}}_{H^-_{\text{Conus}}}$) to the total extracted H^-_{SP} ion current ($j^{\text{Tot.}}_{H^-_{\text{Conus}}}$). Direct extraction is here defined as extracted H^-_{SP} ions that do not pass through a region with $|E| < 2500$ kV/m, as discussed in Chapter 7. The highest fraction of indirectly extracted H^-_{SP} ions was obtained for the Oct. PG, from which 64% of ions were indirectly extracted. For the IPP PG, it can be seen that there is a section on the beam-side of the meniscus from which H^-_{SP} ions are produced, which are all directly extracted, lowering the fraction. For the Oct. PG on the other hand, the area of the meniscus is smaller, as is shown in Figure 8.2 (a), and the meniscus attaches close to the first knife edge. To obtain a high fraction of indirectly extracted H^-_{SP} ions, the meniscus must (1) attach to the meniscus near the knife edge and (2) have at least a perpendicular angle with the conical PG wall. Of the three PG geometries investigated, the Oct. PG is the one that satisfies these requirements the best. Additionally, f_{core}, θ_{core}, θ_{halo} and $\theta_{\text{stat.}}$ for the H^-_{VP} ions, defined in Equations (2.34) and (2.35), are given in Table 8.2. For the H^-_{VP} ions, the highest core fraction (72%) and lowest core divergence (22 mrad) are obtained for the IPP PG. It is important to note here that the ions labeled as H^-_{VP} ions are labeled as such since they

Table 8.2: *Beam properties for H^-_{SP} ions for the IPP PG, NIFS PG, and Oct. PG, divergences are given for the vertical angle at the end of the grid system.*

Simulation	$j^{\text{Indirect}}_{H^-_{\text{Conus}}} / j^{\text{Tot.}}_{H^-_{\text{Conus}}}$	$f^{\text{VP}}_{\text{core}}$	$\theta^{\text{VP}}_{\text{core}}$	$\theta^{\text{VP}}_{\text{halo}}$	$\theta^{\text{VP}}_{\text{stat}}$
	%	%	mrad	mrad	mrad
IPP PG	38	72	23	71	42
NIFS PG	49	55	27	76	54
Oct. PG	64	59	28	71	50

are injected into the simulation domain from the upstream boundary of the domain, which to a large extent consists of H^-_{SP} ions. This means that the effect on the H^-_{VP} labeled ions also applies to caesiated H^- ion sources, where a large fraction of the H^- ions are surface-produced, since they approach the meniscus from the bulk plasma.

As discussed in Chapter 7, both the shape of the meniscus and the particle properties when extracted have a large impact on the beam optics. Figure 8.5 shows the normalized current density of H^-_{SP} ions on the meniscus for each PG geometry. For the Oct. PG, the effective diameter of the meniscus is smaller, even though the physical diameter of the PG aperture is the same as for the IPP PG and NIFS PG, meaning that a larger fraction of H^-_{SP} ions are extracted through the center of the meniscus, and thus the divergent horns in the extremities of the distribution are less pronounced.

8.2 Elongation of the PG

Since the H^-_{SP} ions are accelerated by the Debye sheath between the plasma and the PG surface, the angle of the conical PG surface determines the transport of the H^-_{SP} ions. To increase the transport of H^-_{SP} ions from the PG towards the center of the meniscus, the IPP PG was elongated towards the plasma side of the computational domain, see Figure 8.6. For the standard IPP PG, the plasma-facing side of the PG extends 3.6 mm from the knife edge of the PG while for the Long IPP PG, it is elongated to 7 mm.

Table 8.3 shows the extracted current densities for the IPP PG and the Long IPP PG. Compared to the IPP PG, the Long IPP PG produces more H^-_{SP} ions due to its larger surface area. For the Long IPP PG, the H^-_{SP} ion current density is higher by 23 Am^{-2} and H^-_{VP} ion current density is lower by 24 Am^{-2}, keeping the total extracted current density j_{ex} similar. The co-extracted current density remained the same. At steady-state, the NI currents were constant in time (< 1 Am^{-2} variation) while the electron currents oscillated by ≈ 10 Am^{-2}. Figure 8.7 (a) shows the meniscus shapes, as for the NIFS PG and Oct. PG, the penetration of the meniscus for the Long IPP PG is the same as for the IPP PG, indicating that the penetration mainly

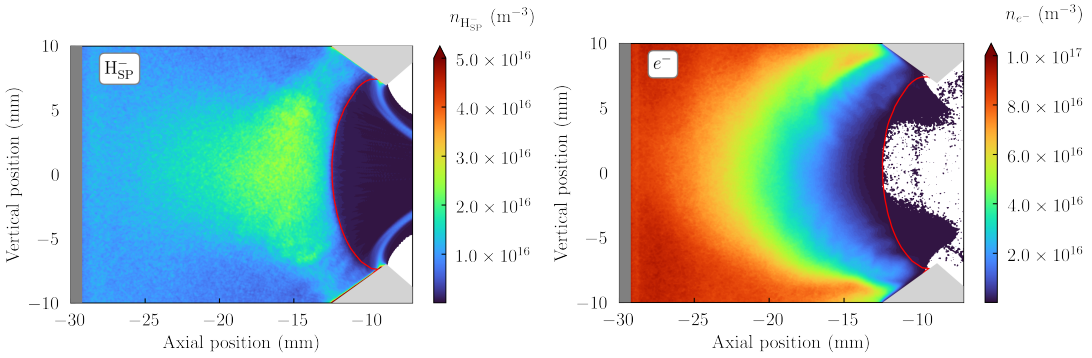

(a) *IPP PG*

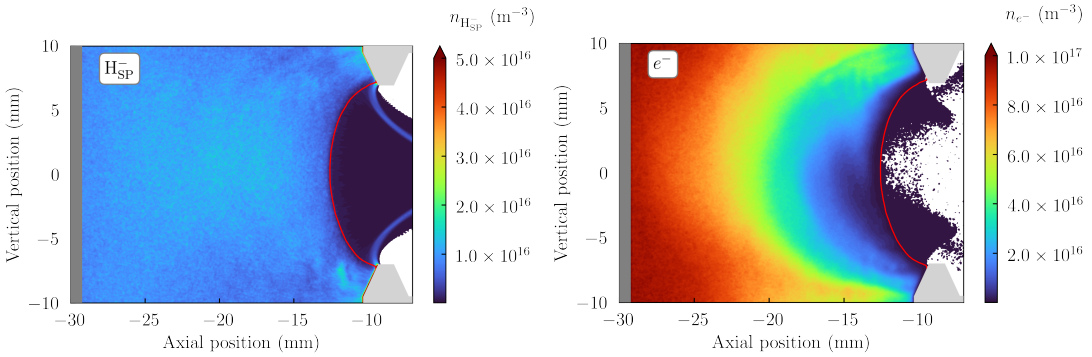

(b) *NIFS PG*

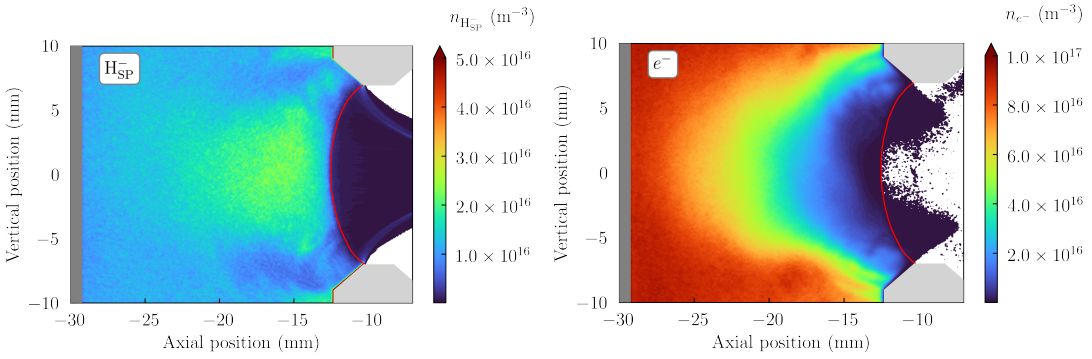

(c) *Oct. PG*

Figure 8.4: *Left:* H_{SP}^- *ions and right:* e^- *densities for the (a) IPP PG, (b) NIFS PG, and (c) Oct. PG.*

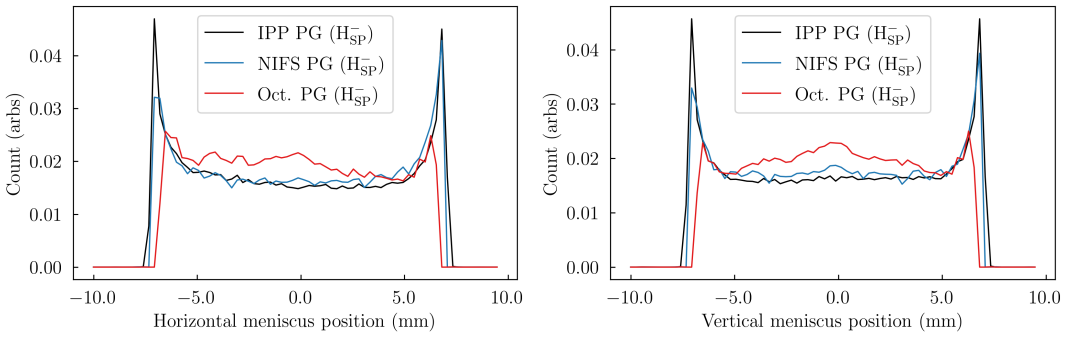

(a) **(b)**

Figure 8.5: *Normalized current density of H^-_{SP} ions along (a) horizontal direction and (b) vertical direction over the meniscus for the IPP PG, NIFS PG, and Oct. PG.*

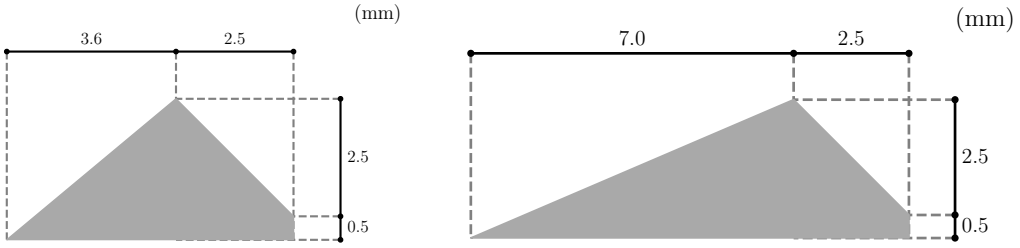

(a) *IPP PG* **(b)** *Long IPP PG*

Figure 8.6: *Simulated grid geometry for the IPP PG and Long IPP PG. The distance from the PG to the EG is kept at 6 mm in both simulations.*

depends on the plasma parameters and extraction voltage, both of which are kept equal in the two simulations. The particle densities along the axial center line are shown in Figure 8.7 (b). The density of H^-_{SP} ions in front of the meniscus is $4 \cdot 10^{16}$ m^{-3} for the Long IPP PG and $2 \cdot 10^{16}$ m^{-3} in the IPP PG case at axial position −15 mm. The higher H^-_{SP} ion density leads to a higher extracted H^-_{SP} ion current density. However, the reason why the increase of $j_{H^-_{SP}}$ is not proportional to the increase of $n_{H^-_{SP}}$ is due to the direct extraction of H^-_{SP} ions. In conclusion, this means that the shallower angle of the PG in the Long IPP PG case leads to an increased extraction through the center of the meniscus and thus fewer directly extracted H^-_{SP} ions, which form the beam halo.

Table 8.3: *Extracted current densities for the IPP PG and Long IPP PG.*

Simulation	$j_{H^-_{VP}}$	$j_{H^-_{SP}}$	j_e	j_{ex}	j_e/j_{ex}
	A/m^2	A/m^2	A/m^2	A/m^2	
IPP PG	88	57	108	146	0.7
Long IPP PG	65	81	102	143	0.7

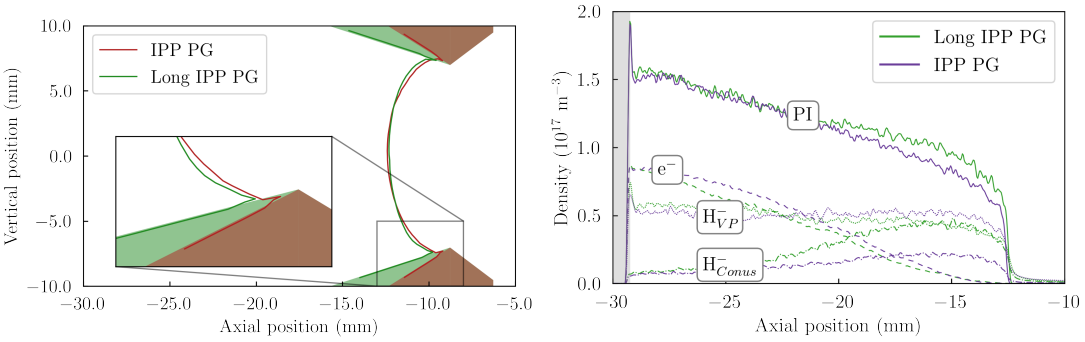

(a) **(b)**

Figure 8.7: *(a) Meniscus shapes and (b) particle densities along the central axis for the IPP PG and Long IPP PG. U_{ext}=10 kV, U_{acc}=55 kV.*

Table 8.4: *Beam properties for H^-_{SP} ions for the IPP PG and Long IPP PG, divergences are given for the vertical angle at the end of the grid system.*

Simulation	$j^{\mathrm{Indirect}}_{H^-_{\mathrm{Conus}}}/j^{\mathrm{Tot.}}_{H^-_{\mathrm{Conus}}}$	$f^{\mathrm{VP}}_{\mathrm{core}}$	$\theta^{\mathrm{VP}}_{\mathrm{core}}$	$\theta^{\mathrm{VP}}_{\mathrm{halo}}$	$\theta^{\mathrm{VP}}_{\mathrm{stat}}$
	%	%	mrad	mrad	mrad
IPP PG	38	72	23	71	42
Long IPP PG	44	79	21	71	38

Table 8.4 shows the fraction of indirectly extracted H^-_{SP} ions ($j^{\mathrm{Indirect}}_{H^-_{\mathrm{Conus}}}$) to the total extracted H^-_{SP} ion current ($j^{\mathrm{Tot.}}_{H^-_{\mathrm{Conus}}}$). The Long IPP PG case has a higher fraction of indirectly extracted H^-_{SP} ions (44%) than the IPP PG (38%), but lower than for the Oct. PG. Due to the sharp knife edge of the PG for the IPP PG and Long IPP PG, compared to the NIFS PG and the Oct. PG, there is a region on the beam side of the meniscus where H^-_{SP} ions are generated, which are all directly extracted. For the Long IPP PG, the core component of the H^-_{VP} ions has the lowest divergence of all PG shapes investigated, 17.8 mrad. The Long IPP PG fulfills the requirement of having a large fraction of indirectly extracted H^-_{SP} ions and has the highest density of H^-_{SP} ions in front of the meniscus. In terms of beam optics, it is important to note that the divergence is higher than the ITER requirement for each of the PG geometries tested since the simulations are done in an underperveant regime with too low j_{ex} for the U_{ext} of 10 kV.

8.3 Effects of beam side PG geometry on meniscus formation

For all the investigated PG shapes, the main cause for the formation of a beam halo is the directly extracted H^-_{SP} ions produced downstream of the meniscus. Designing a PG geometry

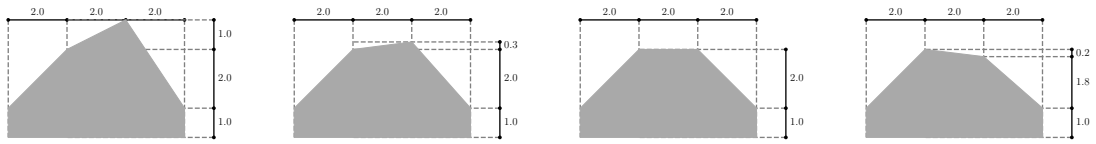

(a) *Oct. PG A* **(b)** *Oct. PG B* **(c)** *Oct. PG C* **(d)** *Oct. PG D*

Figure 8.8: *Simulated grid geometry for Oct. PG A-D where the beam facing knife edge is varied. The distance from the PG to the EG is kept at 6 mm in each simulation.*

that allows for the meniscus to attach further downstream could lead to fewer H^-_{SP} ions being directly extracted. Since the Oct. PG shape was shown to have the lowest fraction of directly extracted H^-_{SP} ions, it was selected as a base shape to study. The radius of the second corner of the flat region of the PG was varied from 1 mm narrower to 2 mm wider than the standard Oct. PG in four steps, as shown in Figure 8.8. The shapes are named Oct. PG A-D, where Oct. PG C corresponds to the previously shown standard case of the Oct. PG.

Figure 8.9 illustrates the meniscus shapes (a) and axial density profiles (b) for Oct. PG A-D. The meniscus penetration is similar for shapes B, C, and D, while Oct. PG A has a 0.2 mm less meniscus penetration since the effective radius of the PG aperture is lower by 1 mm. Additionally, the radius of the outer corner has no impact on the particle densities inside the plasma, which is evident from Figure 8.8 (b). The effect of the meniscus formation on the extracted current densities is shown in Table 8.5, which contains the extracted current densities for the different PG geometries. The extracted e^- and H^- ion currents decrease with the second corner radius. Specifically, Oct. PG A has the lowest extracted H^-_{SP} ion current density among all investigated PG shapes at 9 Am^{-2}. However, due to the reduced extraction of e^-, the fraction j_e/j_{ex} is 1.2, which is 0.2 lower than for Oct. PG B, C, and D. Therefore, even minor shifts in the meniscus position can significantly impact the extracted current densities.

Table 8.5: *Extracted current densities for the Oct. PG A-D.*

Simulation	$j_{H^-_{VP}}$	$j_{H^-_{SP}}$	j_e	j_{ex}	j_e/j_{ex}
	A/m^2	A/m^2	A/m^2	A/m^2	
Oct. PG A	59	9	66	78	1.2
Oct. PG B	72	14	83	115	1.4
Oct. PG C	74	17	87	125	1.4
Oct. PG D	78	20	94	135	1.4

Figure 8.10 shows the particle flux of H^-_{SP} ions produced on the conus of the PG ($\Gamma_{H^-_{Conus}}$) for the extreme cases Oct. PG A and D. For Oct. PG D, the meniscus attaches directly on the first corner of the PG edge, allowing for H^-_{SP} ions to be directly extracted. For Oct. PG A, the

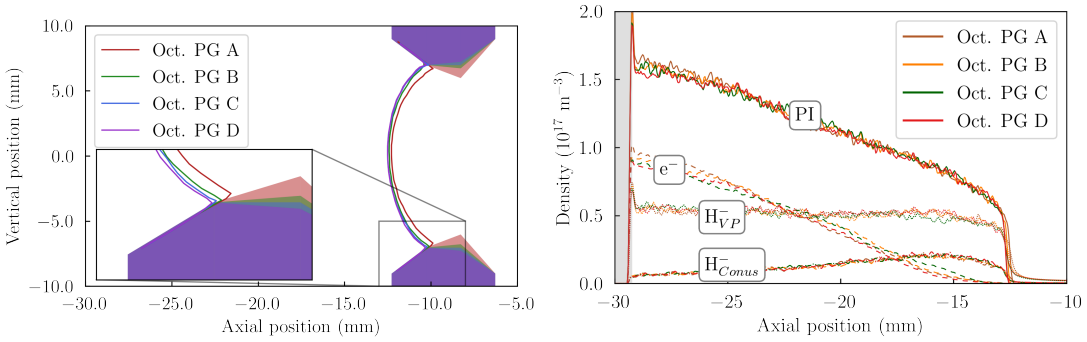

(a) **(b)**

Figure 8.9: *(a) Meniscus shapes and (b) particle densities along the central axis for Oct. PG A-D.* U_{ext}*=10 kV,* U_{acc}*=55 kV.*

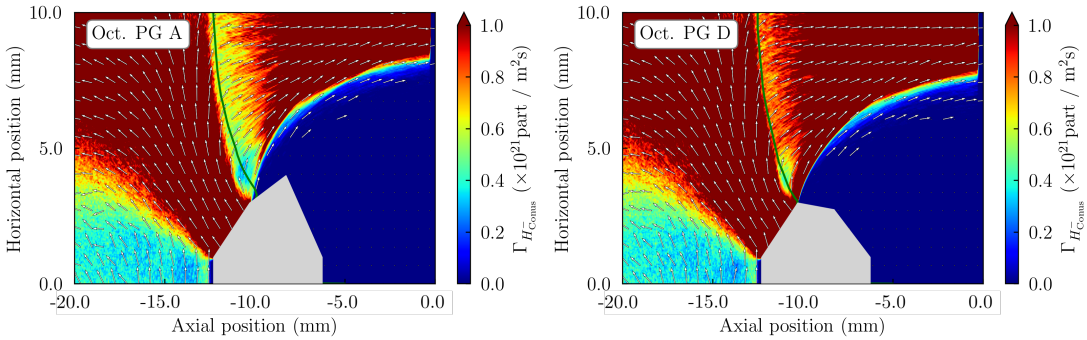

(a) *Oct. PG A* **(b)** *Oct. PG D*

Figure 8.10: *Flux near the PG in the axial-horizontal plane for NIs injected on the conus of (a) Oct. PG A and (b) Oct. PG D. The meniscus is marked with a green line.* U_{ext}*=10 kV,* U_{acc}*=55 kV.*

meniscus is slightly moved towards the second corner, enough to significantly cut off the amount of directly extracted NIs. However, due to the reduction in extracted H^- ion currents, the core divergence of the accelerated H^-_{VP} ion beamlet is 31.4 mrad, higher than for Oct. PG C. In conclusion, the geometry of the PG on the downstream side of the meniscus has a significant impact on both the extracted current densities and the beam optics.

8.4 Negative ion emission from the flattened PG knife

For each simulation with the NIFS PG and Oct. PG, the emission of NIs from the flattened knife edge of the PG was neglected since no plasma is present in this region to keep the work function low. However, the emission of H^-_{SP} ions from the PG also impacts the formation of the plasma and in turn, the meniscus formation. Although it is not known to what extent H^-_{SP} ions are produced on the flattened knife edge of the PG, the impact of such ions has been

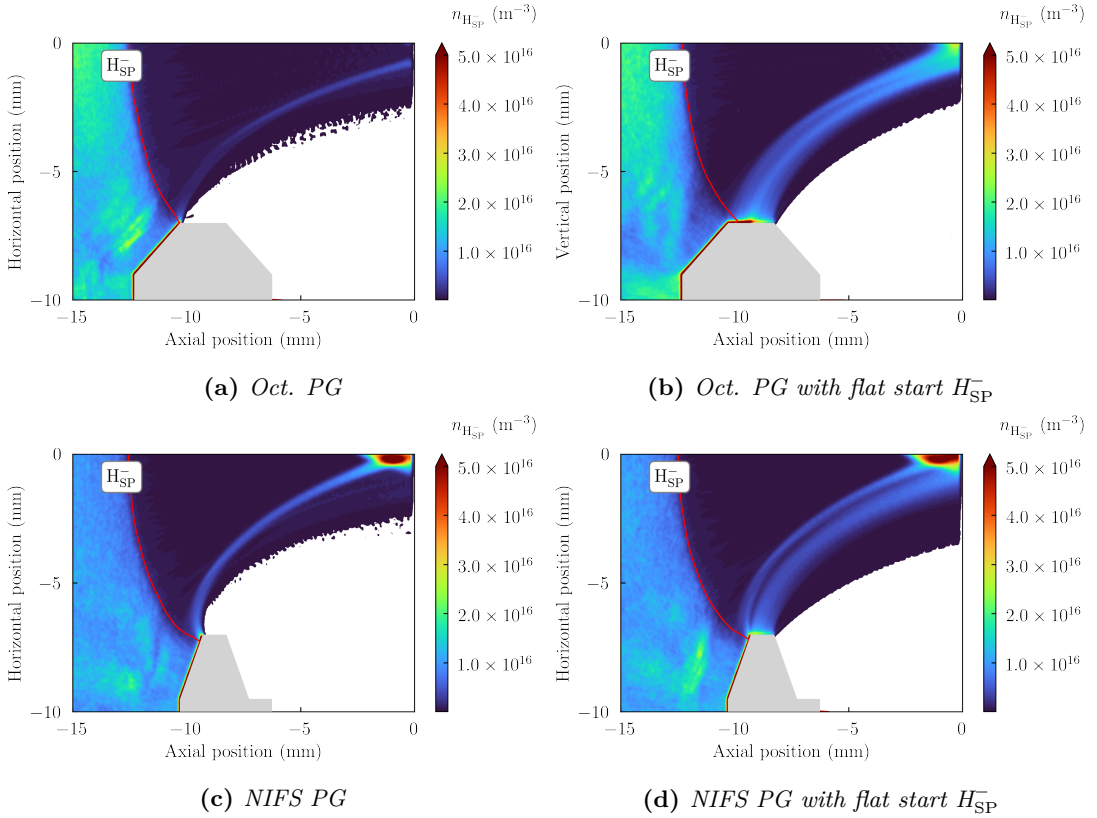

(a) *Oct. PG* **(b)** *Oct. PG with flat start* H_{SP}^-

(c) *NIFS PG* **(d)** *NIFS PG with flat start* H_{SP}^-

Figure 8.11: *H_{SP}^- ion densities for the Oct. PG and NIFS PG, with and without H_{SP}^- ions injected from the flat region of the PG. U_{ext}=10 kV, U_{acc}=55 kV.*

investigated in this section. Simulations for the NIFS PG and Oct. PG were done with the inclusion of H_{SP}^- ions emitted from this region. The emission rate of the H_{SP}^- ions from the flat region was set to 200 Am^{-2}, this represents an additional 8.8 mA and 17.6 mA for the simulated aperture for the NIFS PG and Oct. PG, respectively.

Figure 8.11 shows the particle densities for H_{SP}^- ions for the Oct. PG and NIFS, with and without H_{SP}^- ions starting from the flat region of the PG knife (flat start). The extracted H_{SP}^- ions which are injected on the flattened section of the PG form a beam halo. Additionally, the emission of H_{SP}^- ions from the flat region allows for the meniscus, see Figure 8.12, to attach further downstream on the PG, and H^+ ions are able to travel past the first corner. This leads to the formation of a VC in the first half of the flat region. For the NIFS PG, the effect on the meniscus is negligible due to the position of the first corner; the meniscus penetrates deeper with respect to the first corner and the injection of H_{SP}^- ions from the flat region does not impact the meniscus since it is too far away. This means that if negative ions are produced on the flattened knife edge of the PG, that would impact the meniscus formation depending on the distance between the meniscus and the flattened knife edge.

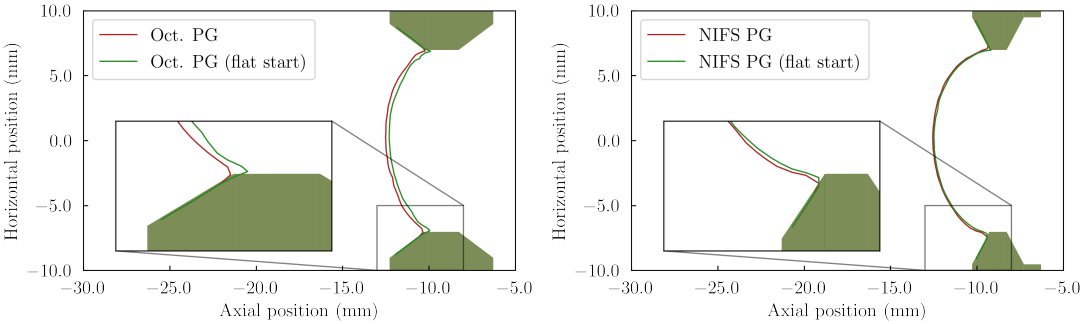

(a) **(b)**

Figure 8.12: *(a) Meniscus shapes for (a) the Oct. PG and (b) NIFS PG, with and without H^-_{SP} ions starting from the flat region of the PG. U_{ext}=10 kV, U_{acc}=55 kV.*

Table 8.6: *Extracted currents for the Oct. PG and NIFS PG, with and without H^-_{SP} ions starting from the flat region of the PG.*

Simulation	$j_{H^-_{VP}}$	$j_{H^-_{SP}}$	j_e	j_{ex}	j_e/j_{ex}
	A/m^2	A/m^2	A/m^2	A/m^2	
Oct. PG	74	17	125	87	1.4
Oct. PG (flat start)	66	97	109	159	0.7
NIFS PG	97	26	109	118	0.9
NIFS PG (flat start)	88	81	102	164	0.6

Table 8.6 shows the extracted current densities for the Oct. PG and NIFS PG, with and without H^-_{SP} ions starting from the flat region of the PG. The H^-_{SP} ions emitted from the flat region are included with all extracted H^-_{SP} ions as $j_{H^-_{SP}}$. The increase of $j_{H^-_{SP}}$ is 84 Am^{-2} for the Oct. PG and 55 Am^{-2} for the NIFS PG, in absolute currents, this represents 12.9 mA and 8.5 mA for the Oct. PG and NIFS PG, respectively. For the Oct. PG, this represents 74% of the additionally injected H^-_{SP} ion current from the flat part of the PG, while for the NIFS PG, the increase is 96%, which means that close to all of the extra H^-_{SP} ions are extracted. This corresponds well to the observation that the extra injected H^-_{SP} ions do not form a VC in the NIFS PG case. Additionally, the $j_{H^-_{VP}}$ decreases by 7 Am^{-2} for the NIFS PG case and 8 Am^{-2} in the Oct. PG case, respectively. This means that, although emission of H^-_{SP} ions from the flattened PG knife does not necessarily affect the meniscus formation (as in the NIFS PG case), the additional negative ions decrease the number of ions extracted from the plasma (indirect extraction), which increases the beam divergence.

8.5 Conclusions

The study compares various geometries of the PG, based on the ITER-like IPP PG, NIFS PG and Oct. PG, shown in Figure 8.1. The main conclusions are as follows.

- The geometry of the PG has little impact on the meniscus penetration, the main impact of the meniscus penetration comes from the extraction potential, plasma density and the distance between PG and EG. This effect has not previously been studied with 3D-PIC modeling.
- The attachment of the meniscus on the PG can be slightly altered by flattening the PG knife and changing the outer radius of the flattened shape. A flattening of the PG knife edge leads to a decrease of directly extracted H^-_{SP} ions, and thus lower beam divergence.
- The highest total extracted current density of NIs was obtained for the IPP PG, mostly due to the large fraction of directly extracted H^-_{SP} ions, which form a beam halo with high divergence.
- The lowest fraction of directly extracted H^-_{SP} ions is achieved with the Oct. PG due to the flattening of the outer region of the PG.
- The amount of co-extracted electrons was similar for all PG geometries.
- The plasma-facing angle of the PG impacts the extraction probability and accumulation of H^-_{SP} ions due to the acceleration by the Debye sheath. With a shallow angle, as in the Long IPP PG case, more ions are transported to the central region near the meniscus, doubling the $n_{H^-_{SP}}$ compared to the IPP PG case.
- The lowest core divergence (17.8 mrad) is produced in the case with the Long IPP PG since a larger fraction of the H^- ions are extracted through the center of the meniscus. For the Long IPP PG, $n_{H^-_{SP}} = 5 \cdot 10^{16}$ m^{-3} in front of the center of the meniscus, which is twice as high as for the IPP PG.

CHAPTER 9

Summary and conclusions

The ITER Neutral Beam Injection (NBI) relies on the acceleration of H^-/D^- ions. These Negative Ions (NIs) are predominantly generated on the plasma-facing surfaces in Radio Frequency (RF)-driven low-temperature, low-pressure plasma sources through the conversion of atoms and positive ions to NIs. The NIs are extracted from the plasma through apertures in the Plasma Grid (PG) by an extraction potential of approximately 10 kV between the PG and the Extraction Grid (EG). Along with the H^- ions, electrons are co-extracted and directed onto the EG using a Magnetic Deflection Field ($\mathbf{B}_{\mathrm{DF}}$). A primary challenge is the quantity and temporal stability of these co-extracted electrons, in particular in deuterium operation. A Magnetic Filter Field ($\mathbf{B}_{\mathrm{FF}}$), aligned in the horizontal direction and perpendicular to both the beam axis and the $\mathbf{B}_{\mathrm{DF}}$, is used to reduce the electron temperature (from $\sim$ 10 eV to $\sim$ 2 eV) and density, subsequently minimizing the NI destruction due to collisions with energetic electrons.

Certain characteristics, such as the sheath formation under the 3D magnetic field produced by $\mathbf{B}_{\mathrm{FF}}$ and $\mathbf{B}_{\mathrm{DF}}$, and the transport of Cs on large time scales, make these ion sources challenging to study via analytical, experimental or numerical modeling approaches. However, in the close vicinity of the extraction region, numerical modeling is essential to study the extraction processes and to develop a methodology for reducing and stabilizing electron co-extraction.

Dimensional reduction and scaling of physical parameters are done to manage computational complexity. While 1D and 2D models simplify the geometry and partly capture magnetic field effects, 2.5D models add more detail by incorporating three-component vectors in a 2D space. Full 3D models offer the most comprehensive representation but require significant computational resources, necessitating parallel processing on computing clusters. Scaling approaches,

used across various model dimensions, help in handling larger simulation domains but require careful calibration to maintain experimental relevance. Despite these advancements, challenges remain, such as accurately modeling Debye sheaths, plasma behavior in magnetized environments, and comprehensive NI transport, highlighting ongoing areas for research and development in this field.

This thesis uses 3D Particle-in-Cell (3D-PIC) Monte Carlo Collisions (MCC) simulations using the code Orsay Negative Ion eXtraction (ONIX) to simulate NI extraction and electron co-extraction under realistic operating conditions without the scaling of physical parameters. The simulation domain covers one PG aperture and the parameters are based on experimental findings in Extraction from a Large Ion Source Experiment (ELISE) and BATMAN Upgrade (BUG), which are operated at Max Planck-Institut für Plasmaphysik in Garching, Germany. In addition to simulations in full-density, simulations in lower density and simulations in a slab-domain have been performed to reduce the computational time required for parametric surveys. This investigation encompasses long-range interactions, especially biased surfaces' influence and electron losses along magnetic field lines, and assesses how plasma and ion source conditions affect the extracted beamlets' optics.

During the course of the work conducted for this thesis, multiple improvements of the ONIX code have been implemented. A particle injection model (flux-injection) has been implemented in order to allow for a biasing of the PG. The ONIX code has been extended to include more complicated geometries, such as multi-aperture simulations and simulations of an Electron Fence (EF), which has been used in National Institute for Fusion Science (NIFS) to suppress the co-extracted electron current. The ONIX code has been coupled with the ion-optics code Ion Beam Simulator (IBSimu) to extend the computational domain throughout the grid system and an *a posteriori* particle tracking version of the coupled ONIX-IBSimu simulations has been developed. Such simulations have not previously been done in 3D-PIC simulations for NI extraction.

In Chapter 2, the framework and objectives of this thesis were established and summarized as a list of research questions. In the following, the research findings are contextualized in relation to these questions.

Physics of the co-extracted electrons

In experimental campaigns, it has been shown that the bias of the PG has a large impact on the amount of co-extracted electrons. It is also known that during operation with deuterium, the amount of co-extracted electrons is higher than with hydrogen. The following observations

were made based on 3D-PIC modeling using ONIX in this thesis:

- *Which physical processes and parameters in the plasma determine the amount of co-extracted electrons?*

  - The amount of co-extracted electrons is intricately linked to the meniscus penetration and the electron temperature near the PG. A lower plasma density ($n_e = 6{\cdot}10^{16}$ m^{-3}) at a distance of $\sim$ 15 mm from the PG aperture leads to an increased meniscus penetration of 1.1 mm compared to a higher plasma density ($n_e = 12 \cdot 10^{16}$ m^{-3}). Since the $\mathbf{B}_{\mathrm{DF}}$ limits the e$^-$ transport towards the meniscus, the electron density decreases significantly compared to the bulk plasma. In addition, a higher electron temperature of 2 eV leads to an increased mobility of the electrons compared to 1 eV, and a deeper Debye sheath towards the PG. The combined effect of a higher temperature and lower density was shown to lead to an increase of the co-extracted electron current density by a factor of four due to the higher mobility of the electrons and the deeper penetration of the meniscus. [Chapter 5]

  - The emission rate of H$^-$ ions from the PG surface has a small effect on the co-extraction of electrons. This is because the Surface Produced H$^-$ ($\mathrm{H^-_{SP}}$) ions do not accumulate significantly near the plasma meniscus. However, the majority of the extracted H$^-$ ions, which originate from the bulk plasma, are denoted as Volume Produced H$^-$ ($\mathrm{H^-_{VP}}$) ions in the simulations presented in this thesis, although they are predominantly produced via surface production in the real ion source. [Chapter 5]

- *How do biased surfaces in the ion source impact the co-extracted electron current and plasma properties near the PG?*

  - Biasing of the PG above the floating potential causes more electrons to be collected on the surface of the PG and fewer electrons extracted through the meniscus. This observation is in agreement with experimental investigations. Steps towards the simulation of an electron-attracting sheath have been taken, and show a further reduction of the co-extracted electron current. [Chapter 6]

  - Biased surfaces introduced in the ion source near the PG can strongly reduce the amount of co-extracted electrons. One effective example is the EF which consists of cylindrical rods placed on each aperture row or column close to the PG. By biasing the EF close to the plasma potential, a significant reduction in the co-extracted electron current density was obtained. Without the EF, a large portion of electrons

drift across multiple aperture columns in the horizontal direction (along $\mathbf{B}_{\mathrm{FF}}$) before extraction, but when the EF is present, these electrons are collected on the fence. Since the Bias Plate (BP) is not included in the ONIX domain, simulations comparing the effect of the EF and BP have not been done. [Chapter 6]

- *Why are more electrons extracted during operation with deuterium than with hydrogen?*
  - During operation with deuterium, the floating potential is higher, which leads to a deeper Debye sheath towards the PG and decreases the electron flux towards its surface. This results in a higher electron accumulation near the meniscus, and in turn a higher co-extracted electron current. [Chapter 5]
- *What are viable strategies for reducing the amount of co-extracted electrons?*
  - Elevated electron temperatures will strongly increase the co-extraction of electrons. Keeping the electron temperature around 1 eV can reduce the amount of co-extracted by a factor of 4 compared to 2 eV.
  - Simulation of PG bias variation was made possible by the development of a new particle injection method (flux-injection). Biasing the PG above floating potential offers a mechanism to reduce the co-extraction of electrons by collecting the electrons on the surface of the PG. [Chapter 6]
  - Introducing an electron fence in close proximity to the PG, based on experimental investigations in NIFS, has been shown to strongly reduce the amount of co-extracted electrons. The construction of an electron fence is planned for BUG in 2024. [Chapter 6]
  - Multiple PG geometries were studied, all with an aperture diameter of 14 mm, but with varying angles of the plasma-facing surface, with and without a flattened knife edge of the PG. However, none of the PG geometries tested had a large impact on the amount of co-extracted electrons. [Chapter 8]

Physics of ion extraction and beam optics

It's well-established that certain plasma parameters and configurations play an important role in both ion accumulation near the PG and the behavior of ion beamlets post-extraction. Insights derived from 3D-PIC simulations using ONIX have aided in the understanding of beamlet formation. However, it is important to note that two key parameters do not match the experimental conditions: the extracted current density of NIs is lower than the ITER parameters, which means that the results are in an underperveant regime. Also, the number of $\mathrm{H}^-_{\mathrm{SP}}$ ions

accumulated in the plasma is lower than in experiments, therefore, additional H^-_{VP} ions are injected into the simulation domain.

- *Which plasma properties determine the accumulation of NI and formation of an ion-ion plasma near the PG in NI sources?*
  - The depth of the Virtual Cathode (VC), which forms in front of the walls from which H^-_{SP} ions are emitted, determines the accumulation of H^-_{SP} ions in the plasma volume. [Chapter 5]
  - The primary determinants for the depth of the VC are the H^-_{SP} ion emission rate, temperature, and the density of the surrounding plasma. For a given plasma density, the H^-_{SP} ion density saturates at a specific emission rate. The higher the plasma density, the more the VC formation is shielded by positive ions, and thus more H^-_{SP} ions can accumulate in the plasma. [Chapter 5]
  - Biasing of the PG did not show a large impact on the accumulation of H^-_{SP} ions. [Chapter 6]
- *Which plasma properties determine the beam optics and what can be done to reduce the divergence of NI beamlets?*
  - H^-_{VP} ions and H^-_{SP} ions have different angular distributions in the accelerated beamlets. Most extracted H^-_{SP} ions are directly extracted without entering the bulk plasma since the meniscus penetrates past the knife of the PG, and the H^-_{SP} ions are accelerated perpendicular to the beam axis, resulting in a high divergence ($\sim$ 100 mrad). [Chapter 7]
  - The Debye sheath between the plasma and the PG reduces the divergence of the H^-_{VP} ions since these ions are reflected by the sheath towards the PG and therefore cross the meniscus closer to its center. This was revealed by coupling ONIX with the ion-optics code IBSimu. [Chapter 7]
  - The bias of the PG impacts the energy of the H^-_{SP} ions in the plasma by changing the depth of the Debye sheath between the plasma and the PG. For a sheath at floating potential, the H^-_{SP} ions are accelerated by approximately 5 eV along the normal of the PG. This increases the energy component perpendicular to the beam axis of the H^-_{SP} ions by $\approx$ 3.5 eV. These ions will have a higher divergence at the end of the grid system than ions that have a smaller perpendicular energy component. However, since most of the H^-_{SP} ions are directly extracted in the simulations, the bias of the

PG only has a small impact on the beam divergence (a few mrad) of the H^-_{SP} ions. [Chapter 6]

- *Which plasma grid geometries are the most favorable for extraction of NIs?*
  - None of the PG geometries studied in the scope of this thesis had a large impact on the meniscus shape. [Chapter 8]
  - The angular distribution and the spatial ion distribution across the aperture play important roles in the beam optics of extracted NIs from specific grid geometries. [Chapter 8]
  - The plasma-facing angle of the PG impacts the extraction probability and accumulation of H^-_{SP} ions due to the acceleration by the Debye sheath. With a shallow angle, more ions are transported to the central region near the meniscus. In addition, a shallow angle leads to the lowest core divergence of the extracted H^- ion beam since more ions are extracted through the central region of the PG. [Chapter 8]

Multiple avenues for continuing the work are possible. Firstly, there's a necessity to incorporate a self-consistent physical process for the accumulation of H^-_{SP} ions in the simulated plasma volume. This is challenging due to the time scale and domain size constraints inherent in 3D-PIC modeling. Experimentally, it has been shown that a majority of H^- ions in the extraction region are surface produced, but as of now, reaching equivalent densities of H^-_{SP} ions with 3D-PIC modeling has not been achieved.

The behavior of deuterium in comparison to hydrogen is another area to probe deeper into, especially given the differences in the co-extraction of electrons. This work has provided insights into the physical effects governing the co-extraction of electrons on time scales on the order of μs, but in experiments, a time-dependent effect on the order of seconds (and longer) also shows an increase in the co-extracted electron current density. The heavier isotope impacts the Cs adsorption and desorption which changes the work function over time. Finding the corresponding properties of the plasma or the conversion surfaces that govern this increase in the co-extracted electron current density is of high importance for limiting this effect.

Bibliography

[1] United Nations Development Programme, "Human development report," New York, NY, 2019.

[2] I. P. on Climate Change (IPCC), Global Warming of 1.5°C: IPCC Special Report on Impacts of Global Warming of 1.5°C above Pre-industrial Levels in Context of Strengthening Response to Climate Change, Sustainable Development, and Efforts to Eradicate Poverty. Cambridge University Press, 2022.

[3] National Aeronautics and Space Administration. "Climate change: How do we know?" (2020), [Online]. Available: `https://climate.nasa.gov/evidence/` (visited on 05/05/2023).

[4] ITER Organization. "Safety and environment." (2024), [Online]. Available: `https://www.iter.org/mach/safety` (visited on 05/05/2023).

[5] A. Lépine-Szily and P. Descouvemont, Nuclear astrophysics: Nucleosynthesis in the Universe, *Int. J. Astrobiol.*, **11**, no. 4, pp. 243–250, 2012.

[6] EUROfusion. "Fusion on the sun." (2024), [Online]. Available: `https://euro-fusion.org/fusion/fusion-on-the-sun/`.

[7] F. Chen, Introduction to Plasma Physics and Controlled Fusion; 3rd ed. Springer, 2016.

[8] W. M. Stacey, Fusion: An Introduction to the Physics and Technology of Magnetic Confinement Fusion. Wiley, 2010.

[9] S. Pfalzner, An Introduction to Inertial Confinement Fusion. CRC Press, 2006.

[10] A. V. Burdakov, A. A. Ivanov, and E. P. Kruglyakov, Modern magnetic mirrors and their fusion prospects, *Plasma Phys. Control. Fusion*, **52**, no. 12, p. 124 026, 2010.

[11] M. Ariola and A. Pironti, Magnetic Control of Tokamak Plasmas. Springer London, 2008.

[12] J. Freidberg, Plasma Physics and Fusion Energy. Cambridge University Press, 2007.

[13] M. Kikuchi, A review of fusion and Tokamak research towards steady-state operation: A JAEA contribution, *Energies*, **3**, no. 11, pp. 1741–1789, 2010.

[14] V. Belyakov, A. Mineev, and V. Bykov, "Chapter 2 - Facilities with magnetic plasma confinement," in *Fundamentals of Magnetic Thermonuclear Reactor Design*, ser. Woodhead Publishing Series in Energy, V. Glukhikh, O. Filatov, and B. Kolbasov, Eds., Woodhead Publishing, 2018, pp. 7–37.

[15] P. C. Thonemann *et al.*, Controlled release of thermonuclear energy: Production of high temperatures and nuclear reactions in a gas discharge, *Nature*, **181**, no. 4604, pp. 217–220, 1958.

[16] N. J. Peacock *et al.*, Measurement of the electron temperature by Thomson scattering in Tokamak T3, *Nature*, **224**, no. 5218, pp. 488–490, 1969.

[17] Tokamak Fusion Test Reactor - Final conceptual design report, 1976.

[18] P. Rebut, R. Bickerton, and B. Keen, The Joint European Torus: Installation, first results and prospects, *Nucl. Fusion*, **25**, no. 9, p. 1011, 1985.

[19] ITER Organization. "About ITER." (2020), [Online]. Available: `https://www.iter.org/proj/inafewlines` (visited on 05/05/2023).

[20] D. Maisonnier *et al.*, DEMO and fusion power plant conceptual studies in Europe, *Fusion Eng. Des.*, **81**, no. 8, pp. 1123–1130, 2006, Proceedings of the Seventh International Symposium on Fusion Nuclear Technology (ISFNT7).

[21] G. Zhuang *et al.*, Progress of the CFETR design, *Nucl. Fusion*, **59**, no. 11, p. 112 010, 2019.

[22] A. J. Creely *et al.*, Overview of the SPARC Tokamak, *J. Plasma Phys.*, **86**, no. 5, p. 865 860 502, 2020.

[23] A. Komori *et al.*, Goal and achievements of Large Helical Device project, *Fusion Sci. Technol.*, **58**, no. 1, pp. 1–11, 2010.

[24] T. Klinger *et al.*, Overview of first Wendelstein 7-X high-performance operation, *Nucl. Fusion*, **59**, no. 11, p. 112 004, 2019.

[25] A. B. Zylstra *et al.*, Experimental achievement and signatures of ignition at the National Ignition Facility, *Phys. Rev. E*, **106**, no. 2, p. 025 202, 2022.

[26] R. Pearson, Preface to the special issue: The emergence of private fusion enterprises, *J. Fusion Energy*, **42**, no. 2, p. 47, 2023.

[27] J. D. Lawson, Some criteria for a power producing thermonuclear reactor, *Proc. Phys. Soc.*, **70**, no. 1, p. 6, 1957.

[28] K. Berkner, R. Pyle, and J. Stearns, Intense, mixed-energy hydrogen beams for CTR injection, *Nucl. Fusion*, **15**, no. 2, p. 249, 1975.

[29] U. Fantz *et al.*, Negative ion RF sources for ITER NBI: Status of the development and recent achievements, *Plasma Phys. Control. Fusion*, **49**, no. 12B, B563, 2007.

[30] R. S. Hemsworth *et al.*, Overview of the design of the ITER heating neutral beam injectors, *New J. Phys.*, **19**, no. 2, p. 025 005, 2017.

[31] R. Koch, Fast particle heating, *Fusion Sci. Technol.*, **57**, no. 2T, pp. 185–195, 2010.

[32] A. Chakraborty *et al.*, Diagnostic neutral beam for ITER-concept to engineering, *IEEE Trans. Plasma Sci.*, **38**, no. 3, pp. 248–253, 2010.

[33] P. Veltri *et al.*, Towards low divergence beams for the ITER neutral beam injection system, Talk presented at 8th International Symposium on Negative Ions, Beams and Sources (NIBS), 2022.

[34] V. Candeloro, E. Sartori, and G. Serianni, Influence of plasma parameters on the effectiveness of multi-cusp magnetic field confinement in negative ion sources, *J. Instrum.*, **18**, no. 06, p. C06028, 2023.

[35] U. Fantz *et al.*, Negative hydrogen ion sources for fusion: From plasma generation to beam properties, *Front. Phys.*, **9**, 2021.

[36] A. Staebler *et al.*, Development of a RF-driven ion source for the ITER NBI system, *Fusion Eng. Des.*, **84**, no. 2, pp. 265–268, 2009, Proceeding of the 25th Symposium on Fusion Technology (SOFT-25).

[37] T. Inoue *et al.*, 1 MeV, ampere class accelerator R&D for ITER, *Nucl. Fusion*, **46**, no. 6, S379, 2006.

[38] P. Massmann *et al.*, Design and fabrication of the "ITER-like" SINGAP D- acceleration system, *Fusion Eng. Des.*, **74**, no. 1, pp. 409–412, 2005, Proceedings of the 23rd Symposium on Fusion Technology (SOFT-23).

[39] R. S. Hemsworth *et al.*, Status of the ITER heating neutral beam system, *Nucl. Fusion*, **49**, no. 4, p. 045 006, 2009.

[40] R. K. Janev, D. Reiter, and U. Samm, Collision processes in low-temperature hydrogen plasmas. Forschungszentrum, Zentralbibliothek, 2003, vol. 4105.

[41] S. Lishev *et al.*, Fluid-model analysis on discharge structuring in the RF-driven prototype ion-source for ITER NBI, *Plasma Sources Sci. Technol.*, **27**, no. 12, p. 125 008, 2018.

[42] V. Toigo *et al.*, Progress in the realization of the PRIMA neutral beam test facility, *Nucl. Fusion*, **55**, no. 8, p. 083 025, 2015.

[43] V. Toigo *et al.*, The PRIMA test facility: SPIDER and MITICA test-beds for ITER neutral beam injectors, *New J. Phys.*, **19**, no. 8, p. 085 004, 2017.

[44] P. Agostinetti *et al.*, Physics and engineering design of the accelerator and electron dump for SPIDER, *Nucl. Fusion*, **51**, no. 6, p. 063 004, 2011.

[45] P. Agostinetti *et al.*, Detailed design optimization of the MITICA negative ion accelerator in view of the ITER NBI, *Nucl. Fusion*, **56**, no. 1, p. 016 015, 2015.

[46] H. P. L. de Esch *et al.*, Physics design of the HNB accelerator for ITER, *Nucl. Fusion*, **55**, no. 9, p. 096 001, 2015.

[47] M. Wada *et al.*, Damage to N-NBI systems due to positive ion back-streaming, *AIP Conf. Proc.*, **2373**, no. 1, p. 080 001, 2021.

[48] L. Schiesko *et al.*, A study on backstreaming positive ions on a high power negative ion source for fusion, *Nucl. Fusion*, **51**, no. 11, p. 113 021, 2011.

[49] A. Krylov and R. S. Hemsworth, Gas flow and related beam losses in the ITER neutral beam injector, *Fusion Eng. Des.*, **81**, no. 19, pp. 2239–2248, 2006.

[50] N. den Harder *et al.*, Modeling neutral beam transport in fusion experiments: Studying the effects of reionisation and deflection, *Fusion Eng. Des.*, **146**, pp. 518–521, 2019, Proceedings of the 30th Symposium on Fusion Technology (SOFT-30).

[51] A. Ferro *et al.*, The design of the residual ion dump power supply for ITER neutral beam injector, *Fusion Eng. Des.*, **124**, pp. 69–72, 2017, Proceedings of the 29th Symposium on Fusion Technology (SOFT-29).

[52] M. Urbani *et al.*, The ITER neutral beam front end components integration, *Fusion Eng. Des.*, **88**, no. 9, pp. 2110–2114, 2013, Proceedings of the 27th Symposium On Fusion Technology (SOFT-27).

[53] P. Franzen *et al.*, In-line magnetic residual ion dump for the ITER neutral beam system, *Fusion Eng. Des.*, **66-68**, pp. 585–590, 2003, 22nd Symposium on Fusion Technology.

[54] P. Franzen *et al.*, An alternative residual ion dump for the ITER neutral beam system, *Fusion Eng. Des.*, **56-57**, pp. 511–515, 2001.

[55] T. Tabata and T. Shirai, Analytic cross sections for collisions of H^+, H_2^+, H_3^+, H, H_2, and H^- with hydrogen molecules, *At. Data Nucl. Data Tables*, **76**, no. 1, pp. 1–25, 2000.

[56] M. Bacal and M. Wada, Negative hydrogen ion production mechanisms, *Appl. Phys. Rev.*, **2**, no. 2, p. 021 305, 2015.

[57] D. Wünderlich *et al.*, NNBI for ITER: Status of long pulses in deuterium at the test facilities BATMAN upgrade and ELISE, *Nucl. Fusion*, **61**, no. 9, p. 096 023, 2021.

[58] D. Wünderlich *et al.*, Formation of large negative deuterium ion beams at ELISE, *Rev. Sci. Instrum.*, **90**, no. 11, p. 113 304, 2019.

[59] D. Wünderlich *et al.*, Long pulse, high power operation of the ELISE test facility, *AIP Conf. Proc.*, **1869**, no. 1, p. 030 003, 2017.

[60] A. Pimazzoni *et al.*, Co-extracted electrons and beam inhomogeneity in the large negative ion source SPIDER, *Fusion Eng. Des.*, **168**, p. 112 440, 2021.

[61] M. Fröschle *et al.*, Magnetic filter field for ELISE - Concepts and design, *Fusion Eng. Des.*, **88**, no. 6, pp. 1015–1019, 2013.

[62] R. Gutser *et al.*, Negative hydrogen ion transport in RF-driven ion sources for ITER NBI, *Plasma Phys. Control. Fusion*, **51**, no. 4, p. 045 005, 2009.

[63] M. Barbisan, U. Fantz, and D. Wünderlich, Influence of the magnetic filter field topology on the beam divergence at the ELISE test facility, 1, **1869**, 2017, p. 030 030.

[64] N. den Harder *et al.*, Computational design of magnetic beamlet deflection correction for NNBI, *Fusion Eng. Des.*, **173**, p. 112 837, 2021.

[65] ITER Technical Basis (ITER EDA Documentation Series 24). Vienna: International Atomic Energy Agency, 2002.

[66] U. Fantz *et al.*, Towards powerful negative ion beams at the test facility ELISE for the ITER and DEMO NBI systems, *Nucl. Fusion*, **57**, no. 11, p. 116 007, 2017.

[67] U. Fantz, "RF-driven ion sources for neutral beam injectors for fusion devices," in *Physics and Applications of Hydrogen Negative Ion Sources*. Cham: Springer International Publishing, 2023, pp. 427–463.

[68] B. Heinemann *et al.*, Upgrade of the BATMAN test facility for H^- source development, *AIP Conf. Proc.*, **1655**, no. 1, p. 060 003, 2015.

[69] B. Heinemann *et al.*, Achievements of the ELISE test facility in view of the ITER NBI, *Fusion Eng. Des.*, **146**, pp. 455–459, 2019, Proceedings of the 30th Symposium on Fusion Technology (SOFT-30).

[70] M. Lieberman and A. Lichtenberg, Principles of Plasma Discharges and Materials Processing. Wiley, 1994.

[71] B. Smirnov and H. Reiss, Physics of Ionized Gases. Wiley, 2008.

[72] J. Townsend, The Theory of Ionization of Gases by Collision. Van Nostrand, 1910.

[73] H. Conrads and M. Schmidt, Plasma generation and plasma sources, *Plasma Sources Sci. Technol.*, **9**, no. 4, p. 441, 2000.

[74] P. Chabert and N. Braithwaite, Physics of Radio-Frequency Plasmas. Cambridge University Press, 2011.

[75] P. C. Stangeby, Plasma sheath transmission factors for Tokamak edge plasmas, *Phys. Fluids*, **27**, no. 3, p. 682, 1984.

[76] L. A. Schwager and C. K. Birdsall, Collector and source sheaths of a finite ion temperature plasma, *Phys. Fluids B*, **2**, no. 5, pp. 1057–1068, 1990.

[77] K.-U. Riemann, The Bohm criterion and sheath formation, *J. Phys. D: Appl. Phys*, **24**, no. 4, p. 493, 1991.

[78] S. Baalrud *et al.*, Interaction of biased electrodes and plasmas: Sheaths, double layers, and fireballs, *Plasma Sources Sci. Technol.*, **29**, no. 5, p. 053 001, 2020.

[79] B. Scheiner *et al.*, Theory of the electron sheath and presheath, *Phys. Plasmas*, **22**, no. 12, p. 123 520, 2015.

[80] M. Bacal, Volume production of hydrogen negative ions, *Nucl. Instrum. Methods Phys. Res. B*, **37-38**, pp. 28–32, 1989.

[81] J. P. Boeuf, B. Chaudhury, and L. Garrigues, Physics of a magnetic filter for negative ion sources. I. collisional transport across the filter in an ideal, 1D filter, *Phys. Plasmas*, **19**, no. 11, p. 113 509, 2012.

[82] D. Fink *et al.*, H^- extraction systems for CERN's Linac4 H^- ion source, *Nucl. Instrum. Methods Phys. Res. A*, **904**, pp. 179–187, 2018.

[83] L. Schiesko *et al.*, Magnetic field dependence of the plasma properties in a negative hydrogen ion source for fusion, *Plasma Phys. Control. Fusion*, **54**, no. 10, p. 105 002, 2012.

[84] D. Wünderlich *et al.*, Influence of the magnetic field topology on the performance of the large area negative hydrogen ion source test facility ELISE, *Plasma Phys. Control. Fusion*, **58**, no. 12, p. 125 005, 2016.

[85] M. Bacal and M. Wada, Negative ion source operation with deuterium, *Plasma Sources Sci. Technol.*, **29**, no. 3, p. 033 001, 2020.

[86] M. Bacal, Physics aspects of negative ion sources, *Nucl. Fusion*, **46**, no. 6, S250, 2006.

[87] U. Fantz *et al.*, Spectroscopy - a powerful diagnostic tool in source development, *Nucl. Fusion*, **46**, no. 6, S297–S306, 2006.

[88] J. R. Hiskes, Cross sections for the vibrational excitation of the $H_2(X^1\sum_g^+)$ state via electron collisional excitation of the higher singlet states, *J. Appl. Phys.*, **51**, no. 9, pp. 4592–4594, 1980.

[89] M. Bacal and M. Wada, Negative ion production by plasma-surface interaction in caesiated negative ion sources, *AIP Conf. Proc.*, **1515**, no. 1, pp. 41–48, 2013.

[90] B. Rasser, J. N. M. van Wunnik, and J. Los, Theoretical models of the negative ionization of hydrogen on clean tungsten, ceasiated tungsten and cesium surfaces at low energies, *Surf. Sci.*, **118**, pp. 697–710, 1982.

[91] J. N. M. van Wunnik, J. J. C. Geerlings, and J. Los, The velocity dependence of the negatively charged fraction of hydrogen scattered from cesiated tungsten surfaces, *Surf. Sci.*, **131**, no. 1, pp. 1–16, 1983.

[92] M. Seidl *et al.*, Negative surface ionization of hydrogen atoms and molecules, *J. Appl. Phys.*, **79**, no. 6, pp. 2896–2901, 1996.

[93] J. R. Hiskes and P. Schneider, Formation of H^- and D^- ions by hydrogen and deuterium particle backscattering from alkali-metal surfaces, *Phys. Rev. B*, **23**, pp. 949–956, 3 1981.

[94] H. B. Michaelson, The work function of the elements and its periodicity, *J. Appl. Phys.*, **48**, no. 11, pp. 4729–4733, 1977.

[95] G. Alton, Semi-empimcal mathematical relationships for electropositive adsorbate induced work function changes, *Surf. Sci.*, **175**, no. 1, pp. 226–240, 1986.

[96] S. Cristofaro *et al.*, Design and comparison of the Cs ovens for the test facilities ELISE and SPIDER, *Rev. Sci. Instrum.*, **90**, no. 11, p. 113 504, 2019.

[97] S. Cristofaro, R. Friedl, and U. Fantz, Correlation of Cs flux and work function of a converter surface during long plasma exposure for negative ion sources in view of ITER, *Plasma Res. Express*, **2**, no. 3, p. 035 009, 2020.

[98] A. Heiler, R. Friedl, and U. Fantz, Ultra-low work function of caesiated surfaces and impact of selected gas species, *J. Instrum.*, **19**, no. 1, p. C01057, 2024.

[99] Y. Belchenko, G. Dimov, and V. Dudnikov, A powerful injector of neutrals with a surface-plasma source of negative ions, *Nucl. Fusion*, **14**, no. 1, p. 113, 1974.

[100] M. Bacal *et al.*, Optimum plasma grid bias for a negative hydrogen ion source operation with Cs, *Rev. Sci. Instrum.*, **87**, no. 2, 02B132, 2016.

[101] A. Mimo *et al.*, Studies of Cs dynamics in large ion sources using the CsFlow3D code, *AIP Conf. Proc.*, **2052**, no. 1, p. 040 009, 2018.

[102] A. Mimo *et al.*, Modelling of caesium dynamics in the negative ion sources at BATMAN and ELISE, 1, **1869**, 2017, p. 030 019.

[103] U. Fantz, R. Friedl, and M. Fröschle, Controllable evaporation of cesium from a dispenser oven, *Rev. Sci. Instrum.*, **83**, no. 12, p. 123 305, 2012.

[104] M. Fröschle *et al.*, Recent developments at IPP on evaporation and control of caesium in negative ion sources, *Fusion Eng. Des.*, **84**, no. 2, pp. 788–792, 2009.

[105] C. Wimmer, L. Schiesko, and U. Fantz, Investigation of the boundary layer during the transition from volume to surface dominated H^- production at the BATMAN test facility, *Rev. Sci. Instrum.*, **87**, no. 2, 02B310, 2016.

[106] N. Hershkowitz, How does the potential get from A to B in a plasma? *IEEE Trans. Plasma Sci.*, **22**, no. 1, pp. 11–21, 1994.

[107] S. Nishioka *et al.*, Effect of Coulomb collision between surface produced H^- ions and H^+ ions on H^- extraction mechanism and beam optics in a Cs-seeded H^- ion source by 3D particle in cell model, *J. Appl. Phys.*, **123**, no. 6, p. 063 302, 2018.

[108] D. Wünderlich *et al.*, Effects of the magnetic field topology on the co-extracted electron current in a negative ion source for fusion, *J. Appl. Phys.*, **130**, no. 5, p. 053 303, 2021.

[109] R. Celiberto *et al.*, Cross section data for electron-impact inelastic processes of vibrationally excited molecules of hydrogen and its isotopes, *At. Data Nucl. Data Tables*, **77**, no. 2, pp. 161–213, 2001.

[110] B. Heinemann *et al.*, Design of the "half-size" ITER neutral beam source for the test facility ELISE, *Fusion Eng. Des.*, **84**, no. 2, pp. 915–922, 2009, Proceeding of the 25th Symposium on Fusion Technology (SOFT-25).

[111] D. Wünderlich *et al.*, Initial caesium conditioning in deuterium of the ELISE negative ion source, *Plasma Phys. Control. Fusion*, **60**, no. 8, p. 085 007, 2018.

[112] S. Abe *et al.*, Analysis of H^- extraction in the Linac4 negative ion source by 2.5D particle simulation, *AIP Conf. Proc.*, **2011**, no. 1, p. 080 020, 2018.

[113] D. Yordanov *et al.*, On the effect of biased surfaces in the vicinity of the large extraction area of the ELISE test facility, *J. Phys.: Conf. Ser.*, **2244**, no. 1, p. 012 050, 2022.

[114] K. Tsumori *et al.*, Challenges toward improvement of deuterium-injection power in the Large Helical Device negative-ion-based NBIs, *Nucl. Fusion*, **62**, no. 5, p. 056 016, 2022.

[115] U. Fantz *et al.*, A comparison of hydrogen and deuterium plasmas in the IPP prototype ion source for fusion, *AIP Conf. Proc.*, **1515**, no. 1, pp. 187–196, 2013.

[116] W. Kraus *et al.*, Deuterium results at the negative ion source test facility ELISE, *Rev. Sci. Instrum.*, **89**, no. 5, p. 052 102, 2018.

[117] C. D. Child, Discharge from hot CaO, *Phys. Rev. (Series I)*, **32**, pp. 492–511, 5 1911.

[118] S. T. Kosonen *et al.*, Critical assessment of the applicability of the Child-Langmuir law to plasma ion source extraction systems, *Plasma Sources Sci. Technol.*, **32**, no. 7, p. 075 005, 2023.

[119] T. Kalvas, Development and use of computational tools for modelling negative hydrogen ion source extraction systems, PhD thesis, University of Jyväskylä, 2013.

[120] K. Miyamoto *et al.*, Effect of basic physical parameters to control plasma meniscus and beam halo formation in negative ion sources, *J. Appl. Phys.*, **114**, no. 10, p. 103 302, 2013.

[121] S. Nishioka *et al.*, Study of plasma meniscus formation and beam halo in negative ion source using the 3D3VPIC model, *AIP Conf. Proc.*, **1655**, no. 1, p. 020 012, 2015.

[122] S. Okuda *et al.*, Study of plasma meniscus formation and beam halo in negative hydrogen ion sources, *AIP Conf. Proc.*, **1515**, no. 1, pp. 107–113, 2013.

[123] M. Lindqvist *et al.*, From meniscus formation to accelerated H^- beam: Coupling of 3D-PIC and ion-optics simulations, *Nucl. Fusion*, **62**, no. 12, p. 126 068, 2022.

[124] U. Fantz and D. Wünderlich, A novel diagnostic technique for H^- (D^-) densities in negative hydrogen ion sources, *New J. Phys.*, **8**, no. 12, p. 301, 2006.

[125] B. Heinemann *et al.*, Towards large and powerful radio frequency driven negative ion sources for fusion, *New J. Phys.*, **19**, no. 1, p. 015 001, 2017.

[126] A. Mimo *et al.*, Cavity ring-down spectroscopy system for the evaluation of negative hydrogen ion density at the ELISE test facility, *Rev. Sci. Instrum.*, **91**, no. 1, p. 013 510, 2020.

[127] C. Wimmer, M. Lindauer, and U. Fantz, Determination of the Cs distribution along a line of sight by the Zeeman splitting in an inhomogeneous magnetic field, *J. Phys. D: Appl. Phys.*, **51**, no. 39, p. 395 203, 2018.

[128] R. Nocentini *et al.*, Beam diagnostic tools for the negative hydrogen ion source test facility ELISE, *Fusion Eng. Des.*, **88**, no. 6, pp. 913–917, 2013, Proceedings of the 27th Symposium On Fusion Technology (SOFT-27).

[129] G. Orozco *et al.*, Design and first results of a retractable 1D-CFC beam target for BATMAN upgrade, *Fusion Eng. Des.*, **165**, p. 112 225, 2021.

[130] I. Mario *et al.*, Reconstruction of the large multi-aperture beam via IR calorimetry technique and beam emission spectroscopy at the ELISE test facility, *Nucl. Fusion*, **60**, no. 6, p. 066 025, 2020.

[131] A. Hurlbatt *et al.*, Improved understanding of beamlet deflection in ITER-relevant negative ion beams through forward modelling of beam emission spectroscopy, *Fusion Eng. Des.*, **153**, p. 111 486, 2020.

[132] A. Hurlbatt *et al.*, First direct comparison of whole beam and single beamlet divergences in a negative ion source with simultaneous BES and CFC tile calorimetry measurements, *AIP Adv.*, **11**, no. 2, p. 025 330, 2021.

[133] M. Barbisan *et al.*, Beam characterization by means of emission spectroscopy in the ELISE test facility, *Plasma Phys. Control. Fusion*, **59**, no. 5, p. 055 017, 2017.

[134] F. Taccogna *et al.*, Modeling of a negative ion source. III. two-dimensional structure of the extraction region, *Phys. Plasmas*, **17**, no. 6, p. 063 502, 2010.

[135] F. Taccogna *et al.*, Plasma grid shape and size effects on the extraction of negative ions, *AIP Conf. Proc.*, **1515**, no. 1, pp. 3–11, 2013.

[136] F. Taccogna and P. Minelli, PIC modeling of negative ion sources for fusion, *New J. Phys.*, **19**, no. 1, p. 015 012, 2017.

[137] G. Fubiani *et al.*, Modeling of plasma transport and negative ion extraction in a magnetized radio-frequency plasma source, *New J. Phys.*, **19**, no. 1, p. 015 002, 2017.

[138] A. Revel *et al.*, Massive parallel 3D PIC simulation of negative ion extraction, *J. Appl. Phys.*, **122**, no. 10, p. 103 302, 2017.

[139] S. Nishioka *et al.*, Study of ion-ion plasma formation in negative ion sources by a three-dimensional in real space and three-dimensional in velocity space particle in cell model, *J. Appl. Phys.*, **119**, p. 023 302, 2016.

[140] D. Wünderlich *et al.*, Review of particle-in-cell modeling for the extraction region of large negative hydrogen ion sources for fusion, *Rev. Sci. Instrum.*, **89**, no. 5, p. 052 001, 2018.

[141] D. Matsushita *et al.*, Modeling of the plasma electrode bias in the negative ion sources with 1D PIC method, *AIP Conf. Proc.*, **1097**, no. 1, pp. 38–46, 2009.

[142] D. Wünderlich, R. Gutser, and U. Fantz, PIC code for the plasma sheath in large caesiated RF sources for negative hydrogen ions, *Plasma Sources Sci. Technol.*, **18**, no. 4, p. 045 031, 2009.

[143] F. Taccogna *et al.*, Negative-ion-source modeling: From expansion to extraction region, *IEEE Trans. Plasma Sci.*, **36**, no. 4, pp. 1589–1599, 2008.

[144] T. Sakurabayashi, A. Hatayama, and M. Bacal, Effects of the weak magnetic field and electron diffusion on the spatial potential and negative ion transport in the negative ion source, *Rev. Sci. Instrum.*, **75**, no. 5, pp. 1770–1773, 2004.

[145] K. Miyamoto *et al.*, Numerical analysis of surface produced H^- ions by using two-dimensional particle-in-cell method, *Rev. Sci. Instrum.*, **83**, no. 2, 02A723, 2012.

[146] F. Taccogna *et al.*, The characterization and optimization of NIO1 ion source extraction aperture using a 3D particle-in-cell code, *Rev. Sci. Instrum.*, **87**, no. 2, 02B145, 2015.

[147] S. Nishioka *et al.*, Code-to-code benchmark tests for 3D simulation models dedicated to the extraction region in negative ion sources, *AIP Conf. Proc.*, **1869**, no. 1, p. 050 006, 2017.

[148] S. Nishioka, Study of formation mechanism of ion-ion plasma layer and negative ion beam optics in negative hydrogen ion sources, PhD thesis, Keio University, 2018.

[149] M. Lindqvist *et al.*, Effects of the extraction voltage on the beam divergence for a H^- ion source, *J. Appl. Phys.*, **126**, no. 12, p. 123 303, 2019.

[150] S. Mochalskyy, Modeling of the negative ion extraction from a hydrogen plasma source : application to ITER neutral beam injector, PhD thesis, Université Paris Sud - Paris XI, 2011.

[151] S. Mochalskyy *et al.*, 3D numerical simulations of negative hydrogen ion extraction using realistic plasma parameters, geometry of the extraction aperture and full 3D magnetic field map, *Rev. Sci. Instrum.*, **85**, no. 2, 02B301, 2014.

[152] S. Mochalskyy *et al.*, Towards a realistic 3D simulation of the extraction region in ITER NBI relevant ion source, *Nucl. Fusion*, **55**, no. 3, p. 033 011, 2015.

[153] S. Mochalskyy *et al.*, Comparison of ONIX simulation results with experimental data from the BATMAN testbed for the study of negative ion extraction, *Nucl. Fusion*, **56**, no. 10, p. 106 025, 2016.

[154] I. M. Montellano *et al.*, 3D-PIC modelling of a low temperature plasma sheath with wall emission of negative particles and its application to NBI sources, *J. Phys. D: Appl. Phys.*, **52**, no. 23, p. 235 202, 2019.

[155] M. Lindqvist *et al.*, Sensitivity of the negative ion beam extraction to initial plasma parameters by 3D particle modelling, *Plasma Sources Sci. Technol.*, **31**, no. 12, p. 125 001, 2022.

[156] G. Fubiani, L. Garrigues, and J. P. Boeuf, Modeling of negative ion extraction from a magnetized plasma source: Derivation of scaling laws and description of the origins of aberrations in the ion beam, *Phys. Plasmas*, **25**, no. 2, p. 023 510, 2018.

[157] A. Hatayama *et al.*, Present status of numerical modeling of hydrogen negative ion source plasmas and its comparison with experiments: Japanese activities and their collaboration with experimental groups, *New J. Phys.*, **20**, no. 6, p. 065 001, 2018.

[158] I. M. Montellano, Application of a 3D Monte Carlo PIC code for modeling the particle extraction from negative ion sources, PhD thesis, Universität Augsburg, 2020.

[159] C. K. Birdsall and A. B. Langdon, Plasma Physics via Computer Simulation. McGraw-Hill, 1991.

[160] T. Takizuka and H. Abe, A binary collision model for plasma simulation with a particle code, *J. Comput. Phys.*, **25**, no. 3, pp. 205–219, 1977.

[161] K. Nanbu, Probability theory of electron-molecule, ion-molecule, molecule-molecule, and coulomb collisions for particle modeling of materials processing plasmas and cases, *IEEE Trans. Plasma Sci.*, **28**, no. 3, pp. 971–990, 2000.

[162] Y. N. Grigoryev, V. A. Vshivkov, and M. P. Fedoruk, Numerical "Particle-in-Cell" Methods: Theory and Applications. De Gruyter, 2002.

[163] R. W. Hockney and J. W. Eastwood, Computer simulation using particles. Hilger, 1988.

[164] H. Qin *et al.*, Why is Boris algorithm so good? *Phys. Plasmas*, **20**, no. 8, p. 084 503, 2013.

[165] V. Ufnarovski and A. Holst, Matrix Theory. KFS AB, 2012.

[166] J. R. Shewchuk, "An introduction to the conjugate gradient method without the agonizing pain," Carnegie Mellon University, Usa, Tech. Rep., 1994.

[167] F. Gibou *et al.*, A second-order-accurate symmetric discretization of the Poisson equation on irregular domains, *J. Comput. Phys.*, **176**, no. 1, pp. 205–227, 2002.

[168] C.-K. Huang *et al.*, Finite grid instability and spectral fidelity of the electrostatic particle-in-cell algorithm, *Comput. Phys. Commun.*, **207**, pp. 123–135, 2016.

[169] R. Courant, K. Friedrichs, and H. Lewy, Über die partiellen differenzengleichungen der mathematischen physik, *Mathematische Annalen*, **100**, pp. 32–74, 1928.

[170] A. Isidori, Control Theory for Automation: Fundamentals - Springer Handbook of Automation. Springer Berlin Heidelberg, 2009.

[171] J. Qiang and X. Li, Particle-field decomposition and domain decomposition in parallel particle-in-cell beam dynamics simulation, *Comput. Phys. Commun.*, **181**, no. 12, pp. 2024–2034, 2010.

[172] B. di Martino *et al.*, Parallel PIC plasma simulation through particle decomposition techniques, *Parallel Comput.*, **27**, no. 3, pp. 295–314, 2001.

[173] F. Iannone *et al.*, MARCONI-FUSION: The new high performance computing facility for European nuclear fusion modelling, *Fusion Eng. Des.*, **129**, pp. 354–358, 2018.

[174] H. Shoukourian *et al.*, SuperMUC - The first high-temperature direct liquid cooled Petascale Supercomputer operated by LRZ. 2019.

[175] T. Kalvas *et al.*, IBSIMU: A three-dimensional simulation software for charged particle optics, *Rev. Sci. Instrum.*, **81**, no. 2, 02B703, 2010.

[176] R. Nocentini, Private Communication, 2020.

[177] A. Revel *et al.*, Transport of realistic beams in ITER neutral beam injector accelerator, en, *Nucl. Fusion*, **53**, no. 7, p. 073 027, 2013.

[178] Y. Ohara, "Beam trajectory calculation code of ion source "IONORB"," Japan Atomic Energy Research Institute, Tech. Rep. JAERI-M-6757, 1976.

[179] W. Herrmannsfeldt, "Electron trajectory program," Stanford Linear Accelerator Center, Tech. Rep. Slac-226 Uc-28 (A), 1979.

[180] J. Pamela, A model for negative ion extraction and comparison of negative ion optics calculations to experimental results, *Rev. Sci. Instrum.*, **62**, no. 5, pp. 1163–1172, 1991.

[181] P. Spädtke and S. Wipf, KOBRA3, A Code for the Calculation of Space-Charge Influenced Trajectories in 3 Dimensions. GSI, 1989.

[182] Vector Fields Co. Ltd, Opera-3D, `http://operafea.com/`, 20, 2020.

[183] J. Hiratsuka *et al.*, Achievement of high power and long pulse negative ion beam acceleration for JT-60SA NBI, *Rev. Sci. Instrum.*, **91**, no. 2, p. 023 506, 2020.

[184] M. J. Singh and H. P. L. de Esch, Physics design of a 100 keV acceleration grid system for the diagnostic neutral beam for international tokamak experimental reactor, *Rev. Sci. Instrum.*, **81**, no. 1, p. 013 305, 2010.

[185] H. P. L. de Esch *et al.*, The optimization of neutral beams for ignition and burn control on next-step reactors, *Fusion Eng. Des.*, **26**, no. 1, pp. 589–604, 1995, Proceedings of the Fifth International Toki Conference on Plasma Physics and Controlled Nuclear Fusion (ITC-5).

[186] G. Chitarin *et al.*, Experimental validation of an innovative deflection compensation method in a multi-beamlet negative-ion accelerator, *AIP Conf. Proc.*, **1869**, no. 1, p. 030 026, 2017.

[187] N. den Harder *et al.*, ITER-HNB plasma and extraction grids in BUG: Characterization of magnetic deflection correction, *J. Phys. Conf. Ser.*, **2244**, no. 1, p. 012 053, 2022.

[188] N. den Harder *et al.*, Computationally studying H^- extraction and beamlet formation: The impact of the plasma model, *J. Instrum.*, **18**, no. 08, p. C08005, 2023.

[189] E. Speth *et al.*, Overview of the RF source development programme at IPP Garching, *Nucl. Fusion*, **46**, no. 6, S220–S238, 2006.

[190] P. McNeely *et al.*, A Langmuir probe system for high power RF-driven negative ion sources on high potential, *Plasma Sources Sci. Technol.*, **18**, no. 1, p. 014 011, 2008.

[191] S. Briefi and U. Fantz, Spectroscopic investigations of the ion source at BATMAN upgrade, *AIP Conf. Proc.*, **2052**, no. 1, p. 040 005, 2018.

[192] C. Wimmer *et al.*, Improved understanding of the Cs dynamics in large H^- sources by combining TDLAS measurements and modeling, *AIP Conf. Proc.*, **2011**, no. 1, p. 060 001, 2018.

[193] A. Manhard *et al.*, "Spectroscopic studies on positive ion based neutral beam injection systems," Max-Planck-Institut für Plasmaphysik, IPP 4/289, 2008.

[194] U. Fantz *et al.*, Technology developments for a beam source of an NNBI system for DEMO, *Fusion Eng. Des.*, **136**, pp. 340–344, 2018.

[195] U. Fantz *et al.*, Physical performance analysis and progress of the development of the negative ion RF source for the ITER NBI system, *Nucl. Fusion*, **49**, no. 12, p. 125 007, 2009.

[196] M. Giacomin, Application of collisional radiative models for atomic and molecular hydrogen to a negative ion source for fusion, Master's thesis, Università degli Studi di Padova, 2017.

[197] D. Wünderlich *et al.*, On the proton flux toward the plasma grid in a RF-driven negative hydrogen ion source for ITER NBI, *Plasma Phys. Control. Fusion*, **54**, no. 12, p. 125 002, 2012.

[198] F. Merk *et al.*, TALIF at H^- ion sources for the determination of the density and EDF of atomic hydrogen, *J. Phys. D: Appl. Phys.*, **56**, no. 15, p. 155 201, 2023.

[199] H. Nakano *et al.*, Initial results of a plasma grid comparison experiment between NIFS and ITER-like types at BATMAN upgrade, Talk presented at 7th International Symposium on Negative Ions, Beams and Sources (NIBS), 2020.

[200] J. Lettry *et al.*, Beam formation studies on the CERN IS03b H source, *J. Phys. Conf. Ser.*, **2244**, no. 1, p. 012 036, 2022.

[201] R. Gutser *et al.*, Simulations for the generation and extraction of negative hydrogen ions in RF-driven ion sources, *AIP Conf. Proc.*, **1097**, no. 1, pp. 297–306, 2009.

Acknowledgements

Finishing this thesis has been a challenge, and I could not have done it without a lot of support. To everyone who has helped, and to everyone who has supported me, thank you! Firstly, I would like to thank all the members of the ONIX team, who have spent many long Friday afternoon discussions with me.

- **Prof. Dr.-Ing. Ursel Fantz**, your supervision has been excellent and I am grateful that you welcomed me to ITED.
- **Prof. Dr. Tiberiu Minea**, thank you for the guidance and supervision, and for all the ideas and advice you have given me.
- **Dr. Dirk Wünderlich**, our frequent discussions have been a cornerstone of this project.
- **Dr. Serhiy Mochalskyy**, thank you for teaching me everything about the ONIX code.
- **Dr. Adrien Revel**, thank you for all the discussions on numerical modeling.
- **Dr. Alessandro Mimo**, thank you for all the times helped me when I was struggling.

Thank you to our collaborators at CERN in Switzerland: **Dr. Anna Vnuchenko** and **Dr. Jacques Lettry**.

Thank you to our collaborators at Keio University in Japan: **Prof. Akiyoshi Hatayama** and **Prof. Kazuo Hoshino**, who also taught me PIC modeling during my Master's degree.

Dr. Niek den Harder, thank you for all the work with the ONIX-IBSimu coupling, and for sharing my interest in making beautiful plots.

All other coworkers in ITED and LPGP with whom I have shared many pleasant moments during the last few years: **Bernd Heinemann**, **Dr. Christian Hopf**, **Christian Kiefer**, **Dr. Christian Wimmer**, **Dr. Dimitar Yordanov**, **Daniele Mussini**, **Dr. Dominikus Zielke**, **Dr. Federico D'Isa**, **Dr. Federica Bonomo**, **Dr. Frederik Merk**, **Dr. Georgiy Zadvitskiy**, **Dr. Giuseppe Starnella**, **Guillermo Orozco**, **Ian Boshoff**, **Dr. Isabella Mario**, **Karin Eisenträger**, **Dr. Loïc Schiesko**, **Marc Bisson**, **Kurt Ritter**, **Markus Fröschle**, **Dr. Michael Barnes**, **Nicolas Dessaints**, **Dr. Riccardo Nocentini**, **Richard Bergmayr**, **Dr. Roland Friedl**, **Dr. Sofia Cristofaro**, and **Waltraud Sinz**.

My family, mamma, pappa and Mati, thank you for your support, and for helping me focus on what matters. You are all an inspiration. Lastly, a special thank you to Perla, you have done more than I ever could have asked for, thank you for your love.